

TECHNISCHE UNIVERSITÄT MÜNCHEN  
MAX-PLANCK-INSTITUT FÜR EXTRATERRESTRISCHE PHYSIK

PhD Thesis

**Study of highly magnetised  
accreting neutron stars in the  
Magellanic Clouds and beyond**

Georgios Vasilopoulos

---

# TECHNISCHE UNIVERSITÄT MÜNCHEN

MAX-PLANCK-INSTITUT FÜR EXTRATERRESTRISCHE  
PHYSIK

## **Study of highly magnetised accreting neutron stars in the Magellanic Clouds and beyond**

GEORGIOS VASILOPOULOS

Vollständiger Abdruck der von der Fakultät für Physik der Technischen Universität  
München zur Erlangung des akademischen Grades eines

Doktors der Naturwissenschaften

genehmigten Dissertation

Vorsitzender: Prof. Dr. Andreas Weiler  
Prüfer der Dissertation: 1. Priv.-Doz. Dr. Jochen Greiner  
2. Prof. Dr. Lothar Oberauer

Die Dissertation wurde am 23.07.2018 bei der Technischen Universität München  
eingereicht und durch die Fakultät für Physik am 04.10.2018 angenommen.

I confirm that this PhD thesis is my own work and I have documented all sources and material used.

Munich,

Georgios Vasilopoulos

# Contents

<b>Zusammenfassung</b>	<b>ix</b>
<b>Abstract</b>	<b>xi</b>
<b>List of original publications</b>	<b>xiii</b>
<b>1 Overview</b>	<b>1</b>
<b>I Introduction</b>	<b>3</b>
<b>2 X-ray binaries</b>	<b>5</b>
2.1 High mass X-ray binaries . . . . .	6
2.1.1 Be X-ray binaries . . . . .	6
2.1.2 Supergiant X-ray binaries . . . . .	7
2.2 Ultra-luminous X-ray binaries . . . . .	8
<b>3 Basic physical mechanisms in X-ray binaries</b>	<b>9</b>
3.1 Interaction between the accretion disc and the magnetised NS . . . . .	9
3.1.1 Propeller transition . . . . .	10
3.2 Radiative transfer in X-ray binaries . . . . .	12
3.2.1 X-ray emission . . . . .	12
3.2.2 X-ray absorption . . . . .	14
3.3 Magnetised NS . . . . .	14
3.3.1 Accretion column . . . . .	14
3.3.2 Soft excess . . . . .	15
3.4 X-ray pulsars: understanding the emission pattern . . . . .	15
<b>4 The Magellanic Clouds</b>	<b>21</b>
<b>II Data and methodology</b>	<b>23</b>
<b>5 Observations and data analysis</b>	<b>25</b>
5.1 Multi-wavelength observations . . . . .	25
5.1.1 X-ray . . . . .	25
5.1.2 Optical . . . . .	27
5.2 Measurement of basic parameters from the X-ray data . . . . .	28
5.2.1 Temporal analysis . . . . .	28
5.2.2 Spectral analysis . . . . .	29
5.3 OGLE data: Time series analysis . . . . .	30

<b>III</b>	<b>High mass X-ray binaries population in the LMC</b>	<b>33</b>
<b>6</b>	<b>Point source population of the LMC</b>	<b>35</b>
6.1	An updated catalogue of HMXBs in the LMC . . . . .	35
6.2	The star formation history of the LMC through its X-ray binary population	43
<b>7</b>	<b>New SgXRBs in the LMC</b>	<b>47</b>
7.1	General Information . . . . .	47
7.2	Observations . . . . .	48
7.2.1	X-ray data . . . . .	48
7.2.2	Optical data . . . . .	49
7.3	Results . . . . .	50
7.3.1	X-ray positions . . . . .	50
7.3.2	X-ray temporal properties . . . . .	51
7.3.3	X-ray spectral properties . . . . .	53
7.3.4	Optical properties of donor stars . . . . .	56
7.4	Discussion . . . . .	59
7.4.1	XMMU J053108.3-690923: a $\sim 2013$ s pulsar with a bright giant (or supergiant Ib) companion . . . . .	59
7.4.2	XMMU J053320.8-684122: A probable SFXT in the LMC . . . . .	60
7.5	Conclusions . . . . .	63
<b>IV</b>	<b>Hunting BeXRB outbursts in the Magellanic Clouds</b>	<b>65</b>
<b>8</b>	<b>Characteristics of outburst</b>	<b>67</b>
<b>9</b>	<b>LXP 28.77: August 2012 outburst</b>	<b>69</b>
9.1	Observations and data reduction . . . . .	69
9.1.1	X-ray observations . . . . .	69
9.1.2	Optical spectroscopy . . . . .	70
9.2	X-ray data analysis and results . . . . .	70
9.2.1	X-ray position . . . . .	70
9.2.2	Spectral analysis . . . . .	71
9.2.3	X-ray long-term variability . . . . .	73
9.2.4	Timing analysis . . . . .	73
9.3	Analysis and results of optical data . . . . .	74
9.3.1	Optical counterpart . . . . .	74
9.3.2	Spectral classification . . . . .	76
9.3.3	MACHO light curve . . . . .	78
9.4	Discussion . . . . .	79
9.5	Conclusions . . . . .	80
<b>10</b>	<b>LXP 8.04: January 2013 outburst</b>	<b>83</b>
10.1	X-ray observations and data reduction . . . . .	83
10.1.1	X-ray observations . . . . .	83
10.1.2	X-ray position . . . . .	84
10.1.3	Timing analysis . . . . .	85

10.1.4	Spectral analysis . . . . .	85
10.1.5	X-ray long-term variability . . . . .	88
10.2	Analysis and results of optical data . . . . .	89
10.2.1	Optical counterpart . . . . .	89
10.2.2	OGLE light curve . . . . .	89
10.3	Discussion . . . . .	90
10.4	Conclusions . . . . .	94
<b>11</b>	<b>LXP 8.04: December 2013 outburst</b>	<b>95</b>
11.1	Observations and data analysis . . . . .	95
11.1.1	X-ray data . . . . .	95
11.1.2	Optical data . . . . .	103
11.2	Discussion . . . . .	106
11.2.1	Phase-averaged spectra: . . . . .	106
11.2.2	Phase resolved spectrum: Pulse profile modelling . . . . .	107
11.3	Conclusions . . . . .	109
<b>12</b>	<b>LXP 38.55: October 2014 outburst</b>	<b>111</b>
12.1	Analysis and results of X-ray observations . . . . .	111
12.1.1	X-ray observations . . . . .	111
12.1.2	X-ray position . . . . .	111
12.1.3	Timing analysis . . . . .	114
12.1.4	Spectral analysis . . . . .	114
12.2	Analysis and results of optical data . . . . .	117
12.2.1	SWIFT UVOT . . . . .	117
12.2.2	GROND . . . . .	117
12.2.3	OGLE . . . . .	120
12.3	Discussion . . . . .	121
12.4	Conclusions . . . . .	125
<b>13</b>	<b>SXP 2.16: November 2015 outburst</b>	<b>127</b>
13.1	XMM-Newton observations during the November 2015 outburst . . . . .	127
13.1.1	X-ray position . . . . .	127
13.1.2	X-ray timing analysis . . . . .	128
13.1.3	Spectral analysis . . . . .	129
13.2	Swift/XRT X-ray light curve . . . . .	134
13.3	Optical/X-ray Variability . . . . .	135
13.4	Discussion . . . . .	136
13.4.1	Optical period . . . . .	137
13.4.2	Propeller transition . . . . .	138
13.4.3	X-ray spectral and temporal properties . . . . .	139
13.4.4	Limitations - Motivation for future observations . . . . .	141
<b>14</b>	<b>SXP 15.6: June 2016 outburst</b>	<b>143</b>
14.1	General information about the system . . . . .	143
14.2	Observations and data analysis of SXP 15.6 . . . . .	144
14.2.1	X-ray data analysis . . . . .	144

## CONTENTS

---

14.2.2	X-ray timing analysis . . . . .	146
14.2.3	X-ray spectral analysis . . . . .	147
14.2.4	Phase-resolved properties . . . . .	148
14.2.5	X-ray and optical light curve of the outburst . . . . .	150
14.3	Discussion . . . . .	152
14.4	Conclusions . . . . .	155
<b>15</b>	<b>SMC X-2: September 2015 outburst</b>	<b>157</b>
15.1	Historic X-ray activity of SMC X-2 . . . . .	157
15.2	Observations and data analysis . . . . .	157
15.2.1	X-ray data analysis . . . . .	157
15.2.2	X-ray timing analysis . . . . .	158
15.2.3	X-ray phase-averaged spectral analysis . . . . .	160
15.2.4	Phase-resolved spectroscopy . . . . .	162
15.2.5	RGS spectroscopy . . . . .	163
15.3	Discussion . . . . .	164
<b>16</b>	<b>SMC X-3: June 2016 outburst</b>	<b>167</b>
16.1	Spectral and temporal properties . . . . .	167
16.2	Pulse profile evolution . . . . .	168
16.3	Conclusions . . . . .	171
<b>V</b>	<b>Neutron stars powering ultraluminous X-ray sources</b>	<b>173</b>
<b>17</b>	<b>Highly magnetised accreting neutron stars powering ultraluminous X-ray sources</b>	<b>175</b>
17.1	Accretion funnels and envelopes around neutron stars during extreme accretion . . . . .	177
17.1.1	Accretion column in high accretion rates . . . . .	179
17.2	ULX spectra . . . . .	181
17.3	Conclusions . . . . .	183
<b>18</b>	<b>NGC 300 ULX1: A test case for accretion torque theory</b>	<b>185</b>
18.1	Observational data . . . . .	185
18.2	Results . . . . .	186
18.3	Conclusions . . . . .	189
<b>VI</b>	<b>Summary</b>	<b>191</b>
<b>19</b>	<b>Conclusions and outlook</b>	<b>193</b>
19.1	Summary and conclusions . . . . .	193
19.2	Outlook . . . . .	197
	<b>Acknowledgments</b>	<b>201</b>
	<b>References</b>	<b>203</b>

Acronyms

231

## CONTENTS

---

# Zusammenfassung

Meine Doktorarbeit zielt darauf ab, neue Erkenntnisse zu akkretierenden Systemen zu gewinnen, die stark magnetisierte ( $B \gtrsim 10^{12}$  G), langsam rotierende ( $P_s \gtrsim 1$  s) Neutronensterne enthalten, indem ich sowohl einzelne Systeme als auch die Eigenschaften ihrer Populationen untersuche. Meine Dissertation enthält Ergebnisse zu verschiedenen Röntgen-Binärsystemen, die sich ergänzen und es ermöglichen ein Gesamtbild der Akkretion in verschiedenen Regimen und Umgebungen zu zeichnen. Die Spitze des Eisbergs bildet das Studium der Super-Eddington-Akkretion auf Neutronensterne. Dieses Thema wurde durch die jüngste Entdeckung von pulsierenden Neutronensternen, die bei Röntgenhelligkeiten emittieren, die die Eddington-Grenze für einen typischen Neutronenstern deutlich überschreiten, top-aktuell. Um diese Ziele zu erreichen, führe ich gründliche Studien von Röntgenausbrüchen von Systemen durch, die junge Neutronensterne beherbergen, und darauf abzielen ihre Eigenschaften bei verschiedenen Helligkeitsstufen zu entschlüsseln.

Im ersten Teil führe ich eine Untersuchung von Röntgen-Binärsystemen bestehend aus jungem Neutronenstern und massereichem Begleitstern durch. Da ich am Studium der Akkretion bei unterschiedlicher Leuchtkraft und verschiedenen Akkretionsregimen interessiert bin, sind zwei Dinge wichtig; die Qualität der Daten und genaue Entfernungsbestimmungen. Daher sind Systeme in nahen Galaxien mit hoher Sternentstehungsrate ideal für diese spezielle Studie. Aus diesem Grund werde ich mich auf Systeme in den nahen Magellanschen Wolken konzentrieren. Als Mitglied der Röntgenarbeitsgruppe "Nahe Galaxien" am Max-Planck-Institut für extraterrestrische Physik war ich an der Untersuchung der beiden Galaxien beteiligt, für die Röntgendaten hoher Qualität aus einer Durchmusterung und Überwachungsbeobachtungen zur Verfügung standen. Insbesondere analysierte ich Archiv- und jüngste Daten aus einer großen *XMM-Newton*-Untersuchung der Großen Magellanschen Wolke und stellte einen aktualisierten Katalog von bestätigten und in Frage kommenden massereichen Röntgen-Binärsystemen in der Galaxie zusammen. Außerdem beantragte ich mit Erfolg weitere Überwachungsprogramme und Folgebeobachtungen um Systeme in den Magellanschen Wolken während Röntgenausbrüchen zu studieren. Dies führte zur Entdeckung mehrerer neuer Pulsare und einem der ersten extragalaktischen "Supergiant Fast X-ray Transients". Durch das Studium der Systeme im Ausbruch konnte ich eine eingehende Studie ihrer spektralen Eigenschaften durchführen, verschiedene Kontinuumskomponenten in den Röntgenspektren erkennen und ihre Eigenschaften bei unterschiedlichen Akkretionsraten studieren. Darüber hinaus konnte ich durch Pulsphasen-aufgelöste Spektralanalyse den pulsierenden Teil des vom Neutronenstern ausgehenden Spektrums, von einer weichen Komponente, die aus der äußeren Magnetosphäre und der inneren Akkretionsscheibe stammt, trennen. Außerdem habe ich gezeigt, dass diese weiche Komponente auch schwach pulsierend sein kann, da sie zum wesentlichen Teil aus reprozeszierter Emission vom Pulsar besteht. Durch eine physikalisch motivierte Modellierung des Pulsprofils mehrerer Neutronensterne habe ich das 3D-Emissionsmuster der Systeme erklären können.

Im zweiten Teil verwendete ich das Wissen, das ich durch das Studium von Neutronensternen bei typischen Akkretionsraten gewonnen habe, um ihre spektralen und

## CONTENTS

---

temporalen Eigenschaften bei Akkretionsraten, die die Eddington-Grenze weit überschreiten, zu untersuchen. Ich konnte demonstrieren, dass das Röntgenspektrum aufgrund der erhöhten optischen Tiefe des angesammelten Materials durch eine thermische Komponente charakterisiert sein würde. Ich habe diese Vorhersage verwendet, um die Spektren der meisten nicht-pulsierenden ultra-leuchtenden Röntgen-Binärsysteme erfolgreich anzupassen und habe gezeigt, dass ein großer Teil von ihnen Neutronensterne anstelle von stellaren Schwarzen Löchern beherbergen könnte. Schließlich war ich an der Untersuchung des 4. identifizierten ultra-leuchtenden Röntgenpulsars NGC300 ULX1 beteiligt. Mit der Untersuchung seiner schnellen Periodenentwicklung von 120 s auf 18 s innerhalb von 4 Jahren habe ich Drehmomentmodelle getestet und gezeigt, dass die spektralen und temporalen Eigenschaften des Systems mit Super-Eddington-Akkretionsraten auf einen Neutronenstern kompatibel sind.

# Abstract

My PhD thesis is aimed at gaining new insights on accreting systems hosting highly magnetised ( $B \gtrsim 10^{12}$  G) slowly rotating ( $P_s \gtrsim 1$  s) neutron stars, by studying individual systems and the properties of their populations. My dissertation contains results on different X-ray binary systems, that yet are complementary into building a story around accretion in different regimes and environments. The tip of the iceberg is the study of super-Eddington accretion onto neutron stars, a quest that was fuelled by the recent discovery of pulsating neutron stars that emit at X-ray luminosities greatly exceeding the Eddington limit for a typical neutron star. But in order to arrive at this goal, I first perform a thorough study of X-ray outbursts of systems hosting young neutron stars, aiming in deciphering their properties at different luminosity levels.

For the first part I perform a study of X-ray binaries containing young neutron stars and massive companions. Since I am interested in the study of accretion at different luminosity levels and accretion regimes two things are important; quality of data and accurate distance determinations. Thus, systems located in nearby star-forming galaxies are ideal for this particular study. For that reason I will focus on systems located in the nearby Magellanic Clouds. Being a member of the “Nearby Galaxy X-ray Group” at Max Planck institute for extraterrestrial Physics I have been involved in the study of the two galaxies through high quality survey and monitoring X-ray observations. Specifically, I analysed archival and recent data from a large *XMM-Newton* survey of the Large Magellanic Cloud and constructed an updated catalogue of confirmed and candidate high mass X-ray binaries in the galaxy. Moreover, I obtained monitoring and triggered observations to further study systems located in the Magellanic Clouds during outbursts. This resulted in the discovery of several new pulsars and one of the first extragalactic supergiant fast X-ray transients. By the study of outbursting systems I was able to perform an in-depth study of their X-ray spectral properties, recognise different continuum emission components and study their properties at different accretion rates. In addition, by performing phase-resolved spectral analysis I disentangled the pulsating part of the spectrum that originates from the neutron star, from a softer component that originates from the outer magnetosphere and the inner accretion disk. Moreover, I demonstrated that this soft component can also be weakly-pulsating as it can reprocess a significant part of the emission originating from the pulsar. By performing a physically motivated modelling of the pulse profile of several neutron stars I explained the 3D emission pattern of the systems.

For the second part I used the knowledge obtained by the study of typical accreting neutron stars in order to probe their spectral and temporal properties at rates that greatly exceed the Eddington limit. I have demonstrated that their X-ray spectrum would be characterised by a thermal signature due to the increased optical depth of the accreted material. I have used this prediction to successfully fit the spectra of most non-pulsating ultra luminous X-ray binary systems and have demonstrated that a large fraction of them could host neutron stars instead of stellar mass black holes. Finally, I have been involved in the study of the 4<sup>th</sup> identified ultra luminous X-ray pulsar, NGC 300 ULX1. By studying its fast period evolution from 120 s down to 18 s within 4 years I have tested torque models and have demonstrated that spectral and temporal

## CONTENTS

---

properties of the system are compatible with super-Eddington accretion rates onto a neutron star.

## List of original publications

Below I provide detailed information of all publications (in inverse chronological order) that have been produced during by PhD studies. Those marked with an asterisk (\*) deal with topics from the broader field of high-energy astrophysics and are not included in this dissertation for coherency purposes.

**PAPER I: Vasilopoulos, G.;** Haberl, F.; Carpano, S.; Maitra, C. (2018),  
*NGC 300 ULX1: A test case for accretion torque theory*  
submitted

**\*PAPER II:** Maravelias, G.; Kraus, M.; Cidale, L. S.; Borges Fernandes, M.; Arias, M. L.; Curé, M.; **Vasilopoulos, G.** (2018),  
*Resolving the kinematics of the disks around Galactic B[e] supergiants*  
MNRAS in press

- **My contribution:** Involved in obtaining spectroscopic observations of the systems, and discussion of temporal variability of optical data.

**\*PAPER III:** Carpano, S.; Haberl, F.; Maitra, C.; **Vasilopoulos, G.** (2018),  
*Discovery of pulsations from NGC 300 ULX1 and its fast period evolution*  
MNRAS, volume 476L, 45

- **My contribution:** Discover the long term spin evolution. Involved in temporal analysis, and the discussion about the estimation of the magnetic field.

**PAPER IV:** van Jaarsveld, N.; Buckley, D. A. H.; McBride, V. A.; Haberl, F.; **Vasilopoulos, G.;** Maitra, C.; Udalski, A.; Miszalski, B. (2018),  
*Identification of high-mass X-ray binaries selected from XMM-Newton observations of the LMC*  
MNRAS, volume 475, page 3253, 2018

- **My contribution:** selection of targets, and analysis of optical light-curves

**PAPER V: Vasilopoulos, G.;** Maitra, C.; Haberl, F.; Hatzidimitriou, D.; Petropoulou, M. (2018),  
*Identification of two new HMXBs in the LMC: a  $\sim 2013$  s pulsar and a probable SFXT*  
MNRAS, Volume 475, page 220, 2018

**PAPER VI:** Koliopanos, F.; **Vasilopoulos, G.** (2018),  
*Accreting, highly magnetized neutron stars at the Eddington limit: A study of the 2016 outburst of SMC X-3*  
A&A in Press

- **My contribution:** All authors contributed equally.

**\*PAPER VII:** Petropoulou, M.; **Vasilopoulos, G.;** Christie, I. M.; Giannios, D.; Coe M. J. (2018),  
*X-ray mapping of the stellar wind in the binary PSR J2032+4127/MT91 213*  
MNRAS, volume 474L, 22 - arxiv:1710.05042

## CONTENTS

---

- **My contribution:** First two authors contributed equally to the bulk of the text. I also led the X-ray data analysis and modelling of the interaction of the in-homogeneous stellar wind the the Pulsar Wind.

**\*PAPER VIII:** Petropoulou, M.; Coenders, S.; **Vasilopoulos, G.**; Kamble, A.; Sironi, L. (2017),  
*Point-source and diffuse high-energy neutrino emission from Type II<sub>n</sub> supernovae*  
MNRAS, volume 470, 1881 - arxiv:1705.06752

- **My contribution:** implementation of the Monte Carlo simulation, statistical analysis of the data.

**PAPER IX:** Koliopanos, F.; **Vasilopoulos, G.**; Gobet, O.; Bachetti, M.; Webb, N. A.; Barret, D. (2017),  
*ULX spectra revisited: Accreting, highly magnetized neutron stars as the engines of ultraluminous X-ray sources*  
A&A, volume 608A, 47

- **My contribution:** first 2 authors contributed equally to the bulk of the work.

**PAPER X:** **Vasilopoulos, G.**; Zezas, A.; Antoniou, V.; Haberl, F. (2017),  
*SXP 15.6; X-ray spectral and temporal properties of a newly discovered pulsar in the SMC*  
MNRAS, volume 470, 4354

**PAPER XI:** **Vasilopoulos, G.**; Haberl, F.; Maggi, P. (2017),  
*Identification of IGR J01217-7257 with the transient SMC pulsar XTE J0119-731 (SXP 2.16) using XMM-Newton*  
MNRAS, volume 470, 1971

**\*PAPER XII:** Haberl F., Israel G. L., Rodriguez Castillo G. A., **G. Vasilopoulos**, and 9 co-authors, (2017):  
*EXTraS discovery of two pulsators in the direction of the LMC: a Be/X-ray binary pulsar in the LMC and a candidate double-degenerate polar in the foreground*  
A&A, volume 598A, 69 - arxiv:1610.00904

- **My contribution:** spectral and temporal analysis of X-ray data. Temporal analysis of optical light-curves.

**\*PAPER XIII:** Petropoulou, M.; **Vasilopoulos, G.**; Giannios, D. (2017),  
*The TeV emission of Ap Librae: a hadronic interpretation and prospects for CTA*  
MNRAS, volume 464, 2213 - arxiv:1608.07300

- **My contribution:** Analysis of multi-wavelength data. Simulated data sets for CTA. Observational predictions for future flares.

**PAPER XIV:** **Vasilopoulos, G.**; Haberl, F.; Delvaux, C.; Sturm, R.; Udalski, A., (2016),  
*Multi-wavelength properties of IGR J05007-7047 (LXP 38.55) and identification as a Be X-ray binary pulsar in the LMC*,  
MNRAS, volume 461, 1875

- \*PAPER XV: Vasilopoulos, G.** & Petropoulou, M. (2016),  
*The X-ray dust scattered rings of the black hole low mass X-ray binary V404 Cygni*,  
MNRAS, Volume 455, 4426
- \*PAPER XVI: Maggi, P.; Haberl, F.; Kavanagh, P. J.; Sasaki, M.; Bozzetto, L. M.; Filipovic, M. D.; Vasilopoulos, G.;** and 7 coauthors (2016),  
*The population of X-ray supernova remnants in the Large Magellanic Cloud*,  
A&A, Volume 585A, 162M, 2016 - arXiv:1509.09223
- **My contribution:** Statistical properties of the SNR population, e.g. X-ray luminosity function.
- \*PAPER XVII: Sturm, R.; Haberl, F.; Vasilopoulos, G.;** and 5 coauthors (2014),  
*Discovery of SXP265, a Be/X-ray binary pulsar in the Wing of the Small Magellanic Cloud*,  
MNRAS, volume 444, 3571
- **My contribution:** Temporal analysis of the optical light-curve
- PAPER XVIII: Vasilopoulos, G.;** Haberl, F.; Sturm, R.; Maggi, P.; Udalski, A. (2014),  
*Spectral and temporal properties of RX J0520.5-6932 (LXP 8.04) during a type-I outburst*,  
Astronomy & Astrophysics, Volume 567, A129
- PAPER XIX: Vasilopoulos, G.;** Maggi, P.; Haberl, F.; Sturm, R.; Pietsch, W.; Bartlett, E. S.; Coe, M. J. (2013),  
*Swift J053041.9-665426, a new Be/X-ray binary pulsar in the Large Magellanic Cloud*,  
Astronomy & Astrophysics, Volume 558, A74

## CONTENTS

---

# Overview

In this work I focus on the study of [High Mass X-ray Binaries \(HMXBs\)](#) and in particular on the young highly magnetised accreting [Neutron Stars \(NSs\)](#) that are the engines behind their X-ray emission. The [Magellanic Clouds \(MCs\)](#) are our two closest star forming galaxies that despite their small mass are hosts to a large number of [HMXBs](#). The [Small Magellanic Cloud \(SMC\)](#) is the smaller of our two nearby galaxies and has been extensively studied. Its sibling, the [Large Magellanic Cloud \(LMC\)](#) has received much less attention in the X-rays mainly due to its larger extent in the sky and the apparent lack of many bright [X-ray binaries \(XRBs\)](#) compared to the [SMC](#). In this work I focus on two different but related subjects, the X-ray population of the [LMC](#) and the study of individual [XRBs](#) through observations performed during high luminosity stages. Moreover, fuelled by the recent discovery of pulsating [NSs](#) that emit at X-ray luminosities that greatly exceed the Eddington limit for a typical [NS](#), I investigated the X-ray spectral and temporal properties of pulsating and non-pulsating [Ultra-luminous X-ray sources \(ULXs\)](#) in the context of [NS](#) accretion. Within my study I investigate accretion theory onto a [NS](#) for a range of accretion rates that span over 5 orders of magnitude, up to 100 times the Eddington limit. I investigated different spectral components and their dependency on the accretion rate, while recognising unambiguous patterns of variability that are shared in the regime of extreme accretion.

A large part of this current work has already been published in astrophysical journals ([Koliopanos and Vasilopoulos 2018](#); [Vasilopoulos et al. 2018, 2017d,a, 2016c, 2014b, 2013b](#)), while several findings appear in other relevant publications ([Haberl et al. 2017b](#); [Koliopanos et al. 2017](#); [van Jaarsveld et al. 2017b](#)) – see also publications in §.

In Part [I](#) I introduce the theoretical framework that will be used throughout this thesis. In Part [II](#) I give a description of the various observational data used in this study and the analysis techniques that were adopted or developed for the goals of the study. In Part [III](#) I describe the main findings relevant to the [HMXB](#) population of the [LMC](#). This is the first main outcome of this thesis, as it provides an updated catalogue of the population, which can be used for various population studies and candidate systems can provide the basis for future multi-wavelength observations. In Part [IV](#) I present outbursts of individual [HMXBs](#) located in the [MCs](#). I provide various information about the spectral and temporal properties of several systems that were observed during outbursts reaching luminosities from  $10^{36}$  erg s<sup>-1</sup> up to super Eddington rates (i.e.  $10^{39}$  erg s<sup>-1</sup>). The study of these systems provides the basis of understanding accretion properties in highly magnetised [NS](#). A major outcome of this study is the connection of [Be X-ray Binary \(BeXRB\)](#) pulsars and the elusive [Ultra-luminous X-ray Pulsars \(ULXPs\)](#) that have been recently discovered and challenge our understanding of accretion physics (see Part [V](#)). In Part [VI](#) I give an overview of the current work by summarising the most important results.

## 1. OVERVIEW

---

**Part I**  
**Introduction**



## X-ray binaries



-rays are unambiguous among the Universe, they can be detected from a plethora of astrophysical systems residing as close as our Sun and as far as the more distant galaxies. A short list of such systems include the solar wind, stellar coronae, shocked plasma around [Supernova Remnants \(SNR\)](#), cooling compact objects like isolated [NS](#), collimated jets of [Active Galactic Nucleus \(AGN\)](#), Galaxy Clusters, and last but not least emission from accretion onto compact objects like [Black Holes \(BH\)](#), [White Dwarfs \(WDs\)](#) and [NSs](#).

[XRBs](#) are the brightest X-ray point sources in the sky ([Casares et al. 2017](#)). They consist of a compact object, usually a [BH](#) or a [NS](#), that accretes matter from a donor star. Since their first “accidental” discovery (Scorpius X-1 by OSO-3) they have been the centre of extensive studies and the driving force of many past and future X-ray missions (e.g. UHURU, EXOSAT, RXTE, Chandra, *XMM-Newton*, NICER, STROBE-X). This comes as no surprise, since [XRBs](#) are unique laboratories for studying the physics in environments of strong gravity and dense matter!

[XRBs](#) have many subcategories of classes, that are characterised by the mass of the donor star (e.g. low mass systems  $\lesssim 1M_{\odot}$ , versus high mass systems  $\gtrsim 10M_{\odot}$ ) and the nature of the compact object.

[HMXBs](#) are a major category of [XRBs](#) containing the vast majority of X-ray pulsars (i.e. accreting, highly magnetised [NS](#)), while they are considered the evolutionary product of a massive stellar binary system. More interestingly, they can lead to a formation of a double [NS](#) system, thus being a gravitational wave progenitor ([Tauris et al. 2017](#)). Since [HMXBs](#) are composed of two young objects it is not surprising that their number is related to the recent [Star Formation History \(SFH\)](#) of a galaxy ([Antoniou et al. 2010](#)). [HMXBs](#) can be divided into two categories depending on the luminosity class of the donor: [Supergiant X-ray binaries \(SgXRBs\)](#) where accretion occurs mainly through a strong stellar wind, and [BeXRBs](#) ([Reig 2011](#)) where the optical companion is a OBe star rotating close to its critical velocity and losing matter through a slow equatorial wind (i.e. decretion disk). During periods of increased accretion (e.g. periastron passage of the [NS](#)) material can be captured from the [NS](#) and an accretion disc can be formed.

[Low Mass X-ray Binaries \(LMXBs\)](#) are the other major category of [XRBs](#) where mass transfer occurs via Roche-lobe overflow. These systems are usually formed by gravitational capture and they are primarily found in the dense environment of old globular clusters and galactic centres. Given the long evolutionary time of low mass stars their number is proportional to the mass of the galaxy and the integrated [SFH](#) of the galaxy. Thus, although in our Galaxy we expect more than 1000 [LMXBs](#), in the [MCs](#) that are much less massive galaxies, we expect null to a handful of these systems (no such system is discovered in the [SMC](#) yet, only LMC X-2 in the [LMC](#)). [LMXBs](#) are characterised by somehow steady mass accretion and an accretion disc can be formed around the compact object. X-ray outbursts can be triggered due to disc instabilities ([Lasota 2001](#)) in which cases a jet can be formed and the luminosity of the system can increase by a factor of more than 1000 (e.g. 2015 outburst of V404 Cygni [Tetarenko](#)

et al. 2017).

### 2.1 High mass X-ray binaries

In a **HMXB**, matter is usually accreted onto an **NS**. When created, the **NS** has high magnetic field strength and short spin period. At this stage, matter cannot be accreted and the pulsar is in the *ejector phase*, which is characterised by a strong pulsar wind and radio pulsations. As the **NS** spins down, material can penetrate the light cylinder and the system enters its *propeller phase* (Illarionov and Sunyaev 1975b). The interaction of the **NS** magnetosphere and the surrounding material results in a fast spin down, and the **NS** can end up having a slow rotation period (100-1000 s). The origin of slow rotating pulsars can be explained by the subsonic propeller phase (Ikhsanov 2007), as the **NS** spins down until its spin period becomes larger than a critical value. In simple terms, when the corotation radius becomes larger than the **NS** magnetospheric radius, the binary transits to the *accretor phase* (Davies et al. 1979; Davies and Pringle 1981). Due to accretion the **NS** can spin-up (Parfrey et al. 2017) to short spin periods (Sugizaki et al. 2017). During periods of diminished accretion the magnetospheric radius becomes larger than the corotation radius and the pulsar can slowly spin-down again (Postnov et al. 2015b). The spin period distribution of the **BeXRB** population is complex, as it is connected to: (i) the orbital properties of the population (Corbet 1984), (ii) different types of supernovae progenitors (Knigge et al. 2011), and (iii) different accretion schemes (Cheng et al. 2014b). A snapshot of the population consists of systems that have reached equilibrium and systems that evolve rapidly (Haberl et al. 2012b). Moreover, there are many low-luminosity systems with low variability that are far less studied (see their population study in the **SMC** by Haberl and Sturm 2016).

In the accretor phase, the accreted material flows towards the **NS** magnetic poles, following the magnetic field lines. X-ray pulsations are observed from **NSs** with misaligned magnetic and rotation axis (Basko and Sunyaev 1975). For high enough accretion rates an *accretion column* is formed, inside which, material is heated to high energies and thermal X-rays are scattered by the in-falling particles (Becker and Wolff 2007b). X-ray emission is mainly escaping from the sides of the accretion column (fan-beam) and part of the emission is reflected to the **NS** surface (polar-beam), while the total emission pattern is affected by gravitational bending. Our understanding of the anisotropic emission mechanism has improved through the years (Illarionov and Sunyaev 1975b; Nagel 1981; Meszaros and Nagel 1985; Kraus et al. 1995; Trümper et al. 2013). The same principles concerning the accretion column and the 3D emission pattern are also applicable to any highly magnetised **NS** in a variety of systems, such as **Anomalous X-Ray Pulsars (AXP)** (e.g. Trümper et al. 2013), **Ultra-compact X-ray Binaries (UCXBs)** (e.g. Koliopanos and Gilfanov 2016) or **ULXPs**.

#### 2.1.1 Be X-ray binaries

**BeXRBs** are characterised by the properties of the donor star. The massive star loses material through a highly anisotropic wind that can take the form of a slowly expanding disc in the equatorial plane. The binary configuration comes in a variety of eccentricities and orbital periods. Typical systems have orbital periods of weeks to months, while the most extreme orbital period measured is 48 years (PSR J2032+4127/MT91 213 Ho et al. 2017). **BeXRBs** exhibit several forms of variability. X-ray outbursts occur

when the **NS** captures an enhanced amount of matter from the Be disk. Historically, these outbursts have been explained by a simple model in which the **NS** interacts with the equatorial disc while orbiting the Be star.

Type-I outbursts ( $L_x \sim 10^{36-37} \text{ erg s}^{-1}$ ) are the result of a brief interaction between the **NS** and the Be disk, and are usually correlated with the systems orbital period. Sporadically, **BeXRBS** may exhibit giant type-II outbursts ( $L_x \geq 10^{37} \text{ erg s}^{-1}$ ) that are proposed to be associated with warping episodes of the Be disc (Okazaki et al. 2013). In some cases a temporary accretion disc can be formed around the **NS**, as indicated by the strong spin-up measured during bright outbursts.

It is clear that the long-term X-ray variability of **BeXRBS** is related to the binary orbit and the reservoir of available material (i.e. the decretion disk). But **BeXRBS** are also extremely variable in the optical band, thus we can gain abundant information by the study of their optical properties. The optical signature of **BeXRBS** is affected by many components like: (i) the Be star itself (Porter and Rivinius 2003), that can exhibit non-radial pulsations with periods of 0.1-2.0 d, (ii) the Be star decretion disc as it gravitationally interacts with the **NS** during periastron passage, and (iii) semi-stable distortions of the disk, like warping, that are responsible for long-term super-orbital variability. Based on multi-year surveys of **BeXRBS** pulsars in the **SMC** it has been shown that the majority of the systems shows at least one of those characteristic optical signatures, while more than 40% of them have optical variability related to the binary orbit (Schmidtke et al. 2013; Bird et al. 2012).

### 2.1.2 Supergiant X-ray binaries

**SgXRBS** are the second major subclass of **HMXBs**. In this case the donor star is an evolved (Supergiant (**Sg**)) massive star. In attached binaries accretion occurs through Roche-lobe overflow, thus the **NS** can reach very short spin periods. Wind-fed systems typically have larger orbits and longer spin periods. Both systems can exhibit variability due to clumps in the stellar wind of the massive star.

#### Supergiant fast X-ray transients

The standard **HMXB** classification is challenged by newly discovered systems that do not seem to fit into this scheme. Within the last decade a new population of **HMXBs** (Bird et al. 2016), which is demographically different to the previously studied **HMXB** population, has been discovered by the **International Gamma-ray Astrophysics Laboratory (INTEGRAL)**. This new population of **HMXB** systems is usually characterised by large obscuration, while it exhibits extreme flaring activity on timescales of a few hours. Both properties led to their identification as **Supergiant Fast X-ray Transient (SFXT)** (Negueruela et al. 2006; Sidoli 2017). It has been proposed that the **SFXT** phenomenon is fairly common (Ducci et al. 2014), but the detection of the entire population in the Galaxy is hindered by their transient properties and the large Galactic absorption. Given the above observational biases, it is no surprise that only one extra-

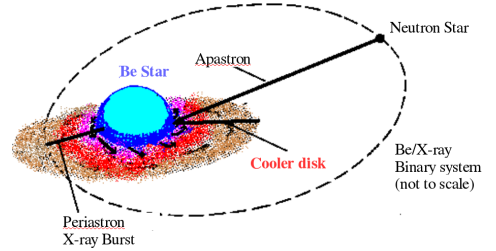


**Figure 2.1:** Schematic of a **BeXRBS**. Periodic X-ray and optical modulation is caused by the interaction of the Be disc and the **NS**. Super-orbital variability is caused by depletion/re-formation of the Be disk.

## 2. X-RAY BINARIES

---

galactic SFXT has been detected so far (IC 10 X-2, [Laycock et al. 2014](#)).

It is however known that SFXTs have many in common with classical SgXRBs, like companions and orbital period distributions and the presence of pulsations (i.e. accreting NSs) in both systems (see recent review by [Walter et al. 2015](#)). There have been a couple of models proposed to explain the extreme X-ray variability of SFXTs, but their validity is still a matter of debate. The three prominent explanations are that flares can be caused by either clumpy stellar wind ([in't Zand 2005](#); [Oskinova et al. 2012](#); [Bozzo et al. 2016](#)), magnetic gating ([D'Angelo and Spruit 2010](#); [Bozzo et al. 2008](#)), or settling of quasi-spherical accretion ([Shakura et al. 2012](#); [Vasilopoulos et al. 2018](#)). In the latter scenario it is interesting to point out that the dynamical range of the outbursts is decreasing with increasing persistent luminosity of the system, providing a smooth transition between the less luminous SFXTs and the more luminous SgXRBs. Interestingly a recent population study of their properties has shown that SgXRBs are characterised by systematically higher X-ray absorption and luminosity compared to SFXTs, while the equivalent width of the fluorescence Fe  $K_\alpha$  line is also significantly higher in typical SgXRBs ([Pradhan et al. 2017](#)). The above observational properties indicate that a stronger and possibly clumpy wind is found in typical SgXRBs.

### 2.2 Ultra-luminous X-ray binaries

ULXs are extragalactic X-ray sources with luminosities that exceed the Eddington limit (assuming isotropic emission) for a stellar-mass BH ( $M_{\text{BH}} \gtrsim 1 M_\odot$ : for up-to-date and comprehensive reviews see [Bachetti 2016](#); [Kaaret et al. 2017](#)). They were initially suggested to be rare instances of intermediate-mass BHs accreting at sub-Eddington rates ([Colbert and Mushotzky 1999](#); [Makishima et al. 2000](#)); essentially a scaled-up version of standard galactic BH XRBs. However, it was also suggested that a considerable fraction of the ULXs population can be powered by a stellar-mass BH accreting at super-Eddington rates (e.g. [Gilfanov et al. 2004](#); [Poutanen et al. 2007](#); [King 2009](#)). The recent discovery of ULXs ( $L_X > 10^{40}$  erg s $^{-1}$ ) that are powered by a highly magnetised NS (e.g. [Bachetti et al. 2014](#)) challenges our understanding of accretion physics. After the initial discovery, three more pulsating ULXs (ULXPs) have been detected ([Israel et al. 2017a](#); [Fürst et al. 2016](#); [Carpano et al. 2018](#)). There have now been several studies showing that even non-pulsating ULXs share much more spectral similarities with systems like BeXRBs that host an accreting NS ([Koliopanos et al. 2017](#); [Walton et al. 2018](#)).

## Basic physical mechanisms in X-ray binaries

### 3.1 Interaction between the accretion disc and the magnetised NS

In what follows, I will describe the principles for the interaction between the NS and the accretion disc around it (see also review; [Lai 2014](#)). Throughout the calculations I will assume typical values of  $M_{NS} = 1.4M_{\odot}$  and  $R_{NS} = 10 \text{ km}$  for the NS mass and radius, respectively. In a highly magnetised NS the disc cannot reach the NS surface and is truncated at generally large radii, at a position where the ram pressure of the in-falling material equals the magnetic pressure. If the inner radius of the Keplerian disc is inside the corotation radius ( $R_c$ ), then accretion along the magnetic field lines can occur. If the inner disc radius is outside  $R_c$ , accretion is halted by the centrifugal barrier (i.e. propeller regime [Illarionov and Sunyaev 1975b](#); [Campana et al. 2017](#)). In this case the disc is truncated at the magnetospheric radius  $R_M$ , which in term is proportional to the Alfvén radius  $R_A$  (i.e.  $R_M = \xi R_A$ ). The  $\xi$  parameter can be derived by simulations and it usually takes a value of  $\sim 0.5$ , while for super-Eddington accretion analytical approximations can be used to express it as a function of the accretion rate ( $\dot{M}$ ) and the NS magnetic field  $B$  (see eq. 61 of [Chashkina et al. 2017a](#)). During accretion, the basic observational signatures of the interaction of the in-falling material and the NS are (i) the luminosity of the pulsating X-ray emission which is equal to the rate at which gravitational energy of the in-falling matter is released ( $L_x \simeq GM_{NS}\dot{M}/R_{NS}$ ), and commonly expressed as a fraction of its rest-mass energy  $n_{eff}\dot{M}c^2$  (i.e. with efficiency  $n_{eff} = GM_{NS}/(R_{NS}c^2) \sim 0.2$ ), and (ii) the change of the NS spin period based on the torque that is acting onto the NS. The applied torque due to mass accretion is proportional to  $\dot{M}$  and depends on  $R_M$ , as it acts like a lever arm onto the star (i.e.  $N_{acc} \approx \dot{M}\sqrt{GM_{NS}R_M}$ ). Additional torque is acting due to coupling of magnetic field lines and the disk. The total torque can be expressed in the form of  $N_{tot} = n(\omega_{fast})N_{acc}$  where  $n(\omega_{fast})$  is a dimensionless function, and  $\omega_{fast} = (R_M/R_c)^{3/2}$  is known as the fastness parameter ([Elsner and Lamb 1977](#)). We note that the above paradigm is only applicable when  $R_M < R_c$ , while  $\omega_{fast} \rightarrow 1$  describes the transition to the propeller regime. Several models have used the above paradigm to express the applied torque onto a NS based on the system’s properties (e.g. [Wang 1987](#); [Ghosh and Lamb 1979](#)). In this study we will use the function  $n(\omega_{fast})$  given by [Wang \(1995\)](#):

$$n(\omega_{fast}) = \frac{7/6 - (4/3)\omega_{fast} + (1/9)\omega_{fast}^2}{1 - \omega_{fast}} \quad (3.1)$$

but we refer the reader to the work of [Parfrey et al. \(2016a\)](#) for more details and a comparison between different regimes and solutions.

For a NS having moment of inertia  $I_{NS} = 2M_{NS}R_{NS}^2/5$  it is straightforward to calculate its spin period ( $P$ ) derivative ( $\dot{P}$ ) as (cgs units):

$$-\frac{\dot{P}}{P} = \frac{P}{I_{NS}2\pi} n(\omega_{fast}) L_x \frac{GM_{NS}}{R_{NS}} \sqrt{GM_{NS}R_M} \quad (3.2)$$

### 3. BASIC PHYSICAL MECHANISMS IN X-RAY BINARIES

---

The above differential equation connects observable quantities (i.e.  $L_X$ ,  $P$ ,  $\dot{P}$ ) and quantities that are fairly well constrained from theory where the only unknown is the magnetisation of the NS. The above recipe has been proven sufficient to describe the spin evolution of many BeXRBs during outbursts, and to our current understanding all the available models can explain to a certain degree the available observational measurements of X-ray pulsars during the accretor phase. However by studying systems close to their propeller transition one can gain useful insight onto the NS-disc interaction.

#### 3.1.1 Propeller transition

The propeller transition occurs as the magnetospheric radius  $R_M$  becomes equal to the corotation radius  $R_c$  of the system. In an accreting system this can happen in two ways,  $R_M$  is increasing while  $R_c$  remains constant, or the other way around,  $R_c$  is increasing while  $R_M$  remains constant. The first case requires the system to maintain almost constant spin and the accretion rate to decrease gradually. This is typically observed during outbursts of BeXRB systems, where the transition time scale can be less than the binary orbital period. The second case requires a system to maintain constant X-ray luminosity and the spin period of the NS to decrease significantly as the NS spins up. Since the acting torque onto the NS approaches to zero as  $R_M$  and  $R_c$  become equal, the evolutionary time scale for this transition can be much longer than the lifetime of the system. However, once the NS spin period comes close to this equilibrium period, the system becomes much more sensitive to small changes of the accreting material, thus transitions between propeller and accretor phase can occur due to dynamical effects such as orbital modulation, or precession of the accretion disk. Recently, Parfrey and Tchekhovskoy (2017) have performed axisymmetric general-relativistic MHD simulations for the first time demonstrate how the interaction of a turbulent accretion flow with a pulsar's electromagnetic wind. These simulations depict with high accuracy the four possible accretion regimes in accreting NS. Snapshots of the simulations are plotted in the sub-panels of Fig. 3.1, in order of decreasing mass accretion rate: (a) crushed magnetosphere and direct accretion; (b) magnetically channeled accretion onto the stellar poles; (c) the propeller state, where material enters through the light cylinder but is prevented from accreting by the centrifugal barrier; (d) almost perfect exclusion of the accretion flow from the light cylinder by the pulsar wind.

#### Measuring the magnetic field of the NS

For X-ray pulsars, the transition to the propeller regime offers a unique way to measure the magnetic field  $B$  of the NS. In the accretor phase the  $R_M$  is smaller than  $R_c$ , allowing material to fall onto the NS. As the mass accretion rate drops,  $R_M$  begins to increase and at some point reaches  $R_c$ . At that point material cannot be accreted as it is stopped by the centrifugal barrier. While the source transits from the accretor to the propeller regime there is a sudden drop in its bolometric luminosity that is proportional to the gravitational potential difference between the NS surface and  $R_c$  (Campana et al. 2002).

Using the detected minimum luminosity as observed in the X-rays, before the source becomes undetectable, we can estimate the magnetic field strength of the NS. The

### 3.1 Interaction between the accretion disc and the magnetised NS

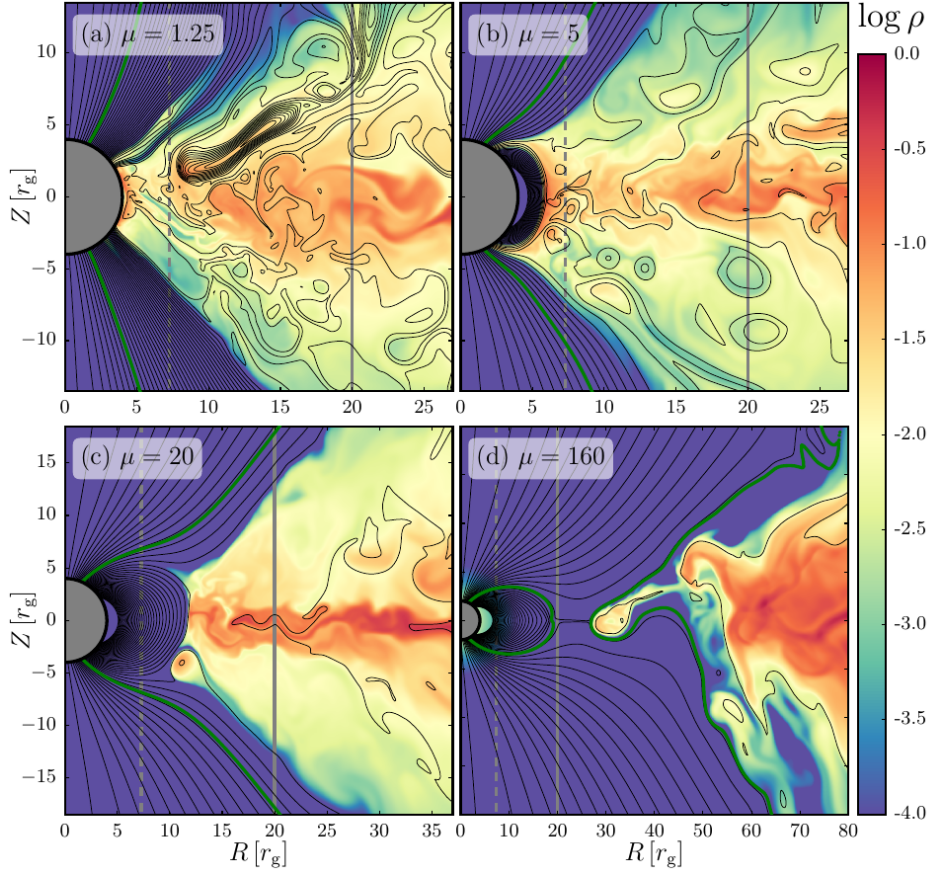


**Figure 3.1:** Four accretion states, determined by the stellar magnetic moment  $\mu$  for the same initial torus and stellar spin frequency. Poloidal magnetic field lines are in black, equispaced in magnetic flux, with the thicker green line representing the last closed field line for an equivalent isolated pulsar. Gray vertical lines indicate  $R_c$  (dashed) and light cylinder (solid). Different panels show: (a) Direct accretion. (b) Magnetically channeled accretion onto the stellar poles. (c) The propeller state. (d) Exclusion of the accretion flow from the light cylinder, shown immediately following the clearing of the inner magnetosphere. Credit: [Parfrey and Tchekhovskoy \(2017\)](#).

corotation radius is written in terms of NS spin period  $P$  and mass:

$$R_c = \left( \frac{GM_{NS}P^2}{4\pi^2} \right)^{1/3}. \quad (3.3)$$

We can define the critical mass accretion rate where  $R_M = R_c$  ([D’Angelo and Spruit 2012](#)), as a function of NS spin period, mass and magnetic field strength:

$$\dot{M}_{lim} = \frac{\eta B^2 R_{NS}^5 P}{8\pi R_c^5}, \quad (3.4)$$

where  $\eta$  is defined as the relative strength of the generated magnetic field toroidal component ( $\eta \equiv B_\phi/B_z$ ) and has typical values of the order of  $\sim 0.1$  ([D’Angelo and Spruit 2012](#); [Spruit and Taam 1993](#)). Finally, we assume that during accretion the energy release in X-rays is approximately equal to the Newtonian gravitational potential at the surface of the NS ([Mushtukov et al. 2015b](#); [Campana et al. 2002](#)). This is of the order of 16%-20% of the infalling rest-mass energy, while under certain conditions can

### 3. BASIC PHYSICAL MECHANISMS IN X-RAY BINARIES

---

reach even higher values (Sibgatullin and Sunyaev 2000). Based on these assumptions we estimate the limiting luminosity for the propeller effect:

$$L_{lim} \simeq GM_{NS}\dot{M}_{lim}R_{NS}^{-1} \simeq 5.6 \times 10^{37} \eta P^{-7/3} M_{1.4}^{-2/3} R_6^5 B_{12}^2 \text{ ergs}^{-1} \quad (3.5)$$

where the convention  $X_y = X/10^y$  is used for the NS radius and magnetic field strength in cgs units and  $X_y = X/yM_\odot$  for the NS mass in solar-mass units. We note that the estimated limiting luminosity is in agreement to that estimated by other approaches (Tsygankov et al. 2016; Campana et al. 2002; Stella et al. 1986), but a systematic uncertainty of the order of 2 can be expected due to model assumptions.

## 3.2 Radiative transfer in X-ray binaries

A fundamental introduction in radiative transfer can be found in many textbooks (e.g. Rybicki and Lightman 1979). Here I will present the basic X-ray emission mechanisms that take place in XRBs.

### 3.2.1 X-ray emission

#### Black-body radiation

This is the basic thermal radiation that is described by Planck's law, where the spectral radiance of a body of temperature  $T$  at a frequency  $\nu$  is given by:

$$B_\nu(T) = 2h(\nu^3/c^2)(e^{h\nu/kT} - 1)^{-1} \text{ ergs s}^{-1} \text{ cm}^{-2} \text{ Hz}^{-1} \text{ sr}^{-1}, \quad (3.6)$$

where  $h$  is the Planck constant,  $c$  is the speed of light,  $k$  is the Boltzmann constant. It is straightforward to show that the maximum flux is emitted at  $\nu_{\max} \sim 2.82kT/h$ , and that the total radiated power is equal to  $\sigma T^4$ , where  $\sigma = (2\pi^5 k^4)/(15h^3 c^2)$ . In astrophysical terms, Planck's law provides a good approximation for the surface of a star, a NS or a WD.

An important model used in the study of thin accretion disks around XRBs is the Multitemperature Blackbody (MTB) or Disc Blackbody (DBB) that has been in the literature for more than 40 years (e.g. see Shakura and Sunyaev 1973). Over the years several assumptions have been used to model X-ray spectra with this model. It is interesting that one family of models uses a zero-torque boundary condition applied to the inner edge of the disk, while others assume a non-zero torque (Zimmerman et al. 2005). The above models have been generally very successful in reproducing the  $L_X \propto T^4$  dependence in BH systems. But in magnetised NSs one has to account for the truncation of the disc at the magnetospheric radius and other effects such as the illumination of the disc from the NS. Moreover, at very high accretion levels the disc shape can deviate significantly from that in the thin approximation. Study of the DBB in these conditions can be done numerically (e.g. Chashkina et al. 2017a) or with simulations (e.g. Parfrey et al. 2017). While the X-ray spectrum of such a disc can differ from the thin disc approximation, there will be a characteristic temperature that dictates the spectral turn-off, but one should be very careful when extracting other physical parameters (i.e. disc inner radius) from the X-ray spectrum of such emission.

#### Synchrotron & Bremsstrahlung radiation

Accelerated charged particles emit radiation. A single non-relativistic charged particle moving in the presence of a magnetic field  $B$  gyrates at the Larmor frequency

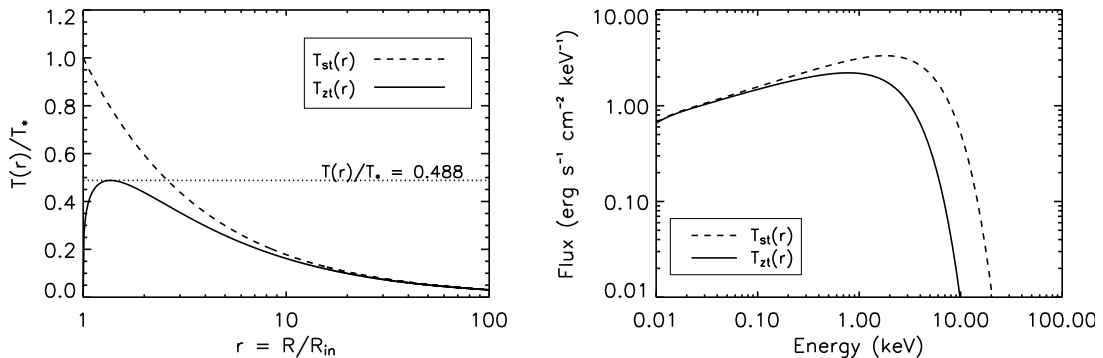


**Figure 3.2:** *Left:* Disk temperature as a function of radius for the standard torque (dashed line) and the zero torque (solid line) models. *Right:* MTB disc spectra corresponding to the temperature profiles shown in the left, for  $T_* = 2\text{keV}$  and  $R_{in} = 10\text{km}$ . Both plots taken from (Zimmerman et al. 2005).

$\omega = eB/mc$  and emits radiative power equal to  $(2/3)(e^2/c^2)a^2$  where  $a$  is the proper acceleration. The synchrotron spectrum of a population of particles can usually be described as a power law, but only if the distribution of energies of the particles follows also a power law.

Bremsstrahlung or braking radiation is the radiation produced by the deceleration of charged particles. Electrons with a Maxwellian distribution of energies can be accelerated in the Coulomb field of slow moving protons. The energy emitted is characterised by a flat spectrum with an exponential drop at an energy  $kT$  with total power proportional to  $\sqrt{T}$ :

$$F_\nu(T) \propto N_e N_i Z^2 T^{-1/2} e^{-h\nu/kT} \text{ergs s}^{-1} \text{cm}^{-3} \text{Hz}^{-1}, \quad (3.7)$$

This is the most basic mechanism by which hot gas cools down by emitting radiation.

### Scattering

Thomson scattering is the elastic scattering of low-energy photons by low-energy electrons, with a cross-section of  $\sigma_T = (8\pi/3)(e^2/mc^2)$ . Compton scattering is the inelastic scattering of low-energy photons on non-relativistic electrons, where the photon transfers part of its energy to the electrons. The cross-section of the interaction is reduced with photon energy. In the case of relativistic electrons we have the so-called Inverse Compton scattering, where photons gain energy in the observer's rest frame.

### Radiative recombination

In the radiative recombination, a free/unbound electron (energy  $E_e$ ) is captured by an ion  $z$  in a state  $n$  to a given bound level and a photon is emitted. A characteristic recombination continuum has edges at the ionization potential of the ions state (i.e.  $I_{z,n}$ ).

### X-ray Lines

Emission lines can be produced by inelastic collision of electrons with ions, which cause them to be excited and emit at appropriate energies (Tucker and Gould 1966). This is a characteristic mechanism of energy loss for a hot gas, where the emitted photons may

### 3. BASIC PHYSICAL MECHANISMS IN X-RAY BINARIES

be re-absorbed and re-emitted at different energy levels, but would eventually escape from the hot gas.

#### 3.2.2 X-ray absorption

The presence of matter between the observer and a given source is the main cause for X-ray absorption, with photo-electric absorption being the main mechanism. The intensity of the absorption depends on the amount of matter (i.e. the equivalent hydrogen column density) present in the line of sight. In the X-ray band the cross-section of metals becomes dominant compared to hydrogen (Wilms et al. 2000), but we usually refer to total absorption using the inferred hydrogen column density with an adopted metallicity (see Fig. 3.3). In addition to atoms, the ISM is full of cold matter that forms dust grains. Although often neglected these grains can contribute significantly to the attenuation of X-rays (Hoffman and Draine 2016). A spherical shape can serve as a first approximation for the grain shape, while their size distribution can be assumed to have a power-law shape (Mathis et al. 1977) although more complicated assumptions can be made (Draine 2011).

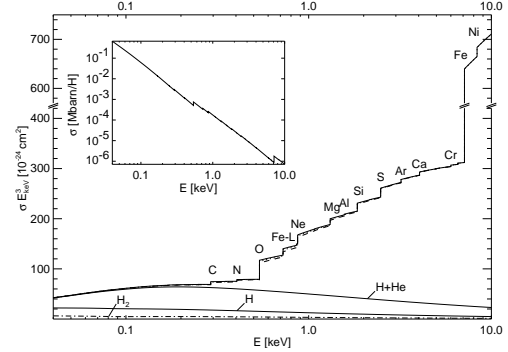


**Figure 3.3:** Absorptivity per hydrogen atom of the Inter Stellar Medium (ISM) as derived by Wilms et al. (2000). Figure taken from Wilms et al. (2000).

### 3.3 Magnetised NS

All the physical processes described above have to be combined in order to explain the X-ray spectrum of a NS in an XRB.

#### 3.3.1 Accretion column

The basic component in the X-ray spectrum of an X-ray Pulsars (XRP) is originating from its accretion columns. This term is used to describe the thermal mound of material that is accumulated over the NS hot spot during episodes of increased accretion. The spectral formation process can be described in terms of radiative transfer based on a detailed treatment of the bulk and thermal Comptonization occurring in the accreting, shocked gas (Becker and Wolff 2007b). Bremsstrahlung and cyclotron processes create the photons throughout the column (Baan and Treves 1973), while blackbody photons are emitted near the surface of the NS at the base of the thermal mound (see Fig. 3.4). The emitted spectrum that escapes the NS is a result of bulk and

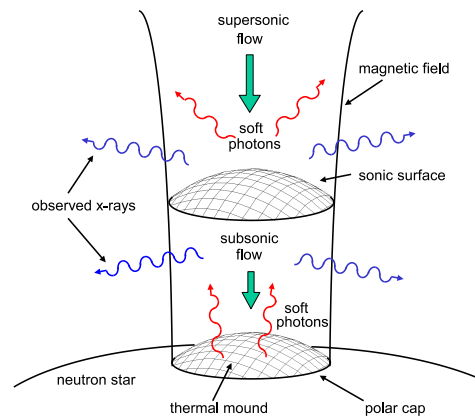


**Figure 3.4:** Schematic of accreting gas onto the polar cap of a NS taken from (Becker and Wolff 2007b).

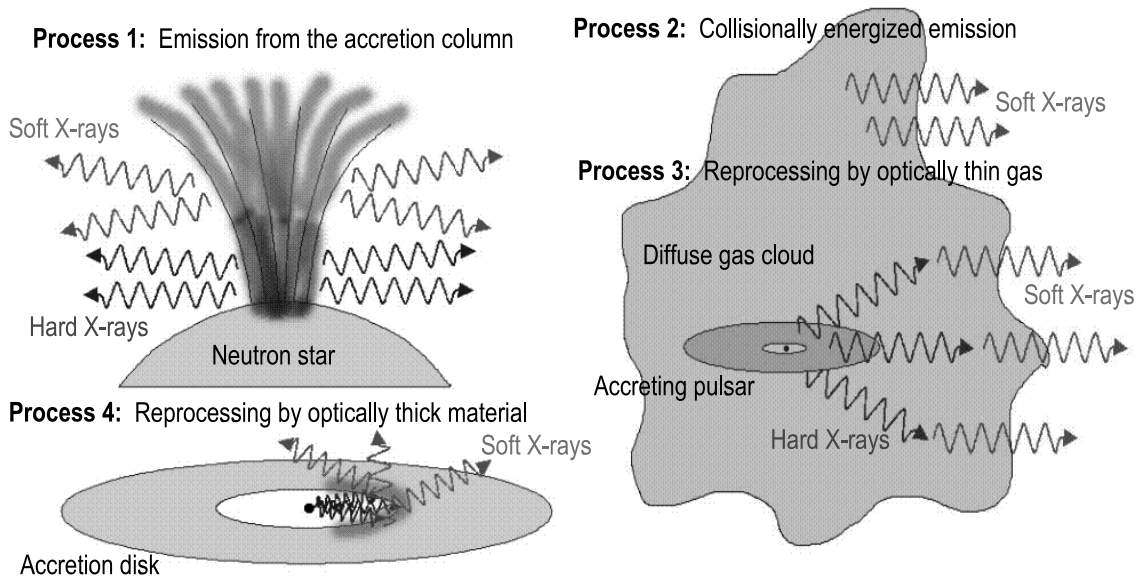


**Figure 3.5:** Schematic showing the soft-excess emission processes discussed by [Hickox et al. \(2004\)](#).

thermal Comptonization in the optically thick environment of the accretion column. Due to the presence of a strong magnetic field and the anisotropic pressure in the accretion column, the X-ray emission is non-isotropic as we will discuss in §3.4. The spin-phase average X-ray spectrum of the accretion column can be phenomenologically described as a power-law with a cut-off at high energies (i.e.  $\gtrsim 10$  keV).

#### 3.3.2 Soft excess

The emission originating from the accretion column provides the basic component of the X-ray spectrum of accreting *XRP*s. However, the spectrum of many *XRP*s shows evidence of an additional low energy component, the so-called soft excess ([Hickox et al. 2004](#)). This component is often modeled by a low-temperature **Black Body (BB)** ( $kT_{BB} \sim 0.1$  keV), however the physical origin of this perhaps ubiquitous feature of accreting *NS* can be much more complex. The most prominent mechanisms for the observed soft excess have been discussed by [Hickox et al. \(2004\)](#) and are (see also [Fig. 3.5](#)): (1) emission from the accretion column, (2) thermal emission from collisionally energized, diffuse gas around the *NS*, (3) reprocessing of the hard X-rays by diffuse material around the *NS*, and 4. reprocessing by optically thick, dense material around the *NS*. The first process might be prominent in low-luminosity pulsars ([La Palombara and Mereghetti 2006](#)) where due to the low optical depth of the accretion column we can see X-rays directly from the hot polar cap of the *NS*. The last process should be dominant in high luminosity systems where the accretion disc becomes inflated and has a larger angular size around the *NS* ([Endo et al. 2000](#)).

### 3.4 X-ray pulsars: understanding the emission pattern

From the discovery of the first pulsating X-ray systems (Her X-1 & Cen X-3, [Giacconi et al. 1971](#); [Tananbaum et al. 1972](#)) it was clear that an anisotropic accretion mechanism

### 3. BASIC PHYSICAL MECHANISMS IN X-RAY BINARIES

was needed to explain the observed X-ray pulsations.

It was thus proposed, what it is generally accepted today, that in highly magnetised compact stars accretion occurs through an accretion funnel that drives matter onto the magnetic poles of the compact star (Baan and Treves 1973). It is also accepted that within the accretion column, X-rays are produced through synchrotron (cyclotron) and bremsstrahlung radiation (Becker and Wolff 2007a). As a first attempt to explain the observed pulsations it was proposed that the observed pulse profile can be a result of two components, a knife and a pencil beam (Gnedin and Sunyaev 1973). A knife beam (or otherwise referred to as fan beam) is emitted perpendicular to the accretion column. This is a result of cyclotron radiation at high harmonics emitted perpendicular to the magnetic field (see Fig. 3.6). The pencil beam is a result of cyclotron radiation (at the first harmonic of the gyrofrequency). This radiation is directed along the magnetic field lines and should be strongly circularly polarised. It has also been

shown by solving the problem of radiative transfer that in the case of accreting pulsars due to the high anisotropy in the scattering cross section of photons by electrons, an anisotropic highly polarised pencil beam pattern is formed (Basko and Sunyaev 1975). It is interesting to note that the aforementioned treatment predicted that the lower energy photons would produce a narrower beam than the higher energy photons ( $h\nu > kT_e$ ). It is worth noting that the local thermodynamic equilibrium that is often invoked for the description of the accretion is an oversimplification (Postnov et al. 2015a). The emerging spectrum can be estimated by solving the radiation transfer which is taking place in the saturated Compton regime, with extraordinary mode 1 photons escaping from the sides of the column (i.e. polarised perpendicular to the  $k - B$  plane, where  $k$  is the photon wavevector and  $B$  the magnetic field vector). The intensity of ordinary mode 2 photons (i.e. polarised in the  $k - B$  plan) can be comparable to the mode 1 only at large angles (Lyubarskii 1986; Lyubarskii and Syunyaev 1988).

The basic picture of accretion onto highly magnetised NSs has been developed by many authors (e.g. Nagel 1981; White et al. 1983; Mészáros 1992; Paul et al. 1997; Rea et al. 2004; Trümper et al. 2013). But, after more than 40 years of theoretical efforts there is no self-consistent treatment of the accretion column radiation and the three-dimensional emission pattern. Some authors attempted to solve the problem by addressing the asymmetry of the observed pulse profiles in a pure mathematical way (Kraus et al. 1995), by reconstructing the asymmetric pulse profile as a sum of two symmetric (sum of cosines) periodic functions written as Fourier series. With this

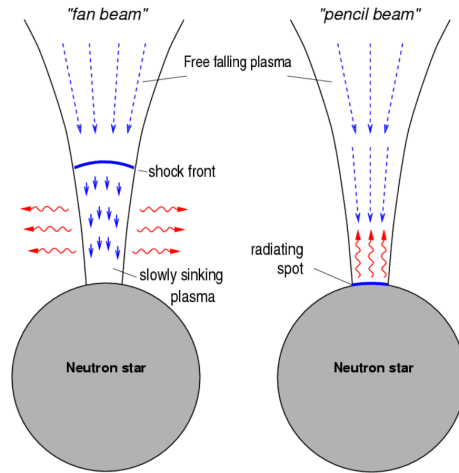


**Figure 3.6:** Schematic of accretion column. During low accretion rates radiation can escape parallel to the magnetic field lines. After a critical accretion limit (Schönherr et al. 2007b) the top of the accretion column becomes optically thick, a shock front is formed and radiation can only escape from the sides.

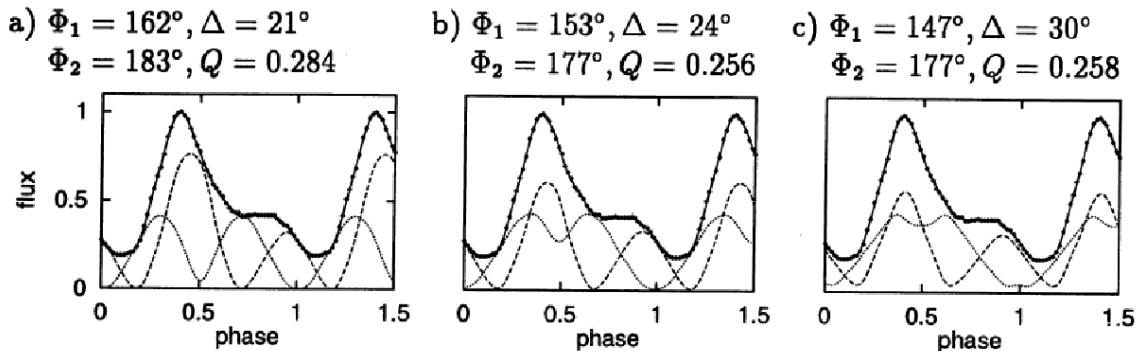


**Figure 3.7:** Three of the nine possible decompositions of the Cen X-3 pulse profile. Figure is taken from Kraus et al. (1995).

method information of the beamed pattern and, in some cases, the location of the magnetic poles can be extracted. We note that due to the large number of coefficients a list of possible decompositions is derived (Fig. 3.7). Another characteristic approach is the one used for the study of anomalous X-ray pulsars (Trümper et al. 2013). The NS is assumed to have a centred magnetic dipole, and that the emission originates from 2 points located at a given height above the NS. The beaming functions of the polar and fan beams are given by  $f \sin^m \phi$  and  $p \cos^k \phi$ , where  $\phi$  is the angle between the photon propagation and the magnetic field axis. Another free parameter is the angle between the rotation and magnetic axis. In this case the problem is solved by a hierarchical grid search and a best solution with its errors derived.

From the above, it is clear that the shape of the pulse profile in different energy bands and at different luminosities provides valuable insights to the shape of the emission pattern from the accretion column and may also shed light on the geometry and size of the accretion column itself. Thus, understanding the underlying physical mechanism of accretion onto a highly magnetised NS, requires detailed spectral and temporal analysis of numerous pulsating systems. But first, it is important to state that, although a model can fit a given pulse profile, the physical origin of the emission can still be under debate. This is similar to the notion that emission due to different mechanisms can still have the same observable signatures.

The term **pencil-beam** was initially used (Gnedin and Sunyaev 1973; Basko and Sunyaev 1975, 1976) to describe the radiation that escaped parallel to the magnetic field lines of the NS at low-luminosity accretion rates. Above a critical limit, the accretion rate becomes locally super-Eddington in the environment of the accretion column allowing radiation to escape perpendicular to the magnetic field lines in a **fan-beam** pattern (Basko and Sunyaev 1976). Partial beaming of the fan-beam emission towards the NS surface is expected due to scattering by fast electrons at the edge of the accretion column (Kaminker et al. 1976; Lyubarskii and Sunyaev 1988; Poutanen et al. 2013), and to a lesser degree due to gravitational bending of the fan-beam emission (Beloborodov 2002). A fraction of the fan beam can illuminate the NS surface, off which it will be reflected resulting in a secondary **polar-beam** that is directed perpendicular to the fan-beam.

The size and height of the accretion column is a function of the NS surface magnetic field strength and the mass accretion rate (Mushtukov et al. 2015b). As the accretion

### 3. BASIC PHYSICAL MECHANISMS IN X-RAY BINARIES

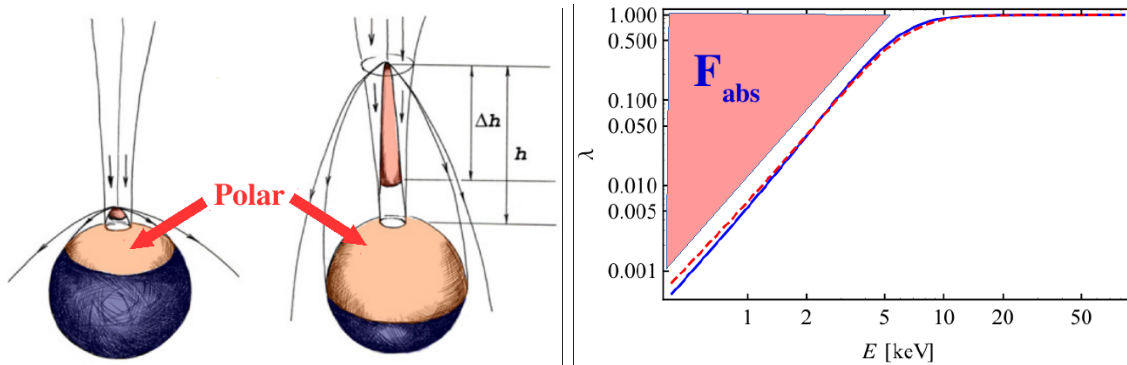


**Figure 3.8:** *Left:* Adaptation of figure by [Poutanen et al. \(2013\)](#), the reflected emission by the accretion column will illuminate the NS resulting in a polar beam. *Right:* Single-scattering Compton albedo of a NS atmosphere with strong magnetic field ([Postnov et al. 2015a](#)). Extraordinary and ordinary photons are shown with solid-red and dashed-blue lines. The absorbed part of the in-falling radiation will be re-emitted as a thermal component.

rate changes, the size of the accretion column will change and, in turn, it will affect the size of the illuminated region on the NS surface and therefore the strength of the reflected “polar” emission (see Fig. 3.8). If the accretion rate drops below the critical limit, the accretion column becomes optically thin in the direction parallel to the magnetic field lines, and the primary emission is then described by the pencil beam pattern ([Basko and Sunyaev 1975](#)). At this point, the surface of the NS itself is heated by the in-falling material and a hot spot is formed around the polar cap of the NS ([La Palombara and Mereghetti 2006](#)). If the only source of X-ray emission is the region of the polar cap, then the observed pulsed profile would have a simpler structure and resemble that of a WD in an intermediate polar ([de Martino et al. 2004](#); [Beuermann et al. 2012](#)). To conclude on the different patterns, phenomenologically the polar-cap emission as well as the polar-beam and pencil-beam emission patterns can be described by the same algebraic model with variations on the beaming angle. This similarity allows us to use the basic modelling ([Beloborodov 2002](#)) of the black-body pulsed emission from a hot spot and typically classify systems based on their pulse profile (Fig. 3.9).

So far we extensively use the term beaming (i.e. pencil, fan, polar), but it should be made clear that in all these analogs X-rays are not strictly emitted in one direction and the beaming is not a result of Lorentz boosting (e.g. like in a [Gamma Ray Burst \(GRB\)](#) or [AGN jets](#)). In X-ray pulsars X-ray photons are not isotropically emitted in the 3D sphere, and are indeed preferentially emitted in certain orientations compared to the accretion column, but in the sphere around the NS the intensity of this emission only changes by a factor of a few (see Fig. 3.10 for an example). To put this into perspective, in [GRB](#) the on-axis to off-axis emission intensity can change by a factor of  $10^4$  ([Kathirgamaraju et al. 2018](#)) while the observed luminosity is also enhanced by the high relativistic motion of the emitting region.

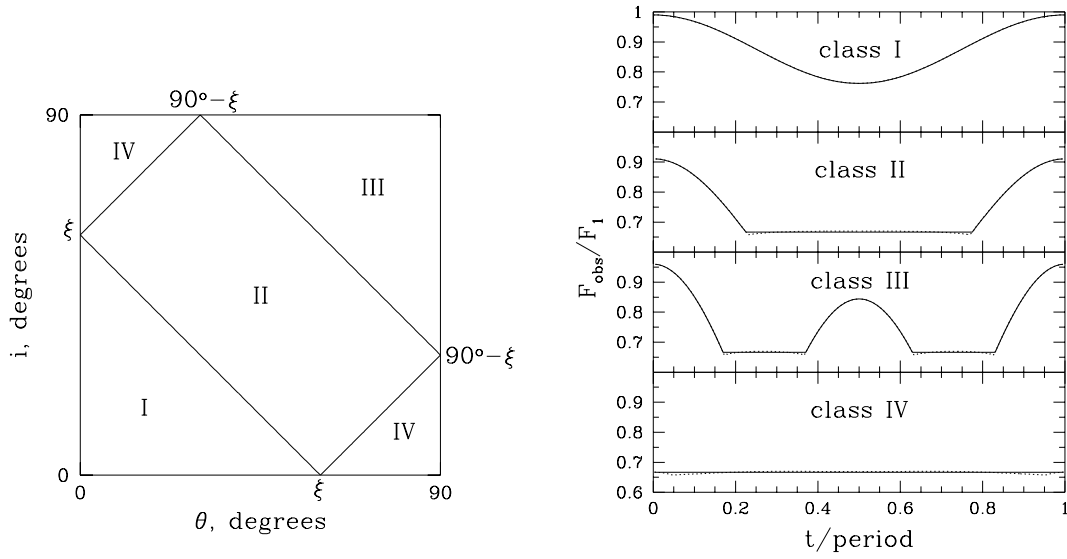


**Figure 3.9:** *Left:* Locations of the I-IV pulsar classes in the  $i - \theta$  plane. *Right:* Typical black-body pulse profiles for the four classes defined in the left figure. Figures are taken from Beloborodov (2002).

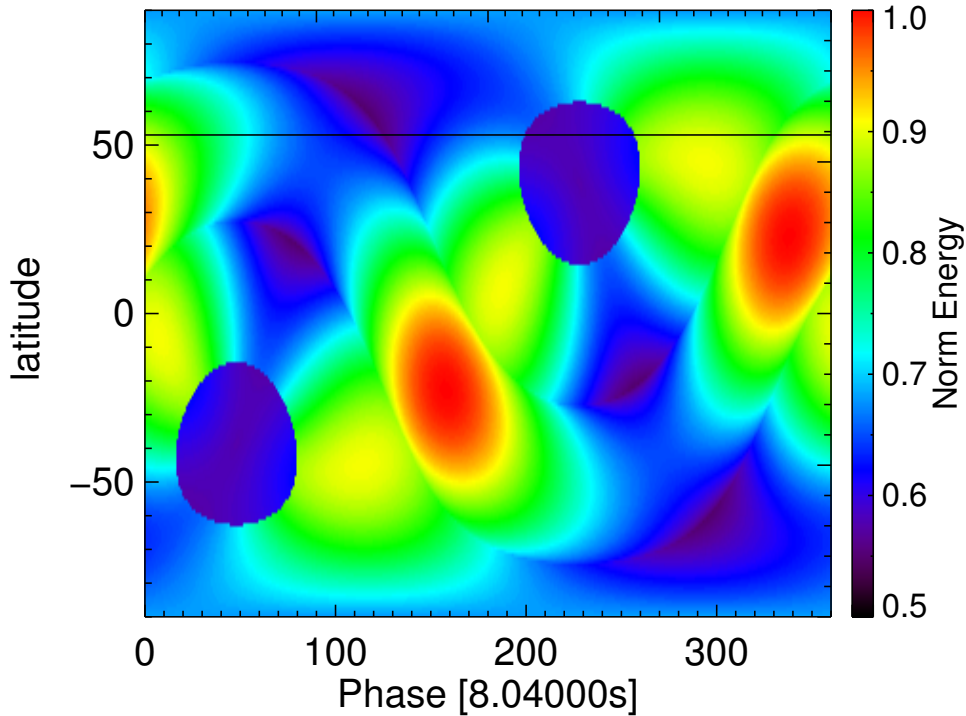


**Figure 3.10:** Heat map of the 3D emission pattern of X-ray pulsar LXP 8.04. The particular solution is based on the modeling of the pulse profile of the system during its 2014 major outburst. The X-ray intensity only changes by a factor of 2 in the 3D sphere, and the total X-ray luminosity is comparable to the Eddington limit. The two dark-blue spots are caused by the NS eclipsing one of the accretion columns, thus an observer at appropriate latitude (i.e. horizontal black line) can detect a sharp drop in the pulse profile of the system.

### 3. BASIC PHYSICAL MECHANISMS IN X-RAY BINARIES

---

## The Magellanic Clouds

The **MCs** are the nearest star-forming galaxies, thus providing a unique laboratory for the study of young stellar populations. Both **MCs** are projected away from the Galactic plane and, as a result, observations are marginally affected by foreground absorption ( $\sim 6 \times 10^{20} \text{ cm}^{-2}$ ; [Dickey and Lockman 1990b](#)). The **LMC** is an irregular dwarf galaxy at a distance of 50 kpc ([Pietrzyński et al. 2013](#)), while the **SMC** lies a bit further away at 62.1 kpc ([Graczyk et al. 2014](#)). Given their proximity and their dynamical interaction with our Galaxy the **MCs** have received a lot of attention. Of great interest is the study of their recent **SFH**, as it is believed to be connected with the density of **HMXBs**. The first global study of the **MCs**'s **SFH** has been recently performed based on **UBVI** data from photometric surveys ([Harris and Zaritsky 2004, 2009](#)). For the **SMC** it has been shown that there is a correlation between the number of **HMXBs** and regions with recent **Star Formation (SF)** ([Antoniou et al. 2010](#)). Specifically, it has been shown that the highest density of **BeXRBs** is found in the **SMC** Bar and in regions where the **SFH** is strongly peaked at  $\sim 42$  Myr ago. Moreover, regions with more recent **SF** are deficient in **BeXRBs**. Finally, it is characteristic that within the **SMC** only one **SgXRB** (i.e. accretion through Roche-lobe in SMC X-1) is found. For the **LMC** a similar correlation has been proposed but for younger stellar populations (i.e. 12.6 Myr [Antoniou and Zezas 2016](#)). However, since the **HMXB** population of the **LMC** suffers through multiple observational biases compared to the **SMC** one, a robust comparison with the **SFH** of the **LMC** has yet to be performed.

## 4. THE MAGELLANIC CLOUDS

---

# Part II

## Data and methodology



## Observations and data analysis

Despite what their name might suggest, X-ray binaries emit in a wide range of the electromagnetic spectrum, ranging from radio wavelengths to gamma rays. While for Galactic systems it is possible to detect [XRBs](#) in all these wavelengths, for systems located in the [MCs](#) it is more common to detect them in the X-ray and optical band due to instrument sensitivity issues. The discovery of new transient [HMXBs](#) and especially [BeXRBs](#) are often a result of monitoring regions of recent star formation where these systems are expected to reside, while persistent [HMXBs](#) are wind-fed in nature ([SgXRBs](#)). Nevertheless, there are several [BeXRBs](#) that remain active through their whole orbit, thus could be classified as persistent systems. Thus, by obtaining relatively deep X-ray observations we can discover most of the persistent [SgXRBs](#) and quiescent [BeXRBs](#) down to a certain luminosity level (i.e.  $L_X \sim 10^{33-34} \text{ erg s}^{-1}$ ). In this chapter I will discuss the observations and data reduction and analysis methods that were used for this study.

### 5.1 Multi-wavelength observations

The majority of the findings presented in this work are based on the analysis of newly acquired X-ray and optical data, as a result of proposals submitted to multiple facilities with me or other collaborators serving as principal investigator. This includes X-ray data from *XMM-Newton*, *Swift*, Chandra and NuSTAR space observatories, as well as optical data from the 2.2 m MPG/ESO telescope located at La Silla, Chile, and from the Southern African Large Telescope. The *XMM-Newton* [LMC](#) Very Large Programme (VLP) (PI: F. Haberl), has been the most ambitious project wherein I participated. The survey involves 70 pointed observations of the [LMC](#) aiming at a homogeneous study of a large fraction (about half) of the nearby galaxy. Moreover, through multiple collaborations I gained access to optical photometric data of the [MCs](#) obtained by the Optical Gravitational Lensing Experiment (OGLE). In the following sections I will discuss the characteristics of the instruments used to obtain these multi-wavelength data sets.

#### 5.1.1 X-ray

##### X-ray telescopes

X-ray telescopes are fundamentally different from the standard optical telescopes as, contrary to the visible light, X-rays are highly absorbed by lenses. In X-ray astronomy two main methods are used to perform quality observations, aperture modulation and grazing-incidence telescopes. Aperture modulation is a common technique used in collimators. Devices of this type create images of the X-ray sky through multiple snapshots. A rotating aperture selectively blocks and unblocks X-rays in a way which depends on their incoming direction, converting image information into time variations. An image of the source can then be reconstructed through mathematical transformations. Most of the modern X-ray observatories use reflective “mirrors” to focus X-rays onto CCD detectors. The idea is based on the original work of Hans Wolter ([Wolter](#)

## 5. OBSERVATIONS AND DATA ANALYSIS

---

1952), who noted that a set of parabolic mirrors could focus X-rays. A Wolter telescope is a telescope for X-rays using only grazing incidence optics. In the so-called Wolter-I configuration, X-rays are first reflected off a paraboloid, before undergoing a second reflection off a hyperboloid. In order to improve the effective area of the telescope, several mirrors of decreasing diameter can be nested within each other. Most of the orbiting X-ray observatories use Wolter telescopes. *XMM-Newton* has one of the largest collecting areas (peaking at 4260 cm<sup>2</sup>) and is ideal for surveying large areas of the sky. Chandra has the best angular resolution (<1'') and can resolve sources with accuracy better than most ground based optical telescopes.

### XMM-Newton observations

*XMM-Newton* holds three co-aligned X-ray telescopes. In the focal plane of each telescope, a [European Photon Imaging Camera \(EPIC\)](#) detects X-rays. The light of one telescope is deposited in a pn-CCD (EPIC-pn; [Strüder et al. 2001](#)), while about 44% of the photons from the other two telescopes is deposited in two Metal Oxide Semiconductor CCD arrays (EPIC-MOS; [Turner et al. 2001](#)). The remaining light of the two telescopes is collected by two Reflection Grating Spectrometers (RGS; [den Herder et al. 2001](#)) that enable high-resolution spectroscopy of bright sources observed on-axis. *XMM-Newton* orbits Earth with a period of  $\sim 48$  h in an elliptic orbit. Thus, it can perform uninterrupted observations with duration up to 130 ks. In combination with the large effective area and superb energy and spatial resolution of the X-ray telescopes, this satellite is ideally suited to carry out survey observations of large areas on the sky.

The *XMM-Newton* [LMC very large program \(LMC-VLP\)](#) survey offers the deepest and most complete coverage of a major part of the [LMC](#). The analysis of the survey data and other individual pointings of the [LMC](#) has been based on a pipeline developed by the ‘‘Nearby Galaxy X-ray Group’’ at [Max Planck Institute for extraterrestrial Physics \(MPE\)](#). Details about the pipeline can be found in several publications about surveys of nearby galaxies (M31, M33, SMC, LMC; [Pietsch et al. 2004, 2005](#); [Stiele et al. 2011](#); [Sturm et al. 2013a](#); [Maggi et al. 2016](#)). The pipeline consists of several *bash* scripts that make use of *XMM-Newton* Science Analysis Software<sup>1</sup> and *FTOOLS* packages<sup>2</sup>. In short, the pipeline is creating the event list, filtering the data for CCD defects and flaring background events, extracts images, and performs source detection similarly to the *XMM-Newton* serendipitous survey ([Rosen et al. 2016](#); [Watson et al. 2009](#)).

### Swift observations

*XMM-Newton* may be the most suitable X-ray telescope to study [HMXBs](#) in the [MCs](#) as it combines large effective area and superb temporal resolution, enabling us to perform innovative spectral and temporal studies of [HMXBs](#). However, telescopes with other capabilities are equally important in an in-depth study of these variable systems. *Swift* is an example of such an observatory. *Swift* is a low-orbit satellite that is known for its fast response time. It is the ideal instrument to follow up transient targets hours after their discovery. Moreover, due to its capabilities it can be ideally used to perform short monitoring observations of large regions in the sky through tiling observations. Given that the typical *Swift*/XRT exposure is 500-1000 s, the satellite can perform more than 100 pointed observations during one day. We have used *Swift* [target of opportunity](#)

---

<sup>1</sup><https://www.cosmos.esa.int/web/xmm-newton>

<sup>2</sup><https://heasarc.gsfc.nasa.gov/ftools/>

(ToO) observations to follow up the evolution of XRB outbursts. In addition, we have requested multiple monitoring observations of regions within the LMC aiming at the discovery of new transient systems. In order to ensure the fastest response time for a potential discovery of new systems we have set-up a collection of automated scripts to analyse all *Swift* data as soon as they become available and send email alerts. The scripts consists of a collection of *bash*, *python* and *FTOOLS* commands that perform the following tasks:

1. The script is automatically initialised every day at a predefined hour.
2. Searches the *Swift* on-line archive of quick-look data for all *Swift*/XRT observations that have been performed the last N hours (e.g. 24 h) within a certain region in the sky (i.e. MCs).
3. Downloads all data from the web, and performs a basic data reduction and source detection.
4. Email chains are being generated providing basic information about the status of the tasks that were performed.

### 5.1.2 Optical

#### Photometric data

In the literature several optical surveys of the LMC exist. The most broadly used surveys are the Two Micron All Sky Survey (2MASS: [Skrutskie et al. 2006](#)) and the Magellanic Clouds Photometric Survey (MCPS) ([Zaritsky et al. 2004](#)). The 2MASS survey covers 99.998% of the celestial sphere in the near-infrared J, H, and Ks band-passes. The MCPS catalogue provides U, B, V, and I photometric data for a 64 deg<sup>2</sup> area of the LMC with almost no incompleteness evidence for bright stars ( $V < 20$ ). In addition, the Spitzer SAGE Infrared Photometric catalogues provide magnitudes for a large subset ( $\sim 60\%$ ) of the massive stars in the MCs ([Bonanos et al. 2009, 2010](#)).

#### Variability information

HMXBs are extremely variable objects throughout the electromagnetic spectrum. Thus, data from photometric surveys are ideal for identifying counterparts of HMXBs but should be used with caution for studying their properties as they are not obtained simultaneously in all bands. Fortunately, for the case of the MCs we can gain insight on the properties of the HMXBs through monitoring campaigns. Both the MCs have been monitored by the Optical Gravitational Lensing Experiment (OGLE) ([Udalski et al. 2015](#)). OGLE started its initial observations in 1992 ([Udalski et al. 1992](#)) and continues observing till today, with its most recent data release (OGLE III) in 2008 ([Udalski et al. 2008](#)). Observations were made with the 1.3 m Warsaw telescope at Las Campanas Observatory. Images are taken in the V and I filter pass-bands, while the data reduction is described in [Udalski et al. \(2008\)](#). The OGLE-IV I band photometric data of the optical counterpart of known HMXBs are publicly available through the OGLE XROM<sup>1</sup> web page ([Udalski 2003, 2008](#)). Given that OGLE is obtaining

<sup>1</sup>XROM: OGLE-IV real time monitoring of X-ray variables: <http://ogle.astrouw.edu.pl/ogle4/xrom/xrom.html>

observations of the same region every 1-4 days, its data can be ideally used to extract information about the long-term variability of [HMXBs](#).

## 5.2 Measurement of basic parameters from the X-ray data

### 5.2.1 Temporal analysis

Given a time series, the most common way to study its variability is to convert the time series into the frequency domain using a Fourier decomposition. This transforms the time series from a function of time into a power as a function of frequency. The study of the power spectrum can give us insight into what kind of variability is dominant, if the time series is dominated by red or white noise and also if there is any periodicity detectable in the data. Detection of periodic behaviour is one of the most important aspects in the study of [XRBs](#) as it can provide crucial information about the nature of the system. Unfortunately, since the data are not always ideal one has to rely on different techniques to search for periodic signals.

#### Spin-period measurement

In X-ray astronomy, telescopes collect event rates which in general are very low. Thus, the best way to search for a periodic signal in an event based time series is by using an [epoch folding \(EF\)](#) technique ([Davies 1990](#); [Larsson 1996](#)). The method uses a set of trial periods within a predefined range and performs a  $\chi^2$  test based on the constant signal hypothesis. If the data are folded with an arbitrary period the result will be a flat signal, and any deviation will be consistent with Poisson statistics. If the real period is used, the pulse profile will significantly diverge from a flat profile (constant signal hypothesis). Thus, a large value of the  $\chi^2$  indirectly supports the presence of a periodic signal. A disadvantage of this method is that it lacks proper determination of the period uncertainty. Normally, the full-width-at-half maximum of the  $\chi^2$  distribution gives an order of magnitude estimate for the uncertainty, but this value only improves with the length of the time series and not with the number of events ([Gregory and Loredo 1996](#)). A better estimate for both the period and its error can be established via bootstrapping the original data. In this case the real-data are sampled randomly and the epoch folding test is performed on each of the samples, in a probabilistic sense the best period and its uncertainty can be derived from the distribution of the periods derived from the drawn subsamples. Alternatively, we can derive a period using a Bayesian framework. For the purpose of measuring spin periods one of the best available algorithms is the Gregory-Loredo method of Bayesian Periodic Signal Detection ([Gregory and Loredo 1996](#)).

However, we note that the significance of any detection should be established by performing simulated tests. One can create multiple fake event-based light curves, using Monte Carlo simulations, with the same properties as the observed ones but without the presence of periodic signal. Then, one can compute the significance of the detected signal in the real data by comparing it to the percentiles of the fake data (e.g. [Emmanoulopoulos et al. 2013](#)).

Any simple period search method (i.e. [EF](#)) starts with the assumption that the spin period has not changed within the duration of the observation. However, for [NSs](#)

with high spin-up rate the above assumption does not hold. Thus, one has two choices, either restrict the period search in very small intervals or take into account the period derivative. The first option can be performed in several systems, but in specific cases where the count rate is very low the second alternative is the only option. Given the high spin-up/spin-down rate ( $\dot{P}$ ) in some cases one should perform an accelerated epoch folding (AEF) test (Leahy et al. 1983b). This method uses a grid of points in the  $P$ - $\dot{P}$  space to perform an EF test.

Finally having obtained an accurate calculation of the ephemeris of the pulsar we can estimate the pulse profile. The pulse profile enables us to compute the **Pulsed Fraction (PF)**, which is defined as the ratio between the difference and the sum of the maximum and minimum count rates over the pulse profile i.e.

$$PF = (F_{max} - F_{min}) / (F_{max} + F_{min}). \quad (5.1)$$

This definition of PF will be used throughout the thesis, unless otherwise specified.

### Long-term evolution

When dealing with long-term variability of a system we are limited by the sampling pattern of the data. If the data are irregularly sampled the best approach is to use the **Lomb-Scargle (LS)** periodogram (Scargle 1982; Horne and Baliunas 1986). However, this recipe has two major points of concern (see VanderPlas 2017): (I) It assumes a sinusoidal pulse shape, thus for complex pulse shapes the power of the strength can be divided among multiple harmonics, and the true period might appear less significant than its harmonic, and (II) the window function used to sample the data will often generate spurious peaks and probable aliases of the true period. Again, to estimate the significance of any detection one should perform Monte Carlo simulations.

### 5.2.2 Spectral analysis

By performing X-ray spectral analysis we are interested in answering two questions, whether a model describes the data better than another, and given a model what are the uncertainties of the parameters that best describe the data. The most popularly used method is the chi-square ( $\chi^2$ ) minimisation. Given a model, it is common practice to vary its parameters until a statistical optimization is reached. However, despite its popularity some of its aspects are commonly neglected (Andrae et al. 2010). When testing non-linear models (which are the most common in astrophysics) it is not straight-forward to compute the degrees of freedom of the problem and the effect of noise in the reduced  $\chi^2$ . Thus, in order to assess the goodness of the fit of a model to some data it is important to inspect the residuals, which should have a Gaussian distribution for the best model.

Assuming a good fit has been established through the  $\chi^2$  method, error estimation is not straight forward. The common practice of stepping through a parameter space and estimating the change in the  $\chi^2$  is affected by the ‘‘curse’’ of dimensionality. Simply put, multiple solutions due to separate local probability maxima are neglected. Even the commonly used practice of computing contours of some  $\Delta\chi^2$  value can only be done for a maximum of two parameters at a time, and is only valid when the probability distributions are Gaussian-like and any dependency between parameters is negligible. An alternative approach is to use Markov chain Monte Carlo simulations for a Bayesian parameter estimation. A recent algorithm that has successfully been integrated to

## 5. OBSERVATIONS AND DATA ANALYSIS

---

the most common X-ray fitting environments is the [Bayesian X-ray analysis \(BXA\)](#) ([Buchner et al. 2014](#)). Thus, whenever we need to compare models for an unknown system, or estimate parameter uncertainties with increased accuracy we can adopt this method.

Apart from modelling the X-ray continuum it is sometimes important to search for features like narrow emission or absorption lines. These features are mostly affected by statistical noise, thus in order to determine their significance level we have to perform simulations. A common approach is to create simulated spectra based on the continuum model and search the fake spectrum for Gaussian-like features. Any such feature in the simulated spectrum is a result of noise. Thus, by performing numerous simulations we can determine the significance of the originally detected feature and argue if it can be a result of noise and with what probability ([Koliopanos and Vasilopoulos 2018](#)).

Finally, we note that depending on the scientific goal we do not always need to perform a detailed spectral analysis. In some cases, it might be sufficient to derive crude information about the spectral shape. This is especially important in low-luminosity systems, or when searching for rapid spectral changes when we cannot average many counts to perform spectral fitting. Basic information about the spectrum of an X-ray source can be derived from the so called [Hardness Ratio \(HR\)](#). HR can be defined in different ways, but it usually involves two energy bands, a soft and a hard. A simple definition is the ratio of the number of counts of the two bands. However, this can result in numerical issues in systems with low count rates, where an energy band can have very few to none counts. A more appropriate definition is the ratio of the difference over the sum of the number of counts in the two bands:

$$\text{HR} = (\text{R}_{\text{HARD}} - \text{R}_{\text{SOFT}})/(\text{R}_{\text{HARD}} + \text{R}_{\text{SOFT}}) \quad (5.2)$$

where  $\text{R}_{\text{HARD/SOFT}}$  is the background-subtracted count rate in the two energy bands. For harder spectra  $\text{HR} \rightarrow 1$ , while for softer  $\text{HR} \rightarrow -1$ . It is important to note that the value of [HR](#) depends on the detector and its characteristics, thus one should not compare [HRs](#) from different instruments. For *XMM-Newton* we commonly define 4 [HRs](#) by using the 5 standard energy bands (0.2-0.5, 0.5-1.0, 1.0-2.0, 2.0-4.5, 4.5-10 keV).

### 5.3 OGLE data: Time series analysis

Inspection of optical data from [BeXRBs](#) is important as it can reveal periodicities related to various mechanisms. Super-orbital variability can be a result of the Be disc precession, or formation/depletion cycle. Be stars are known to exhibit non-radial pulsations with periods between 0.5 and 2 days. However, the most important parameter we can derive from the optical data is the orbital period of the binary system. The most commonly used tool to search for periodicities in the [OGLE](#) data is the [LS](#) periodogram, and has been successfully used to measure orbital periods of many [BeXRBs](#) ([Rajaelimanana et al. 2011](#); [Schmidtke et al. 2013](#)). Nevertheless, it is not uncommon for optical light-curves of [BeXRBs](#) to show all the patterns of variability described above. Thus, in order to properly recover any periodic signature on short time scales one might need to remove any longer trends, a procedure called detrending. This is usually done by fitting the original data with a high-order polynomial and subtracting the best fit from the data. During this procedure one has to carefully

choose the polynomial order and only detrend parts of the light curve at a time in order not to erroneously remove the periodic signal.

## 5. OBSERVATIONS AND DATA ANALYSIS

---

## Part III

# High mass X-ray binaries population in the LMC



## Point source population of the LMC

It has been more than 10 years since the most recent catalogue of hard X-ray systems in the LMC has been released (Liu et al. 2005). Back then the number of known and candidate HMXB systems in the SMC and the LMC were 92 (47 pulsars) and 36 (7 pulsars), respectively. For the SMC, there has recently been an effort to investigate the properties of the HMXB population (Haberl and Sturm 2016). This detailed work resulted in the identification of a relatively clean sample of 121 HMXB of which 63 are pulsars. Moreover, the authors have shown that about 27 other systems previously identified as HMXBs were a result of misidentification. Thus, within 10 years a  $\sim 30\%$  increase in the number of known HMXB population has been made. The above work demonstrates the difficulty in any effort of obtaining and improving the complete XRB population in nearby galaxies.

For the LMC no similar collective effort has been made. Given the transient nature of the objects this task can take multiple years and require multiple observational resources. Our group has been involved in several observational campaigns aiming in increasing our understanding of the X-ray population within the LMC, with the *XMM-Newton* LMC-VLP survey providing the basis of this attempt. In the following paragraphs I describe the steps we took that resulted in an updated census of HMXBs in the LMC.

### 6.1 An updated catalogue of HMXBs in the LMC

In order to construct an updated catalogue of HMXBs in the LMC, we followed specific steps. From the literature we collected a catalogue of known and candidate HMXBs, and we enriched this catalogue with new candidate systems that arose from the *XMM-Newton* LMC-VLP. For the new candidate systems we selected X-ray sources with hard spectrum that are spatially correlated with an early type star following selection criteria that were optimised for the SMC (Sturm et al. 2013a). Hard X-ray sources were selected based on the HR values as defined for the 5 standard *XMM-Newton* energy bands (see §5.2.2). Specifically, we selected sources which satisfied the following:

$$\text{Hard} : 8\text{HR}_2 + 3\text{HR}_3 > -3 \text{ or } \text{HR}_2 > 0 \text{ if } \text{HR}_3 \text{ N/A} \quad (6.1)$$

$$\text{UltraHard} : 8\text{HR}_3 + 3\text{HR}_4 > -1.4 \text{ or } \text{HR}_3 > 0.2 \text{ if } \text{HR}_4 \text{ N/A} \quad (6.2)$$

For identifying the optical counterparts we used the MCPS optical catalogue. These selection criteria resulted in the selection of about 40 candidate HMXBs. However, most of them were observed at low luminosity levels thus no firm identification was possible (i.e. no X-ray pulsations). In order to strengthen our selection criteria we need additional information about the X-ray and optical properties of the systems. We thus followed a multi-step process to gain insight onto the nature of the systems:

- We obtained and analysed the OGLE light-curves of the systems, in order to search for long term variability or orbital period.
- We requested observing time in medium-sized optical telescopes (i.e.  $\sim 2$  m class) in order to perform spectral classification of the donor stars.

## 6. POINT SOURCE POPULATION OF THE LMC

---

- We requested monitoring observations with *Swift*/XRT aiming at the detection of type-I X-ray outbursts.

The above initiative has resulted in a substantial increase in the number of identified XRBs in the LMC. Our findings on individual systems have already been published in the form of refereed papers or astrophysical telegrams (Vasilopoulos et al. 2018, 2016b, 2014a; Sturm et al. 2014a; Vasilopoulos et al. 2014c, 2013a,d,c), while van Jaarsveld et al. (2018) have reported on the optical properties of a sub-sample of these systems. We now have a catalogue of 60 confirmed and candidate HMXB systems located in the nearby galaxy. Of them 19 have measured pulsations and thus host a NS as a compact object. In addition, we have firmly identified 2 intriguing SgXRBs, one being a very long period pulsar with spin period of 2013 s and the other the first confirmed extra-Galactic SFXT (Vasilopoulos et al. 2018) (see also §7). For the creation of our catalogue we have separated the systems into 3 categories. Class 1 systems, are those where the nature of the compact object is known; most of the systems in this category are BeXRB pulsars, while 2 identified BH HMXBs are also included in the same class (i.e. LMC X-1 & LMC X-3). Class 2 systems are hard X-ray systems with early type counterparts that exhibit either, (i) long term X-ray variability, (ii) optical variability or periodicity. Class 3 systems are hard X-ray systems with early type companions. For these systems further spectroscopic (optical) and X-ray monitoring observations are needed to securely classify them as HMXBs. Apart from the 60 HMXBs, we also identified 2 new Super-soft sources (SSS) that host a pulsating accreting WD. One of the two systems is a low luminosity Galactic SSS with a spin period of 1418 s (Haberl et al. 2017b), and the other one a very bright 160 s pulsar. The outcome of our project is summarised in Fig. 6.1 and Tables 6.1 and 6.2.

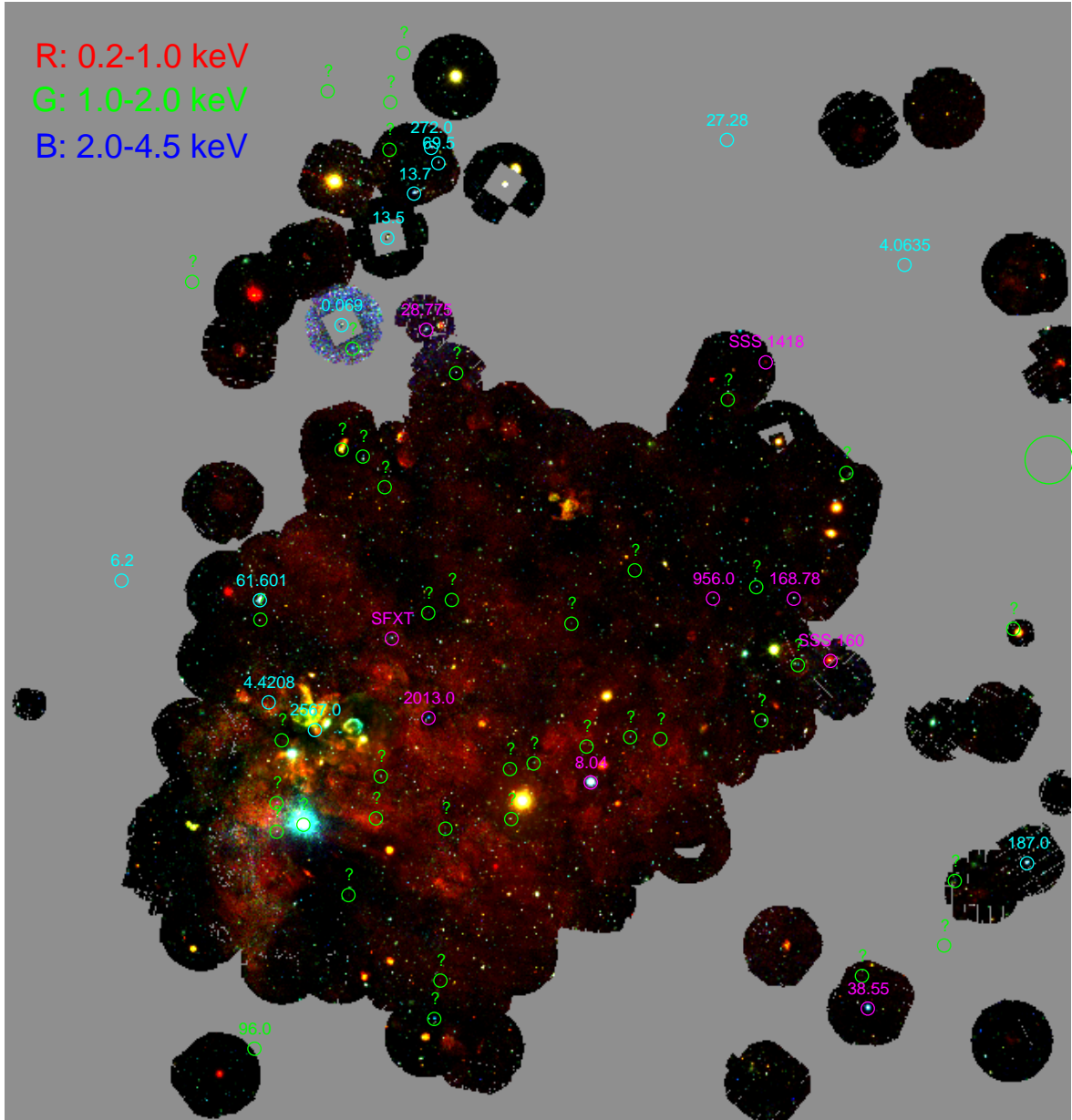


**Figure 6.1:** X-ray mosaic image of the LMC. Labels indicate spin period of the compact object if it is known. Systems that have been extensively studied by our group within the last years are marked with magenta.

Table 6.1: LMC HMXBs

index	RA (DEG)	DEC (DEG)	ERR <sup>(a)</sup> (")	P <sub>spin</sub> <sup>(b)</sup>	P <sub>orb</sub>	P <sub>long</sub>	XrayName	AZ16	Class <sup>(c)</sup>
1	72.77854156	-69.80088806	0.1-2M	187.0	21.631		Swift J045106.8-694803	1	1B
2	73.49624633	-68.46749877	3.0-X				2XMMJ045359.1-682803		3
3	73.94338989	-69.95565032	1.6-X		76.0				2B
4	73.99517059	-70.33332824	0.1-2M				Swift J045558.9-702001	2	3B
5	75.19204711	-70.74352264	0.1-M	38.55	30.77	442.0	IGR J05007-7047	5	1B
6	75.34947204	-70.55944824	0.09-U				CAL 9, RX J0501.6-7034	6	2B
7	75.71564483	-66.44081115	0.09-U	4.0635			CAL E, RX J0502.9-6626	7	1B
8	76.31435394	-67.66835021	0.9-X						3
9	76.84229278	-68.79960632	5.6-X				XMMU J050722.1-684758		3B
10	76.98041534	-68.41833496	4.5-X	168.78			XMMU J050755.3-682506	9	1B
11	77.37122344	-69.13346099	1.0-X						3
12	77.58093261	-68.36518859	3.0-X						3
13	78.17416381	-67.28971862	7.0-R				RX J0512.6-6717	10	3
14	78.25070190	-68.44446563	3.0-X	956.0	1350.0		3XMM J051259.8-682640		1
15	78.36783599	-65.78844451	0.5-SU	27.28	27.4		Swift J0513.4-6547	11	1B
16	78.99919128	-69.26933288	1.2-X				RX J0516.0-6916	12	3
17	79.49394226	-69.26489257	3.0-X						3
18	79.49517822	-68.29867553	1.4-X						3S
19	80.12442016	-69.53211212	0.1-2M	8.04	24.5		RX J0520.5-6932	14	1B
20	80.20407104	-69.32515716	0.9-X		440.0				3
21	80.47688293	-68.61492156	3.0-X						3
22	81.07118988	-69.42613220	1.0-X		547.0				3
23	81.44257354	-69.74754333	1.3-X						3
24	81.46089172	-69.45835113	0.9-X						3B

Continued on next page

<sup>a</sup> Instrument/Survey/catalogue used for position determination: XMM-Newton (X), ROSAT (R), Swift/XRT (SX), Swift/UVOT (SU), Chandra (C), 2MASS (2M), MACHO (M), GROND (G), USNO UCAC2 Catalog (U), the GSC II all-sky catalog (oG)

<sup>b</sup> For spin (P<sub>spin</sub>), orbital (P<sub>orb</sub>) or super-orbital (P<sub>long</sub>) periods see Antoniou and Zezas (2016), van Jaarsveld et al. (2018) and references within. AZ16 is the index number used in the Antoniou and Zezas (2016) catalogue.

<sup>c</sup> Classification of systems, class 1-2 systems are identified HMXBs while class 3 are good candidates (see text). Letter refer to the nature of the donor star when known, i.e. Sg (S) or Be (B) star.

Table 6.1: LMC HMXBs Continued.

index	RA (DEG)	DEC (DEG)	ERR <sup>(a)</sup> (")	P <sub>spin</sub> <sup>(b)</sup>	P <sub>orb</sub>	P <sub>long</sub>	XrayName	AZ16	Class <sup>(c)</sup>
25	82.24302673	-67.16297149	0.7-X			193.0			3B
26	82.36974334	-68.47607421	1.1-X						3
27	82.44935607	-65.94543457	0.03-U	69.5			RX J0529.8-6556	20	1B
28	82.54547882	-69.79878234	1.0-X						3B
29	82.54666900	-65.85610961	1.5-X	272.0			XMMU J053011.2-655122	21	1B
30	82.67458343	-66.90805816	3.6-SX	28.775			Swift J053041.9-665426	22	1
31	82.68861389	-70.67613220	1.2-X			280.0			3B
32	82.74644470	-68.54840087	1.4-X						3
33	82.78404235	-69.15618896	4.5-X	2013.0			XMMU J053108.3-690923		1S
34	82.80472564	-66.11854553	0.03-U	13.7			EXO 0531-660905	24	1B
35	82.81380462	-70.89664459	3.0-X					25	3
36	82.90320587	-65.30449676	0.1-2M				RX J0531.5-6518	27	3B
37	83.10500335	-65.58583068	17.4-R				RX J0532.4-6535	29	3B
38	83.13594055	-65.86125946	0.015-U				RX J0532.5-6551	30	3S
39	83.20647430	-66.37033081	0.02-U	13.5	1.40841		LMC X-4	31	1S
40	83.33603668	-68.69006347	4.5-X			560.0	XMMU J053320.8-684122	32	1S (SFXT)
41	83.36728668	-67.81288909	5.0-X				XMMU J053328.1-674846		3B
42	83.59556579	-69.48495483	1.6-X						3
43	83.68334960	-67.63090515	3.0-X						3
44	83.70307159	-69.72689056	3.0-X						3
45	83.77489471	-67.00437927	0.04-U		241.0		RX J0535.0-6700	33	3B
46	83.92080688	-66.86489105	0.03-U	0.069	16.6515	420.8	1A 0535-66	34	1B
47	83.97416687	-65.50944519	13.0-R				RX J0535.8-6530	35	3
48	84.000417	-67.585417	0.7-C				CXOU J053600.0-673507		3?
49	84.22245025	-70.16296386	1.3-X						3

Continued on next page

<sup>a</sup> Instrument/Survey/catalogue used for position determination: *XMM-Newton* (X), ROSAT (R), *Swift*/XRT (SX), *Swift*/UVOT (SU), Chandra (C), 2MASS (2M), MACHO (M), GROND (G), USNO UCAC2 Catalog (U), the GSC II all-sky catalog (oG)

<sup>b</sup> For spin (P<sub>spin</sub>), orbital (P<sub>orb</sub>) or super-orbital (P<sub>long</sub>) periods see Antoniou and Zezas (2016), van Jaarsveld et al. (2018) and references within. AZ16 is the index number used in the Antoniou and Zezas (2016) catalogue.

<sup>c</sup> Classification of systems, class 1-2 systems are identified HMXBs while class 3 are good candidates (see text). Letter refer to the nature of the donor star when known, i.e. Sg (S) or Be (B) star.

Table 6.1: LMC HMXBs Continued.

index	RA (DEG)	DEC (DEG)	ERR <sup>(a)</sup> (")	P <sub>spin</sub> <sup>(b)</sup>	P <sub>orb</sub>	P <sub>long</sub>	XrayName	AZ16	Class <sup>(c)</sup>
50	84.63920593	-69.19973754	0.1-oG	2567.0			CXOU J053833.4-691158	46	1S
51	84.73587799	-64.08427429	0.1-oG		1.70479		LMC X-3	36	1B (BH)
52	84.91698455	-69.74269104	0.015-U		4.22		LMC X-1	37	1S (BH)
53	85.18895721	-69.24754333	1.7-X				RX J0541.4-6936	39	3B
54	85.34249877	-69.60805511	6.6-R				IGR J05414-6858	38	1B
55	85.36108398	-69.02324676	0.4-G	4.4208	19.9		XMMU J054129.4-694621	40	1B
56	85.37267303	-69.77294158	5.0-X				XMMU J054134.7-682550	41	3
57	85.39299774	-68.43008422	1.0-SU	61.601	31.5		RX J0541.6-6832	43	1B
58	85.40458679	-68.54222106	4.5-R				RX J0544.1-7100	44	3B
59	86.02163696	-71.01409912	0.024-U	96.0			H 0544-665	47	1
60	86.06562042	-66.56319427	0.015-U				Swift J0549.7-6812		
61	87.52691650	-68.24906158	0.5-SU	6.2					

<sup>a</sup> Instrument/Survey/catalogue used for position determination: *XMM-Newton* (X), ROSAT (R), *Swift*/XRT (SX), *Swift*/UVOT (SU), Chandra (C), 2MASS (2M), MACHO (M), GROND (G), USNO UCAC2 Catalog (U), the GSC II all-sky catalog (oG)

<sup>b</sup> For spin (P<sub>spin</sub>), orbital (P<sub>orb</sub>) or super-orbital (P<sub>long</sub>) periods see Antoniou and Zezas (2016), van Jaarsveld et al. (2018) and references within. AZ16 is the index number used in the Antoniou and Zezas (2016) catalogue.

<sup>c</sup> Classification of systems, class 1-2 systems are identified HMXBs while class 3 are good candidates (see text). Letter refer to the nature of the donor star when known, i.e. Sg (S) or Be (B) star.

## 6.1 An updated catalogue of HMXBs in the LMC

**Table 6.2:** Optical counterparts of LMC HMXBs

index <sup>(a)</sup>	SpClass <sup>(b)</sup>	U <sub>Z</sub>	B <sub>Z</sub>	V <sub>Z</sub>	I <sub>Z</sub>	J <sub>2M</sub>	H <sub>2M</sub>	K <sub>2M</sub>
1	B0-1 III-Ve	13.736	14.702	14.6	14.512	14.513	14.452	14.205
2		13.827	14.986	14.926	14.947			
3	B1 IIIe (N18)	13.402	14.521	14.466	14.446	14.31	14.218	14.179
4	B1-2e	13.179	14.104	14.153	14.072	14.024	13.886	13.625
5	O9Ve (N18)	16.676	14.672	14.727	14.622	14.674	14.483	14.172
6	B0Ve	13.839	14.806	14.982	15.209	13.976	13.167	13.063
7	B0Ve	13.051	14.171	14.364	13.988	14.111	14.033	13.885
8		15.139	15.86	15.99	16.234	16.366	15.733	16.726
9	B3 IIIe (N18)	15.05	15.658	15.787	15.797	15.656	15.344	14.599
10	OB (N18)	14.018	15.016	14.945	14.894	14.77	13.806	14.354
11		0.0	16.662	16.401	15.434	14.527	14.015	13.972
12		13.073	14.002	14.078	14.277	14.515	14.556	14.522
13		15.369	16.09	16.187	16.394			
14		13.883	14.874	14.74	14.679	14.228	13.998	13.719
15	B0-B1Ve (N18)	14.122	15.067	15.098	15.328	15.226	15.091	14.773
16		0.0	19.056	17.603	16.533	15.351	15.148	13.919
17		14.623	13.264	11.536	0.0	7.61	6.779	6.462
18		15.959	16.315	16.232	16.406			
19	O9Ve <sup>*</sup>	0.0	14.312	16.004	0.0	14.372	14.211	14.276
20		14.42	15.072	15.178	15.146	15.35	15.192	14.814
21		0.0	16.715	15.655	0.0			
22		15.164	15.865	15.962	16.319			
23		16.05	16.393	16.312	16.806			
24	B2 IVe-Ve (N18)	14.624	15.299	15.12	15.272	15.26	15.053	14.676
25	B0-B0.5Ve (N18)	14.224	15.072	15.04	0.0	15.568	15.845	15.471
26		15.312	16.309	16.309	16.436	16.066	15.734	16.61
27	B0.5Ve	13.761	14.477	14.594	14.741	14.661	14.686	14.635
28	B2-B3 IIIe (N18)	15.273	15.97	16.073	16.353			
29	B1-3 III-Ve(N18)	13.933	14.894	14.877	14.691	14.698	14.496	14.296
30		14.312	15.007	15.321	15.586	15.258	14.979	14.908
31	B0.5-B1Ve (N18)	14.68	15.391	15.583	15.824	15.835	15.272	15.406
32		14.699	15.764	15.907	16.179	16.379	15.971	15.803
33	B0 IIIe (N18)	13.058	13.632	13.701	13.429	13.296	13.336	13.267
34	B0.5IIIe	13.862	14.749	14.798	14.763	14.394	14.089	14.072
35		13.158	14.009	14.051	13.799	13.72	13.555	13.362
36	B2Ve	15.401	15.875	16.007	16.226	16.256	16.364	15.3
37								
38	B0II - B0.5II	12.212	12.474	13.048	13.162			
39	O8III	15.449	13.94	14.167	0.0	14.586	14.78	14.75
40	B0.5 Ib (N18)	11.673	12.684	12.776	12.239	12.746	12.78	12.789
41	<B0.5 IIIe (N18)	13.872	14.712	14.816	14.722	14.655	14.42	14.186
42		15.258	15.992	16.11	16.418			
43		15.051	15.999	15.586	15.226	14.507	14.157	13.505
44		15.597	15.317	14.957	14.681	14.345	14.123	14.102
45	B0Ve	13.941	14.728	14.873	14.91	14.876	14.783	14.463
46	B0.5/III/III	13.828	14.584	14.824	15.281	15.152	15.099	15.736
47								

*Continued on next page*

<sup>a</sup> Index number as in Table 6.1. Optical magnitudes from the 2MASS (2M) (Skrutskie et al. 2006) and Zaritsky et al. (2004) (Z) catalogues.

<sup>b</sup> For spectral classification see Antoniou and Zezas (2016), or van Jaarsveld et al. (2018) [N18]

## 6. POINT SOURCE POPULATION OF THE LMC

---

**Table 6.2:** Optical counterparts of LMC HMXBs Continued.

index	SpClass <sup>(b)</sup>	U <sub>Z</sub>	B <sub>Z</sub>	V <sub>Z</sub>	I <sub>Z</sub>	J <sub>2M</sub>	H <sub>2M</sub>	K <sub>2M</sub>
48	O5III(f)	12.253	13.344	13.516	14.504	13.643	13.711	13.822
49		15.686	15.5	15.035	14.726			
50	O9III <sub>n</sub>	15.172	15.983	15.84	15.593	15.482	15.606	14.828
51	B2.5Ve pec							
52	O8III	11.745	12.295	12.08	11.493	11.196	11.002	10.857
53	B1-3 III-Ve(N18)	15.332	16.052	15.98	15.943	15.785	15.854	15.562
54								
55	B0-1 IIIe	14.463	15.296	15.329	15.527	15.084	14.853	14.989
56	O9.7 II-Ib	11.515	12.17	12.285	12.303	12.629	12.674	12.63
57	B0-1 IIIe (N18)	13.138	14.072	14.043	13.911	13.843	13.736	13.63
58		13.121	14.136	14.24	14.356	14.673	14.71	14.64
59	B0Ve	14.598	15.292	15.235	15.22	15.133	15.025	15.168
60	B0Ve	14.127	15.075	15.201	15.202	14.792	14.721	14.585
61		14.164	15.091	15.028	15.003	14.846	14.767	14.444

<sup>a</sup> Index number as in Table 6.1. Optical magnitudes from the 2MASS (2M) (Skrutskie et al. 2006) and Zaritsky et al. (2004) (Z) catalogues.

<sup>b</sup> For spectral classification see Antoniou and Zezas (2016), or van Jaarsveld et al. (2018) [N18]

## 6.2 The star formation history of the LMC through its X-ray binary population

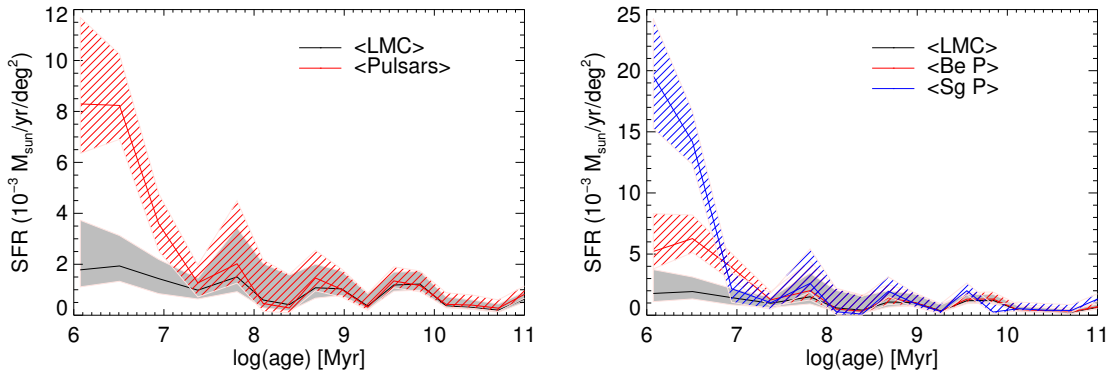


**Figure 6.2:** SFH of the regions containing pulsating HMXBs versus the average SFH of the LMC.

## 6.2 The star formation history of the LMC through its X-ray binary population

The MCs are our nearest star forming galaxies thus an excellent laboratory to study their binary population and compare it to that of our own Galaxy. The study of the SMC population has revealed the difference in the spectral-type distributions of the donor stars, as it is evident by the lack of SgXRBs in SMC (only 1 known system out of  $\sim 100$ ). In contrast to the SMC, the LMC has received much less attention. Having obtained a clean sample of HMXBs in the LMC we can thus perform a first comparison of the spatial distribution of the population and the SFH of the galaxy. Given the low number of identified systems a thorough comparison between different populations cannot be performed. Nevertheless we have selected 3 different sub-samples of sources, (1) all the known pulsars, (2) all the known BeXRB pulsars, and (3) all the identified SgXRB systems. For each individual system we have computed the local SFH using the study of Harris and Zaritsky (2009). Then we computed the total SFH by summing the local rate around each system. Moreover, we computed the average SFH by normalising by the area where the total SFH was computed. In Fig 6.2 you can see the results of our study. Comparing the SFH around pulsars with the average one of the LMC we note an enhanced star formation rate below 25 Myr.

It is important to note that at recent epochs (i.e. closer to the present era) the available SFH catalogue lacks the resolution for a detailed study (see Harris and Zaritsky 2009, for more information). Moreover, given the way the data are provided it is not possible to estimate uncertainties in a probabilistic way, mainly due to the fact that the errors are not Gaussian and no information about the marginalised distributions of the parameters is given. To estimate uncertainties we just used the lower and upper rates provided by the catalogue following the instructions in their work.

Given the low number of sources it is important to calculate the chance coincidence of the above correlation. In other words, assuming there was no correlation between the spatial distribution of HMXB and the regions with enhanced recent SFH what would be the probability of reproducing the results of 6.2. To answer that we created random distributions of sources with the same population number, i.e. 16 BeXRB pulsars and 4 SgXRBs. We selected 10000 random samples of each population size and for each of them we estimated the average SFH. Then we estimated the uncertainties of each each

## 6. POINT SOURCE POPULATION OF THE LMC

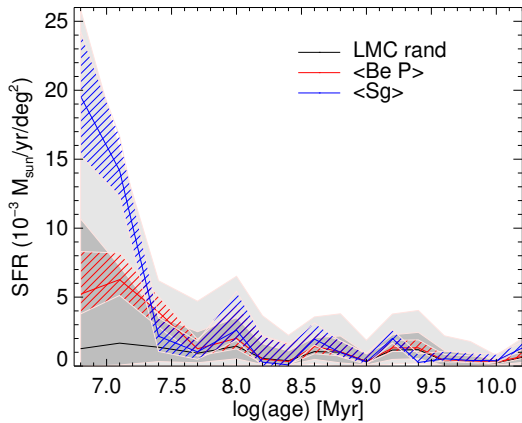


**Figure 6.3:** SFH of the regions containing identified BeXRB pulsars (red) and SgXRBs (blue). The average SFH of a randomly selected population is plotted with a black solid line. The 99.7 percentile of a population with the same size as the the BeXRB pulsars and SgXRBs samples are marked with dark and light grey colours respectively.

distribution using the  $3\sigma$  percentiles (i.e. 99.7% probability). The results are plotted in Fig. 6.3 where it is clear that we cannot claim that the correlation is not a result of a chance coincidence with more than  $3\sigma$  probability.

Apart from the study of the SFH and its relation with the binary formation efficiency, we can perform some additional population tests and comparisons. One of the important characteristics of BeXRB systems is the observed correlation between the binary orbital period ( $P_{\text{orb}}$ ) and the spin period ( $P$ ) of the NS (Corbet 1984). This is believed to be a result of the angular momentum evolution of the pulsar under the influence of the accreting material, although the underlying physical mechanism remains unclear. Any theoretical model about binary formation and/or accretion schemes in magnetised NS should be able to reproduce the observed correlation.

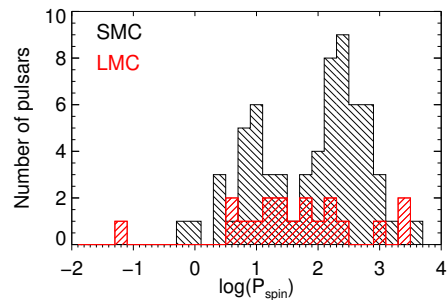


**Figure 6.4:** Spin period distributions of HMXBs in the MCs.

The spin period distribution of BeXRBs follows a bimodal distribution (see Fig. 6.4); this has been proposed to be related to two different types of supernovae (iron-core-collapse and electron-capture) that produce the majority of NS (Knigge et al. 2011). Alternatively, it has been proposed that the bimodal spin distribution is linked to different accretion schemes (Cheng et al. 2014a). The latter scenario is also supported by the different long-term X-ray variability of objects with short and long spin periods (Haberl and Sturm 2016). Another property worth exploring is the spin evolution of both spin-up and spin-down pulsars, which seems to be driven by the same mechanism (i.e. accretion Christodoulou et al. 2017a). Finally, a relationship between spin and outburst amplitude has been reported, with the short-period pulsars exhibiting the strongest outbursts (Haberl and Sturm 2016).

**Long Period Pulsars (LPP)** are a subclass of HMXBs with  $P \gtrsim 1000$  s. The slowest spinning pulsar has a period of  $\sim 36200$  s (Sidoli et al. 2017a). Although one can define different sub-groups of LPP (e.g., systems with high spin-up/down rates versus systems close to spin equilibrium), any classification by standardised criteria is challenged by newly discovered systems that do not seem to comply with any scheme.

## 6.2 The star formation history of the LMC through its X-ray binary population

---

**Accretion mechanisms:** Below we highlight the main characteristics of accretion in LPP systems. The long spin period of the pulsar suggests that the magnetosphere is also rotating at a slow rate. Thus, LPP systems are always in the accretor phase. Assuming that an LPP system rotates near its equilibrium period and that an accretion disc has formed around the NS, we can derive a relation between the main quantities of the system (Li and van den Heuvel 1999; Davies and Pringle 1981):

$$P_{\text{eq,d}} \approx 20 \text{ s } B_{12}^{6/7} \dot{M}_{15}^{-3/7} R_6^{18/7} M_{1.4}^{-5/7} \quad (6.3)$$

This scenario, however, fails to explain long spin periods ( $P > 1000 \text{ s}$ ) without invoking a NS with magnetar-like magnetic field strength (Clark et al. 2015). In addition, it falls short in explaining systems with non-zero spin derivatives. An indicative example is SXP 1062, where the NS exhibits a surprisingly high spin-down rate that challenges available scenarios of accretion physics and spin period evolution (Haberl et al. 2012a).

Another way to explain the LPP at equilibrium is to invoke models of quasi-spherical accretion settling in wind-fed systems (Shakura et al. 2012). In this case, the spin equilibrium period is related to the wind properties of the donor star (e.g., wind velocity  $v_w$ ) and the orbital period ( $P_{\text{orb}}$ ) of the binary. The torques acting on the shell of quasi-static plasma above the magnetosphere can either spin-up or spin-down the NS. Because of the short relaxation time ( $10^4 \text{ yr}$  – see also Sidoli et al. 2017a), it is reasonable to assume that the NS is at an equilibrium state, where its spin period remains constant with time and is given by (Shakura et al. 2012):

$$P_{\text{eq,w}} \approx 1000 \text{ s } \mu_{30}^{12/11} \dot{M}_{16}^{-4/11} \left( \frac{P_{\text{orb}}}{10 \text{ d}} \right) \left( \frac{v_w}{10^3 \text{ km s}^{-1}} \right)^4, \quad (6.4)$$

where  $\mu = 10^{30} \mu_{30} \text{ G cm}^3$  corresponds to a NS magnetic field strength of  $10^{12} \text{ G}$  and  $\dot{M} = 10^{16} \dot{M}_{16} \text{ g s}^{-1}$  is the accretion rate onto the NS inferred by the X-ray luminosity as  $L_X \simeq 10^{36} \dot{M}_{16} \text{ erg s}^{-1}$ .

To conclude, the SFH of the LMC make it ideal target to further study the low-luminosity HMXB population, which should host many wind-fed systems. As it is shown by the demographics of its HMXB population, the galaxy hosts a much higher number of SgXRB systems than the SMC. Thus, without proper classification any comparison of the population and the local SFH is incomplete. The sample of known LMC pulsars is yet too small for any comparison with the Galactic and the SMC sample, thus we can not argue in favour of a bimodal distribution. Still, the LMC hosts a similar number of LPP (3) as the SMC despite the fact that observational biases (e.g. numerous deep pointings) would favour the detection of such systems in the SMC. The number of HMXBs in the SMC correlates with the star-formation rate 40 Myr ago (Antoniou et al. 2010). There is evidence for a similar correlation between HMXBs and a younger stellar population in the LMC (Antoniou and Zezas 2016), but a larger sample of *confirmed* systems is needed to establish a statistically significant result. The presence of a correlation between LPP systems and episodes of younger star formation in LMC remains to be investigated.

## 6. POINT SOURCE POPULATION OF THE LMC

---

## New SgXRBs in the LMC

**I**n this chapter I report on the X-ray and optical properties of two high-mass X-ray binary systems located in the **LMC**. Based on the obtained optical spectra, we classify the massive companion as a supergiant star in both systems. Timing analysis of the X-ray events collected by *XMM-Newton* revealed the presence of coherent pulsations (spin period  $\sim 2013$  s) for XMMU J053108.3-690923 and fast flaring behaviour for XMMU J053320.8-684122. The X-ray spectra of both systems can be modelled sufficiently well by an absorbed power law, yielding hard spectra and high intrinsic absorption from the environment of the systems. Due to their combined X-ray and optical properties we classify both systems as **SgXRBs**: the 19<sup>th</sup> confirmed **XRP** and a probable **SFXT** in the **LMCs**, the second such candidate outside our Galaxy.

### 7.1 General Information

In the case of the **MCs** all but one of the known **XRB** systems (i.e. LMC X-2 is low-mass X-ray binary [Smale et al. 2003](#)) are **HMXBs** in nature (e.g. [Antoniou et al. 2010](#); [Antoniou and Zezas 2016](#)). The **SMC** alone harbours about 120 **HMXBs** of which 64 are confirmed **BeXRB** pulsars and only one is a confirmed **SgXRB** ([Haberl and Sturm 2016](#); [Vasilopoulos et al. 2017c](#); [Maravelias et al. 2014](#)). The population of **BeXRBs** was shown to be associated with the recent star formation history of the galaxy that peaks at  $\sim 40$  Myr ago; this is also the time needed for the evolution of a high mass binary system into a **BeXRB** ([Antoniou et al. 2010](#)). The **LMC** shows evidence for more recent star formation than the **SMC** ([Harris and Zaritsky 2009](#)), and could be thus a good candidate for detecting more **SgXRB** systems. Our knowledge of the X-ray population of the **LMC** is much less complete than that of the **SMC**. This is mainly due to its larger projected angular size in the sky that hinders extensive monitoring observations, while deep X-ray observations with modern observatories can only cover a small fraction of the galaxy. Nevertheless, the **LMC** is known to harbour four **SgXRB** systems out of the  $\sim 40$  **HMXB** candidates ([Antoniou and Zezas 2016](#)). The recent *XMM-Newton* **LMC** survey aimed to address the lack of deep X-ray observations in the **LMC**, by homogeneously covering a  $\sim 15$  square degree area of the nearby galaxy down to a limiting point source luminosity of  $2 \times 10^{33}$  erg s<sup>-1</sup>.

In the following paragraphs I report on the properties of two new **HMXBs** in the **LMC**. Both systems were detected at a moderate luminosity of  $\sim 10^{35}$  erg s<sup>-1</sup> during the *XMM-Newton* **LMC** survey allowing a detailed spectral and temporal study of their properties. The study of their long-term X-ray variability is complemented by *Swift*/XRT observations. Finally, the physical characteristics of the donor stars are derived with the aid of follow-up optical spectroscopic observations using the FEROS spectrograph on the ESO/MPG 2.2 m telescope.

## 7. NEW SGXRBS IN THE LMC

Observation Target/Observatory	ObsID	Date MJD	Instrument	Mode <sup>a</sup>	Net Exp [ks]	rate counts/s	$L_x$ <sup>b</sup> $10^{35}$ erg s <sup>-1</sup>
XMMU J053108.3-690923							
<i>XMM-Newton</i>	0690744601	2012-10-10	EPIC-pn	ff-thin	40	0.20±0.03	6.4
			EPIC-MOS1	ff-medium	41	0.071±0.002	
			EPIC-MOS2	ff-medium	41	0.073±0.002	
<i>Swift</i>	00032616001	56237.55421	XRT	pc	4	<0.0025	<0.8
	00045434001	56241.56838	XRT	pc	0.2	<0.027	<8.8
	00045434003	56247.04019	XRT	pc	1.3	<0.015	<4.8
	00045436002	56247.17643	XRT	pc	1.4	<0.007	<2.3
	00045436004	56257.85074	XRT	pc	0.8	<0.008	<2.6
	00045463001	56268.25574	XRT	pc	2.5	<0.006	<1.95
	00032616002	56967.49831	XRT	pc	0.8	0.015±0.005	4.9
	00032616003	56969.69179	XRT	pc	0.8	<0.017	5.2
XMMU J053320.8-684122							
<i>XMM-Newton</i>	0690743801	2012-04-27	EPIC-pn	ff-thin	26	0.137±0.004	2.8
			EPIC-MOS1	ff-medium	28	–	
			EPIC-MOS2	ff-medium	28	0.040±0.002	
<i>XMM-Newton</i>	0690743701	2012-08-23	EPIC-pn	ff-thin	30	–	0.21
			EPIC-MOS1	ff-medium	31	0.004±0.001	
			EPIC-MOS2	ff-medium	31	0.003±0.001	
<i>Swift</i>	00045431001	55999.30753	XRT	pc	2.0	0.013±0.003	3.5
	00032310001	56006.38836	XRT	pc	2.9	0.021±0.003	5.7
	00045431003	56067.34919	XRT	pc	0.3	<0.04	<11.
	00032310002	56967.76268	XRT	pc	1.0	<0.006	<1.6
	00045567001	56376.06192	XRT	pc	2.6	<0.009	<2.5
	00045566002	56379.25832	XRT	pc	1.2	<0.009	<2.5
	00032310003	57109.74894	XRT	pc	0.2	<0.15	<40.

<sup>a</sup> Instrument setup modes. For *XMM-Newton* a full-frame (ff) mode with thin or medium filter was used. For *Swift*/XRT the photon counting (pc) operation mode was used.

<sup>b</sup> To convert *Swift*/XRT count rates to luminosities we used the spectral parameters obtained from the fit to the *XMM-Newton* data. The conversion factor is  $3.25 \times 10^{37}$  erg s<sup>-1</sup> (c/s)<sup>-1</sup> for XMMU J053108.3-690923 (see case I in Table 7.3) and  $2.73 \times 10^{37}$  erg s<sup>-1</sup> (c/s)<sup>-1</sup> for XMMU J053320.8-684122.

**Table 7.1:** X-ray observations log

## 7.2 Observations

### 7.2.1 X-ray data

The two targets were serendipitously discovered in X-rays by *Swift* and *XMM-Newton*. XMMU J053320.8-684122 was firstly identified as a **HMXB** candidate following a *Swift*/XRT detection (*Swift* J053321.3-684121: [Sturm et al. 2012](#)) during a *Swift*/UVOT survey observation of the **LMC** (PI: S. Immler) performed on 2012 March 13. It was later serendipitously detected during two *XMM-Newton* pointings, performed on April 27 and August 23 of 2012, as part of the *XMM-Newton* large survey of the LMC. XMMU J053108.3-690923 was identified as a **HMXB** candidate in the data of an *XMM-Newton* observation performed on October 10 2012 as part of the **LMC** survey. Additional *Swift*/XRT observations were obtained at the position of each source to monitor their long-term X-ray variability. A detailed log of the *XMM-Newton* and *Swift* observations that were analysed for the current work is presented in Table 7.1.

*XMM-Newton*/EPIC ([Strüder et al. 2001](#); [Turner et al. 2001](#)) data were processed using the latest *XMM-Newton* data analysis software SAS, version 16.1.0<sup>1</sup>. Observa-

<sup>1</sup>Science Analysis Software (SAS): <http://xmm.esac.esa.int/sas/>

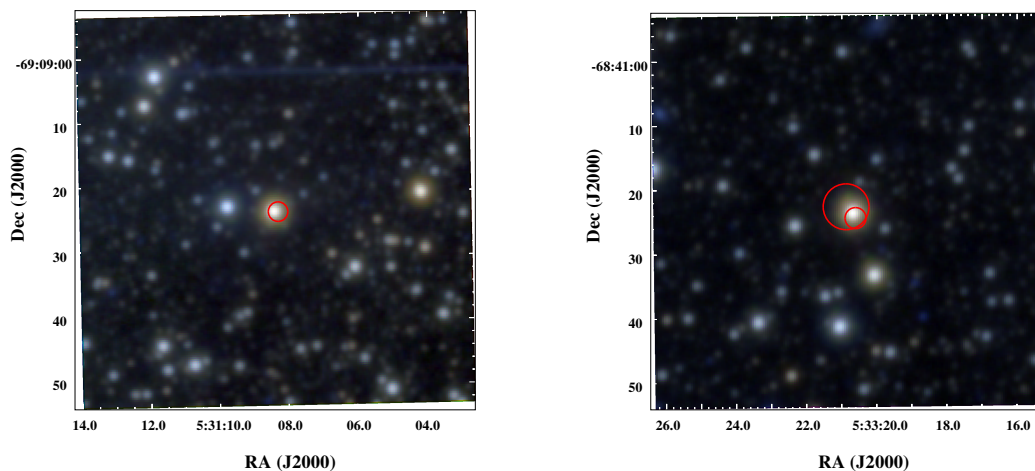


**Figure 7.1:** Vista images of the regions around XMMU J053108.3-690923 (left) and XMMU J053320.8-684122 (right). Each image covers a  $1' \times 1'$  sky area, with RGB colours based on the J, H, and K Vista filters respectively. Red circles are centred on the inferred *XMM-Newton* positions with a radius corresponding to  $3\sigma$  confidence (including statistical and systematic errors). The two circles in the case of XMMU J053320.8-684122 correspond to two different *XMM-Newton* observations. During the April 2012 observation the source was brighter and the position more accurate (smaller circle).

tions were inspected for high background flaring activity by extracting the high-energy light curves ( $7.0 \text{ keV} < E < 15 \text{ keV}$  for both MOS and pn detectors) with a bin size of 100 s. Event extraction was performed with SAS task `evselect` using the standard filtering flags (`#XMMEA_EP && PATTERN<=4` for EPIC-pn and `#XMMEA_EM && PATTERN<=12` for EPIC-MOS). Circular regions with a radius of  $20''$  and  $50''$  were used for the source and background extraction to maximize the number of extracted photons. For the spectral analysis the SAS tasks `rmfgen` and `arfgen` were used to create the redistribution matrix and ancillary file. The grouped spectra were binned to achieve a minimum signal-to-noise ratio of five for each bin. For the timing analysis the event arrival times were corrected to the solar-system barycentre by using the SAS task `barycen`.

The *Swift*/XRT data were analysed following standard procedures described in the *Swift* data analysis guide<sup>1</sup> (Evans et al. 2007). We used the `xrtpipeline` to generate the *Swift*/XRT products. Because of the low luminosity of the systems in most observations, we only performed a simple source detection and position determination using a sliding-cell detection algorithm implemented by `XIMAGE`<sup>2</sup>. For non-detections we estimated the  $3\sigma$  upper limits using a Bayesian method introduced by Kraft et al. (1991).

### 7.2.2 Optical data

Based on the accurate X-ray positions as determined by *XMM-Newton* we identified the most probable counterpart in the LMC field. A high-mass star is located within the X-ray error circle of each system (see Table 7.2). We consider these as the most likely counterparts, since it is very unlikely to find LMXBs in the LMC (Gilfanov 2004) due to its recent star formation history and its total mass (Harris and Zaritsky 2009;

<sup>1</sup><http://www.swift.ac.uk/analysis/xrt/>

<sup>2</sup><https://heasarc.gsfc.nasa.gov/xanadu/ximage/ximage.html>

## 7. NEW SGXRBS IN THE LMC

X-ray	XMMU J053108.3-690923	XMMU J053320.8-684122
[M2002] <sup>a</sup>	LMC 150004	LMC 157075
V	13.68±0.01	12.72±0.01
B	13.76±0.01	12.63±0.01
U	12.89±0.01	11.67±0.01
R	13.6±0.01	12.71±0.01
[AAVSO] <sup>b</sup>	-	-
g'	13.654±0.047	12.548±0.010
r'	13.769±0.077	12.792±0.040
i'	13.872±0.066	12.968±0.083

<sup>a</sup> Catalogue number and photometric magnitudes from [Massey \(2002\)](#), typical photometric uncertainties are below 0.01 mag.

<sup>b</sup> AB magnitudes using Sloan filters ([Henden et al. 2015](#))

**Table 7.2:** Optical counterparts

[Antoniou and Zezas 2016](#)). The X-ray detected systems are not background AGN, given their large X-ray variability (AGN have typical normalized excess variance  $<1$ , [Lanzuisi et al. 2014](#)) and their hard X-ray spectra (see §7.3). In Fig. 7.1 we present a finding chart for each system. The images were constructed using J, H and K publicly available VISTA images<sup>1</sup>.

Optical spectra were obtained using ESO’s Fibre-fed Extended Range Optical Spectrograph (FEROS, [Kaufer et al. 1999](#)) mounted on the ESO/MPG 2.2 m telescope at La Silla (Chile). Observations were performed using the MPE high-energy group internal observing time. Observations were scheduled around full moon periods when observing conditions were not optimal for photometric observations with GROND ([Greiner et al. 2008](#)), that is the telescope’s main instrument. The targets were observed during non-photometric nights during 2014 November 7, with  $\sim 1$  h of total exposure for each target. Reduction of the FEROS spectra was performed with the ESO Data Reduction System (DRS), provided to the FEROS users <sup>2</sup>.

## 7.3 Results

In the following subsections, I present results on the X-ray position, spectral and temporal properties of the two HMXB systems as well as report on the optical properties of their donor stars.

### 7.3.1 X-ray positions

X-ray positions were determined by performing a maximum-likelihood source detection analysis on the *XMM-Newton*/EPIC images. Fifteen images were created from the three EPIC cameras in five energy bands: 1  $\rightarrow$  (0.2 – 0.5) keV, 2  $\rightarrow$  (0.5 – 1.0) keV, 3  $\rightarrow$  (1.0 – 2.0) keV, 4  $\rightarrow$  (2.0 – 4.5) keV, 5  $\rightarrow$  (4.5 – 12.0) keV ([Watson et al. 2009](#);

<sup>1</sup><http://horus.roe.ac.uk/vsa/index.html>

<sup>2</sup>[www.eso.org](http://www.eso.org)

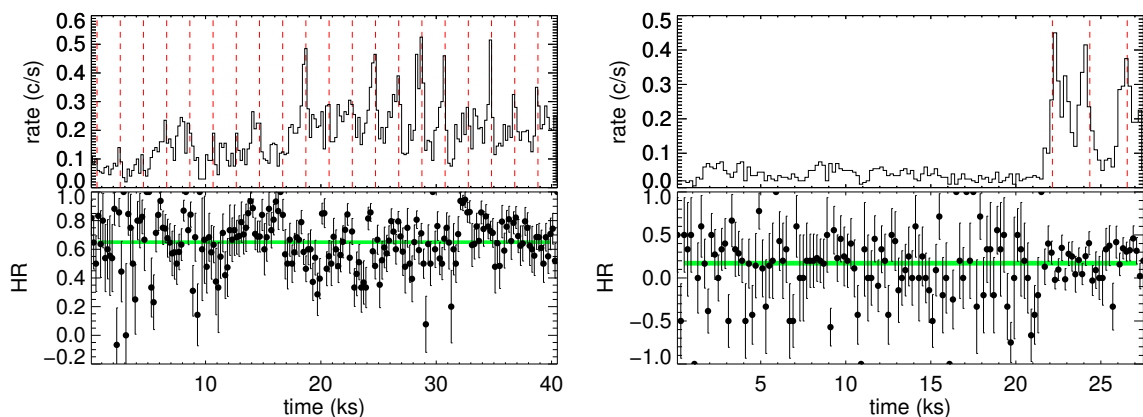


**Figure 7.2:** *XMM-Newton*/EPIC X-ray (0.3-10.0 keV) light curves with 200s binning, and the corresponding hardness ratios using the 0.3-2.0 keV and the 2.0-10.0 keV bands. XMMU J053108.3-690923 (left) shows clear evidence of periodic bursts every  $\sim 2013$ s (red vertical lines). During the April 2012 observation (obsid: 0690743801) XMMU J053320.8-684122 (right) remained at a relatively constant luminosity ( $\sim 0.035$  counts  $s^{-1}$ ) for the first  $\sim 22$  ks of the exposure, while exhibiting three consecutive bursts separated by  $\sim 2200$ s at the end of the exposure.

Sturm et al. 2013a). Source detection was performed simultaneously on all the images using the SAS task `edetect_chain`. Astrometric boresight corrections were performed using a catalogue of background AGN with known redshifts or selected using ALLWISE mid-infrared colour selection criteria (Mateos et al. 2012; Secrest et al. 2015) with the task `eposcorr` accounting for a linear shift. The inferred shifts in right ascension and declination were applied to the attitude file of the pointings and the data reprocessed. For XMMU J053108.3-690923 we derived boresight corrected positional coordinates of R.A. =  $05^{\text{h}}31^{\text{m}}08.^{\text{s}}33$  and Dec. =  $-69^{\circ}09'23''.5$  (J2000), with a  $1\sigma$  statistical uncertainty of  $0.1''$ . From the two observations of XMMU J053320.8-684122 we determined an error-weighted mean of the position to R.A. =  $05^{\text{h}}33^{\text{m}}20.^{\text{s}}87$  and Dec. =  $-68^{\circ}41'22''.6$  (J2000) with a  $1\sigma$  statistical uncertainty of  $0.55''$ . The positional error is usually dominated by systematic astrometric uncertainties. Following Sturm et al. (2013a) we added a systematic error of  $0.5''$  in quadrature. We note, however, that subsequent analysis of *XMM-Newton* observations of the SMC with the newest SAS version has reduced the systematic uncertainty to  $0.33''$  (Maitra et al., in prep). Our analysis provides an improved X-ray position for both candidates. For XMMU J053320.8-684122, the improved position is consistent with the one reported by Sturm et al. (2012) confirming the initially reported counterpart (i.e. blue supergiant Sk-68 122; Sanduleak 1970) as the true optical companion.

### 7.3.2 X-ray temporal properties

Both systems exhibit strong variability during the *XMM-Newton* observations (see Fig. 7.2). XMMU J053108.3-690923 shows periodic bursts every  $\sim 2000$ s. In order to compute the X-ray variability from the *XMM-Newton*/EPIC light-curve we compared the highest count rate with the 5% percentile of the count rate distribution. We infer an X-ray variability factor of about 10. XMMU J053320.8-684122 remained at a lower luminosity level ( $\sim 0.035$  counts  $s^{-1}$ ) for the first  $\sim 22$  ks of the exposure (obsid:

## 7. NEW SGXRBS IN THE LMC

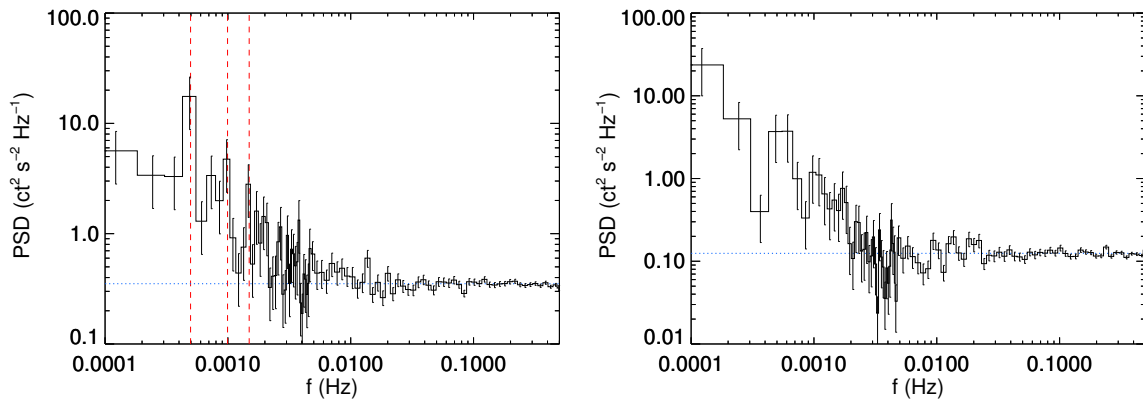


**Figure 7.3:** Power density spectra of XMMU J053108.3-690923 (left) and XMMU J053320.8-684122 (observation April 2012, right). For XMMU J053108.3-690923 a periodic behaviour is evident at  $\sim 2013$  s seen together with two harmonics (red vertical lines).

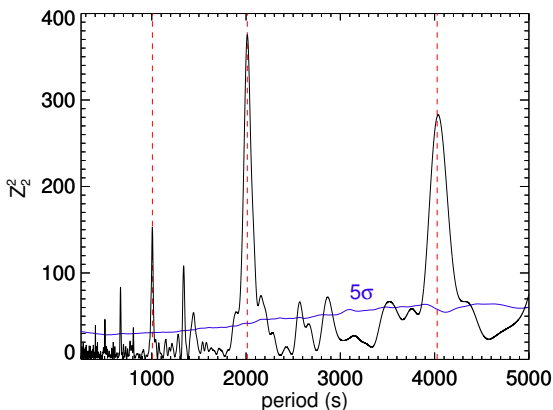


**Figure 7.4:** Results of period search for XMMU J053108.3-690923. Epoch folding (EF) method (Rayleigh  $Z_2^2$  test) was applied to the combined *XMM-Newton*/EPIC events (obsid:0690744601). The significance of the derived period was estimated by applying the EF method on simulated light curves (Timmer and Koenig 1995; Emmanoulopoulos et al. 2013).

0690743801). During the last  $\sim 8$  ks the light curve shows three consecutive bursts separated by  $\sim 2200$  s reaching a maximum count rate of  $\sim 0.45$  counts  $s^{-1}$ . By comparing the highest count rate recorded by *XMM-Newton*/EPIC with the lower 5% percentile of the total X-ray light curve, we find an X-ray variability factor of at least 30.

To further investigate the X-ray variability we used the fast Fourier transform (van der Klis 1988) and constructed the power density spectra for the two systems (see Fig. 7.3). The power spectra are normalized such that their integral over a range of frequencies gives the square of the root mean square (RMS). The power density spectra were grouped using a geometrical rebinning (Papadakis and Lawrence 1993). The spectra of both systems are dominated by white noise at high frequencies ( $\gtrsim 10 - 30$  mHz), while they can be well described by a power-law at lower frequencies. The power spectrum of XMMU J053108.3-690923 shows additional features at 0.5 mHz, 1 mHz, and 1.5 mHz that are related to the pulsar’s spin-period and its harmonics. In order to estimate the significance of these features and better determine the period and its uncertainty we used an epoch folding technique (EF: Davies 1990; Larsson 1996). We used the combined EPIC-pn and EPIC-MOS barycentric corrected arrival times to search for a periodic signal. We applied an EF method, while implementing the Rayleigh  $Z_2^2$  normalization (Bucccheri et al. 1983).

For XMMU J053108.3-690923 a clear period of 2013.5 s was found, while the periodogram shows peaks at the multiples of this period (see Fig. 7.4). To estimate the uncertainty of the derived period we used two approaches. First, we analytically estimated the uncertainty to be 4-10 s using equation (14) of Horne and Baliunas (1986). Then, we performed a numerical estimation by bootstrapping the event arrival times and by performing the EF method to the bootstrapped samples. An uncertainty of  $\sim 3$  s was derived from the distribution of the derived periods. The pulse-profile of the system is single peaked (Fig. 7.5). We also investigated the hardness ratio (HR) evolution along the spin phase of the system by using two different energy bands (0.3-2.0, 2.0-10.0 keV). The HR is defined as  $(R_{\text{hard}} - R_{\text{soft}})/(R_{\text{hard}} + R_{\text{soft}})$ , with  $R_{\text{hard/soft}}$  denotes the background-subtracted count rates in the hard and soft energy band. The spin phase folded light-curves of the system, for the complete energy range of *XMM-Newton* as well as the soft and hard energy bands, are plotted together with the spin phase resolved HR in Fig. 7.5.

For XMMU J053320.8-684122 any periodicity search is hampered by the three late flares that dominate the statistics. Thus, we searched for periodic signal only in the first 22 ks of the exposure. No significant period was derived from the periodicity search.

### 7.3.3 X-ray spectral properties

X-ray spectral analysis was performed using the XSPEC fitting package, version 12.9.1 (Arnaud 1996). We fitted the time-averaged X-ray spectra of both systems with an absorbed power-law model. X-ray absorption was modeled using the `tbabs`<sup>1</sup> code (Wilms et al. 2000) with atomic cross sections adopted from Verner et al. (1996). For the modelling we used two absorption components, one to describe the Galactic foreground absorption and another to account for the column density of both the interstellar medium of the LMC and the intrinsic absorption of the sources. For the Galactic photo-electric absorption we used a fixed column density (Dickey and Lockman 1990a) with abundances taken from Wilms et al. (2000).

For XMMU J053320.8-684122 the X-ray spectrum was adequately described by an absorbed power-law model ( $\chi^2_{\text{red}} \sim 1.03$ ). For XMMU J053108.3-690923 the absorbed power-law model yielded an acceptable goodness of fit with reduced  $\chi^2 \sim 1.1$ , but failed to describe the data in terms of residual distribution (Andrae et al. 2010). The introduction of an additional spectral component reduces the structures in the residuals. Such a component is commonly seen in the spectra of HMXB systems below 10 keV and is usually referred to as “soft excess” (Hickox et al. 2004). For HMXB systems observed

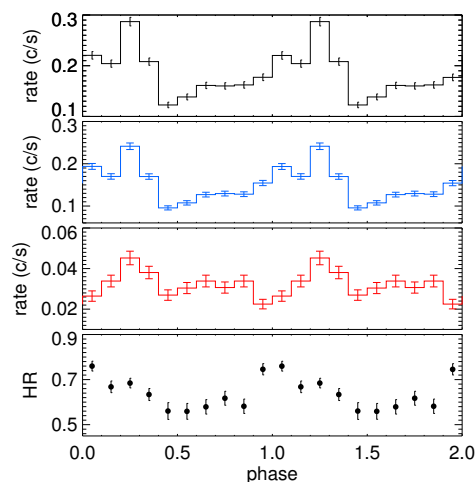


**Figure 7.5:** From top to bottom we present the phase folded pulse profile of XMMU J053108.3-690923 in the 0.3-10 keV, 2.0-10.0 keV and 0.3-2.0 keV bands and the hardness ratio between the two sub-bands.

<sup>1</sup>Commonly referred to as `tbnew`, this model is now included in the latest release of XSPEC. The code is available through: <http://pulsar.sternwarte.uni-erlangen.de/wilms/research/tbabs/>

## 7. NEW SGXRBS IN THE LMC

XMMU J053108.3-690923			
CASE I: constant*TBabs*TBvarabs*(powerlaw+bodyrad)			
Component	Parameter	Value	units
TBabs <sup>a</sup>	nH	0.0618 (fixed)	10 <sup>22</sup> cm <sup>-2</sup>
TBvarabs	nH	2.3±0.7	10 <sup>22</sup> cm <sup>-2</sup>
powerlaw	Γ	0.8 <sup>+0.8</sup> <sub>-0.5</sub>	-
	norm	1.3 <sup>+0.3</sup> <sub>-0.5</sub>	10 <sup>-12</sup> erg cm <sup>-2</sup> s <sup>-1</sup>
bodyrad	kT	1.75 <sup>+0.5</sup> <sub>-0.4</sub>	keV
	norm	0.01 <sup>+0.01</sup> <sub>-0.04</sub>	-
	R	0.5 <sup>+0.2</sup> <sub>-0.1</sub>	km
Observed Flux <sup>b</sup>		1.87 <sup>+0.06</sup> <sub>-0.4</sub>	10 <sup>-12</sup> erg cm <sup>-2</sup> s <sup>-1</sup>
Luminosity <sup>c</sup>		6.4 <sup>+0.3</sup> <sub>-0.2</sub>	10 <sup>35</sup> erg s <sup>-1</sup>
$\chi^2_{\text{red}}/\text{DOF}$		0.99/252	
CASE II: constant*TBabs*TBvarabs1*(partcov*TBvarabs2)*powerlaw			
Component	Parameter	Value	units
TBabs <sup>a</sup>	nH	0.0618 (fixed)	10 <sup>22</sup> cm <sup>-2</sup>
TBvarabs1	nH	3.2±0.5	10 <sup>22</sup> cm <sup>-2</sup>
partial covering: partcov*TBvarabs2			
partcov	covering fraction	0.52 <sup>+0.09</sup> <sub>-0.11</sub>	-
TBvarabs2	nH	18 <sup>+8.0</sup> <sub>-7.0</sub>	10 <sup>22</sup> cm <sup>-2</sup>
powerlaw	Γ	1.30±0.20	-
	norm	3.1 <sup>+0.6</sup> <sub>-0.4</sub>	10 <sup>-12</sup> erg cm <sup>-2</sup> s <sup>-1</sup>
Observed Flux <sup>b</sup>		1.87 <sup>+0.06</sup> <sub>-0.4</sub>	10 <sup>-12</sup> erg cm <sup>-2</sup> s <sup>-1</sup>
Luminosity <sup>c</sup>		9.4 <sup>+0.3</sup> <sub>-0.2</sub>	10 <sup>35</sup> erg s <sup>-1</sup>
$\chi^2_{\text{red}}/\text{DOF}$		1.00/252	
XMMU J053320.8-684122			
constant*TBabs*TBvarabs*powerlaw			
Component	Parameter	Value	units
TBabs <sup>a</sup>	nH	0.0609 (fixed)	10 <sup>22</sup> cm <sup>-2</sup>
TBvarabs	nH	0.61 <sup>+0.21</sup> <sub>-0.18</sub>	10 <sup>22</sup> cm <sup>-2</sup>
powerlaw	Γ	0.91±0.12	-
	norm	0.94±0.06	10 <sup>-12</sup> erg cm <sup>-2</sup> s <sup>-1</sup>
Observed Flux <sup>b</sup>		0.85 <sup>+0.05</sup> <sub>-0.06</sub>	10 <sup>-12</sup> erg cm <sup>-2</sup> s <sup>-1</sup>
Luminosity <sup>c</sup>		2.8±0.1	10 <sup>35</sup> erg s <sup>-1</sup>
$\chi^2_{\text{red}}/\text{DOF}$		1.03/65	

<sup>a</sup> Contribution of Galactic foreground absorption, column density fixed to the weighted average value of (Dickey and Lockman 1990a)

<sup>b</sup> Absorbed flux of the fitted model in the 0.3-10.0 keV energy band.

<sup>c</sup> Unabsorbed Luminosity of the fitted model in the 0.3-10.0 keV energy band, for a distance of 50 kpc (Pietrzyński et al. 2013).

**Table 7.3:** Results of the X-ray spectral modelling

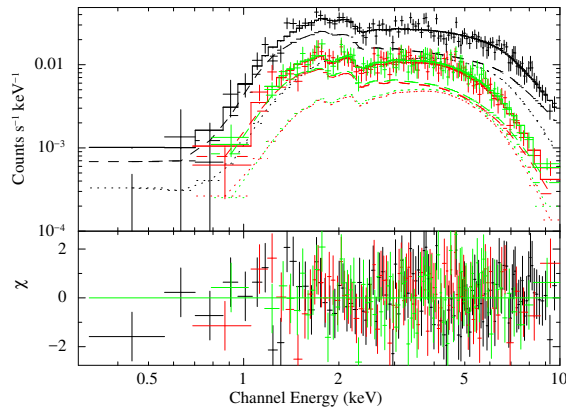


**Figure 7.6:** EPIC spectra of XMMU J053108.3-690923 (black: pn, red: MOS1, green: MOS2) together with the best-fit model (solid lines) composed of absorbed power-law and black-body components (CASE I in Table 7.3). The power-law (dash-dotted lines) and black-body (dotted lines) contributions are also indicated. The bottom panel shows the fit residuals.

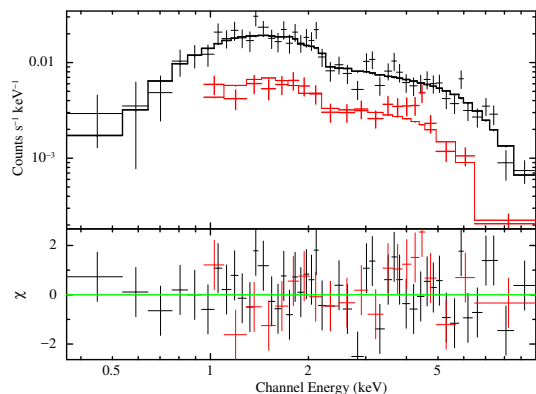


**Figure 7.7:** EPIC spectra of XMMU J053320.8-684122 from April 2012 (black: pn, red: MOS2) together with the best-fit power-law model (solid lines). The bottom panel shows the fit residuals.

at low luminosities this soft excess can have two different origins. It can be due to the NS hot spot (CASE I) and can therefore be modelled by a black-body component with typical size of 1 km radius (La Palombara and Mereghetti 2006; Bartlett et al. 2013a; Vasilopoulos et al. 2013a; Sidoli et al. 2017b). Alternatively, it can be associated with X-ray absorption from the clumpy wind of a supergiant star (CASE II). In this case, it can be modelled by a partial-covering absorption component (Tomsick et al. 2009). Often, it is difficult to distinguish between the two cases (e.g. Fornasini et al. 2017).

In the case of XMMU J053108.3-690923, both models for the soft excess provide equally good fits (CASE I: 0.99 vs CASE II: 1.01) and identical residual structure. It is thus impossible to statistically distinguish between the two scenarios. In the case of XMMU J053320.8-684122, any additional component would result in over-fitting the data and would not constrain any of the physical parameters of the system.

The X-ray spectra along with the data-to-model residual plots for both systems are presented in Fig. 7.6 and 7.7. The best fit model parameters are given in Table 7.3. Interestingly, the intrinsic absorption of both systems is larger than that of the typical BeXRB pulsars located in the LMC (e.g. Vasilopoulos et al. 2014a, 2016b; Haberl et al. 2017a). Moreover, by comparing the two systems, XMMU J053108.3-690923 is both brighter and exhibits higher intrinsic absorption.

From our temporal analysis (see §7.3.2 and Fig. 7.2), we find that XMMU J053108.3-690923 and XMMU J053320.8-684122 reached a maximum luminosity of  $1.1 \times 10^{36}$  erg  $s^{-1}$  and  $8.5 \times 10^{35}$  erg  $s^{-1}$  respectively during the two *XMM-Newton* observations.

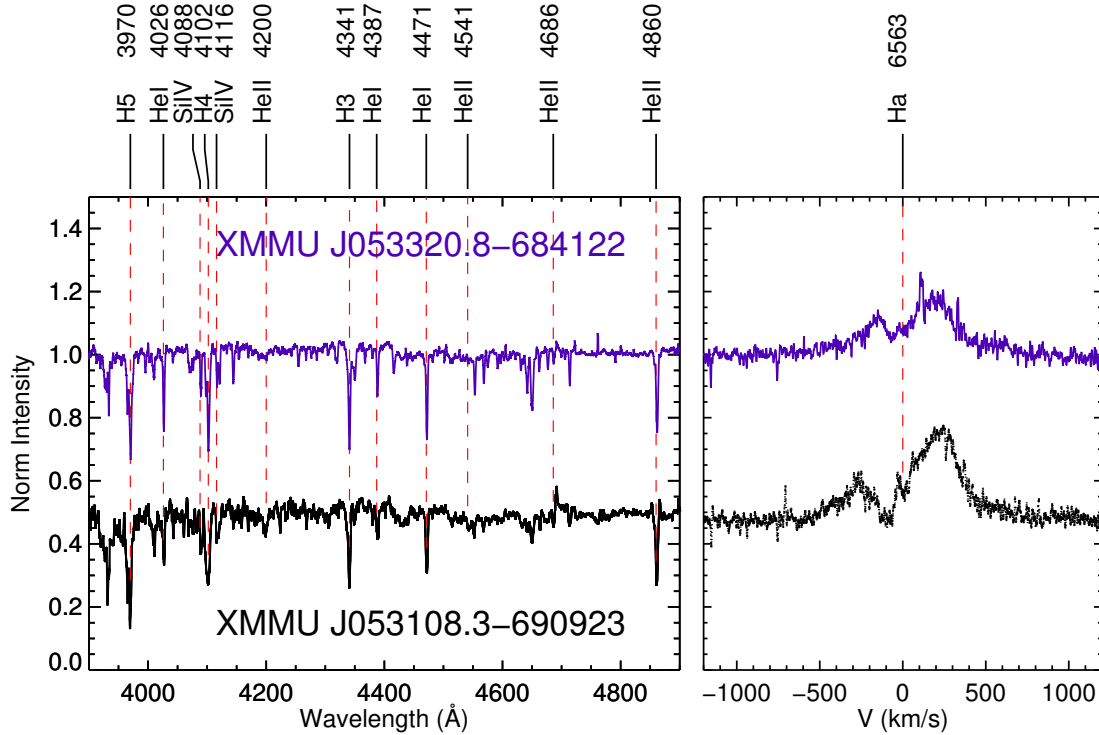


**Figure 7.8:** FEROS spectra of XMMU J053108.3-690923 and XMMU J053320.8-684122. Intensities have been normalised according to the underlying continuum flux and arbitrarily shifted for plotting purposes. Lines that have been used for the spectral classification are marked with vertical dashed red lines.

### 7.3.4 Optical properties of donor stars

The reduced optical spectra of the two massive stars (see Table 7.2) that are interpreted as the companion stars of the corresponding HMXB systems XMMU J053108.3-690923 and XMMU J053320.8-684122, have been classified using the criteria described in Evans et al. (2004, 2015), which take into account the lower metallicity of the LMC’s massive stars (compared to massive Galactic stars).

#### Spectral classification

The optical companion of XMMU J053108.3-690923 is consistent with a B0e spectral class, as absorption lines He II 4686Å and 4541Å are weak but present, while the He II 4200Å line is very weak or absent. The optical companion of XMMU J053320.8-684122 is consistent with B0.5e spectral class, as absorption lines He II 4200Å and 4541Å are absent, while the He II 4686Å line is clearly present (but weak). Figure 7.8 shows part of the optical spectra obtained for the two stars with the main lines marked.

#### H-alpha line profiles

In Fig. 7.8 we show the H-alpha line region for the two stars. The narrow nebular emission lines and cosmic rays have been subtracted from the spectra. Both profiles are double peaked. Simultaneous fits with Gaussian profiles were performed and the

results are summarised in Table 7.4. Usually, the profiles of supergiants of this type are expected to show P-Cygni profiles in the Balmer lines. However the absence of P-Cygni signature does not prove that a star is not a supergiant, as the profile is variable and goes through phases with no P-Cygni signature (e.g. Grundstrom et al. 2007; Negueruela et al. 2006).

### Luminosity Classification

The luminosity class of the systems was determined using a combination of spectroscopic and hybrid spectro-photometric criteria.

Spectroscopically, the spectra of both XMMU J053108.3-690923 and XMMU J053320.8-684122 show clear Si III lines (4553Å, 4568Å, 4575Å), N III 4097Å, and O II lines (4640Å, 4643Å, 4650Å, 4699Å, 4705Å), that indicate a supergiant luminosity class (Hendry et al. 2008). The equivalent width of the Balmer H $\gamma$  line is  $\simeq 1.06\text{\AA}$  for the case of XMMU J053108.3-690923 and  $\simeq 1.17\text{\AA}$  for XMMU J053320.8-684122. Both values are consistent with a supergiant luminosity class given the spectral type of the objects (see e.g. Cananzi et al. 1993).

Classification based on photometric or spectrophotometric criteria requires an estimate of the absolute magnitude of the systems, which can be derived from the apparent magnitudes of the objects given in Table 7.2, corrected for the distance modulus of the LMC of  $\mu_0=18.49$  mag (Pietrzyński et al. 2013) and for interstellar extinction. As an indicative values for the interstellar absorption in the direction of XMMU J053108.3-690923 and XMMU J053320.8-684122, we used the values provided by Haschke et al. (2011). By averaging the provided values over a 10' area around the two systems we derived E(B-V) values of 0.076 and 0.086 for XMMU J053108.3-690923 and XMMU J053320.8-684122, respectively. Given the spectral class of the two stars (B0-B0.5) one would expect a (B-V) $_0$  colour of  $\simeq -0.2$ . Comparing with the actual B-V colours from Table 7.2, reddenings of  $\simeq 0.28$  mag for XMMU J053108.3-690923 and  $\simeq 0.11$  mag for XMMU J053320.8-684122 are inferred. For the case of XMMU J053320.8-684122 the two reddening estimates are consistent, while in the case of XMMU J053108.3-690923, the actual reddening of the star is significantly higher than expected according to Haschke et al. (2011), probably indicating the presence of absorption related to the system itself, or, alternatively the colour of the star may be affected by the contribution of a circumstellar disk. Adopting the first set of E(B-V) values, and applying the corresponding extinction correction, we derive,  $M_V = -5.07$  and  $M_V = -6.05$  for XMMU J053108.3-690923 and XMMU J053320.8-684122 respectively. For the second set E(B-V) estimates the corresponding absolute magnitudes of  $M_V = -5.70$  and  $M_V = -6.11$  for XMMU J053108.3-690923 and XMMU J053320.8-684122 respectively, assuming that the observed B-V colour is only due to reddening and not to the contribution from a possible disk.

Given these values for the absolute magnitudes of the two donor stars and the values for the equivalent widths of the H $\gamma$  line mentioned earlier, we can apply the hybrid luminosity class criteria appropriate for Magellanic Cloud metallicity (see Table 3 of Evans et al. 2004). Note that the ranges given in this paper refer to a distance modulus of 19.2 (for the SMC). After taking this into account, XMMU J053108.3-690923 can be assigned a hybrid luminosity class of (II), while XMMU J053320.8-684122 is clearly of luminosity class (Ib), with the parentheses indicating that these are not truly morphological luminosity classes, but are based on both spectroscopic

## 7. NEW SGXRBS IN THE LMC

XMMU J053320.8-684122			
	$\lambda_{\text{central},1}$ (Å)	FWHM (Å)	EW
Red	$6558.8 \pm 0.1$	$4.1 \pm 0.4$	$-0.44 \pm 0.03$
Blue	$6566.9 \pm 0.1$	$7.8 \pm 0.2$	$-1.35 \pm 0.04$
XMMU J053108.3-690923			
	$\lambda_{\text{central},1}$ (Å)	FWHM (Å)	EW
Red	$6556.54 \pm 0.06$	$4.8 \pm 0.2$	$-0.51 \pm 0.02$
Blue	$6567.50 \pm 0.03$	$7.1 \pm 0.1$	$-2.06 \pm 0.02$

**Table 7.4:** H-alpha profile characteristics

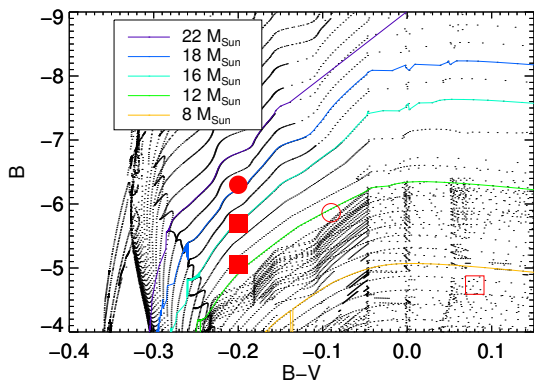


**Figure 7.9:** Colour-magnitude diagram of the MESA evolutionary models for the LMC metallicity (Choi et al. 2016; Dotter 2016). Stellar tracks for different mass-ranges are overplotted with coloured solid lines. The position of XMMU J053108.3-690923 (squares) and XMMU J053320.8-684122 (circles) in the diagram are marked using both their corrected (filled symbols) and uncorrected (open symbols) colour and magnitude values. For XMMU J053108.3-690923 the two corrected values correspond to the case of local extinction (brighter) or disc contribution (see text for details).

and photometric criteria.

Using only photometric criteria, based on the expected range of absolute magnitudes for B0-B0.5 spectral types of different luminosity classes (e.g. Wegner 2006; Urbaneja et al. 2017), both XMMU J053108.3-690923 and XMMU J053320.8-684122 are consistent with luminosity class I supergiants.

To summarize, all classification criteria indicate that XMMU J053108.3-690923 is a B0 II-Ib bright giant or supergiant and XMMU J053320.8-684122 is a B0.5 Ib supergiant. For XMMU J053108.3-690923 there is indication of either heavy local reddening, or of contribution of a circum-stellar disc component (even present in supergiant systems; Mennickent et al. 2017).

### Masses of donor stars

For both systems we can use their combined spectro-photometric properties to estimate the masses of the donor stars. For this purpose we can use the Modules for Experiments in Stellar Astrophysics (MESA; Paxton et al. 2011) Isochrones and Stellar Tracks (MIST Choi et al. 2016; Dotter 2016). We compared the photometric properties of the systems with the MIST curves produced for the LMC metallicity taking into account the effect of rotation on stellar models. This is presented in Fig. 7.9. In both systems, the  $(B - V)_0$  colour of the star (i.e its temperature) is better determined by its spectral class than by its photometric properties. The photometric colour is affected by the uncertainties in interstellar and circumstellar reddening and the possible contribution from a circum-stellar disk. Therefore, we used  $B - V \simeq -0.2$  as the de-reddened colour of the donor. Regarding the absolute magnitude, we use the values calculated

earlier, with the clarification that in the case of XMMU J053108.3-690923 the absolute magnitude can have an uncertainty of the order of 0.5 mag in B. This is a result of the different interpretations that are possible for the observed large B-V value. If it is caused by high local or circumstellar absorption, then the corresponding extinction needs to be taken into account in the derivation of  $M_B$  (leading to the brighter value of  $M_B$ ). This interpretation is supported by the high absorption of the X-ray spectrum. If, on the other hand, the high B-V value is due to a disc component, which is expected to contribute mostly to the red and infrared,  $M_B$  is not expected to be affected appreciably. In this case, we only correct for the known interstellar extinction in the region from [Haschke et al. \(2011\)](#). Interestingly, the ratio between E(B-V) and the equivalent width of the H $\alpha$  line is consistent with the expected relation for BeXRB systems ([Riquelme et al. 2012](#)), thus supporting this interpretation.

Taking into account all these uncertainties, and according to Fig. 7.9, we estimate that the mass of XMMU J053108.3-690923 is in the range 12-18  $M_{\odot}$  and of XMMU J053320.8-684122 around 18-22  $M_{\odot}$ . We note that the upper limits on these ranges are mainly driven from our assumption on the expected color of the donor star that was assumed  $B - V \simeq -0.2$ , but could be as low as -0.25.

## 7.4 Discussion

We have presented a detailed study of the X-ray spectral and temporal properties of two newly discovered HMXB systems in the direction of the LMC. Below we summarise the results of our study and discuss the properties of the systems in the context of quasi-spherical accretion in the subsonic regime.

### 7.4.1 XMMU J053108.3-690923: a $\sim 2013$ s pulsar with a bright giant (or supergiant Ib) companion

Timing analysis of the *XMM-Newton* data revealed the presence of coherent pulsations with a period of  $\sim 2013$  s. The phase resolved hardness ratio of the system (see Fig. 7.5) reveals a week correlation between its luminosity and hardness ratio (harder when brighter), which is in agreement with the general trend of accreting XRB pulsars in the MCs (e.g. [Vasilopoulos et al. 2014a](#); [Sturm et al. 2014b](#); [Koliopanos and Vasilopoulos 2017](#)). The optical companion of the system was identified as a B0e II-Ib with a mass in the range of 12-18  $M_{\odot}$  (see § 7.3.4).

From all the available X-ray observations we can set a lower limit on the long-term (i.e. not due to pulsations) X-ray variability of the system (factor of 8; see Table 7.1). This is relatively low compared to pulsating HMXBs located in the MCs ([Haberl and Sturm 2016](#), for SMC systems). The small long-term variability of the system can be a result of the nature of the donor star (i.e. supergiant). BeXRBs can exhibit variability in their X-ray light curves on timescales of months to years that can be connected to the activity of the donor star and changes of its decretion disc (e.g. [Reig et al. 2010](#)). Very long optical variations related to modulations of the Be disc size is present in most of the SMC pulsars ([Rajoelimanana et al. 2011](#)). Similarly, analysis of optical monitoring data of SMC BeXRB pulsars obtained by OGLE<sup>1</sup>, have revealed optical periodicities that can be interpreted as orbital period or non-radial pulsations of the Be star ([Schmidtke et al. 2013](#); [McBride et al. 2017](#)). In many cases, orbital

<sup>1</sup>OGLE: Optical Gravitational Lensing Experiment ([Udalski et al. 2015](#))

## 7. NEW SGXRBS IN THE LMC

---

periods of individual BeXRB systems in both the LMC and SMC have been inferred from their OGLE optical light-curves<sup>1</sup> (e.g. Vasilopoulos et al. 2016b, 2017c; Sturm et al. 2014b; Boon et al. 2017). It is therefore atypical for BeXRB systems not to exhibit some sort of optical variability due to the presence of a disc around the massive star. We analysed the available OGLE data of XMMU J053108.3-690923 (Udalski, A.: private communication) using the Lomb-Scargle periodogram (Scargle 1982; Horne and Baliunas 1986). The OGLE-IV light curve of XMMU J053108.3-690923 reveal no long-term modulation or periodic signal that could be interpreted as orbital period (see also van Jaarsveld et al. 2017a). Due to the above, we interpret the measured pulsations as the NS spin period, and classify the system as a SgXRB pulsar, the 2<sup>nd</sup> known in the LMC. In this scenario the long-term X-ray variability of the system is easily explained in terms of orbital modulation due to an eccentric orbit (e.g. Haberl 1991).

The X-ray spectrum of the system can be satisfactorily described by (i) an absorbed power law plus black-body component or by (ii) a partial-covered absorbed power law (see §7.3.3). In the first scenario, the black-body component has a temperature of  $\sim 1.75$  keV and a size of  $\sim 0.5$  km, and can be explained by the presence of a hot spot at the NS magnetic pole. In the second interpretation, the high X-ray absorption can be associated with the presence of a clumpy wind originating from the supergiant star. Another physical alternative for explaining the presence of a partial-covering absorber is that the NS is covered by a dense shell of material or an accretion curtain. In this scenario, any changes in the HR with pulse profile may be explained by variations in the covering fraction with pulse phase, if the covering material is locked with the NS rotation period. To investigate this possibility, we used the best-fit model to create simulated spectra for different values of the covering fraction. The minimum observed HR ( $\sim 0.57$  at phase  $\sim 0.5$ ) can be reproduced by a covering factor of 0.33, whereas the maximum observed HR ( $\sim 0.74$  at phase  $\sim 1$ ) requires a covering factor of 0.8. Nevertheless, this interpretation makes it difficult to explain such high absorptions from ionized gas as it would require very high densities and the resulting optical depth would probe much higher accretion rates than the one inferred from the observed X-ray luminosity.

### 7.4.2 XMMU J053320.8-684122: A probable SFXT in the LMC

Timing analysis of the X-ray events collected by *XMM-Newton* (obsid: 0690743801) did not reveal the presence of any statistically significant periodic signal. During the first 22 ks of the *XMM-Newton* observation, the X-ray luminosity of the system shows small variations around a mean value of  $L_{X,\text{low}} \sim 1.4 \times 10^{35}$  erg s<sup>-1</sup>. Towards the end of the observation the system's luminosity increased rapidly (within  $\sim 0.5$  ks) by a factor of  $\sim 13$ , while three subsequent flares appear to occur every  $\sim 2200$  s (see Fig. 7.2). We propose that this indicates the onset of fast bright X-ray flares which have been detected in HMXB systems with supergiant companions (Negueruela et al. 2006). This is also consistent with the quasi-periodic flaring activity observed in other galactic SFXT (e.g. IGR J11215-5952 & IGR J16418-4532: Sidoli et al. 2017b, 2012).

Following this scenario the low X-ray luminosity of XMMU J053320.8-684122 prior

---

<sup>1</sup>The OGLE-IV I band photometric data are publicly available online through the OGLE real time monitoring of X-ray variables web page (Udalski 2008): <http://ogle.astrouw.edu.pl/ogle4/xrom/xrom.html>

to the three flares may be the result of quasi-spherical settling accretion in a wind-fed HMXB (Shakura et al. 2012; see also Shakura and Postnov 2017 for a recent review). The optical counterpart of XMMU J053320.8-684122, which has been identified as a B0.5e Ib star with a mass of  $18 - 22M_{\odot}$  (see Fig. 7.9), is also compatible with the classification of the system as an SFXT.

The X-ray spectrum of the system can be described well by an absorbed power-law model, but due to low photon statistics we were not able to test more complex models. Nevertheless, the high value of intrinsic column density that is required to model the system's X-ray spectrum is in favour of a dense environment expected in a wind-fed accreting system. It is typical for the X-ray spectrum of wind-fed systems to exhibit large intrinsic absorption. Obscured HMXBs are naturally explained by a compact object orbiting inside a cocoon of dust and/or cold gas formed by a strong and clumpy stellar wind of the companion (Chaty 2008a,b; Blay et al. 2012). Typical SgXRBs show larger persistent luminosities and higher absorption ( $N_{\text{H}} > 10^{22} \text{ cm}^{-2}$ ) indicating a stronger wind, while SFXTs are known to show lower intrinsic absorption values ( $10^{21} \text{ cm}^{-2} < N_{\text{H}} < 10^{22} \text{ cm}^{-2}$ ). The latter is consistent with the scenario that XMMU J053320.8-684122 is most probably an SFXT system.

### Quasi-spherical accretion onto an NS

By adopting the scenario of quasi-spherical accretion onto a slowly rotating NS, we provide rough estimates for the physical properties of XMMU J053320.8-684122.

In the scenario of quasi-spherical accretion, the stellar wind material that is being gravitationally captured by the orbiting NS can either fall supersonically towards the NS magnetosphere (supersonic regime) or it can form a quasi-static shell of hot plasma above it (subsonic regime) (Shakura et al. 2012). The latter is relevant for systems with  $L_{\text{X}} \lesssim 4 \times 10^{36} \text{ erg s}^{-1}$ , whereas the supersonic regime settles in for higher X-ray luminosities. Thus, the quasi-spherical accretion model is applicable to both persistent and SFXT systems with slowly rotating pulsars.

As the X-ray luminosity of XMMU J053320.8-684122 never exceeds  $4 \times 10^{36} \text{ erg s}^{-1}$  for the duration of the *XMM-Newton* observation (obsid: 0690743801), it is reasonable to assume that accretion takes place in the subsonic regime. The entry of accreting matter through the magnetosphere determines the X-ray luminosity from the NS<sup>1</sup> and is being regulated by the plasma cooling processes. These lead effectively to a lower radial plasma velocity ( $v_{\text{r}}$ ) than the free-fall velocity at a given radius  $r$  ( $v_{\text{ff}} = \sqrt{2GM_{\text{NS}}/r}$ ) and can be incorporated into the dimensionless factor  $f(v) = v_{\text{r}}/v_{\text{ff}} \lesssim 1$ . For  $L_{\text{X}} \gtrsim 10^{35} \text{ erg s}^{-1}$ , which is relevant to XMMU J053320.8-684122, Compton cooling dominates over the radiative cooling due to free-free emission and  $f_{\text{C}}$  is given by (Shakura and Postnov 2017):

$$f_{\text{C}}(v) \approx 0.22 \zeta^{7/11} \dot{M}_{16}^{4/11} \mu_{30}^{-1/11}, \quad (7.1)$$

where  $\zeta \lesssim 1$ ,  $\dot{M} = 10^{16} \dot{M}_{16} \text{ g s}^{-1}$  is the accretion rate inferred from the X-ray luminosity, and  $\mu = 10^{30} \mu_{30} \text{ G cm}^3$  is the NS magnetic moment. The X-ray luminosity of

<sup>1</sup>We assume  $L_{\text{X}} = \epsilon \dot{M} c^2$ , where  $\epsilon = 0.1$  is the accretion efficiency.

## 7. NEW SGXRBS IN THE LMC

the non-flaring state can be then derived (Shakura et al. 2014):

$$\frac{L_{X,\text{low}}}{5 \times 10^{35} \text{erg s}^{-1}} \simeq f_{\text{C}}(v) \left( \frac{M}{10M_{\odot}} \right)^{s-2/3} \left( \frac{v_{\infty}}{10^3 \text{ km s}^{-1}} \right)^{-1} \left( \frac{v_{\text{w}}}{500 \text{ km s}^{-1}} \right)^{-4} \left( \frac{P_{\text{orb}}}{10 \text{ d}} \right)^{-4/3}, \quad (7.2)$$

where  $s = 2.76$  is the power law index of the phenomenological mass-luminosity relation for massive stars (see Vitrichenko et al. 2007),  $v_{\infty}$  is the terminal wind velocity of massive stars (typically  $1000 \text{ km s}^{-1}$ ),  $v_{\text{w}}$  is the wind velocity at the NS Bondi radius, and  $P_{\text{orb}}$  is the orbital period. Hence, we adopt  $M = 18M_{\odot}$  as an reference value (see Fig. 7.9).

An estimate of  $v_{\text{w}}$  can be obtained, if one matches the mean duration of the observed X-ray flares ( $t_{\text{fl}} \sim 2.2 \times 10^3 \text{ s}$ ) with the free-fall timescale from the outer radius of the plasma shell (i.e., the Bondi radius):

$$v_{\text{w}} = \left( \frac{2GM_{\text{NS}}}{t_{\text{fl}}} \right)^{1/3} = 570 \left( \frac{M_{\text{NS}}}{1.4 M_{\odot}} \right)^{1/3} \left( \frac{t_{\text{fl}}}{10^3 \text{ s}} \right)^{-1/3} \text{ km s}^{-1}, \quad (7.3)$$

By substituting eqs. (7.1), (7.3) and the measured mean X-ray luminosity (i.e,  $L_{X,\text{low}} \simeq 1.4 \times 10^{35} \text{ erg s}^{-1}$ ) into eq. (7.2), we find that  $P_{\text{orb}} \sim 10 \text{ d}$ . Interestingly, the derived orbital period is similar to those of supergiant and SFXT systems (e.g. Drave et al. 2012).

The torques acting on the quasi-static plasma shell above the magnetosphere can either spin-up or spin-down the NS. Because of the short relaxation time ( $\sim 10^4 \text{ yr}$  – see also Sidoli et al. 2017a), it is reasonable to assume that the NS is at an equilibrium state, where its spin period remains constant with time and is given by (Shakura et al. 2012; Shakura and Postnov 2017):

$$P_{\text{eq}} \approx 1000 \mu_{30}^{12/11} \dot{M}_{16}^{-4/11} \left( \frac{P_{\text{orb}}}{10 \text{ d}} \right) \left( \frac{v_{\text{w}}}{10^3 \text{ km s}^{-1}} \right)^4 \text{ s} \quad (7.4)$$

Using the estimated values for the wind velocity and the orbital period, we find  $P_{\text{eq}} \sim 200 \text{ s}$  for  $\mu_{30} = 1$ . Below we list other parameters of the shell that we can estimate:

- Bondi radius:  $R_{\text{B}} \simeq 2GM_{\text{NS}}/v_{\text{w}}^2 \sim 10^{11} \text{ cm}$
- Alfvén radius (Shakura et al. 2012; Shakura and Postnov 2017):

$$R_{\text{A}} \simeq \left( \frac{30\Gamma}{\Gamma - 1} \frac{f_{\text{C}}(v)\mu^2}{\dot{M}\sqrt{2GM_{\text{NS}}}} \right)^{2/7} \sim 2 \times 10^9 \text{ cm}, \quad (7.5)$$

where  $\Gamma = 5/3$  is the adiabatic index.

- Temperature of the plasma at Alfvén radius:

$$T(R_{\text{A}}) \approx \frac{\Gamma - 1}{\Gamma} \frac{GM_{\text{NS}}\bar{\mu}}{\mathcal{R}R_{\text{A}}} \sim 2.5 \times 10^8 \text{ K} \quad (7.6)$$

where  $\bar{\mu} \simeq 0.60$  for ionized gas for the LMC chemical composition (Rolleston et al. 2002) and  $\mathcal{R}$  is the gas constant. The derived temperature is sufficiently low to allow the entry of matter through the magnetosphere via the interchange instability (see Shakura et al. 2012).

- Mass of the plasma shell (Shakura et al. 2014):

$$M_{\text{sh}} \approx \frac{2}{3} \frac{\dot{M}}{f_C(v)} t_{\text{ff}}(R_B) \simeq 2 \times 10^{19} \text{ g}. \quad (7.7)$$

- Plasma density at Alfvén radius (Shakura et al. 2012):

$$\rho(R_A) \approx \frac{3M_{\text{sh}}}{8\pi R_A^{3/3} (R_B^{3/2} - R_A^{3/2})} \simeq 8 \times 10^{-13} \text{ g cm}^{-3}, \quad (7.8)$$

where a density profile of  $\rho(R) \propto R^{-3/2}$  was assumed.

In the Compton cooling regime, the ratio of the flaring to the non-flaring luminosity can be estimated as  $L_{X,\text{flare}}/L_{X,\text{low}} \approx 1/f_C(v) \propto L_{X,\text{low}}^{-4/11}$ . Using the mean low luminosity of XMMU J053320.8-684122 in the 0.3-10 keV and equation (7.1), we find  $L_{X,\text{flare}}/L_{X,\text{low}} \approx 7$ . Following this, we made a comparison of our results with those derived for other known SFXT systems. Recently, Shakura et al. (2014) computed the mean dynamic range of INTEGRAL detected flares from SFXT systems by using long-term INTEGRAL archival data in hard X-rays (17-50 keV) (Paizis and Sidoli 2014). This is illustrated in Fig. 7.10 (black crosses). XMMU J053320.8-684122 is well modeled by an absorbed power-law in the 0.3-10 keV band. The X-ray spectrum of accreting NS exhibits a cutoff above 10 keV, thus it is not straight forward to extrapolate the luminosity of accreting NS in different energy bands. Nevertheless, we can estimate an expected range for its hard X-ray luminosity assuming an upper (i.e. 50 keV) and lower (i.e. 10 keV) limit for the cutoff energy. If we assume a cutoff power law with photon index 0.92 (see Table 7.3) and variable cutoff energy, the non-flaring luminosity of XMMU J053320.8-684122 in the 17-50 keV band ranges between  $\sim 1$  and 4 times its luminosity in the 0.3-10.0 keV band. The variability of the system in the soft and hard X-rays is expected to be the same, assuming no significant change in its spectral properties during the flares. The location of XMMU J053320.8-684122 in the  $L_{X,\text{low}}$  vs  $L_{X,\text{flare}}/L_{X,\text{low}}$  diagram, shown as a striped band in Fig. 7.10, is in agreement with the theoretical predictions (dashed and dotted lines). We caution the reader that our estimates for the time-averaged luminosities are limited to a single *XMM-Newton* observation.

In principle, similar estimates can be performed for XMMU J053108.3-690923 by assuming that the observed spin-period corresponds to the equilibrium one (see eq. (7.4)). However, the estimates will suffer from large uncertainties due to the following reasons: No fast bright flares have been detected, thus no flare duration and amplitude can be determined. Subsequently, no wind velocity or orbital period can be estimated. We note that  $P_{\text{eq}}$  has a strong dependence on the wind velocity (see also Shakura et al. 2014). Finally, the nature of the donor star is less certain than in the XMMU J053320.8-684122 system.

## 7.5 Conclusions

I present a detailed analysis of two SgXRBs in the LMC, raising the number of LMC SgXRB systems to five. I studied the X-ray timing and spectral properties of the compact objects as well as the optical properties of the donor stars.

## 7. NEW SGXRBS IN THE LMC

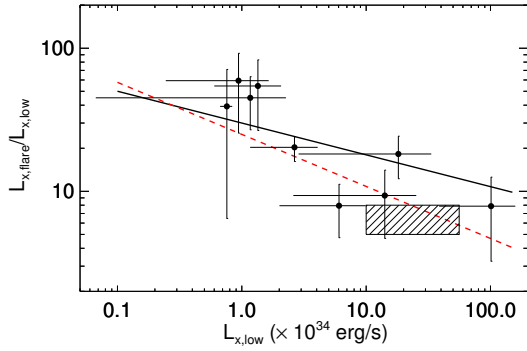


**Figure 7.10:** Comparison of the mean dynamic flare range of other known SFXT systems. Values for the known systems (black crosses) refer to the INTEGRAL/IBIS energy range (17-50 keV) and were obtained from Paizis and Sidoli (2014). For XMMU J053320.8-684122 (striped band) we used the *XMM-Newton* derived rates in the 0.3-10 keV energy range and extrapolated to the 17-50 keV band by assuming a power law with photon index 0.92 with different cutoff energies (10 & 50 keV). Overplotted are the expected dependencies of  $L_{X,flare}/L_{X,low}$  on the non-flaring luminosity in two regimes of plasma cooling in the shell: radiative cooling (black dotted line) (see Shakura et al. 2014) or Compton cooling (red dashed line), as described in the text.

The first system XMMU J053108.3-690923, is a 2013.5 s pulsar having a supergiant (or bright giant) companion, this is the 2<sup>nd</sup> confirmed SgXRB pulsar in the LMC. Its X-ray spectrum is consistent with an absorbed power-law with a soft excess which can be either interpreted to originate from the hot spots of the NS, or as the result of partial absorption by the clumpy stellar wind of the giant companion. We further find indications of the variation of the hardness ratio with the pulse phase. The optical companion is identified as B0e II-Ib with mass in the range of 12-18  $M_{\odot}$ .

The second system XMMU J053320.8-684122, is the first identified SFXT candidate in the LMC. The X-ray light curve, obtained by *XMM-Newton*, displays a long period of quiescence followed by three subsequent flares of high dynamic range. The spectrum is consistent with an absorbed power-law with a moderate value of absorption column density. The optical companion is identified as B0.5e 1b with a mass of 18  $M_{\odot}$ . The above properties are indicative of the SFXT nature of the system.

## Part IV

# Hunting BeXRB outbursts in the Magellanic Clouds



## Characteristics of outburst

**BeXRBS** are among the most variable astrophysical systems. Their X-ray emission typically remains at a quiescent level ( $<10^{34}$  erg s $^{-1}$ ) while exhibiting X-ray outbursts that are related to the availability of matter for accretion. X-ray outbursts of **BeXRBS** are historically characterised as type-I or type-II based on their maximum luminosity, but the physical mechanism that describes the accretion of matter and the X-ray emission is not that different in both cases. As discussed above (see §2), it is now generally accepted that normal or so-called Type-I outbursts ( $L_X \sim 10^{36}$  erg s $^{-1}$ ) can occur as the **NS** passes close to the accretion disk, thus they appear to be correlated with the binary orbital period. Giant or Type-II outbursts ( $L_X \geq 10^{38}$  erg s $^{-1}$ ) that can last multiple orbits are associated with warped Be-disks (Okazaki et al. 2013).

An outburst starts when enough material has been accumulated around the **NS** and the accretion disc pushes its way inside the corotation radius of the **NS**. Then most of the matter falls onto the **NS** surface by following the magnetic field lines. Since matter cannot cross the field lines, it is eventually deposited onto the region marked by the last closed magnetic field lines.

At low accretion rates material is free falling and eventually is deposited around the **NS** magnetic pole. This results in the local heating of the **NS** surface and the creation of two hot spots. As the **NS** rotates the two hot spots are responsible for the characteristic pulsations that are observed from **XRPCs**. At higher accretion rates, the radiation pressure of the hot spot prohibits in-falling material from free-falling onto the **NS** and a shocked region is formed above it. The space below the shocked region is commonly referred to as accretion column, and generally in order for the column to be formed the luminosity of the pulsar should exceed  $10^{37}$  erg s $^{-1}$ . The accretion column is an optically thick structure inside which photons are produced through bremsstrahlung and cyclotron radiation. These seed photons are in turn scattered by the optically thick material in the presence of a strong magnetic field. Finally, most of the photons escape from the sides of the accretion column in a characteristic fan-beam pattern. At even higher accretion rates the material above the accretion column can also become optically thick, thus altering the observational signatures of the accretion column. I will discuss more about this regime in the context of **ULX** systems.

Our aim is to observe as many as possible **BeXRB** systems during outbursts with modern X-ray observatories in order to study multiple aspects of accretion physics. For that reason we have followed the multi-step described below in order to promptly detect and follow these events.

- We have requested observing time for Chandra and *XMM-Newton* telescopes for triggered **ToO** observations, in order to follow these events when they happen. Our aim is to trigger these observations whenever a new or poorly studied system goes into outburst.
- We have requested *Swift*/XRT monitoring observations of particular regions in the **MCs** where there is a higher density of **BeXRBS**. Our aim is to promptly detect random type I or type II outburst from systems within the field of view

## 8. CHARACTERISTICS OF OUTBURST

---

of *Swift*/XRT.

- For candidate [BeXRB](#) systems with known orbital period we request *Swift*/XRT monitoring observations around the expected optical maximum. Our aim is to promptly detect anticipated type I outbursts that occur at periastron passage.
- We have constructed an algorithm that automatically performs a database search and analyses all X-ray observations targeted in the direction of the [MCs](#) as soon as they become public. Typically *Swift*/XRT observations become available within less than 1 day after they are performed. Our aim is to promptly identify outbursts that are serendipitously detected by random X-ray observations.
- Finally, we complement the study of newly discovered outbursting systems with multiwavelength photometric and spectroscopic observations through ground-based facilities.

The above strategy has been successfully implemented the last few years, enabling us to follow up on average 3 X-ray outbursts per year. In the following chapters, I expand on the major discoveries made by our observations.

## LXP 28.77: August 2012 outburst

**I**n this chapter we report on the properties of Swift J053041.9-665426 a newly discovered **BeXRB** in the **LMC**. The source was discovered on 2011 Nov. 6 during a *Swift* observation of the **LMC** nova 2009B (Sturm et al. 2011b). It was then detected in a subsequent *Swift* follow-up observation that yielded an improved position and X-ray spectrum (Sturm et al. 2011c). Based on its spectral properties and the correlation with an early-type optical counterpart the source was characterised as a **BeXRB** candidate. Variability of the optical counterpart has been reported (Charles et al. 2011), which is consistent with such a classification. In addition to the existing *Swift* observations we present the spectral and timing analysis of an *XMM-Newton* target-of-opportunity (ToO) observation as well as the results of optical spectroscopy performed on its companion.

## 9.1 Observations and data reduction

### 9.1.1 X-ray observations

For the current analysis we used six *Swift*, one *XMM-Newton* and one ROSAT observations of the field surrounding the source. The detailed observation log is recorded in Table 9.1. The source was detected in four more *Swift* observations of the field in addition to those reported above. For the spectral extraction we used the **HEASoft**<sup>1</sup> task **xselect** and an extraction region with radius 35'' for the source and 300'' for the background. Following the detection of Swift J053041.9-665426 in the *Swift* observation on 2012 Aug. 28, we obtained an *XMM-Newton* ToO observation (PI: P. Maggi). The observation was performed on 2012 Sep. 03 and allowed us to detect the source during outburst. The source was located on-axis, on CCD4 of the EPIC-pn (Strüder et al. 2001) and on CCD1 of the EPIC-MOS (Turner et al. 2001) detectors. *XMM-Newton* SAS 12.0.1<sup>2</sup> was used for data processing. The observation was affected by high background for the first 10 ks, which then stayed at a moderate level for the rest of the exposure. We used a background threshold of 16 and 8 counts ks<sup>-1</sup> arcmin<sup>-2</sup> for the EPIC-pn and EPIC-MOS detectors respectively which resulted in net exposure times of 22.3/26.0/26.0 ks for EPIC-pn/MOS1/MOS2 after flare removal. The source event extraction was performed using a circle around the source while the background events were extracted from a point-source free area on the same CCD but with different pixel columns for EPIC-pn. We optimised the size of the source extraction area using the SAS task **eregionanalyse**. The final values used for the extraction are given in Table 9.1, which summarises the available X-ray observations. For the EPIC-pn spectra and light curves, we selected single-pixel and double-pixel events (**PATTERN**≤4) while in the case of EPIC-MOS we used single to quadruple events (**PATTERN**≤12). The quality flag **FLAG** = 0 was used throughout. The SAS task **especget** was used to create the spectra for the spectral analysis. The spectra were binned to achieve a minimum signal-to-noise ratio of five for each bin. This allows the use of the  $\chi^2$  statistics in the

<sup>1</sup><http://heasarc.nasa.gov/lheasoft/>

<sup>2</sup>Science Analysis Software (SAS), <http://xmm.esac.esa.int/sas/>

## 9. LXP 28.77: AUGUST 2012 OUTBURST

ObsID	Date	Start time (UT)	Instrument	Mode <sup>a</sup>	Offax <sup>b</sup> [']	Net Exp [ks]	Net Count rates <sup>c</sup> [cts s <sup>-1</sup> ]	R <sub>sc</sub> <sup>d</sup> ["]	F <sub>x</sub> <sup>e</sup> [erg s <sup>-1</sup> cm <sup>-2</sup> ]	L <sub>x</sub> <sup>f</sup> [erg s <sup>-1</sup> ]
<i>XMM</i>										
0700381101	2012-09-03	21:34 – 07:34	EPIC-pn	ff-m	1.12	22.3	0.211±0.003	20	1.79×10 <sup>-12</sup>	5.53×10 <sup>35</sup>
		21:11 – 07:34	EPIC-MOS1	ff-m	0.22	26.0	0.0765±0.0019	32		
		21:11 – 07:34	EPIC-MOS2	ff-m	1.25	26.0	0.0758±0.0018	26		
<i>Swift</i>										
00045769001	2011-11-06	03:54:01	XRT	pc	10.4	0.4	0.35 ±0.03	35	3.49×10 <sup>-11</sup>	1.04×10 <sup>37</sup>
00032172001	2011-11-08	16:41:01	XRT	pc	1.6	1.0	0.498±0.023	35	4.16×10 <sup>-11</sup>	1.24×10 <sup>37</sup>
00032172002	2011-11-10	13:38:00	XRT	pc	1.9	1.2	0.427±0.020	35	3.07×10 <sup>-11</sup>	0.92×10 <sup>37</sup>
00032172003	2011-11-12	13:51:01	XRT	pc	2.0	1.1	0.417±0.021	35	2.88×10 <sup>-11</sup>	0.86×10 <sup>37</sup>
00045769002	2012-08-28	01:08:58	XRT	pc	10.9	1.9	0.098±0.009	35	9.47×10 <sup>-12</sup>	2.83×10 <sup>36</sup>
00045769004	2012-10-18	07:02:34	XRT	pc	11.9	0.5	0.033±0.010	35	3.02×10 <sup>-12</sup>	9.04×10 <sup>35</sup>
<i>ROSAT</i>										
RP900553N00	1999-11-09	15:28 – 22:26	PSPC	-	-	1.1	<0.006	-	<1.58×10 <sup>-12</sup>	<4.70×10 <sup>35</sup>

<sup>a</sup> Observation setup: full-frame mode (ff) and photon-counting mode (pc). For *XMM-Newton*, the medium filter (m) was used. <sup>b</sup> Off-axis angle under which the source was observed. <sup>c</sup> Net counts as used for spectral analysis in the (0.2 – 10.0) keV band for *XMM-Newton* and in the (0.3 – 6.0) keV band for *Swift*. <sup>d</sup> Radius of the circular source extraction region. <sup>e</sup> X-ray flux in the (0.3 – 10.0) keV band, derived from the best fit spectral model. <sup>f</sup> Source intrinsic X-ray luminosity in the (0.3 – 10.0) keV band (corrected for absorption) for a distance to the LMC of 50 kpc (Hilditch et al. 2005).

**Table 9.1:** X-ray observations of *Swift*.

spectral analysis, which was performed with XSPEC (Arnaud 1996) version 12.7.0. A ROSAT archival observation covering the position of Swift J053041.9-665426 is also available, which we used to establish an upper limit for the source luminosity.

### 9.1.2 Optical spectroscopy

The optical data were taken with the ESO Faint Object Spectrograph and Camera (EFOSC2) mounted at the Nasmyth B focus of the 3.6 m New Technology Telescope (NTT), La Silla, Chile on the nights of 2011 Dec. 8, 9 and 10. A slit width of 1.5'' was used, along with Grisms 14 and 20 for blue and red end spectroscopy, respectively. For details on the individual Grisms see Table 9.2. Filter OG530 was used in conjunction with Grism 20 to block second order effects. The resulting spectra were recorded on a Loral/Lesser, thinned, AR-coated, UV flooded, MPP CCD with 2048×2048 pixels. Wavelength calibration was achieved using comparison spectra of helium and argon lamps taken throughout the observing run with the same instrument configuration. The data were reduced using the standard packages available in the Image Reduction and Analysis Facility (IRAF)<sup>1</sup>. The spectra were normalised to remove the continuum and a redshift correction was applied corresponding to the recession velocity of the LMC (-280 km s<sup>-1</sup>, Richter et al. 1987).

## 9.2 X-ray data analysis and results

### 9.2.1 X-ray position

X-ray images were created from all the EPIC cameras using the *XMM-Newton* standard energy sub-bands (Watson et al. 2009). Source detection was performed simul-

<sup>1</sup>Image Reduction and Analysis Facility (IRAF), <http://iraf.noao.edu/>

Grism	Wavelength range [Å]	Grating [lines mm <sup>-1</sup> ]	Dispersion [Å pixel <sup>-1</sup> ]	Resulting resolution [Å]
14	3095–5085	600	1.00	~10
20	6047–7147	1070	0.55	~6

**Table 9.2:** ESO Faint Object Spectrograph grism information.

taneously on all the images using the SAS task `edetect_chain`. Boresight correction was performed on the images based on the position of three identified background X-ray sources in the same field. The positional correction based on these sources was found to be  $\sim 1''$ . The source position was determined to R.A. =  $05^{\text{h}}30^{\text{m}}42.^{\text{s}}17$  and Dec. =  $-66^{\circ}54'31''.0$  (J2000.0) with a  $1\sigma$  statistical uncertainty of  $0.08''$ . The total  $1\sigma$  positional uncertainty, however is determined by the remaining systematic uncertainty assumed to be  $0.5''$  (see section 4.3 of [Sturm et al. 2013b](#)).

### 9.2.2 Spectral analysis

All the EPIC spectra were fitted simultaneously for the same model parameters with an additional scaling factor to account for instrumental differences. For the EPIC-pn we fixed the scaling factor to be 1 while for both EPIC-MOS we obtained values of  $C_{MOS} = 1.08 \pm 0.05$ , which is consistent with the expected value, as EPIC-MOS is known to provide  $\sim 5\%$  higher fluxes than EPIC-pn (see [Stuhlinger et al. 2006](#), or the latest version of the *XMM-Newton* calibration manual<sup>1</sup>). The photoelectric absorption was modelled as a combination of Galactic foreground absorption and an additional column density accounting for both the interstellar medium of the LMC and the intrinsic absorption by the source. The Galactic photoelectric absorption was set to a column density of  $N_{\text{H,GAL}} = 5.86 \times 10^{20} \text{ cm}^{-2}$  ([Dickey and Lockman 1990a](#)) with abundances according to [Wilms et al. \(2000\)](#). The additional column density  $N_{\text{H,LMC}}$  was left as a free parameter with abundances of 0.49 for elements heavier than helium ([Rolleston et al. 2002](#)). All the uncertainties were calculated based on a  $\Delta\chi^2$  statistic of 2.706, equivalent to a 90% confidence level for one parameter of interest.

The spectra were fitted by an absorbed power law, resulting in an acceptable fit with reduced  $\chi^2$  value of  $\chi^2_{\text{red}} = 1.4$ . However, we found systematic deviations in the residuals. Therefore, we further tested the spectra for the existence of additional features

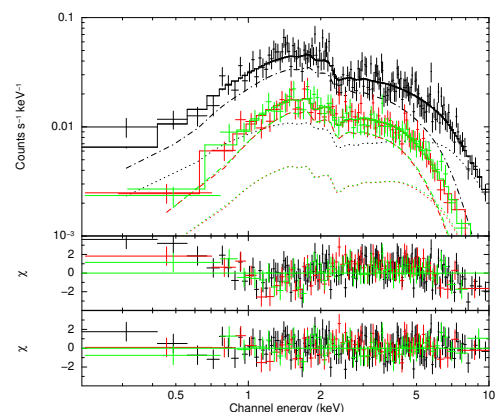


**Figure 9.1:** EPIC spectra of Swift J053041.9-665426. The top panel shows the EPIC-pn (black), EPIC-MOS1 (red) and EPIC-MOS2 (green) spectra, together with the best-fit model (solid line) of an absorbed power law (dotted line) plus a black body (dash-dotted line). The residuals for this model are plotted below (bottom panel) while for comparison the best-fit single power-law model residuals are also plotted (middle panel).

<sup>1</sup>[http://xmm2.esac.esa.int/external/xmm\\_sw\\_cal/calib/cross\\_cal/index.php](http://xmm2.esac.esa.int/external/xmm_sw_cal/calib/cross_cal/index.php)

typically shown by [BeXRBs](#). The best fit was achieved by an absorbed power law plus a black body that contributes to the soft part of the spectrum. The two-component model significantly improves the fit over the simple power-law ( $\chi^2_{\text{red}}=0.98$  vs 1.4 for two additional parameters), with the F-test probability for the additional black-body component being  $\sim 8 \times 10^{-21}$ . The black-body component accounts for 53.8% of the detected flux and demonstrates model dependent uncertainties on the photon index of the power-law model. The black-body model `bodyrad` uses a normalisation proportional to the emission area (norm  $K = R_{km}^2/D_{10}^2$ , where  $R_{km}$  denotes the emission radius in km and  $D_{10}$  the source distance in units of 10 kpc). From this relation we derived a radius for the emission region of  $\sim 800$  m. This area should be indicative of the size of the accretion column from which the black-body radiation is believed to originate ([Hickox et al. 2004](#)). The spectra together with the best-fit power-law and black-body model are presented in [Fig. 9.1](#), where we also compare the residuals with those of the simple power-law model fit.

It should be noted that although the addition of the black-body model improves the quality of the fit it also adds large uncertainties to the best-fit values. Thus, different combinations of parameters can actually provide a similarly good fit (see [Fig. 9.2](#)). Softer power-laws (higher  $\Gamma$ , where  $\Gamma$  is defined as the index in a power law spectrum  $A(E) \propto E^{-\Gamma}$ ) can be compensated with higher absorption values, while for lower  $\Gamma$  the best fit model gives lower absorption values and lower black-body temperature. Therefore, for any constant value of  $\Gamma$  between 0 and 0.8 the reduced  $\Delta\chi^2$  for the fit varies only marginally around one. Also by looking at [Fig. 9.1](#), we can see that the black-body component contributes almost to all the emission below 6 keV. Because of the large uncertainties, we present another more consistent set of parameters for a fixed photon index at the value of 0.7, which is close to the one found with the single power-law fitting. The best-fit results are listed in [Table 9.3](#).

Replacing the black-body component by alternative models such as, a Comptonisation spectrum, a thermal bremsstrahlung or a MEKAL thermal plasma only gives a marginal improvement of the fit compared to the single power-law model. The only models that showed similar goodness of fit were a power-law with high-energy exponential cutoff (*cut-offpl* in *xspec*, with  $\Gamma = -0.68$  and e-folding energy of 2.8 keV) and the broken power-law (*bknpower* in *xspec*, with  $\Gamma_1 = 0.1$ ,  $\Gamma_2 = 1.2$ , break at 3.3 keV). However, we do not expect negative photon indices nor a break at such low energies for [BeXRB](#) systems.

Individual *Swift* observations did not provide sufficient statistics to determine spectral parameters independently, but using a group of them to simultaneously fit a model provided better statistics. For the first four observations that were taken during the same outburst and were at similar flux level we performed the event extraction as described in

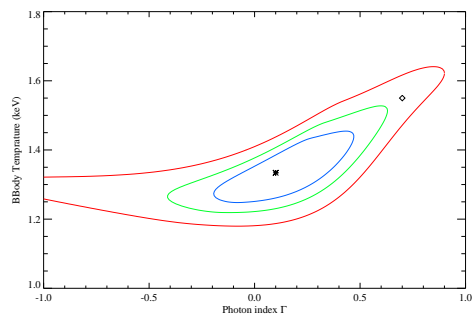


**Figure 9.2:** Photon index  $\Gamma$  vs temperature  $kT$  (keV) confidence contours for the power-law + black-body model. Confidence levels of 1, 2 and 3  $\sigma$  are shown in blue green and red. The star represent the best-fit values while the diamond marks the best fit for a fixed  $\Gamma$  of 0.7.

## 9.2 X-ray data analysis and results

Model <sup>(1)</sup>	LMC N <sub>H</sub> [10 <sup>21</sup> cm <sup>-2</sup> ]	Γ	kT [keV]	R <sup>(2)</sup> [m]	Flux <sup>(3)</sup> [erg cm <sup>-2</sup> s <sup>-1</sup> ]	L <sub>x</sub> <sup>(4)</sup> [erg s <sup>-1</sup> ]	L <sub>BB</sub> <sup>(5)</sup> [%]	χ <sub>red</sub> <sup>2</sup> /dof <sup>(6)</sup>
<i>XMM-Newton</i>								
PL	5.8 <sup>+0.1</sup> <sub>-0.09</sub>	0.78±0.06	–	–	2.07×10 <sup>-12</sup>	5.5×10 <sup>35</sup>	–	1.40/272
PL+BBrad	0 <sup>+1.1</sup>	0.1 <sup>+0.4</sup> <sub>-0.3</sub>	1.33 <sup>+0.14</sup> <sub>-0.09</sub>	850 <sup>+100</sup> <sub>-130</sub>	1.79×10 <sup>-12</sup>	5.3×10 <sup>35</sup>	53.8	0.98/270
PL(fixed)+BBrad	1.4 ± 0.8	0.7 fixed	1.55 <sup>+0.06</sup> <sub>-0.07</sub>	680 ± 60	1.78×10 <sup>-12</sup>	5.3×10 <sup>35</sup>	60.0	1.00/271
<i>Swift</i> <sup>(7)</sup>								
PL	1.0 <sup>+4.4</sup> <sub>-1.0</sub>	1.14 <sup>+0.09</sup> <sub>-0.08</sub>	–	–	–	–	–	0.90/79

Notes:<sup>(1)</sup> For definition of spectral models see text. <sup>(2)</sup> Radius of the emitting area. <sup>(3)</sup> Observed (0.2-10.0) keV flux derived from EPIC-pn. <sup>(4)</sup> Source intrinsic X-ray luminosity in the (0.2-10.0) keV band (corrected for absorption) for a distance to the LMC of 50 kpc (Hilditch et al. 2005). <sup>(5)</sup> Contribution of the black-body component to the total unabsorbed luminosity. <sup>(6)</sup> Degrees of freedom (dof). <sup>(7)</sup> Best-fit parameters for simultaneous fitting of the spectra from the first four *Swift* observations.

**Table 9.3:** Spectral fit results.

Section 9.1.1 and performed a simultaneous spectral fitting with XSPEC. Due to lower statistics compared to the *XMM-Newton* spectra we only tested an absorbed power-law model. The best-fit values are also listed in Table 9.3. For the two *Swift* observations taken in 2012 we used the best-fit parameters for the absorbed power-law model as obtained from the *XMM-Newton* spectrum (near in time) and derived the fluxes of these *Swift* observations by adjusting the normalisation.

From the ROSAT observation we estimated an upper limit for the X-ray flux assuming the same spectral properties as in the *XMM-Newton* detection and assuming that for a detection at least seven counts are needed for an on-axis observation.

### 9.2.3 X-ray long-term variability

In order to study the long-term variability of Swift J053041.9-665426 we estimated the flux level for all available observations (see Table 9.1). The source flux from the *XMM-Newton* ToO observation was determined from the spectra as described in Section 9.2.2. We transformed the observed fluxes to unabsorbed luminosities based on a LMC distance of 50 kpc. The net count rates and unabsorbed luminosities are given in Table 9.1.

The *Swift* observations indicate a variability of up to a factor of  $\sim 14$ . The *XMM-Newton* ToO observation yields a luminosity lower than any *Swift* observation giving a total variability of  $\sim 23$ . The upper limit derived from the ROSAT observation is  $\sim 1.6$  times smaller than the *XMM-Newton* detected flux, providing evidence for even larger variability. However, the photoelectric absorption will have large effect on the soft ROSAT energy band and may introduce large systematic uncertainties.

### 9.2.4 Timing analysis

We corrected the *XMM-Newton* EPIC event arrival times to the solar-system barycentre using the SAS task `barycen`. The X-ray light curves were searched for periodicities using fast Fourier transform (FFT) and light curve folding techniques. The power density spectra derived from time series in various energy bands from all three EPIC

instruments show a periodic signal at  $\omega \sim 0.0347521$  Hz. To increase the signal-to-noise ratio, we then created time series from the merged event list of EPIC-pn and EPIC-MOS (delimited to common good time intervals).

Fig. 9.3 shows the inferred power density spectrum from the (0.2-10) keV energy band with a strong peak at a frequency of 0.0347520(5) Hz. Following Haberl et al. (2008a) we used a Bayesian periodic signal detection method (Gregory and Loredo 1996) to determine the pulse period with  $1\sigma$  uncertainty to  $(28.77521 \pm 0.00010)$  s. The period folded pulse profiles in the EPIC standard energy bands together with the hardness ratios derived from the pulse profiles in two adjacent energy bands ( $HR_i = (R_{i+1} - R_i)/(R_{i+1} + R_i)$  with  $R_i$  denoting the background-subtracted count rate in energy band  $i$ ) are plotted in Fig. 9.4. To achieve better statistics, the first two standard energy bands were combined in the top panel, the bottom panel shows all five energy bands combined. All the profiles are background-subtracted and normalised to the average count rate (0.0215, 0.0813, 0.1403, 0.0950, and 0.3388  $\text{cts s}^{-1}$ , from top to bottom).

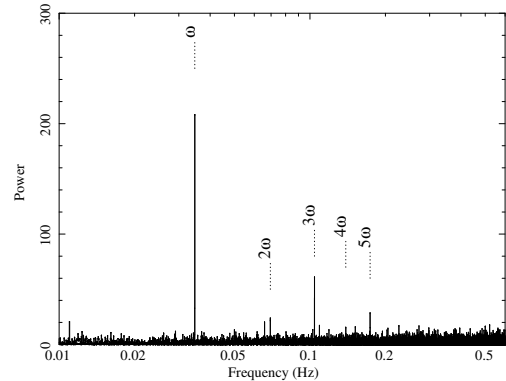


**Figure 9.3:** Power density spectrum created from the merged EPIC-pn and EPIC-MOS data in the (0.2-10.0) keV energy band. The time binning of the input light curve is 0.8156671 s. On the plot we can see the best-fit frequency of  $\omega = 0.034752$  Hz and its first, second and fourth harmonics.

## 9.3 Analysis and results of optical data

### 9.3.1 Optical counterpart

The most precise X-ray position of Swift J053041.9-665426 was derived from *XMM-Newton* data (Sect. 9.1.1). Within the  $3\sigma$  error circle we found only one candidate counterpart at a distance of  $\sim 0.8''$ . The object was identified in 2MASS (Skrutskie et al. 2006; Cutri et al. 2003), IRSF (Kato et al. 2007) and MCPS (Zaritsky et al. 2004) catalogs and the WISE All-sky data release. It is listed as J05304215-6654303 in the 2MASS catalogue. The various magnitudes are summarised in Table 9.4.

A finding chart of Swift J053041.9-665426 is shown in Fig. 9.5. The image was obtained with ESO NTT during the spectroscopic observation of the source and the image coordinates were corrected based on the 2MASS catalogue with a positional uncertainty  $\sim 0.2''$ .

The spectral energy distribution (SED) of Be stars consists of two components (Dougherty et al. 1994), the emission from the surface of the star (stellar atmosphere of  $T \sim (18\,000 - 38\,000)$  K) and an infrared excess from the equatorial disc. Due to the evolution of the disc with time the luminosity of the system may vary. Therefore, simultaneous measurements of individual colours are needed for a meaningful SED. From the available data it is not possible to construct an SED and compare it with available models. However, we see evidences for variability of the optical counterpart, which is typical for BeXRB systems.

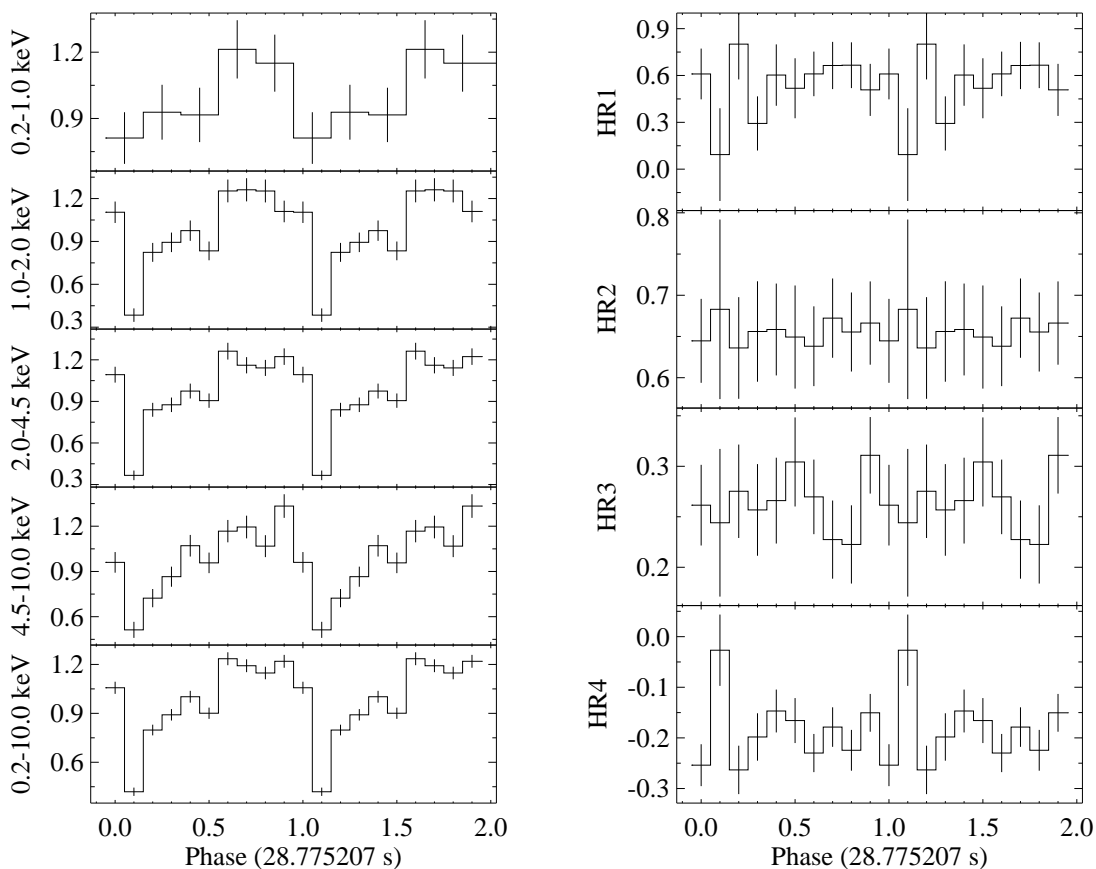


**Figure 9.4:** Left: Pulse profiles obtained from the merged EPIC data in different energy bands. Right: Hardness ratios as a function of pulse phase derived from the pulse profiles in two neighbouring standard energy bands.

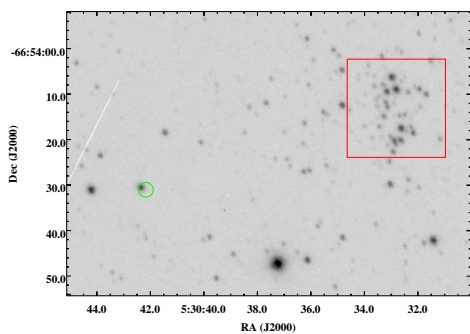


**Figure 9.5:** Finding chart of Swift J053041.9-665426. The image was taken with ESO NTT (V#641 filter) during the spectroscopic observation of the source. The green error circle with radius of  $1.6''$  translates to the  $3\sigma$  *XMM-Newton* positional uncertainty. On the right part of the image at a distance of  $0.95'$  from the *XMM-Newton* position of Swift J053041.9-665426 the nearby star cluster KMHK 987 is seen (dashed red box).

## 9. LXP 28.77: AUGUST 2012 OUTBURST

	Z2004 <sup>(a)</sup>	2MASS <sup>(b)</sup>	2MASS 6X <sup>(c)</sup>	2MASS 6X <sup>(c)</sup>	IRSF <sup>(d)</sup>	WISE <sup>(e)</sup>	SAGE <sup>(f)</sup>
MJD	2004	2000 Feb 28	2000 Dec 8	2001 Feb 4	2003 Jan 28	-	-
	-	51602.0488	51886.3355	51944.1069	52667.896	-	-
U	14.312±0.022	-	-	-	-	-	-
B	15.007±0.033	-	-	-	-	-	-
V	15.321±0.018	-	-	-	-	-	-
I	15.586±0.023	-	-	-	-	-	-
J	-	15.26±0.05	15.83±0.04	15.66±0.04	15.30±0.02	-	-
H	-	14.98±0.09	15.82±0.09	15.86±0.07	15.24±0.02	-	-
K	-	14.91±0.13	15.86±0.16	15.85±0.13	15.17±0.05	-	-
W1	-	-	-	-	-	14.245±0.027	-
W2	-	-	-	-	-	14.125±0.027	-
W3	-	-	-	-	-	<13.898 <sup>(g)</sup>	-
W4	-	-	-	-	-	<10.086 <sup>(g)</sup>	-
[3.6]	-	-	-	-	-	-	14.566±0.039
[4.5]	-	-	-	-	-	-	14.343±0.035
[5.8]	-	-	-	-	-	-	14.247±0.048

<sup>(a)</sup>Zaritsky et al. (2004). <sup>(b)</sup>Cutri et al. (2003). <sup>(c)</sup>Cutri et al. (2012). <sup>(d)</sup>Kato et al. (2007). <sup>(e)</sup>Cutri and et al. (2012). <sup>(f)</sup>Meixner et al. (2006). <sup>(g)</sup> upper limits.

**Table 9.4:** Optical and IR photometry of Swift J053041.9-665426.

The optical counterpart of Swift J053041.9-665426 was also found in the *Spitzer* SAGE catalogs of the Magellanic Clouds (Meixner et al. 2006). Using the J colours from various surveys and the IRAC 3.6, 4.5, 5.8  $\mu\text{m}$  colours (see table 9.4) and based on the analysis of Bonanos et al. (2009, 2010) we determined the position of the source on the  $J_{\text{IRSF}}$  vs.  $J_{\text{IRSF}} - [3.6]$ ,  $J_{\text{IRSF}}$  vs.  $J_{\text{IRSF}} - [5.8]$ ,  $J_{\text{IRSF}}$  vs.  $J_{\text{IRSF}} - [8.0]$  diagrams. Most of the B stars have a  $J - [3.6]$  colour  $\sim [-0.2 : 0.2]$  mag. While, depending on the four available observations in the J filter, the optical counterpart of Swift J053041.9-665426 has a larger colour index between 0.7 and 1.26 mag. Based on that we clearly detect infrared excess of the counterpart of Swift J053041.9-665426. This excess can be attributed to the free-free emission from the disc around the star.

### 9.3.2 Spectral classification

From the optical spectroscopy we clearly see  $\text{H}\alpha$  emission from the proposed counterpart of Swift J053041.9-665426. Fig. 9.6 shows the red end of the spectrum taken on 2011 Dec. 10. The  $\text{H}\alpha$  equivalent width, considered as an indicator for circumstellar disc size (Stevens et al. 1997), is  $-(16.8 \pm 0.9)$  Å.

OB stars in our own Galaxy are classified using the ratio of certain metal and helium lines (Walborn and Fitzpatrick 1990) based on the Morgan-Keenan (MK; Morgan et al. 1943) system. However, in lower metallicity environments such as the Magellanic Clouds this is not possible, due to the absence or weakness of the metal lines. Therefore, the optical spectrum of Swift J053041.9-665426 was classified using the method developed by Lennon

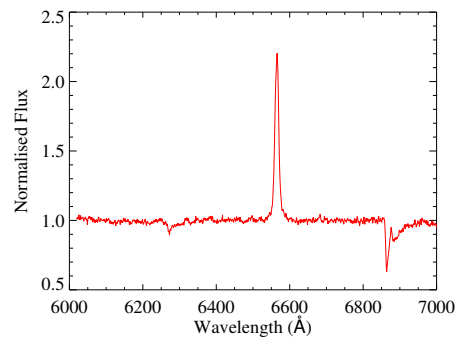


**Figure 9.6:** Spectrum of Swift J053041.9-665426 in the wavelength range  $\lambda 6000\text{--}7000\text{\AA}$  as measured with the NTT on 2011-12-10. The spectrum has been normalised to remove the continuum and redshifted by  $-280 \text{ km s}^{-1}$ .

(1997) for B-type stars in the SMC. The luminosity classification method from Walborn and Fitzpatrick (1990) was assumed in this work.

Figure 9.7 shows two unsmoothed optical spectra of Swift J053041.9-665426 taken on 2011 Dec. 8 and 9, dominated by the hydrogen Balmer series. The equivalent widths of the  $H\beta$  lines are  $(-1.3 \pm 0.2) \text{ \AA}$  and  $(-1.4 \pm 0.2) \text{ \AA}$ , respectively. The SiIV lines at  $\lambda 4088, \lambda 4116 \text{ \AA}$  are both clearly present in both spectra, despite the rotational broadening of the  $H\delta$  line, suggesting a classification earlier than B1.5. The HeII line at  $\lambda 4686 \text{ \AA}$  is just visible above the noise level of the data, implying a classification of B1. There also appears to be marginal evidence for a line at  $\lambda 4541 \text{ \AA}$  (particularly in the lower spectrum) indicating a spectral class of B0.

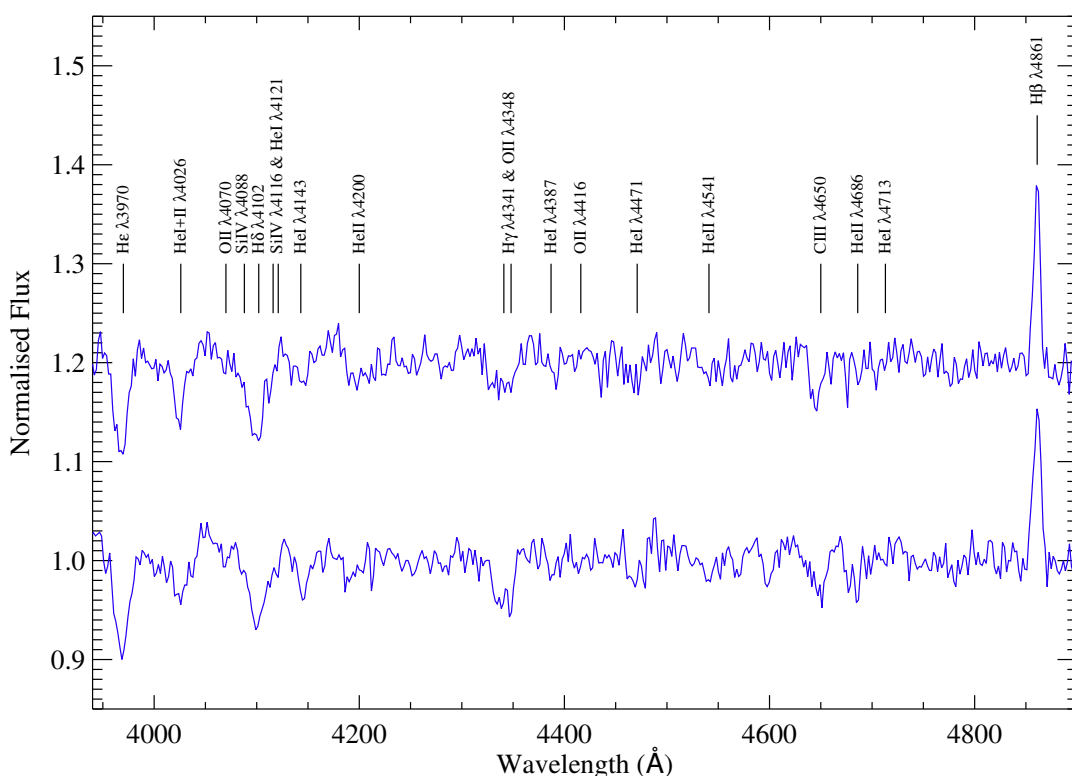


**Figure 9.7:** Spectra of Swift J053041.9-665426 in the wavelength range  $\lambda 3900\text{--}5000\text{\AA}$  taken on concurrent nights with the NTT. The spectra have been normalized to remove the continuum and redshift corrected by  $-280 \text{ km s}^{-1}$ . Atomic transitions relevant to spectral classification have been marked. The lower one was taken on the first night while a different normalization has been used for better representation and comparison.

The luminosity class of the system was determined using the ratios of Si IV  $\lambda 4088$  over He I+II  $\lambda 4026$ , Si IV  $\lambda 4088$  over He I  $\lambda 4143$ , Si IV  $\lambda 4116$  over He I  $\lambda 4121$  and He II  $\lambda 4686$  over He I  $\lambda 4713$ . The first three increase with increasing luminosity (decreasing luminosity class) and the latter increases with decreasing luminosity (increasing luminosity class). All but the Si IV  $\lambda 4116$  over He I  $\lambda 4121$  ratio point to a luminosity class V (the other suggesting a luminosity class III). This is supported by the weak O II spectrum, characteristic of dwarf stars. The  $V$ -band magnitude of the companion star is reported to be  $(15.32 \pm 0.02) \text{ mag}$  by Zaritsky et al. (2004). Along with a distance modulus of  $(18.52 \pm 0.07) \text{ mag}$  (Bonanos et al. 2011) and an  $A_V$  of  $(0.26 \pm 0.02) \text{ mag}$  calculated

using the Galactic column density towards the source of  $(5.8 \pm 0.3) \times 10^{20} \text{ cm}^{-2}$  (Dickey and Lockman 1990a) and the results of Güver and Özel (2009), this leads to an absolute magnitude  $M_V = -3.46 \pm 0.08 \text{ mag}$ , consistent with a B0V star. As such we classify the optical counterpart of Swift J053041.9-665426 as a B0-1.5V star.

### 9.3.3 MACHO light curve

We identified the optical counterpart<sup>1</sup> in the on-line catalogue<sup>2</sup> of the MACHO (MASSIVE Compact Halo Objects) project. The MACHO observations were made using the 1.27-m telescope at Mount Stromlo Observatory, Australia. A dichroic beamsplitter and filters provide simultaneous CCD photometry in two passbands, the  $R_{\text{MACHO}}$  red band (6300 – 7600 Å) and the  $B_{\text{MACHO}}$  blue band (4500 – 6300 Å). The standard MACHO instrumental magnitudes are extracted with SoDoPHOT and are based on point-spread function fitting and differential photometry relative to bright neighbouring stars. SoDoPHOT stands for Son of DoPhot, a revised package based on DoPhot<sup>3</sup> algorithms but optimized to MACHO image data. The SoDoPHOT instrumental magnitude is given as 2.5 times the common logarithm of the integrated number of electrons in the fit to the analytical PSF, divided by 100. MACHO light curves may show systematic variations in brightness due to the different air-mass during individual observations. Additionally, artificial “seasonal rolls” ( $\sim 1 \text{ yr}$  periods) may be a result of the target being observed at progressively higher air-masses as the season progresses. Finally instrumental light curves are affected by observations made from either side of the telescope pier (a German equatorial mount). Thus, stars will alternatively be located on the CCDs rotated by 180 degrees from each other in the focal plane.

In order to use the light curves we need to correct them for the above effects, e.g. the air-mass and the responses of the different CCDs. We followed the analysis of Alcock et al. (1999). In their work they derived corrections for all the instrumental magnitudes based on a statistical analysis of the properties of the detected stars in the MACHO fields of the LMC. But the relations given in their work cannot be applied in a straightforward way to a single star. In particular the coefficients for the air-mass-colour corrections must be derived using separate knowledge of the shape of a light curve (e.g. equations 7 and 8 in Alcock et al. 1999). In order to correct the instrumental light curve, we searched all the parameter space for these coefficients and derived the best solution for a continuous light curve. Finally we transformed the corrected magnitudes to the Johnson V and Cousins R bands. The complete analysis added a systematic uncertainty of  $\sim 0.02 \text{ mag}$  to the light curve.

In Fig. 9.8 we show the light curves for  $R_{\text{MACHO}}$ ,  $B_{\text{MACHO}}$  and the corrected Johnson V magnitude. The  $B_{\text{MACHO}}$  light curve shows evidence for periodicity and both instrumental magnitudes show an outburst at the end of the light curve. The magnitude of the outburst was 0.15 and 0.2 mag in the  $B_{\text{MACHO}}$  and the  $R_{\text{MACHO}}$  filter, respectively. The reddening of the source during the outburst is typical of Be star in the phase of growing the circumstellar disc (de Wit et al. 2006). The  $R_{\text{MACHO}}$  light curve shows several dips up to 0.6 mag, that are more often seen in one of the instrument set-up. These dips are mostly seen during the winter and spring period and

---

<sup>1</sup>Photometry identification number 61:8197:41:64925

<sup>2</sup><http://www.macho.anu.edu.au/>

<sup>3</sup>software: <http://www.astro.puc.cl:8080/astropuc/software-hecho-en-daa>

might be caused by weather conditions, which affect the  $R_{\text{MACHO}}$  filter more. Another characteristic of the dips is that they seem to appear more often in observations at low airmass values  $< 1.25$ . Consequently we believe that these dips are only instrumental artifacts and decided to exclude them from our analysis.

We computed the Lomb-Scargle (LS) periodogram (Scargle 1982) for the light curves of the instrumental magnitudes, excluding the outburst (MJD $>51150$ ). For  $B_{\text{MACHO}}$  we found a period of 373 d which could be artificial as the instrument setup changes approximately every 6 months. For the  $R_{\text{MACHO}}$  we find a period of  $\sim 316$  d. After correcting the instrumental magnitudes, we get a period of  $\sim 390$  d for the V-band light curve with a LS power less than 15. The period is still close to one year. In order to test if all the corrections were done accurately we used the same technique to correct the light curves of other nearby stars. None of the other stars showed a period close to one year or showed a similar light curve. We corrected the light curves of the source by normalising the two data sets obtained by different instrument/pier orientation by their average values, this caused the LS power to fall dramatically. If the period was intrinsic to the sources, we would expect the LS power to rise, not to fall. We would also expect a genuine period to be much more consistent across the different bands. Therefore we conclude that from the light curve we have no clear evidence for the optical period of the optical counterpart of Swift J053041.9-665426, in contrast of what the usage of the uncorrected instrumental data might yield.

## 9.4 Discussion

The X-ray fluxes (see Table 9.1) suggest that Swift J053041.9-665426 was detected during an outburst in Nov. 2011, while the *XMM-Newton* ToO observation was performed at a lower luminosity level. The flux upper limit derived from the ROSAT observation is close to the source luminosity during the *XMM-Newton* ToO observation, suggesting that the non-detection might be explained by high absorption. However, due to the nature of the source, we cannot rule out the possibility that the source was inactive during the ROSAT observation. There are examples of BeXRBs being inactive for a long period before brightening up again (e.g. SAXJ0103.2-7209, Eger and Haberl 2008).

Knowing that the BeXRB population correlates with star formation regions with ages  $\sim 15 - 50$  Myr (Antonioni et al. 2011) it is likely that the system originated from a nearby cluster. Swift J053041.9-665426 is located near the star cluster KMHK 987 at a projected angular distance of  $0.95'$  (see Fig. 9.5). KMHK 987 has a radius of  $0.48'$  and an age of  $\sim 31$  Myr (Glatt et al. 2010). For the case of HMXBs in the SMC a convincing link between the binary systems and near star clusters has been reported, that leads to an average space velocity of these systems arising from a supernova kick (Coe 2005). Assuming a value of 5 Myr for the most likely maximum lifetime of the Be star after the NS has been formed (Savonije and van den Heuvel 1977) we can estimate a lower limit on the runaway velocity imposed to the system by the supernova kick. In our case this leads to a velocity of  $2.6 \text{ km s}^{-1}$ . Knowing that the systems true motion has a random direction to our line of sight the true velocity could be much larger. The true velocity given as function of the angle  $\theta$  between the line of sight and the moving direction of the source is  $u = 2.6 / \sin \theta \text{ km s}^{-1}$ . On a statistical basis this value is smaller than the average velocity reported for BeXRB systems in our galaxy (e.g.

$19 \pm 8 \text{ km s}^{-1}$ , van den Heuvel et al. 2000). A simple explanation could be that the value we used for the time since the creation of the binary is arbitrary and could be much smaller, or that the system could originate from a more distant cluster. Another close cluster NGC 2002, which is even younger with age  $\sim 11 \text{ Myr}$  and is found at a distance of  $2.55'$  ( $\sim 37 \text{ pc}$ ). By doing the same calculations on this cluster we derive a lower limit for the runaway velocity of  $14 \text{ km s}^{-1}$ . Based on the above estimates, Swift J053041.9-665426 could originate from either of those two clusters.

The power-law photon index derived from the EPIC spectra of 0.1–0.8 (depending on the model, and the existence of a black-body component) is on the hard side of the distribution of photon indices of BeXRBs, which has a maximum at  $\sim 0.9 - 1.0$  (Haberl et al. 2008a). A spectral analysis of the available *Swift* data gives a higher index of  $1.7 \pm 0.5$  (Sturm et al. 2011b) and  $1.15 \pm 0.17$  (Sturm et al. 2011c), but in both cases the statistics are much lower than that in the EPIC observation.

The X-ray spectrum is well described with a combination of a power-law and a thermal black-body component, accounting for  $\sim 53\%$  of the flux in the (0.3-10.0) keV band. This soft component has been recently reported in many other BeXRB pulsars (e.g. La Palombara and Mereghetti 2006; Reig et al. 2012). From the parameters of the model, we estimate a black-body radius of  $\sim 800 \text{ m}$  for the emission region (accretion column). This value is in agreement with other persistent HMXBs found in our Galaxy (La Palombara et al. 2013c). In fact we can compare the emission region size with the one estimated by the analysis of Hickox et al. (2004). Assuming standard values for the neutron star mass, radius and magnetic field of  $M_{\text{NS}} = 1.4 M_{\odot}$ ,  $R_{\text{NS}} = 10^6 \text{ cm}$  and  $B_{\text{NS}} = 10^{12} \text{ G}$ , and by using the black-body luminosity derived by the fit we get an estimate of  $\sim 320 \text{ m}$  for the black-body emitting radius. If this description is correct we might expect some variability on the thermal component with the phase of the spin period, that could result in a variable hardness ratio. In the pulse profiles of Swift J053041.9-665426 we see a significant change in the hardness ratio of the harder bands (*HR4*). This behaviour has been well studied in Swift J045106.8-694803, another BeXRB in the LMC (Bartlett et al. 2013b). Unfortunately, for Swift J053041.9-665426 this occurs only for a small time interval and cannot provide good statistics for further investigation of the spectrum.

We note that one should be careful in the interpretation of the two-component model with power-law and black body. Insufficient statistics of the spectral data can lead to strong dependences of the photon index, black-body temperature and absorption column density. For example La Palombara et al. (2009) derive a large negative  $\Gamma$  for RX J1037.5-5647, a known BeXRB pulsar in the Milky Way, when using this model.

Some low strength peaks that are found in the optical periodograms for near one year period can be attributed both to the instrumental setup and weather observing conditions and thus prevent us from deriving a clear periodic behaviour, which could indicate an orbital period.

## 9.5 Conclusions

Analysis of the *XMM-Newton* ToO observation of Swift J053041.9-665426 revealed X-ray pulsations at  $\sim 28.78 \text{ s}$ . The X-ray spectrum is best described by a double component model, composed of an absorbed power law and black body. We have

spectroscopically classified the optical counterpart as a B0-1.5Ve star. The strong IR signal, combined with the clear evidence for significant  $H_\alpha$  emission, points convincingly to the existence of a circumstellar disc as the source of accretion material in the system. The analysis of the optical light curve showed a  $\sim 150$  d burst, but there is no clear optical period found in the two colour light curves. Our results confirm Swift J053041.9-665426 as a [BeXRB](#) with a neutron star primary, making it the 16th known [BeXRB](#) pulsar in the [LMC](#).

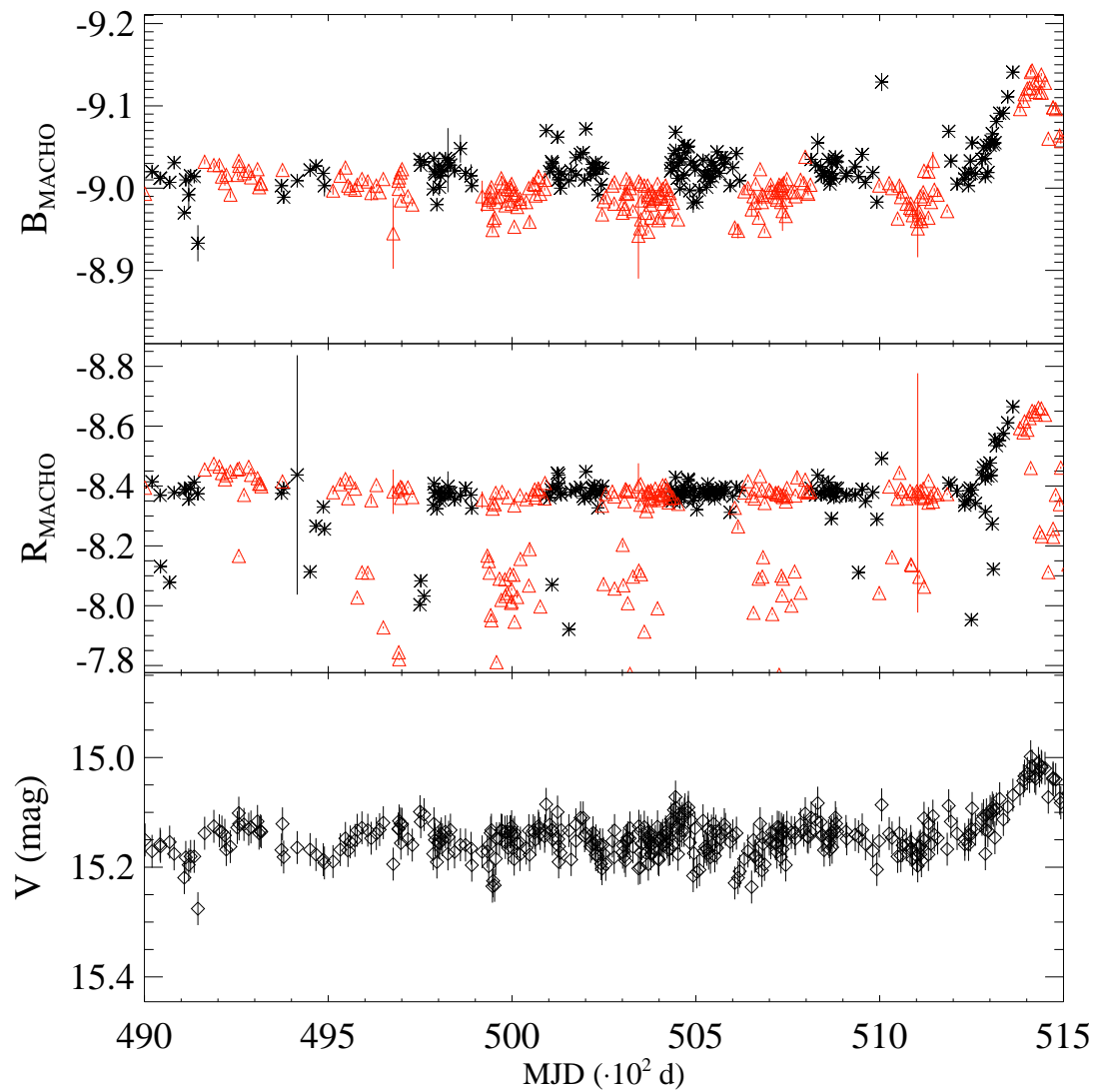


**Figure 9.8:** MACHO light curves for a time period of 2541 days: the “blue”  $B_{\text{MACHO}}$  lightcurve is plotted on the top panel, the “red”  $R_{\text{MACHO}}$  in the middle. In both of them red triangles and black stars indicate instrumental magnitudes taken on different pier setup. The corrected Johnson V magnitude is plotted on the bottom panel.

## LXP 8.04: January 2013 outburst

In this chapter I report on the X-ray and optical properties of a newly confirmed BeXRB in the LMC, RX J0520.5-6932 (Vasilopoulos et al. 2013c). The source was discovered in X-rays by Schmidtke et al. (1994) with the ROSAT HRI. Subsequent ROSAT PSPC observations showed the source to be variable (Haberl and Pietsch 1999). Schmidtke et al. (1994) proposed an O8e star found within the ROSAT 90% error circle as the optical counterpart. Coe et al. (2001) performed optical spectroscopy of the star and determined a spectral type of O9Ve (with one spectral subtype uncertainty). In the same paper, an analysis of the Optical Gravitational Lensing Experiment (OGLE) data revealed a 24.45 d optical periodic modulation of about 0.03 mag. Edge et al. (2004b) confirmed this proposed optical period, based on the analysis of archival data from the Massive Compact Halo Objects (MACHO) project, while also reporting on the presence of an outburst lasting 200 d ( $\sim 0.1$  mag) around March 1995. From the same work, spectroscopic observations of the optical counterpart revealed the presence of a variable H $\alpha$  emission line, with an equivalent width of  $5.2 \pm 0.2$  Å in 2001 November and  $2.0 \pm 0.6$  Å in 2002 December.

The source was later detected by *XMM-Newton* (2XMM J052029.7-693155) in an observation performed on 2004 January 17 (obsid: 0204770101), and in a recent observation performed on 2012 December 5 (obsid: 0690750901), as part of the *XMM-Newton* survey of the LMC (PI: F. Haberl). From the above it is clear that while many of the optical properties of the system have been reported, its X-ray behaviour was still poorly studied until 2013 January, when the source was detected by *Swift*, during the *Swift* UV survey of the LMC (PI: S. Immler), while undergoing a moderately bright X-ray outburst (Vasilopoulos et al. 2013c).

Following the first *Swift* detection, we further monitored the source and triggered an anticipated *XMM-Newton* ToO observation (obsid: 0701990101, PI: R. Sturm) during the observed X-ray maximum flux. In the following paragraphs, I report the results of the spectral and timing analysis of the *XMM-Newton* ToO observation, that resulted in the detection of coherent pulsations and a refined X-ray position. In Section 10.1, I describe the X-ray data reduction and present the results of the spectral and temporal X-ray analysis. From the *Swift* monitoring we had indications that the system experienced several minor X-ray outbursts (possibly type I) that seem to repeat with the optical period of the system. In Section 12.2, I present the updated optical light curve of the counterpart of RX J0520.5-6932. A timing analysis using the combined optical light curve from phase II, III, and IV of the OGLE survey resulted in a refined optical period. In Section 10.3, I discuss the results of the X-ray spectroscopy and summarise the main points that resulted from our analysis.

## 10.1 X-ray observations and data reduction

### 10.1.1 X-ray observations

A *Swift* observation performed on 2013 January 13 as part of the LMC UV survey detected the HMXB candidate RX J0520.5-6932 in a moderately bright X-ray outburst

## 10. LXP 8.04: JANUARY 2013 OUTBURST

---

at a flux of  $1.6 \pm 1.5 \times 10^{-12}$  erg cm<sup>-2</sup> s<sup>-1</sup> (0.3-10 keV). This is significantly brighter compared to the *XMM-Newton* detection on 2012 December 5, which was at a flux level of  $9.5 \pm 1.5 \times 10^{-14}$  erg cm<sup>-2</sup> s<sup>-1</sup> (EPIC-pn: 0.3-10 keV). Following the *Swift* detection we started to monitoring RX J0520.5-6932 with *Swift* to study the ongoing event that revealed a high X-ray variability of the source. After the proceeding rise of the source luminosity we triggered an *XMM-Newton* ToO observation that was performed on 2013 January 22. We continued the *Swift* monitoring after the decline of the outburst, to study its long-term X-ray variability, and to search for a possible correlation between the X-ray and optical light curve. In total we acquired 22 *Swift*/XRT pointings, with a typical exposure of 2000 s (flux limit at  $\sim 5 \times 10^{-13}$  erg cm<sup>-2</sup> s<sup>-1</sup>) within 130 days. Apart from the data collected from our monitoring, additional six *Swift*/XRT fields from other surveys, that covered the position of RX J0520.5-6932, were used in our analysis.

Regarding the *Swift*/XRT data reduction, we downloaded the data from the **Swift Data Center**<sup>1</sup>. We estimated the source count rates by using the **HEASoft**<sup>2</sup> task **ximage**, correcting for the vignetting and background effects, while we used the **uplimit** task to estimate upper limits for the non-detections. For the brightest detections (>100 counts) we created X-ray spectra. For the spectral extraction we used the **HEASoft** task **xselect** and circular regions with radius 35'' for the source and 300'' for the background.

In the *XMM-Newton* ToO observation, the source was located on CCD4 of the EPIC-pn (Strüder et al. 2001) and on CCD1 of both the EPIC-MOS (Turner et al. 2001) detectors. *XMM-Newton* SAS 13.0.1<sup>3</sup> was used for data processing. The background stayed at a low level for almost all the observing time and we excluded less than 2 ks of exposure due to a moderate flare seen in the EPIC-pn detector. We used a background threshold of 8 and 2.5 counts ks<sup>-1</sup> arcmin<sup>-2</sup> for the EPIC-pn and EPIC-MOS detectors, respectively. This resulted in net exposure times of 16.8/20.3/20.3 ks for EPIC-pn/MOS1/MOS2 after flare removal. The event extraction was performed using a circle around the source while the background events were extracted from a point-source free area on the same CCD but on different pixel columns for EPIC-pn. We optimised the size of the source extraction area using the SAS task **eregionanalyse**. For the EPIC-pn spectra and light curves, we selected single-pixel and double-pixel events (**PATTERN**≤4) while in the case of EPIC-MOS we used single to quadruple events (**PATTERN**≤12). The quality flag **FLAG** = 0 was used throughout. The SAS task **especget** was used to create the spectra and response files for the spectral analysis. The spectra were binned to achieve a minimum signal-to-noise ratio of five for each bin.

### 10.1.2 X-ray position

The position of RX J0520.5-6932 was determined from the *XMM-Newton* ToO observation that provided the best statistics. X-ray images were created from all the EPIC cameras using the *XMM-Newton* standard energy sub-bands (Watson et al. 2009). Source detection was performed simultaneously on all the images using the SAS task

---

<sup>1</sup><http://swift.gsfc.nasa.gov/sdc/>

<sup>2</sup><http://heasarc.nasa.gov/lheasoft/>

<sup>3</sup>Science Analysis Software (SAS), <http://xmm.esac.esa.int/sas/>

`edetect_chain`. Boresight correction was performed on the images based on the position of five identified background X-ray sources in the field. The positional correction based on these sources was found to be  $\sim 1''$ . The final source position was determined to R.A. =  $05^{\text{h}}20^{\text{m}}29.^{\text{s}}99$  and Dec. =  $-69^{\circ}31'55''.3$  (J2000), with a  $1\sigma$  statistical uncertainty of  $0.05''$ . The total  $1\sigma$  positional error, however is determined by the remaining systematic uncertainty assumed to be  $0.5''$  (see section 4.3 of [Sturm et al. 2013a](#)).

### 10.1.3 Timing analysis

We used the SAS task `barycen` to correct the *XMM-Newton* EPIC event arrival times to the solar-system barycentre. To increase the signal-to-noise ratio we created time series from the merged event list of EPIC-pn and EPIC-MOS for the common good-time intervals. We used the HEASoft task `powspec` to search the X-ray light curve (0.2 – 10 keV) for periodicities. In Fig. 10.1, we present the inferred power density spectrum with a strong peak at the main period and its first harmonic. To improve the result of our initial estimation, we followed [Haberl et al. \(2008a\)](#). By using a Bayesian periodic signal detection method ([Gregory and Loredo 1996](#)) we determined the pulse period with a  $1\sigma$  uncertainty to 8.035331(15) s. Following the nomenclature introduced by [Coe et al. \(2005\)](#) for the BeXRB pulsars in the SMC we suggest the alternative name of LXP 8.04 for the system in the LMC.

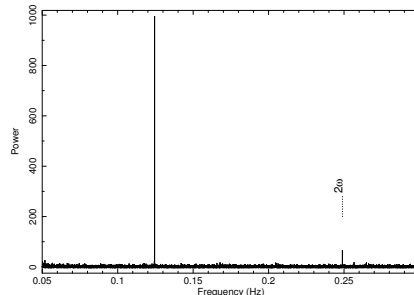


**Figure 10.1:** Power density spectrum created from the merged EPIC-pn and EPIC-MOS data in the 0.2–10.0 keV energy band. The time binning of the input light curve was 0.01 s. The best-fit frequency  $\omega \sim 0.12445$  Hz and its first harmonic are easily distinguished in the plot.

By using the 5 standard energy bands (0.2–0.5, 0.5–1.0, 1.0–2.0, 2.0–4.5, 4.5–10 keV) we defined 4 HRs. The period-folded pulse profiles in the EPIC standard energy bands together with the hardness ratios derived from the pulse profiles in two adjacent energy bands are plotted in Fig. 10.2. To achieve better statistics, the first two energy bands were combined in the top left panel, while the bottom panel shows all five energy bands combined.

From the HR diagrams, it is evident that the pulse behaves differently in the soft and hard X-ray bands. The source becomes first harder (see HR3, HR4 at phase  $\sim 0.3$ – $0.6$ ) in the hard X-ray bands and after the pulse maximum, it becomes harder in the soft X-rays (see HR2). To further investigate this behaviour we created X-ray spectra for different phase intervals.

### 10.1.4 Spectral analysis

The spectral analysis was performed with `xspec` ([Arnaud 1996](#)) version 12.8.0. The high number of counts enabled us to use  $\chi^2$  statistics in the fitting procedure. The *XMM-Newton*/EPIC spectra were fitted simultaneously using the same model parameters with an additional scaling factor to account for instrumental differences. For the EPIC-pn we fixed the scaling factor at 1 while for both EPIC-MOS we obtained values of  $C_{MOS1} = 1.03 \pm 0.03$  and  $C_{MOS2} = 1.00 \pm 0.03$ , which is consistent with the expected values, as EPIC-MOS is known to provide  $\sim 5\%$  higher fluxes than EPIC-

## 10. LXP 8.04: JANUARY 2013 OUTBURST

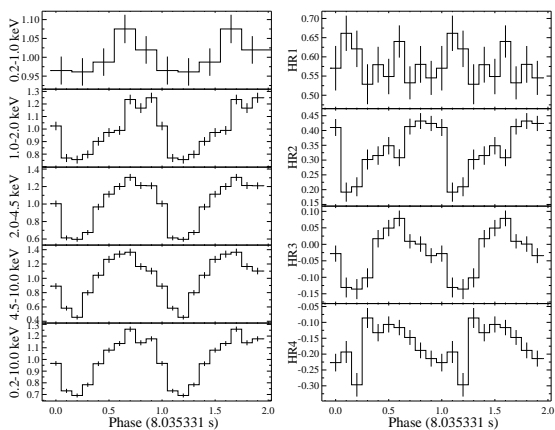


**Figure 10.2:** Left: Pulse profiles obtained from the merged EPIC data in different energy bands ( $P=8.035331$  s). All the profiles are background-subtracted and normalised to the average count rate (0.276, 0.454, 0.438, 0.311, 1.48  $\text{cts s}^{-1}$ , from top to bottom). Right: Hardness ratios as a function of pulse phase derived from the pulse profiles in two neighbouring standard energy bands.

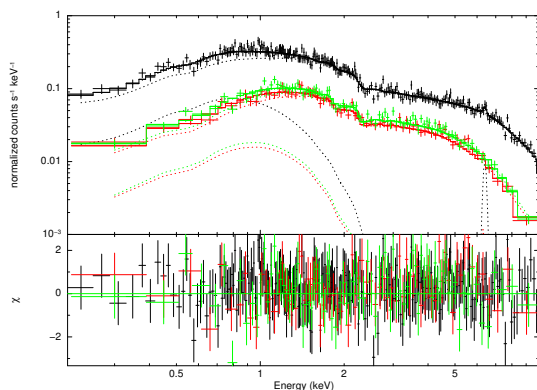


**Figure 10.3:** Pulse-phase averaged EPIC spectra of RX J0520.5-6932. The top panel shows the EPIC-pn (black), EPIC-MOS1 (red) and EPIC-MOS2 (green) spectra, together with the best-fit model (solid lines) composed by an absorbed power law with photon index of 0.83, a black body with  $kT=0.24$  keV (dotted lines) and a Gaussian line at 6.4 keV. The residuals for this model are plotted on the bottom panel.

pn (see [Stuhlinger et al. 2006](#), or the latest version of the *XMM-Newton* calibration manual<sup>1</sup>). The photo-electric absorption was modeled as a combination of Galactic foreground absorption and an additional column density accounting for both the interstellar medium of the LMC and the intrinsic absorption by the source. The Galactic photo-electric absorption was set to a column density of  $N_{\text{H,GAL}} = 6.44 \times 10^{20} \text{ cm}^{-2}$  ([Dickey and Lockman 1990a](#)) with abundances according to [Wilms et al. \(2000\)](#). The LMC-intrinsic column density  $N_{\text{H,LMC}}$  was left as a free parameter with abundances of 0.49 for elements heavier than helium ([Rolleston et al. 2002](#)). All the uncertainties were calculated based on a  $\Delta\chi^2$  statistic of 2.706, equivalent to a 90% confidence level for one parameter of interest.

The pulse-phase averaged spectra were first fitted with an absorbed power law, resulting in a reduced  $\chi^2_{\text{red}} = 0.95$ . We further tested models typically applied to the spectra of BeXRBs. In particular from the residuals of the fitted power-law model, there is evidence that adding a soft energy component ( $\sim 1$  keV) would improve the fit. The overall fit quality was marginally improved by the use of the `mekal` (thermal component based on emission from optically thin plasma), `bbody` or `diskbb` (emission from an accretion disc consisting of multiple black-body components) models available in `xspec`. The tested models with their best-fit parameters are summarised in Table 10.1. However, all the thermal models improved the residuals at energies around 1 keV. The combination of a power-law and a black-body component provided two different solutions with similar residuals. The first solution described a black body that mainly

<sup>1</sup>[http://xmm2.esac.esa.int/external/xmm\\_sw\\_cal/calib/cross\\_cal/](http://xmm2.esac.esa.int/external/xmm_sw_cal/calib/cross_cal/)

contributed to the softer X-rays, while the second solution (hereafter BBrad2) provided a black body of higher temperature ( $kT \sim 2.8$  keV) that contributed most of the flux at higher energies. The photon index of the power law for all the tested models was between 0.8 and 0.9 (apart from model BBrad2), which falls within the typical range of 0.6 to 1.4 as reported by Haberl et al. (2008a). The EPIC-pn data provide an indication of an emission line close to 6.4 keV. The line was fitted with a Gaussian profile ( $E=6.4\pm 0.1$  keV,  $\sigma \sim 0$ ) with equivalent width of  $50 \pm 30$  eV. The best-fit power-law model with the contribution of the low-temperature black body and the Fe line is shown in Fig.10.3.

Given the variations in the HR diagrams (see Fig. 10.2) we continued performing phase-resolved spectroscopy using 5 phase bins. This was achieved with the use of the SAS task `phasecalc`, with zero phase defined as the date of the observation (MJD: 56314.0), the same as used in Fig.10.2. For the phase-resolved analysis we used only the EPIC-pn data, because the frame time of the EPIC-MOS cameras is larger than the duration of each phase bin. The phased-resolved spectra were again fitted with a single power-law and power-law plus thermal component models.

It should be noted that the addition of the thermal component did not always improve the fit without producing unphysical parameters (e.g. black-body temperature of  $>100$  keV). Given this behaviour we used a model with the same absorption for the five phases, linked the temperature of the thermal component and the power-law photon index, and let their normalisations vary. In Fig.10.4 we plot the normalisation, therefore the strength, of each component versus the spin phase. The black-body component significantly contributes to the total flux during the first two phase bins (consistent with the worse fit quality found for the single power-law fit). The variation of the black-body intensity appears to be anti-correlated with that of the power-law component, although formally also a constant black-body flux can not be excluded. When additionally allowing the absorption to vary with phase we note a similar behaviour of the normalisations. Again, there is some indication for a changing column density, but one more free fit parameter increases the errors on the individual parameters further, not allowing any firm conclusion about which parameters are principally variable. Following the detection of an emission line near 6.4 keV in the phase-averaged spectrum, we searched the phased spectra for similar features (see Table 10.1). Because of the lower statistics in the phased-resolved spectra, we tested the significance of the line by fitting the model with a Gaussian line with zero width, stepping the line energy between 2 and 9 keV (100 steps), for all the phased-resolved spectra. The derived equivalent widths of the fitted lines were always less than 60 eV, except close to 6.4 keV. At centroid energies near 6.4 keV the equivalent width of the line exceeded 60 eV in two spectra (phase 0.2-0.4 and 0.6-0.8) suggesting a variation of the line intensity with pulse phase.

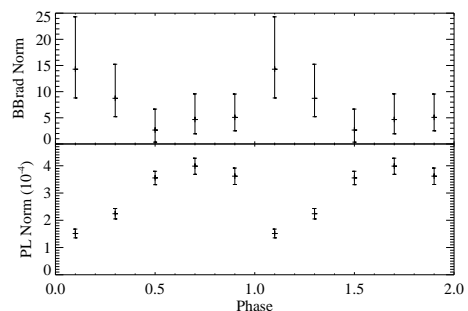


**Figure 10.4:** Best fit values of the normalisation parameters derived from phase-resolved spectroscopy. The absorption values were assumed to be constant. Error bars indicate the 90% confidence level.

## 10. LXP 8.04: JANUARY 2013 OUTBURST

Model <sup>a</sup>	LMC N <sub>H</sub> [10 <sup>20</sup> cm <sup>-2</sup> ]	Γ	Norm <sup>b</sup> [10 <sup>-4</sup> ]	kT [keV]	Norm	-	χ <sub>red</sub> <sup>2</sup> /dof <sup>c</sup>
PL	3.4 ± 1.0	0.925 ± 0.020	3.52 ± 0.09	–	–	–	0.953/975
PL+DiskBB	8.3 <sup>+3</sup> <sub>-2.4</sub>	0.83 ± 0.04	3.05 <sup>+0.19</sup> <sub>-0.21</sub>	0.33 <sup>+0.08</sup> <sub>-0.07</sub>	1.1 <sup>+2</sup> <sub>-0.7</sub>	–	0.917/973
PL+BBrad <sup>d</sup>	5.3 <sup>+2.4</sup> <sub>-1.9</sub>	0.83 ± 0.04	3.05 ± 0.18	0.24 ± 0.04	4.6 <sup>+5</sup> <sub>-2.1</sub>	–	0.914/973
PL+BBrad2 <sup>d</sup>	10.3 <sup>+2.6</sup> <sub>-2.4</sub>	1.35 ± 0.13	3.82 <sup>+0.16</sup> <sub>-0.15</sub>	2.82 <sup>+0.4</sup> <sub>-0.26</sub>	0.007 ± 0.003	–	0.917/973
PL+mekal	3.65 <sup>+1.1</sup> <sub>-1.0</sub>	0.86 ± 0.03	3.20 <sup>+0.14</sup> <sub>-0.13</sub>	1.04 ± 0.3	9.9 <sup>+5</sup> <sub>-3</sub> × 10 <sup>-5</sup>	–	0.924/973
PL+Gauss <sup>e</sup>	LMC N <sub>H</sub> [10 <sup>20</sup> cm]	Γ	Norm 10 <sup>-4</sup>	kT <sub>BB</sub> keV	Norm	Gauss <sup>f</sup> keV/eV	χ <sub>red</sub> <sup>2</sup> /dof
0.0-0.2	3.55 ± 0.02	1.20 ± 0.05	2.86	–	–	~0	1.47/129
0.2-0.4	~ 0	0.88 ± 0.04	2.63	–	–	6.38/227	1.14/160
0.4-0.6	1.76 ± 0.02	0.75 ± 0.04	3.32	–	–	6.38/50	1.11/202
0.6-0.8	4.96 ± 0.02	0.89 ± 0.04	4.34	–	–	6.38/97	1.07/210
0.8-1.0	9.42 ± 0.03	1.02 ± 0.05	4.65	–	–	~0	1.16/181
PL+BBrad <sup>g</sup>	LMC N <sub>H</sub> [10 <sup>20</sup> cm]	Γ	Norm 10 <sup>-4</sup>	kT <sub>BB</sub> keV	Norm	Radius <sup>h</sup> km	χ <sub>red</sub> <sup>2</sup> /dof
0.0-0.2	4.5 <sup>+2.4</sup> <sub>-1.9</sub>	0.83±0.05	1.51±0.16	0.24±0.03	14.3 <sup>+10</sup> <sub>-6</sub>	18.9	1.19/534
0.2-0.4	=	=	2.24±0.19	=	8.7 <sup>+7</sup> <sub>-4</sub>	14.8	
0.4-0.6	=	=	3.55±0.25	=	2.7 <sup>+4</sup> <sub>-2.3</sub>	8.2	
0.6-0.8	=	=	3.99±0.3	=	4.7 <sup>+5</sup> <sub>-2.7</sub>	10.8	
0.8-1.0	=	=	3.62±0.3	=	5.1 <sup>+5</sup> <sub>-2.6</sub>	11.3	
0.0-0.2	0.53 <sup>+4.1</sup> <sub>-0.53</sub>	0.80±0.05	1.41 <sup>+0.18</sup> <sub>-0.08</sub>	0.276 <sup>+0.03</sup> <sub>-0.04</sub>	7.5 <sup>+7.5</sup> <sub>-2.2</sub>	13.7	1.19/530
0.2-0.4	1.0 <sup>+4.2</sup> <sub>-0.99</sub>	=	2.13 <sup>+0.21</sup> <sub>-0.19</sub>	=	4.4 <sup>+4.9</sup> <sub>-1.5</sub>	10.5	
0.4-0.6	1.7 <sup>+3.1</sup> <sub>-1.7</sub>	=	3.44 <sup>+0.27</sup> <sub>-0.27</sub>	=	0.87 <sup>+2.3</sup> <sub>-0.87</sub>	4.7	
0.6-0.8	4.3 <sup>+3.3</sup> <sub>-2.6</sub>	=	3.8 ± 0.3	=	3.5 <sup>+3.9</sup> <sub>-2.0</sub>	9.3	
0.8-1.0	6.15 <sup>+3.6</sup> <sub>-2.9</sub>	=	3.4 ± 0.3	=	4.8 <sup>+3.9</sup> <sub>-2.0</sub>	11.0	

**Table 10.1:** Spectral fit results.

### 10.1.5 X-ray long-term variability

From the spectral analysis of the *XMM-Newton* [ToO](#) observation of RX J0520.5-6932, we calculated a flux of  $6.00^{+0.2}_{-0.16} \times 10^{-12}$  erg cm<sup>-2</sup> s<sup>-1</sup> in the 0.3–10.0 keV band. This translates into an absorption corrected luminosity of  $1.79 \times 10^{36}$  erg s<sup>-1</sup> for a distance to the [LMC](#) of 49 kpc ([Inno et al. 2013](#)). During the *XMM-Newton* observation performed on 2004 January 17, the source was located over a gap of the EPIC-pn camera and near bad columns of the EPIC-MOS cameras and was marginally detected at a flux level of  $2.15 \times 10^{-14}$  erg cm<sup>-2</sup> s<sup>-1</sup>. Based on the *XMM-Newton* observations we estimate a long-term X-ray variability factor of at least 280 for RX J0520.5-6932. Both the lowest and highest fluxes have been measured from *XMM-Newton* observations, while the *Swift* flux was always between these two values. The ROSAT measured flux was near the *XMM-Newton* [ToO](#) value, however it does not provide any additional constraints, given that the two observatories cover different energy bands and that the photo-electric absorption will have a large effect on the soft ROSAT energy band which may introduce large systematic uncertainties.

## 10.2 Analysis and results of optical data

### 10.2.1 Optical counterpart

The most accurate X-ray position of RX J0520.5-6932 was derived from *XMM-Newton* ToO data (Sect. 10.1.1). Within the  $3\sigma$  error circle we found a  $V=14.12$  mag star as only likely counterpart at a distance of  $\sim 0.8''$  to the X-ray position. This star is included in the 2MASS catalogue (2MASS J0520299-6931559). This confirms the previously suggested counterpart by Schmidtke et al. (1994), as the real companion of RX J0520.5-6932.

### 10.2.2 OGLE light curve

In the present work, we used the OGLE I and V band magnitudes for the counterpart of RX J0520.5-6932 that were taken before MJD=56600 (see Table 10.2). The latest I band light curve is seen in Fig. 10.6, where the different OGLE phases have been normalised to the same mean value to account for calibration offsets. The data can be downloaded from the OGLE-IV real time monitoring of X-ray sources web-page<sup>1</sup>.

From the different OGLE data sets of the I band magnitudes we computed periodograms by using the Lomb-Scargle (LS) algorithm (Scargle 1982; Horne and Baliunas 1986). We searched for periodicities up to half of the total OGLE observing period, which at the time of the analysis was  $\sim 5851$  d. Since the LS algorithm does not determine the period error, we use the bootstrap method to estimate the period uncertainties. A random sampling is drawn from the light curve (one epoch can be drawn multiple times) and the period for that sampling is determined with the LS algorithm. This procedure is performed 1000 times for each light curve (OGLE phase), so that the  $1\sigma$  uncertainty can be determined from the resulting distribution. Based on the combined OGLE data, we derived a new improved period of  $24.4302 \pm 0.0026$  d for the optical counterpart, while the average luminosity level was nearly constant for the last 15 years (variability less than 0.1 mag). By analysing the available V band data we found a similar period (24.22 d).

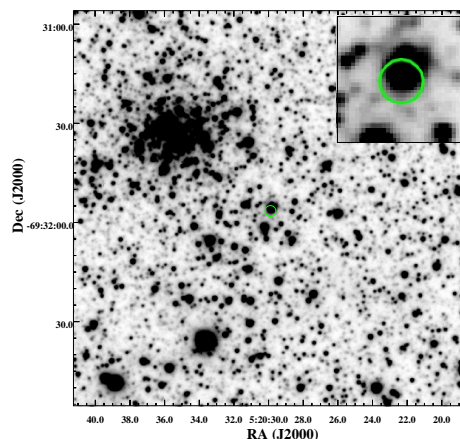


**Figure 10.5:** Finding chart of RX J0520.5-6932. The image is a product of the OGLE project. The  $3\sigma$  X-ray positional uncertainty is marked with a green circle. On the upper left part of the image, we find the star cluster NGC 1926, at a distance of  $\sim 0.64'$ .

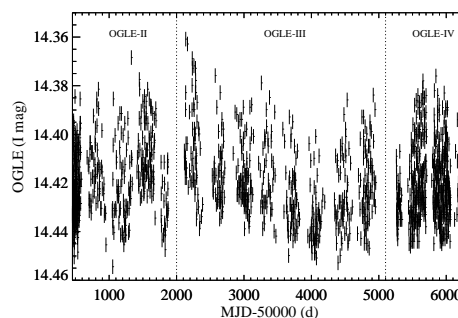


**Figure 10.6:** OGLE I band light curve of RX J0520.5-6932. Data from different OGLE phases are separated with vertical lines.

<sup>1</sup>XROM: <http://ogle.astrow.edu.pl/ogle4/xrom/xrom.html>

## 10. LXP 8.04: JANUARY 2013 OUTBURST

We also analysed the I band data from the three different **OGLE** phases separately, to search for possible differences between them. This resulted in the detection of slightly different periods for the three **OGLE** phases. We also detected short periodicities with values 1.04 d, 0.958 d, 0.509 d and 0.49 d which can be associated to the 0.5 and 1 day aliases of the 24.43 d period ( $1/(0.5^{-1} \pm 24.43^{-1})$  and  $1/(1^{-1} \pm 24.43^{-1})$ ) and are not associated with the NRP phenomenon. When analysing the complete I band light curve from the three available **OGLE** phases we found an indication of a long period of  $\sim 706.9$  d. Such super-orbital periods have been reported from other **BeXRB** systems in the MCs and they might be related to the formation and depletion of the circumstellar disc around the Be star (Rajolimanana et al. 2011). The results of our temporal analysis are listed in Table 10.2. For the period where both I and V band measurements are available we are able to follow the evolution of the colour of the counterpart of RX J0520.5-6932. To calculate the I-V colour we used only the measurements less than one day apart. In Fig. 10.7 we present the folded light curve for the **OGLE** I and V band magnitudes and the V-I colour of the optical counterpart of RX J0520.5-6932. In Fig. 10.8 we present the colour magnitude diagram for the period between 55260 and 56600 (MJD).

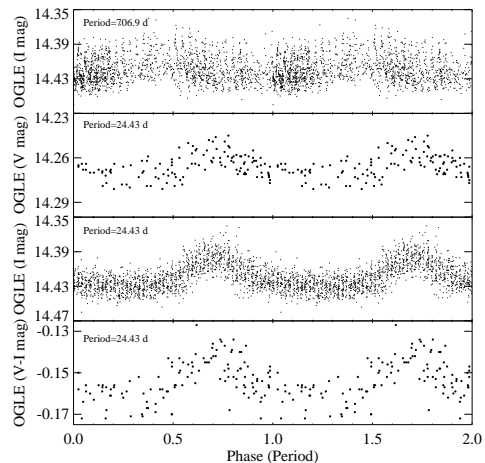


**Figure 10.7:** **OGLE** I band, V band and V-I light-curve profiles, folded for a period of 24.43 d and 706.9 d. The I band curve consists of data from phases II, III and IV, while the V band we only had data from phase IV. All the data are folded using as a zero-phase the first available **OGLE** data point (MJD:  $\sim 50455.67$ ).

OGLE <sup>a</sup>	Data points	Period (d)	Power <sup>b</sup>
I band			
II	510	24.440 $\pm$ 0.011	117
III	489	24.421 $\pm$ 0.006	97
IV	590	24.367 $\pm$ 0.018	149
Total	1589	24.4302 $\pm$ 0.0026	350
		706.9 $\pm$ 3	60
V band			
IV	127	24.22 $\pm$ 0.04	26.6

**Table 10.2:** **OGLE** data for the optical counterpart of RX J0520.5-6932.

### 10.3 Discussion

Analysing the EPIC data of our *XMM-Newton* **ToO** observation of RX J0520.5-6932, performed on 2013 January 22 during the maximum of a type I outburst, we detected coherent X-ray pulsations with a period of 8.035331(15) s ( $1\sigma$ ). During the outburst,

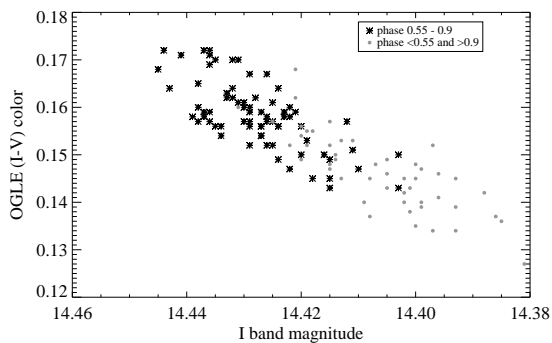


**Figure 10.8:** Colour magnitude diagram of RX J0520.5-6932. The *OGLE* data are divided into two groups according to the phase derived from the 24.43 d period.

the X-ray spectrum is fitted best by an absorbed power law ( $\Gamma = 0.83$ ) plus a low-temperature black-body ( $kT \sim 0.24$  keV) model. From phase-resolved spectroscopy, we found that the spectral shape changes with spin phase. This modulation can be successfully modelled by the same model used for the phase-averaged spectrum, but with normalisations for the different components that vary with phase.

It has been suggested that the presence of a soft spectral component is a common feature intrinsic to X-ray pulsars, which is related to the total luminosity of the source (Hickox et al. 2004). For sources with higher luminosity ( $L_X > 10^{38}$  erg s $^{-1}$ ) it could be a result of reprocessed hard X-rays from the neutron star by optically thick accreting material. While in less luminous sources ( $L_X < 10^{36}$  erg s $^{-1}$ ), a soft excess could be due to emission by photoionised or collisionally heated gas or thermal emission from the surface of the neutron star. Either or both of these types of emission can be present for sources with intermediate luminosity.

In the last decade, a thermal soft excess has been detected in a number of *BeXRB* pulsars. In several persistent systems, with luminosities between  $10^{34}$  erg s $^{-1}$  and  $10^{36}$  erg s $^{-1}$ , the X-ray spectra can be fitted by a power law and a black body with temperature values between 1.1 and 1.8 keV (e.g. La Palombara et al. 2013c; Bartlett et al. 2013a). Some other systems, commonly observed during outburst, also show evidence of thermal emission but with much lower temperatures around 0.3 keV (e.g. Haberl and Pietsch 2008; Sturm et al. 2011a). In the case of RX J0520.5-6932, we note that the system was observed during an outburst, therefore we tried to test thermal models with a larger range in temperature. We find that although, a black-body component of  $\sim 2.8$  keV yields an acceptable fit quality (see PL+BBrad2 in Table 10.1), it also produces some questionable properties for the system. In the case of the higher temperature black-body model, the power-law component accounts for the softer X-rays and the black-body component contributes the majority of the flux at high energies, which is difficult to explain by heating or reprocessing effects.

The change in the normalisations of the power-law and black-body components with spin phase might be explained by a simple picture. First, the maximum radius ( $\sim 20$  km) of the black-body emission region argues against a hot spot on the neutron stars surface. More likely it could be a region in the inner part of an accretion disk. If we imagine that the accretion column originating from the disc and terminating on the *NS* surface, depending of the geometry of the system with respect to the observer, it might be possible for the accretion column to partially obscure the *NS* and/or the inner part of the accretion disk. However, in order to deeper study this behaviour

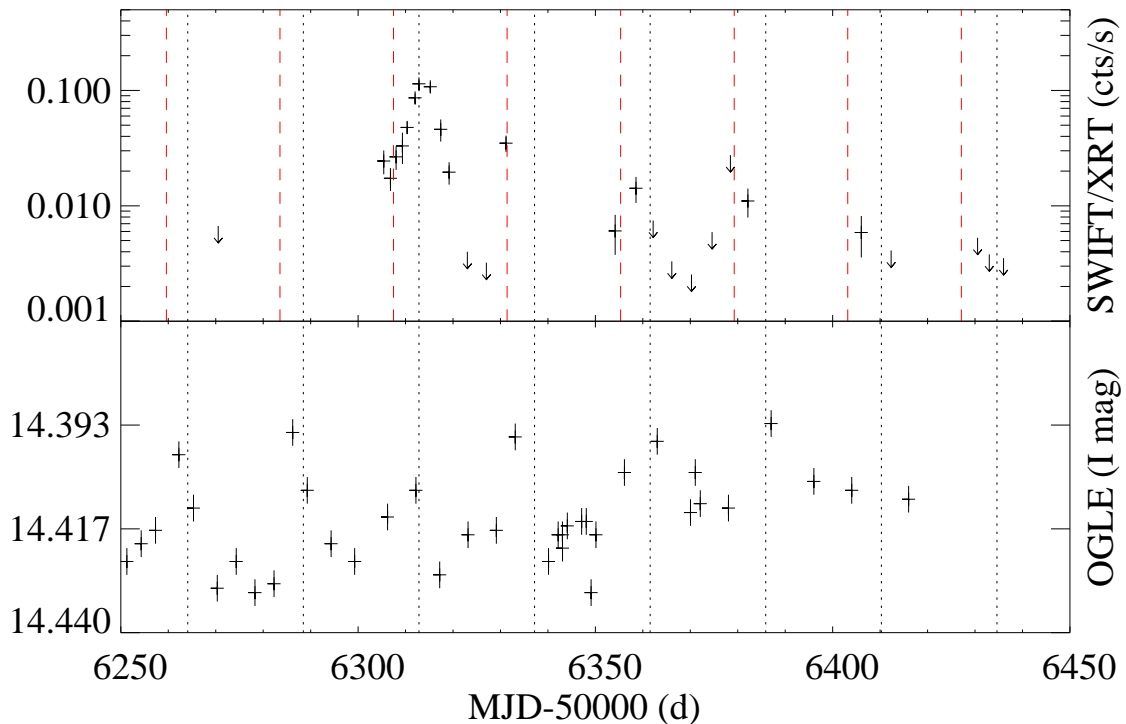


**Figure 10.9:** Optical and X-ray light curve of RX J0520.5-6932. Top panel: *Swift*/XRT count rates (0.3–10 keV band),  $2\sigma$  upper limits are plotted with arrows. The vertical black dotted lines represent the 24.43 d optical period phased on the detected X-ray maximum, while the red dashed lines are spaced based on the 23.93 d orbital solution of [Kuehnel et al. \(2014\)](#) (phased at the mean  $T_{90}$  time). Bottom panel: OGLE-IV I band optical light curve.

observations with better statistics are required.

A total X-ray long-term variability factor of  $\sim 280$  was derived from the available *XMM-Newton* observations of RX J0520.5-6932. In Fig. 10.9, we present the X-ray light curve from our *Swift* monitoring together with the optical I-band light curve from the same period. The *Swift*/XRT fluxes (detections and upper limits) are all within the range found from the *XMM-Newton* observations. There is evidence for three additional outbursts after the first one, these events seem to follow the periodic behaviour of the optical counterpart and the  $\sim 24.4$  d period. Unfortunately, the available X-ray coverage does not allow to make this case stronger.

In Fig. 10.7, we show that a periodic behaviour is seen in both the I and V band light curve as well as in the V-I colour. The colour periodicity is also translated as a larger variability in the I than in the V band magnitude. In Fig. 10.8 we show the evolution of the colour of the optical counterpart of RX J0520.5-6932 during an approximately three year period. From the relative positions of the data points from different phases, it can be seen that the colour of the system correlates well with its luminosity, being redder when brighter. In similar studies concerning the optical properties of Be stars, a colour magnitude variability pattern that follows an anticlockwise path in the colour magnitude diagram (same axes as Fig. 10.8) has been reported (e.g. [de Wit et al. 2006](#);

Coe et al. 2012). Rajoelimanana et al. (2011) studied the colour magnitude diagrams of 31 BeXRB systems finding that only 4 or 5 of them become bluer when brighter. They proposed that this is related with the orientation by which we observe the system, concluding that in systems with bluer-brighter relation the decretion disc obscures the Be star, while the redder-brighter relation describes a system where the disc is observed face-on.

In almost all these studies the systems showed a much higher variability in their magnitudes and exhibit some kind of sharp outburst rather than the case of a flat light curve of RX J0520.5-6932. In systems like XMMUJ010743.1-715953 (Coe et al. 2012) the colour magnitude evolution pattern presumably reflects the growth of the disc as a large cooler component of the Be star. In the case of RX J0520.5-6932 we clearly see that this colour-magnitude relation does not reflect the complete loss and build up of the disc, since we only see a periodic variability of the magnitude with small amplitude. This behaviour indicates that a similar, although less intense, disc evolution happens within the orbital period of the system and is most likely related to the NS motion. The NS orbiting the Be star is perturbing the decretion disk, likely via tidal truncation (Okazaki and Negueruela 2001), resulting in an increased emission from the redder component of the system (e.g. cooler disk).

Kuehnel et al. (2014) have recently analysed the pulse-period evolution provided by the GBM (Fermi Gamma-ray Burst Monitor) pulsar project to derive the orbital parameters of the binary system by modeling the Doppler shift due to the orbital motion. Including a luminosity-dependent intrinsic spin-period derivative, they found an orbital solution with a period of  $23.93 \pm 0.07$  d, a projected semi-major axis of  $a \sin i = 107.6$  ls, an eccentricity  $e = 0.0286$  and the time at which the delay in the arrival of the pulse is maximized  $T_{90} = 2456666.91$ (JD). This period is significantly shorter than the period derived from the OGLE photometry, but should be considered as the most accurate solution for the orbital motion of the binary. By using Kepler's 3<sup>rd</sup> law (neglecting the small eccentricity) and typical values for the masses of the system (1.4 and  $23 M_{\odot}$ , Vacca et al. 1996), we estimate the actual orbit of the system to be  $\sim 2.3$  times larger than the projected semi-major axis. That suggests that the orbital plane of the NS has an inclination of about  $26^{\circ}$  (where  $0^{\circ}$  indicates a face-on system).

It is not uncommon for BeXRB systems to exhibit small differences in the periods derived from the optical and from pulse timing. Townsend et al. (2011) reported that for two SMC pulsars, SXP2.37 and SXP6.85. Their orbital periods derived from pulse timing are smaller than the optical (by 0.22 d and 3.9 d respectively). A likely explanation for this difference is that the variability in the optical data is a combined product of two motions, the Keplerian orbit of the NS around its massive companion and the rotation of the circumstellar disk. In Table 10.2 we see that the periodicity values derived from OGLE phases II and IV are statistically different ( $3.5 \sigma$ ). This might be a result of small changes in the rotation speed or matter distribution of the decretion disk. The observed outbursts in the optical might be a combined result of the co-rotation of the Be disc in the same direction with the NS orbit, and inhomogeneities in the disk. Inhomogeneities are known from cyclic variations observed in emission line profiles of other systems. Okazaki (1991), explained these variations as a result of one armed oscillations in the equatorial disks of the Be stars. Rajoelimanana et al. (2011) confirmed that the long-term variation in the optical light curves of BeXRB systems is

related to the behaviour of the Be circumstellar disk. From the [OGLE](#) light curve of the optical counterpart of RX J0520.5-6932, there is evidence for a super-orbital period. Both the amplitudes of this long-term periodicity and the total variability of the source, are even smaller than the variability within the orbital period. This suggests a Be disc observed nearly face on, consistent with what we derived above.

Knowing that the [BeXRB](#) population correlates with star-formation regions with young ages it is likely that the system originated from a nearby cluster. RX J0520.5-6932 is located near the star cluster NGC 1926 at a projected angular distance of  $0.65'$  (see Fig. 10.5). NGC 1926 has an age of  $31_{-14}^{+30}$  Myr ([Popescu et al. 2012](#)). For the case of [BeXRBs](#) in the SMC a convincing link between the spatial position of the binary systems and near young star clusters has been reported by [Coe \(2005\)](#). Their analysis leads to an average space velocity of  $\sim 30$  km s $^{-1}$  for the binary systems which is proposed to arise from a supernova kick. Assuming a value of 5 Myr for the most likely maximum lifetime of the Be star after the [NS](#) has been formed ([Savonije and van den Heuvel 1977](#)) we can estimate a lower limit for the runaway velocity imposed to the system by the supernova kick. In our case this leads to a velocity of 1.8 km s $^{-1}$ . Knowing that the systems true motion has a random direction to our line of sight the true velocity could be larger. On a statistical basis this value is smaller than the average velocity reported for [BeXRB](#) systems in the SMC, or in our galaxy (e.g.  $19 \pm 8$  km s $^{-1}$ , [van den Heuvel et al. 2000](#)). An independent argument in favour of the small kick velocity is the small eccentricity of the binary system.

RX J0520.5-6932 adds to the important sample of [BeXRBs](#) with known spin period, orbital period and eccentricity. The spin and orbital periods are consistent with the Corbet relation ([Corbet 1984](#)) and the low eccentricity of the system is expected for systems with small spin periods ([Knigge et al. 2011](#)). According to their interpretation, [BeXRB](#) could originate from two different types of supernova progenitors, with electron-capture supernovae preferentially producing systems with short spin period, short orbital periods and low eccentricity like RX J0520.5-6932.

## 10.4 Conclusions

The analysis of our *XMM-Newton* [ToO](#) observation of RX J0520.5-6932 revealed X-ray pulsations with a period of 8.035331(15) s. The X-ray spectrum is best fitted by an absorbed power-law with a spectral index of  $\sim 0.83$  plus a low-temperature black-body component with temperature of  $\sim 0.24$  keV. The detailed pulse-phase resolved analysis of its spectral properties reveals a significant change in its spectral shape. Assuming the same spectral model the changes with pulse phase can be described by variations in the black-body and power-law intensities. A possible anti-correlation of black-body and power-law flux (possibly due to geometrical effects) requires confirmation with data of higher statistical quality. Our analysis of the [OGLE](#) light curve of the optical counterpart confirmed an optical period of 24.43 d. Our results confirm RX J0520.5-6932 as a [BeXRB](#) with a [NS](#) primary, making it the 15<sup>th</sup> known HMXB pulsar in the LMC.

## LXP 8.04: December 2013 outburst


 To follow the X-ray outburst behaviour of RX J0520.5-6932 (LXP 8.04) after its type-I outburst in January 2013, we further monitored the BeXRB pulsar with *Swift*. In the present chapter we present the results of our continuous *Swift* monitoring of LXP 8.04, that led to the detection of a major outburst that started in December 2014, that lasted for over 100 d and exceeded the Eddington luminosity for a  $1.4 M_{\odot}$  NS. During the evolution of the outburst we requested an *XMM-Newton* ToO observation that was performed near the peak luminosity of the event. The *XMM-Newton* observing capability provided the high statistics ( $\sim 1$  M counts) enabling us to perform a detailed X-ray spectral and temporal study of the system during this energetic event. We present the X-ray light-curve of the outburst that lasted for more than four months, or five orbital periods of the system. We report on the spectral properties of the system that were derived from the X-ray spectrum during the brightest state of the LXP 8.04. Moreover, we present a detailed study of the pulsed properties of the system based on a toy model that implements the basic characteristics of the expected emission geometry of the accretion column.

## 11.1 Observations and data analysis

### 11.1.1 X-ray data

Following the detection of a type-I outburst from LXP 8.04 in January 2013 we continued to monitor the source with *Swift* to search for regular X-ray outbursts related to the optical periodicity. The system faded below the detection limit of *Swift* in 2013 May without undergoing another major burst. In search for a possible re-brightening of the source, we requested a *Swift* ToO monitoring to be performed at the time where a type-I outburst was expected. The dates were selected based on the time of maximum luminosity of the January 2013 event and the 24.43 d optical period (Vasilopoulos et al. 2014a). On 2013 November 12 *Swift* detected the source at a luminosity level of  $\sim 3 \times 10^{36}$  erg s $^{-1}$  (0.3-10 keV band), which is  $\sim 20\%$  higher than the previously maximum detected by *Swift* in January 2013. We continued monitoring LXP 8.04 as its luminosity declined and reached a minimum on 2013 December 1. This was followed by a step increase in luminosity, which reached its maximum on 2014 January 13, before fading below detection limit ( $< 5 \times 10^{35}$  erg s $^{-1}$ ) on 2014 April 27 (see Fig. 11.7). An *XMM-Newton* ToO observation (PI:G Vasilopoulos) was performed on 2014 January 22 near the peak luminosity of the outburst. Both the maximum luminosity and the duration, that exceeded five orbital periods, make this major outburst an uncommon event, that is rarely observed in BeXRB systems. For the analysis of *Swift* and *XMM-Newton* data we followed the standard procedures described in the previous chapter.

#### X-ray light curve

The exposure corrected X-ray light curve of the major outburst is presented in Fig. 11.1. Two different binning intervals have been used for better illustrating the short

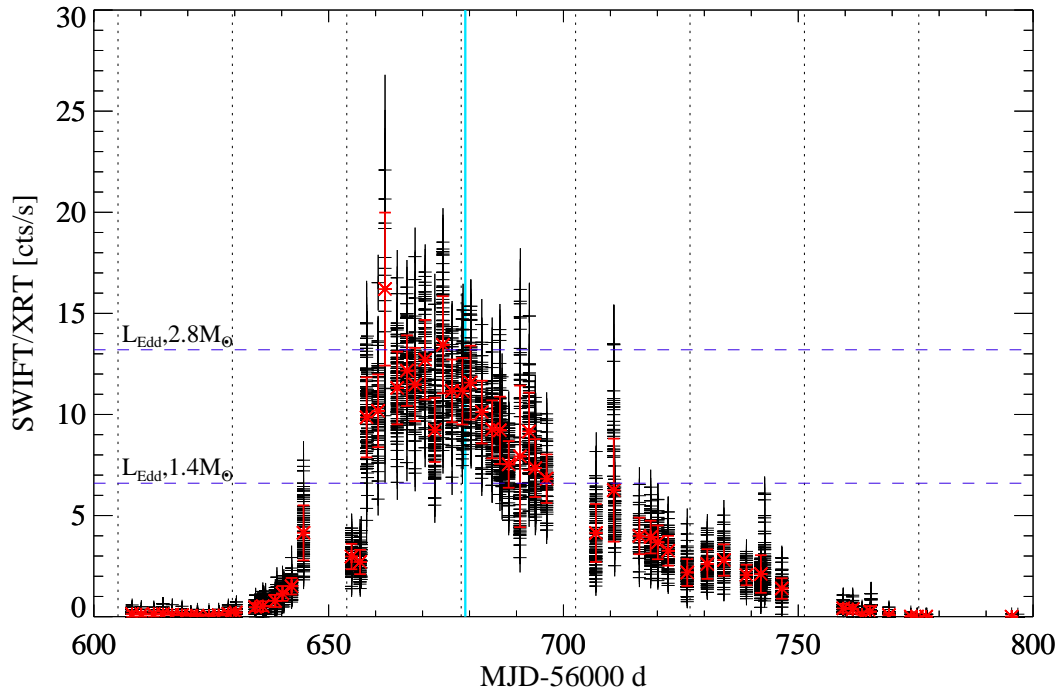


**Figure 11.1:** Exposure corrected *Swift*/XRT light-curve during the major outburst. The black crosses correspond to the 20 s binned intervals during each *Swift*/XRT snapshot, while the red points denote the average count-rate within each snapshot ( $\sim 1000$ s). The error of the averaged count-rates are calculated from the dispersion of the 20 s bins. Vertical line colours are the same as in Fig.11.7. The horizontal lines mark the typical Eddington limiting luminosity for a NS with a 1.4 and 2.8  $M_{\odot}$ .

and long term X-ray variability during the event. Apart from the average count-rate of each *Swift*/xrt snapshot, we also used a bin size similar to the spin period to search for shorter variabilities. We individually applied the exposure correction factors on each time interval that was used in the plot. For most snapshots the correction factors were between 1.07 and 1.15. In the extreme case of obsid: 00032671047 (MJD 56662), where the system was projected on a bad column, the correction factor was between 4 and 12 for the different intervals

From the *Swift*/XRT coverage of the event it is clear that the system goes through at least 3 consecutive outbursts of increased luminosity. The first one was detected during its fade out phase (MJD $\sim$ 56605) and was probably related to the orbital period of the system since its maximum luminosity falls in phase with the outburst of January 2013. The second one started immediately after and continuously increased its luminosity for one orbital period of the system. During this time interval the system became brighter in the optical, diverting from its standard optical modulation that was consistent during the OGLE era. By that time (MJD $\sim$ 56645), due to pointing restrictions we were not able to further monitoring the system for 10 days. When the system was observed, its luminosity had marginally decreased. This is an indication that the system probably reached a maximum luminosity and faded again. This is also supported by the *Swift*/BAT light-curve of the system. The third and brightest out-

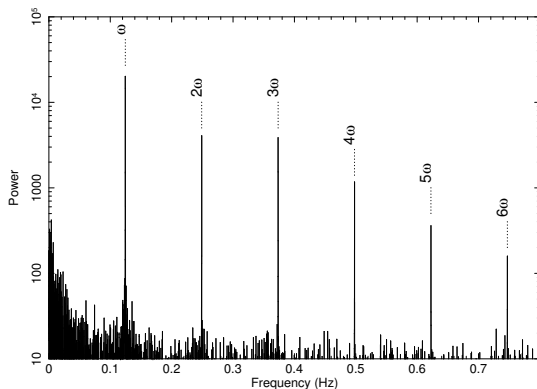


**Figure 11.2:** Power density spectrum created from the EPIC-pn data in the 0.7-10.0 keV energy band. The time binning of the input light curve was 0.01 s. The best-fit frequency  $\omega \sim 0.124497$  Hz and its first five harmonics are easily distinguished in the plot.

burst started immediately after. For a period of  $\sim 50$  d, or two orbital periods, the system retained an X-ray luminosity (0.3-10 keV band) that exceeded the Eddington limit of a  $1.4 M_{\odot}$  NS. While the average luminosity of each *Swift*/XRT snapshot never exceeded the Eddington limit for a  $2.7 M_{\odot}$  NS, that is the maximum mass allowed for a NS (e.g. Pappas and Apostolatos 2014). Nevertheless, the maximum X-ray luminosity of a NS can exceed the above limit as material is not radially accreted onto the NS. The maximum X-ray luminosity emitted from the accretion column is a function of the magnetic field strength of the NS (Mushtukov et al. 2015b), while recent discoveries have established that X-ray pulsars can emit at luminosities much higher than the Eddington limit (e.g. Bachetti et al. 2014; Fürst et al. 2016; Israel et al. 2017a).

### X-ray timing analysis

Temporal analysis was performed on the EPIC-pn data which provided the best time resolution and very high statistics. For this, we used the HEASoFT task `powspec` and the XRONOS task `efsearch` to search the X-ray light curve (0.2 – 10 keV) for periodicities. To get a more accurate estimate of the best period and its uncertainty we performed the EF technique. To estimate the uncertainty of the period we performed multiple repetitions of the above method while bootstrapping the event arrival times. In Fig. 11.2, we present the inferred power density spectrum of the *XMM-Newton* EPIC-pn data. We notice a strong peak at the main period of 8.032302(1) s as derived by the EF method and its first five harmonics. By using the 3 energy bands (0.7-2.0 keV, 2.0-4.5 keV, 4.5-10 keV) we can define 2 hardness ratios,  $HR_S$  for soft and  $HR_H$  for hard X-rays as the ratio of their difference over their sum (i.e.  $(R_{i+1} - R_i)/(R_{i+1} + R_i)$ ) with  $R_i$  denoting the background-subtracted count rate in energy  $i^{\text{th}}$  energy band. These 2 hardness ratios correspond more to the  $HR_3$  and  $HR_4$  of the energy bands commonly used for the *XMM-Newton* standard products: 1  $\rightarrow$  (0.2 – 0.5) keV, 2  $\rightarrow$  (0.5 – 1.0) keV, 3  $\rightarrow$  (1.0 – 2.0) keV, 4  $\rightarrow$  (2.0 – 4.5) keV, 5  $\rightarrow$  (4.5 – 10.0) keV (Watson et al. 2009; Sturm et al. 2013a). The period-folded pulse profiles in the EPIC energy bands together with the hardness ratios derived from the pulse profiles in two adjacent energy bands are plotted in Fig. 11.3.

From the HR diagrams in Fig. 11.3, we note a rapid drop in  $HR_3$  around phase 0.6, which is not observed in the harder energy bands ( $HR_4$ ). This drop occurs in phase with the decline in the total flux that is observed in all energy bands. The definition of the HRs' suggests that this behavior is a result of a relative rise of the flux between the first and second energy bands (0.7-2.0 and 2.0-4.5 keV). A phase dependent modulation

## 11. LXP 8.04: DECEMBER 2013 OUTBURST

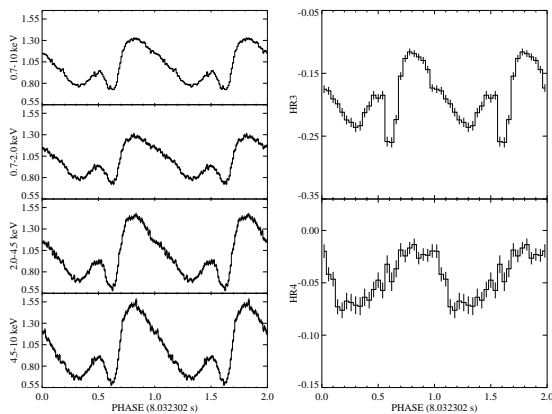


**Figure 11.3:** Left: Pulse profiles obtained from the merged EPIC data in different energy bands ( $P=8.032302$  s, binsize=0.01). All the profiles are background-subtracted and normalized to the average count rates of 91.67 cts  $s^{-1}$ , 39.85 cts  $s^{-1}$ , 26.94 cts  $s^{-1}$ , 24.74 cts  $s^{-1}$  in the (0.7-10) keV, (0.7-2.0) keV, (2.0-4.5) keV, (4.5-10) keV energy bands respectively. Right: Hardness ratios as a function of pulse phase derived from the pulse profiles in two neighbouring energy bands.

of the flux in the lower energy range can explain the drop in  $HR_3$ , as we will see in more details in Sec. 11.1.1.

### Phase-averaged X-ray spectroscopy

The spectral analysis was performed with `xspec` (Arnaud 1996) version 12.8.0. For the fitting procedure we used  $\chi^2$  statistics, while all the uncertainties were calculated based on a  $\Delta\chi^2$  statistic of 2.706, equivalent to a 90% confidence level for one parameter of interest. For the EPIC-pn and EPIC-mos spectra we ignored events below 0.7 keV, while for the RGS spectra we ignored events with energies above 2.0 keV. The *XMM-Newton* spectra were fitted simultaneously using the same model parameters with an additional scaling factor to account for instrumental differences. The the scaling factor accounting for the EPIC-pn model was fixed at 1 while for all the tested models for the EPIC-MOS and RGS detectors we obtained scaling factors with average values of  $C_{MOS1} = 1.002 \pm 0.004$  and  $C_{RGS1} = 0.921 \pm 0.013$   $C_{RGS2} = 0.895 \pm 0.011$  (see Stuhlinger et al. 2006, or the latest version of the *XMM-Newton* calibration manual<sup>1</sup>).

For all the tested spectral models, the photo-electric absorption was modelled as a combination of Galactic foreground absorption and an additional column density accounting for both the interstellar medium of the LMC and the intrinsic absorption by the source. The Galactic photo-electric absorption was set to a column density of  $N_{H,GAL} = 6.44 \times 10^{20} \text{ cm}^{-2}$  (Dickey and Lockman 1990a) with abundances according to Wilms et al. (2000). The LMC-intrinsic column density  $N_{H,LMC}$  was treated as a free parameter with abundances of 0.49 for elements heavier than helium (Rolleston et al. 2002).

The pulse-phase averaged spectra were first fitted with an absorbed power law, resulting in a reduced  $\chi^2_{red} > 5$ , from the residuals there was evidence for a soft component at  $\sim 1$  keV as well as below 0.7 keV. Additionally, an emission line component at  $\sim 6.6$  keV and a high energy break or cutoff was evident in the residuals of the this simple model. We further tested models typically applied to BeXRB spectra. A combination of black-body like emission and disc emission was not able to sufficiently describe the low part of the spectrum ( $< 2$  keV). Thus, we ignored the low energies ( $< 3$  keV) during the fit and tried to constrain only the parameters of the high-energy part. We concluded on a best-fit model composed by a power-law with a high energy cutoff, a seemingly broad emission line and an absorption feature at  $\sim 7.1$  keV.

<sup>1</sup>[http://xmm2.esac.esa.int/external/xmm\\_sw\\_cal/calib/cross\\_cal/](http://xmm2.esac.esa.int/external/xmm_sw_cal/calib/cross_cal/)

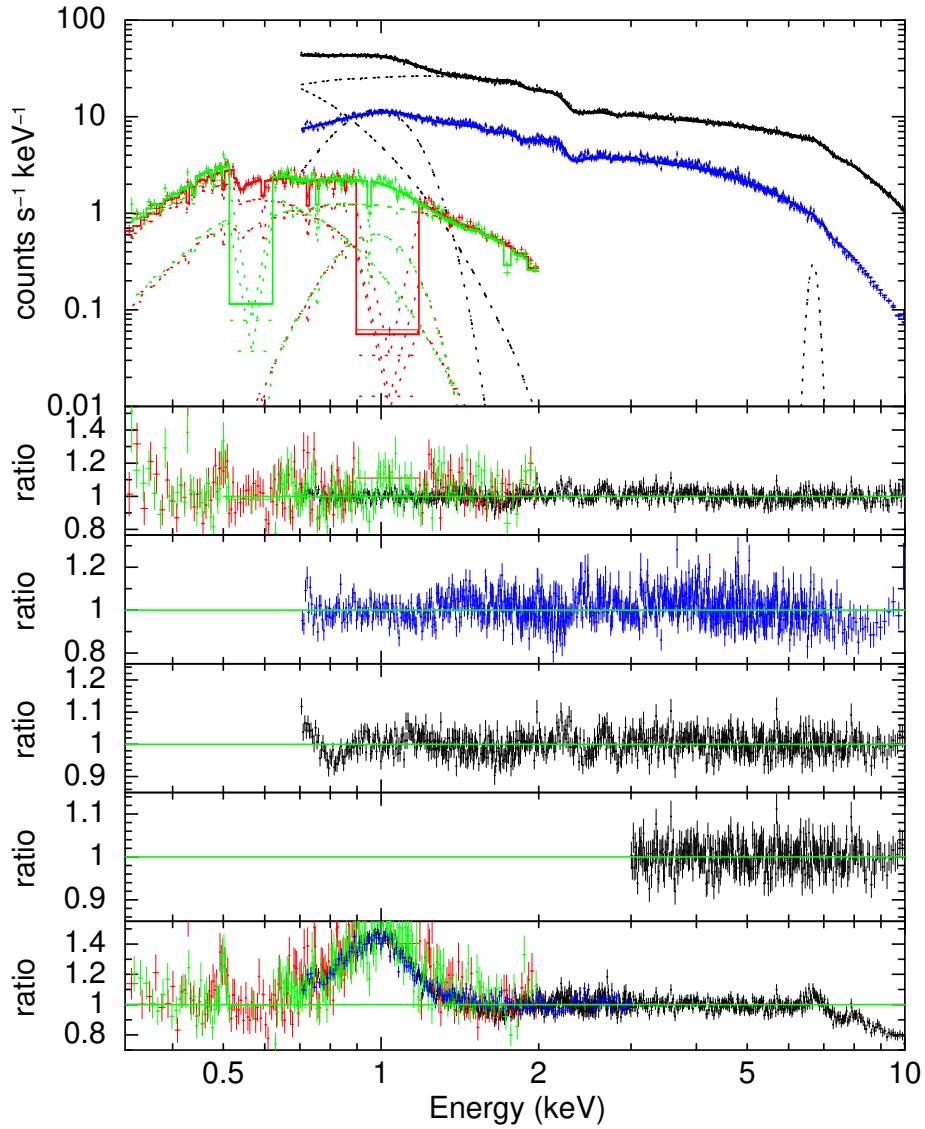


**Figure 11.4:** Pulse-phase averaged EPIC spectra of LXP 8.04. The top panel shows the EPIC-pn (black), MOS2 (blue), RGS1 (red) and RGS2 (green) spectra, together with the best-fit model (solid lines) composed of an absorbed power law with a high-energy cutoff, a multi-temperature black-body component (dotted lines), two Gaussian lines at  $\sim 1$  and  $6.7$  keV and an absorption edge at  $\sim 7.1$  keV. The ratios between the model and the data are plotted in the panels below. For the best fit model shown in the top panel, the ratios are plotted in the second and third panels. In the fourth panel we show the ratios between the EPIC-pn data and a different model, where the low energy Gaussian component is replaced by a vmekal component. The fifth panel presents the ratios of the best fit model when fitted only to the high-energy part of the spectrum. The bottom panel shows the ratios to the best fitted model (top panel), plotted when the high-energy cutoff is removed, and the absorption edge and emission lines strength set to zero.

## 11. LXP 8.04: DECEMBER 2013 OUTBURST

Component	Parameter	Value	units
tbnew*vphabs*			
*(gaussian + ezdiskbb + edge*highcut*powerlaw+ gaussian2)			
vphabs	nH	0.053±0.023	10 <sup>22</sup> cm <sup>-2</sup>
gaussian	LineE	0.971 <sup>+0.014</sup> <sub>-0.019</sub>	keV
	Sigma	0.145 <sup>+0.017</sup> <sub>-0.014</sub>	keV
	norm	0.0050 <sup>+0.0014</sup> <sub>-0.0009</sub>	
ezdiskbb	T <sub>max</sub>	0.133 <sup>+0.010</sup> <sub>-0.012</sub>	keV
	norm	3800 <sup>+3000</sup> <sub>-1500</sub>	
edge	edgeE	7.14±0.04	keV
	MaxTau	0.127±0.015	
highcut	cutoffE	7.86 <sup>+0.14</sup> <sub>-0.22</sub>	keV
	foldE	9.035 <sup>+1.4</sup> <sub>-1.1</sub>	keV
powerlaw	PhoIndex	0.705±0.009	
	norm	0.0273±0.0004	
gaussian2	LineE	6.69 ±0.04	keV
	Sigma	0.04 <sup>+0.1</sup> <sub>-0.04</sub>	keV
	norm	0.00009 <sup>+0.00005</sup> <sub>-0.00003</sub>	
χ <sup>2</sup> /DOF		1.068/4473	

**Table 11.1:** Spectral fit results of the phased averaged spectra.

The spectral properties are in agreement to the two NUSTAR observations performed close to the *XMM-Newton* observation. [Tendulkar et al. \(2014\)](#) report a best fit model composed by a power law with photon index  $\sim 0.74$ - $0.87$ , with a cutoff at  $\sim 8$ - $12$  keV, folding energy  $\sim 7.8$  keV and a gaussian emission line at 6.58 keV with a width  $\sim 0.4$  keV.

Having derived the model parameters for the high-energy part of the spectrum ( $> 3$ keV), we proceeded to improve the fit to the softest part of the X-ray spectrum. For this, we included a multi-temperature black-body component to account for an accretion disk, and a broad Gaussian line to describe the emission around the 1.0 keV region. The values of the best-fit model parameters are summarised in Table 11.1. The best-fit model together with its ratio plots are shown in Fig.11.4

A more sophisticated approach would be to use different absorption components for different model components. E.g. radiation emitted near the NS surface could propagate through the hot plasma near the NS and exhibit higher absorption. Moreover, a partial absorption model could account for a more complex distribution of the absorption material near the emitting region, or for a small percentage of scattered light that remains unabsorbed. Yet, none of these combinations improved the goodness of the fit. Interestingly, in all the tested models a Gaussian component with energies  $\sim 1$  keV was always necessary to improve the goodness of fit.

The RGS1 and RGS2 data were fitted separately to look for emission line features. A model composed of a power-law and multi-temperature disc black-body was used to model the continuous emission in the given energy range. The power-law photon

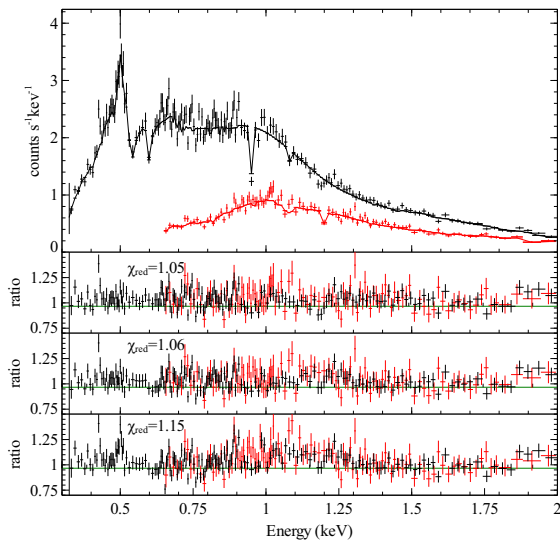


**Figure 11.5:** X-ray spectrum based on the events collected by the of the RGS detectors. top to bottom: 4 gauss, bvapec free , vapec fix.

index was fixed to the best fit value of the EPIC-pn data  $\Gamma = 0.705$ . The above model produced a best fit value of  $\chi^2_{red} = 1.25$ . To improve the emission residuals 4 Gaussian line profiles were added to the model. The addition of a  $\sim 0.97$  keV broad gaussian significantly improved the fit ( $\chi^2_{red} = 1.06$ ) while three narrow gaussian profiles at  $\sim 499$  eV, 566 eV and 683 eV delivered a best fit value of  $\chi^2_{red} = 1.05$ . We further tested a model where the gaussians were replaced by emission by a hot thermal plasma component (`vapec` & `bvapec` in `xspec`). When using a hot thermal plasma model (`vapec`) with abundances fixed to the average LMC values the goodness of fit ( $\chi^2_{red} = 1.15$ ) was worst than the the model that include the single  $\sim 1$  keV broad Gaussian model. In order to produce a model with similar goodness of fit as the best fit model described above we had to use velocity/thermally-broadened emission spectrum from collisionally-ionized diffuse gas `bvapec`, while setting some the Metal abundances (N, O, Ne, Fe, Ni) as free parameters. The latest model produced a best fit value of  $\chi^2_{red} = 1.06$ , marginally worst than the model composed by the 4 Gaussian components. Interestingly the velocity-broadened plasma model had a Gaussian sigma for velocity broadening of  $\sim 4700$  km/s. The above models are presented in Fig. 11.5, while the parameter values are presented in Table 11.2.

### Phase-resolved X-ray spectroscopy

Given the clear variation of the hardness ratios (see HR diagrams in Fig. 11.3), we investigated the characteristics of the phase-resolved X-ray spectrum. For this, we used only the EPIC-pn data, that offers better time resolution. To transform the observed event-arrival times to phased times we used the `SAS` task `phasecalc`, with zero phase defined as the date of the observation (MJD: 56679.0), the same as used in Fig. 11.3. The two-dimensional phase-energy histogram is presented in Fig. 11.6. In the histogram we introduced two consecutive normalizations purpose, one for averaging over phase and one over energy. The purpose of the normalization is to look for any energy dependence in the pulse profile shape. The third histogram emphasizes any diversion from a smooth pulse shape thus it resembles a phase-energy resolved HR. The histogram shows no major variation in the spectral properties of the source in the energy range of 2.0-8.0 keV. Interestingly, there is a anti-correlated variation in

## 11. LXP 8.04: DECEMBER 2013 OUTBURST

Component	Parameter	Value	units
tbnew*(diskbb + powerlaw + gauss1+ gauss2 + gauss3 + gauss4)			
tbnew	nH	0.055±0.006	10 <sup>22</sup> cm <sup>-2</sup>
diskbb	<i>kT</i>	0.149315 <sup>+0.07</sup> <sub>-0.04</sub>	keV
	norm	6700 <sup>+2000</sup> <sub>-700</sub>	
powerlaw	PhoIndex	0.705 (fixed)	
gaussian1	LineE	0.4988 <sup>+0.0019</sup> <sub>-0.0016</sub>	keV
	sigma	0.007±0.002	keV
	EqWidth	0.0050 <sup>+0.0015</sup> <sub>-0.0012</sub>	keV
gaussian2	LineE	0.567 <sup>+0.010</sup> <sub>-0.009</sub>	keV
	sigma	0.017 <sup>+0.010</sup> <sub>-0.007</sub>	keV
	EqWidth	0.0051 <sup>+0.0039</sup> <sub>-0.0032</sub>	keV
gaussian3	LineE	0.684 <sup>+0.017</sup> <sub>-0.019</sub>	keV
	sigma	0.048 <sup>+0.016</sup> <sub>-0.014</sub>	keV
	EqWidth	0.0131475 <sup>+0.010</sup> <sub>-0.0081</sub>	keV
gaussian4	LineE	0.968±0.014	keV
	sigma	01539 <sup>+0.011</sup> <sub>-0.012</sub>	keV
	EqWidth	0.18±0.02	keV
$\chi^2/\text{DOF}$		1.05/1840	
tbnew*(diskbb + powerlaw + vapec)			
tbnew	nH	0.052±0.004	10 <sup>22</sup> cm <sup>-2</sup>
powerlaw	PhoIndex	0.705 (fix)	
diskbb	<i>kT</i>	0.164±0.005	keV
	norm	4000 <sup>+900</sup> <sub>-700</sub>	
vapec	<i>kT</i>	1.23±0.04	keV
	norm	0.0058±0.0006	
$\chi^2/\text{DOF}$		1.15/1849	
tbnew*(diskbb + powerlaw + bvapec)			
tbnew	nH	0.0495±0.005	10 <sup>22</sup> cm <sup>-2</sup>
powerlaw	PhoIndex	0.705 (fix)	
diskbb	<i>kT</i>	0.159±0.005	keV
	norm	4581 <sup>+900</sup> <sub>-800</sub>	
bvapec	<i>kT</i>	1.020±0.024	keV
	Velocity	5159 <sup>+1300</sup> <sub>-900</sub>	km/s
	N <sup>(a)</sup>	34±0.0006	
	Ne <sup>(a)</sup>	3.016±0.0006	
	Fe <sup>(a)</sup>	0.33±0.0006	
	Ni <sup>(a)</sup>	13.46±0.0006	
	norm	0.0033±0.0002	
$\chi^2/\text{DOF}$		1.06/1844	

<sup>a</sup> fitted model cannot produce errors...

**Table 11.2:** Best fit parameters of the RGS spectra

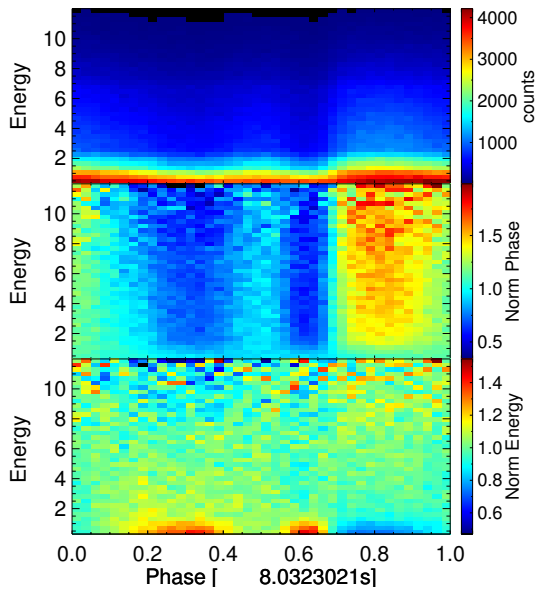


**Figure 11.6:** Phase dependent spectral heat-map, obtained by binning the EPIC-pn source counts to 40 phase bins and 40 energy channels. Top panel: colours are proportional to the number of counts per each bin, middle-panel: data were normalized by the average number of counts in the same energy bin, bottom-panel: data were again normalized according to the average count rate of each phase bin. In each plot the 2D histogram values were projected to a 256 colour table. To specify regions of minimum intensity we used a black colour for the bin with the minimum value, e.g. less than 22 counts in the upper plot.

both the higher-energy and the lower part of the spectra. While the source enters a lower luminosity phase (pulse phase of 0.2-0.4 and 0.6-0.65), its lower-energy relative flux increases while its higher-energy part becomes fainter. In phases between 0.7 and 0.9 during the maximum pulsed X-ray luminosity the relative flux of the soft X-rays becomes fainter. All the above observations associated with the possible presence of two discrete emission components with one being dominant in the soft X-rays. We will further discuss the physical implications that could explain such pulse profile in §11.2.2.

### 11.1.2 Optical data

LXP 8.04 was observed with Robert Stobie Spectrograph (RSS) on the Southern African Large Telescope (SALT) at three epochs during the outburst. The aim was to monitor the  $H\alpha$  emission line and thus the evolution of the Be decretion disk. The spectra were corrected by PySALT, a python/PyRAF-based data reduction and analysis pipeline for SALT (Crawford et al. 2010). The 2D images were wavelength calibrated using observations of an Argon arc lamp and then rectified before one dimensional, background subtracted spectra were extracted. The subtraction of a very narrow  $H\alpha$  line, that is attributed to the LMC extended emission, was of critical importance during this procedure.

The Large Magellanic cloud has been monitored by the Optical Gravitational Lensing Experiment (OGLE, Udalski et al. 2015). The OGLE-IV I band photometric data of the optical counterpart of LXP 8.04 are publicly available through the OGLE XROM<sup>1</sup> web page (Udalski 2008).

#### Optical coverage of the outburst

The evolution of the major outburst can be seen in the optical and X-ray band in Fig. 11.7. The OGLE I-band light curve of the LXP 8.04 reveals a persistent 24.43 d periodic modulation with constant amplitude around a steady mean magnitude during

<sup>1</sup>XROM: OGLE-IV real time monitoring of X-ray variables: <http://ogle.astrouw.edu.pl/ogle4/xrom/xrom.html>

## 11. LXP 8.04: DECEMBER 2013 OUTBURST

---

the OGLE time of operation (Vasilopoulos et al. 2014a). If we adopt the 24.43 d optical period (black-dotted vertical lines), we find that the source becomes optically brighter in phase with the outburst detected on January 2013, as depicted in the middle panel of Fig.11.7. At the beginning of the major X-ray outburst (MJD $\sim$ 56645 d), the optical counterpart of LXP 8.04 became significantly brighter. But its brightening started out of phase of its expected periodic optical modulation (see Fig.7 in Vasilopoulos et al. 2014a). This was followed by a time interval, centered around the X-ray maximum, that lasted almost for one binary orbit and showed no signs of optical periodicity ( $\sim$ 56652-56676 MJD). During the decline of the X-ray luminosity, the optical light curve returned to its 24.43 d periodic modulation, but in a brighter state than before. This interval lasted a little less than two orbital periods ( $\sim$ 56680-56720 MJD), with a mean value of 14.31 mag, which should be compared to the mean value of 14.42 mag before the outburst.

Regarding the OGLE V-band light curve, there are no available observations at the beginning of the burst and during the rise of the X-ray luminosity. The only available observations are made after after MJD 56685 d, namely after the *XMM-Newton* ToO observation (see thick cyan vertical line in Fig.11.7). Previous to the outburst there have been only few measurements of the the OGLE V magnitude: two observations during October 2013, and one on February 2013. The lack of uniform coverage in both filters, does not allow a detailed study of the colour evolution during the burst. However, from the available observations, we can report a similar modulation in the V and I OGLE filters. The system's mean luminosity in the V filter was found to be 14.26 mag and 14.18 mag before and during the burst. Moreover, the source increased its luminosity in the I Band by  $0.097\pm 0.026$  mag, compared to the  $0.11\pm 0.03$  mag rise in the I mag. The I-V colour of the system follows the same dependence with the luminosity (redder when brighter) during the outburst, as in the X-ray quiescence state of the system. In particular, it becomes redder as it becomes brighter, a trend that is also reported for other BeXRB systems when the decretion disc is observed with an inclination  $< 80^\circ$  (Rajoelimanana et al. 2011) Additionally, the systems colour become slightly redder, reaching a maximum value of  $V - I \sim -0.12$  mag, compared to its colour modulation before the burst. We note that the respective value in the quiescence state was -0.15 mag, while the observed V-I colour never exceeded the value of -0.13 mag.

### SALT Spectroscopic observations

The normalised optical spectra in the observer's frame are shown in Fig. 11.8. A double-peaked shaped  $H\alpha$  emission line can be seen in all SALT observations. Prior to deriving the properties of the emission line, we made a redshift correction for the recession velocity of the LMC ( $-280$  km  $s^{-1}$ , Richter et al. 1987). The line was fitted by a combination of two Gaussians.

For the three observation performed on January 18-19 and February 8 the equivalent widths of the  $H\alpha$  line were found to be  $-6.42 \pm 0.12$ ,  $-5.24 \pm 0.17$  and  $-7.00 \pm 0.13$ , respectively. As the three observations were performed at similar orbital phases, it was not possible to establish a relation between the width of the line and the optical colours of the source.

Additional information can be derived by studying the shape of the double-peaked line. The LMC diffuse emission makes the extraction of precise values from the line

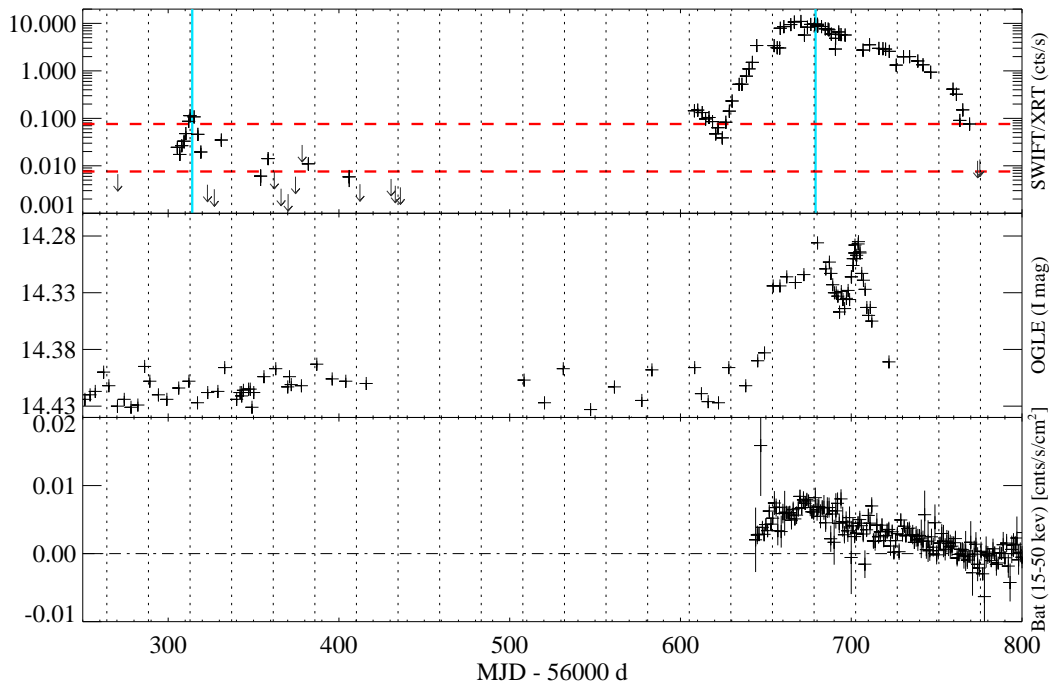


**Figure 11.7:** X-ray and optical light-curves of LXP 8.04 during the period 56250 to 56800 MJD. Upper panel: Swift-XRT (0.3-10.0 keV band). Middle panel: OGLE (I mag). Bottom panel: Swift-BAT (15-50 keV band). The black-dotted Vertical lines indicate the OGLE optical period (24.43 d) phased on the peak of the January 2013 burst. The thick-cyan vertical lines indicate the XMM-Newton observations.

profile uncertain. Thus, the reader should treat these values with caution. We found the separation of the two peaks to be  $4.44 \text{ \AA}$  during the first two, and  $3.66 \text{ \AA}$  during the third observations. Since the inclination of the Be circumstellar disc is not constrained ( $<70^\circ$ ) we can precisely determine the radius of the disk. Instead, we can calculate the relative change of the Be-disk radius in the period between the first and third observations. Using the relation  $R_{disk} = 4GM \sin^2 i \Delta V^{-2}$ , where  $\Delta V$  is the difference in the velocity space between the two peaks of the H $\alpha$  line profile, with the respective values listed in Table 11.3, we estimate that the disc radius increased by  $\sim 32\%$ .

The ratio of the intensities in the violet (V) and the red (R) wings of the double-peaked H $\alpha$  line was found to be 1.056 in the first and 1.037 in the last observations, i.e. it decreases with time. The prograde precession (Telting et al. 1994) of the enhanced density region will cause the blue-shifted peak to reach maximum height when it is perpendicular to the observer’s line of sight, and will slowly decrease in height as the enhanced region moves around the disc until it is in front of the star with respect to our line of sight (where the peaks will be of equal height).

## 11. LXP 8.04: DECEMBER 2013 OUTBURST

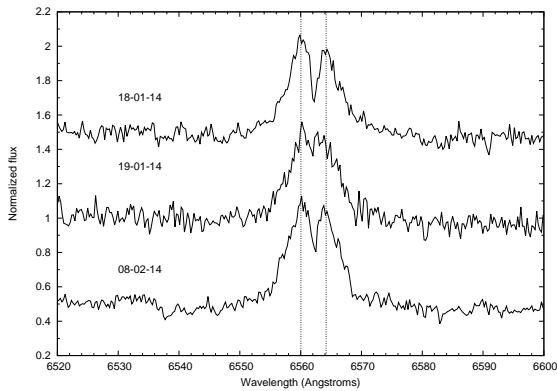


**Figure 11.8:**  $H\alpha$  emission line evolution during the outburst. The dotted-vertical line denotes the central wavelength of the line, redshifted by the recession velocity of the LMC ( $-280 \text{ km s}^{-1}$  or  $6.12 \text{ \AA}$ , Richter et al. 1987). The Violet peak of the profile is blue-shifted to the rest frame of the  $H\alpha$  line.

Date	Equivalent width	Width ( $\sigma$ ) <i>km/s</i>	V/R	Peak separation [ $\text{\AA}$ ]
18/01/14	$-6.526 \pm 0.086$	357	1.056	$4.805 \pm 0.086$
19/01/14	$-5.74 \pm 0.13$	357	1.039	$4.11 \pm 0.19$
08/02/14	$-6.69 \pm 0.14$	346	1.037	$4.022 \pm 0.078$

**Table 11.3:**  $H\alpha$  line properties

## 11.2 Discussion

### 11.2.1 Phase-averaged spectra:

The best fit parameters for the accretion disc model, yielded a max temperature of  $\sim 0.13 \text{ keV}$ , while the normalization of a model provides an estimation for the radius of the disc which was found to be  $850_{-190}^{+290} \text{ Km}$  for a disc with inclination of  $\sim 45^\circ$  or  $650_{-150}^{+220}$  for an inclination of  $\sim 30^\circ$ . The inner radius of the accretion disc should be compared with the magnetospheric radius, where the disc is expected to truncate. This is given by (Ghosh et al. 1977):

$$R_M = \xi R_A = \xi \left( \frac{B^2 R_{NS}^6}{\dot{M} \sqrt{2GM_{NS}}} \right)^{2/7}, \quad (11.1)$$

where  $\dot{M}$  is the accretion rate,  $B$  is the surface magnetic field of the NS and  $M_{NS}$ ,  $R_{NS}$  are, respectively, its mass and radius. The  $\xi$  parameter can be derived by simulations (Parfrey and Tchekhovskoy 2017, e.g.) and it generally takes a value of  $\sim 0.5$ , while for super Eddington accretion analytical approximations can be used to express it as a function of the accretion rate ( $\dot{M}$ ) and the NS magnetic field  $B$  (see eq. 61 of Chashkina et al. 2017a). We note that for relatively strong magnetic field the magnetospheric radius may extend to hundreds of Schwarzschild radii. In the case of LXP 8.04, Tendulkar et al. (2014) calculated the NS's magnetic field using the cyclotron line emission featured, as seen with NuSTAR, and found it to be of the order of  $2 \times 10^{12} \text{ G}$ . By inserting this value to eq. 11.1 and using typical values for the other parameters, namely  $R_{NS} = 10^6 \text{ cm}$ ,  $M_{NS} = 1.4 M_\odot$  and  $\dot{M} \sim 1.5 \times 10^{-8} M_\odot/\text{yr}$  (i.e.  $0.2 L_X$ ), we can estimate the magneto-spheric radius to be  $R_m \sim 2000 \text{ km}$  or  $\sim 500$  Schwarzschild radii. We find, therefore, that  $R_{in}$  is a factor of 2-3 smaller than  $R_m$ . Given the weak

dependence of  $R_m$  on the parameters and the small range of plausible values for  $M_{\text{NS}}$  and  $R_{\text{NS}}$ , our aforementioned result is robust.

According to [Shakura and Sunyaev \(1973\)](#), an accretion disc heated through viscous dissipation would reach at  $R_m$  a maximum temperature of  $\sim 1.5 \times 10^5$  K. At this temperature we expect Fe to be ionized, with most of the ions ( $\sim 50\%$ ) occupying the  $\text{Fe}^{+5}$  stage (see Table 3 of [Shull and van Steenberg 1982](#)). Similarly, we can derive the most probable ionization stages from the best fit spectral model, i.e. for temperature  $T \sim 1.5 \times 10^6$  K. In this case, we calculated that there are three equally abundant ions,  $\text{Fe}^{+11}$ ,  $\text{Fe}^{+12}$  and  $\text{Fe}^{+13}$  with ionization fractions of 25%, 30% and 23%. However, for a line centered at  $\sim 6.7$  keV, a  $2^3P_1 \rightarrow 1^1S_0$  transition in  $\text{Fe}^{+24}$  should occur. In the case, the Fe line emission originates from the accretion disk, such high ionization states can be achieved only at higher temperatures. This in turn requires the inner disc radius to be much smaller than the magnetospheric radius of a highly magnetised NS. Although  $R_m$  is not a strict limit of the disk's boundary, it is not possible for the disc to continue steadily accreting within radii 10 to 20 times smaller than this radius. The above imply that the Fe line emission line should not arise from the disk.

A more plausible scenario is, that these emission lines originate from an area between the accretion disc and the NS, where the accreting matter couples to the NS by the magnetic-field lines. Within this plasma layer, the so-called Alfvén shell, current-driven micro-instabilities may cause relativistic double layers to form ([Basko 1980](#); [Hamilton et al. 1994](#)).

The spectral modelling of the RGS data imply emission originating further away from the NS surface and the inner magnetosphere. The nature of the broadened Gaussian lines could be associated to a blend of lines emitted by regions with multiple temperatures and ionization rates within the magnetospheric radius. Although the velocity broadened emission spectrum produces high abundances (N, Ni) of non physical nature, it produces very good residuals at the region around 1 keV, a plausible explanation is that emission at the  $\sim 0.5$  keV could be originating from a different region with different properties.

### 11.2.2 Phase resolved spectrum: Pulse profile modelling

The pulse profiles of accreting X-ray pulsars comes with a variety of shapes, ranging from sinusoidal single peaked profiles, to double or even multiple peaked shapes. Thus, a simplistic isotropic emission model from the polar cap cannot be adopted to such sources. It has long been suggested that the radiation geometry of a pulsar can vary between a pencil-beam and fan-beam pattern ([Basko and Sunyaev 1975, 1976](#)). Additionally, the plasma layer following the Alfvén surface

This variety of pulses among different – or sometimes the same sources – suggested that the assumption of an isotropically emitting polar cap was rather simplistic and that the pulsar emission is most likely beamed ([Basko and Sunyaev 1975, 1976](#)). Depending on the mass accretion rate (and therefore the luminosity of the source), the radiation geometry of the pulse may switch from a pencil-beam to a fan-beam pattern. Namely, for luminosities lower than  $\approx 10^{37}$  erg/sec – and due to the high anisotropy of the scattering cross-sections – the radiation emitted from the highly magnetised plasma in the accretion column will have a pencil-beam pattern, parallel to the accretion column ([Basko and Sunyaev 1975](#)). On the other hand, in sources with luminosities exceeding  $\approx 10^{37}$  erg/sec, strong deceleration of the accreting material by radiation

pressure, results in increased opacity of the accreting column. In this scenario, photons are expected to escape from the sides of the accretion column (see Fig. ), in a fan-beam pattern (Basko and Sunyaev 1976). Pencil-beamed emission is often associated with sinusoidal-like pulse profiles (or more complex shapes if one includes gravitational effects, and different obscuration mechanisms e.g. (Mészáros 1992) 1992), on the other hand, double peaked profiles are indicative of emission that is fan-beam dominated (Nagel 1981; White et al. 1983; Paul et al. 1996, 1997; Rea et al. 2004).

In order to investigate the origin of the observed modulation, we computed pulse profiles for five consecutive energy bands, confined by the energies 0.7, 1.5, 2.5, 4.0, 7.0, and 10.0 keV, and checked whether they can be reproduced by a beaming model. The model was intentionally kept as simple as possible, so that it can be described by a minimum set of parameters.

We assume that the X-rays are emitted from two point-like regions which are exactly opposite to each other and have identical properties. These are the height above the neutron star surface, the angular separation from the rotation axis, and the beaming pattern. This pattern is modelled by a superposition of a pencil beam component  $p = p_0 \cos^n \theta$  and a fan beam component  $f = f_0 \sin^m \theta$ , where  $\theta$  is the local zenith angle. As this geometry would always produce symmetric pulse profiles, we introduce an azimuthal modulation of the fan beam pattern:  $f = f_0 \sin^m \theta f_{\text{mod}} (1 + \sin 2\varphi)$ . Only the quantities  $p_0$ ,  $f_0$ ,  $f_{\text{mod}}$ ,  $n$ , and  $m$  are allowed to vary with energy.

This model was originally developed for explaining the pulse profiles of anomalous X-ray pulsars (Trümper et al. 2013), but is sufficiently generic to be applied also to other pulsars.

The results are summarised in Fig. 11.10, where the panels at right show the observed pulse profiles together with the modelled flux (red curve), which is the superposition of the pencil (green) and fan (blue) beam component. The panels at left show maps of the radiation which would be observed around the neutron star sufficiently far away that the effect of gravitational bending gets negligible. The horizontal line indicates the radiation which we see during the rotation of the neutron star. This line passes through a distinct region of reduced flux, which is the origin of the pronounced drop around phase 0.6-0.7. The best fit was shown in Figure 11.10 was computed for a height 2.0 km of the emission region above the neutron star surface, and neutron star was assumed to have 1.4 solar mass and 12.5 km radius. The emission regions are located at  $\pm 36.0$  deg latitude, and we see the neutron star at an inclination of 34.4 deg. The fan beam is azimuthally modulated with  $f_{\text{mod}} = 0.74$ , and the exponents  $n$  and  $m$  range between 1.0 and 3.0.

According to our modelling, there is a straightforward explanation for the drop in the pulse at phase 0.6-0.7. In the absence of gravitational bending, any beam originat-

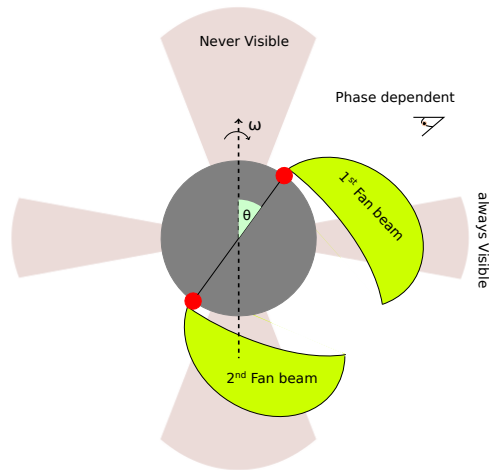


**Figure 11.9:** Fan beam visibility depending on the observers observing angle.

energy keV	chi2r	PB flux	RFB flux	PBE	FME
0.7-1.5	0.72	21.388	0.23	1.0	3.0
1.5-2.5	1.10	10.269	0.35	1.1	1.0
2.5-4.0	1.38	10.823	0.39	1.2	1.0
4.0-7.0	1.33	15.112	0.43	1.5	1.0
7.0-10.0	1.32	9.47	0.49	2.4	1.0

**Table 11.4:** model parameters

ing at the neutron star surface could only irradiate one hemisphere, and the neutron star would cast a sharp shadow. The effect of gravitational bending produces an overlap in the contribution of both fan beams (see Fig. 11.9), leading to the formation of a ‘fan beam belt’, characterised by a sharp intensity drop at both edges. The width of this belt increases with the distance of the height of emission region above the neutron star surface. The ‘hole’ which is seen in the radiation maps is the solid angle which is outside the fan beam belt. When our line of sight crosses this region during the rotation of the neutron star, we see almost exclusively the pencil beam component. This component is spectrally softer, causing the dip in the hardness ratio  $HR_3$  (Fig. 11.3).

Based on the reconstructed 3D emission pattern one can estimate the pulse phase average isotropic  $L_X$  as would be calculated by a random observer (see Fig. 11.11). This result confirms that the isotropic emission from the accretion column can only affect the calculated isotropic luminosity by less than 10% for any random observer. For LXP 8.04 the total X-ray luminosity is  $\sim 5\%$  larger than the one estimated by an observer at Earth assuming isotropic emission, thus LXP 8.04 accretes at a super-Eddington level.

## 11.3 Conclusions

Analysis of high quality X-ray data during the 2013 major outburst of LXP 8.04 has enabled us to probe the spectral and temporal properties of the system during super-Eddington accretion rates. The spectral analysis has revealed the presence of a non-pulsating soft component that is consistent with the presence of an inflated accretion disc truncated at the magnetospheric radius of the NS. Analysis of X-ray grating spectra obtained by the RGS detectors revealed the presence of emission lines that originate from highly ionised plasma, probably originating from the outer magnetosphere and close to the inner accretion disk. Most importantly, for the first time, we have reconstructed the 3D emission pattern of pulsar based on a simple fan-beam pencil-beam geometry. Our analysis showed that the emission is originating from an accretion column with a height of 2 km, that is mainly emitting with a fan-beam geometry. Based on the best fit solution of the energy resolved pulse profile we have calculated the spectral energy distribution in the NS frame, and have shown that the observed X-ray luminosity is not a result of beaming and that for any random observer the calculated isotropic luminosity can only have small variations from the real one.

## 11. LXP 8.04: DECEMBER 2013 OUTBURST

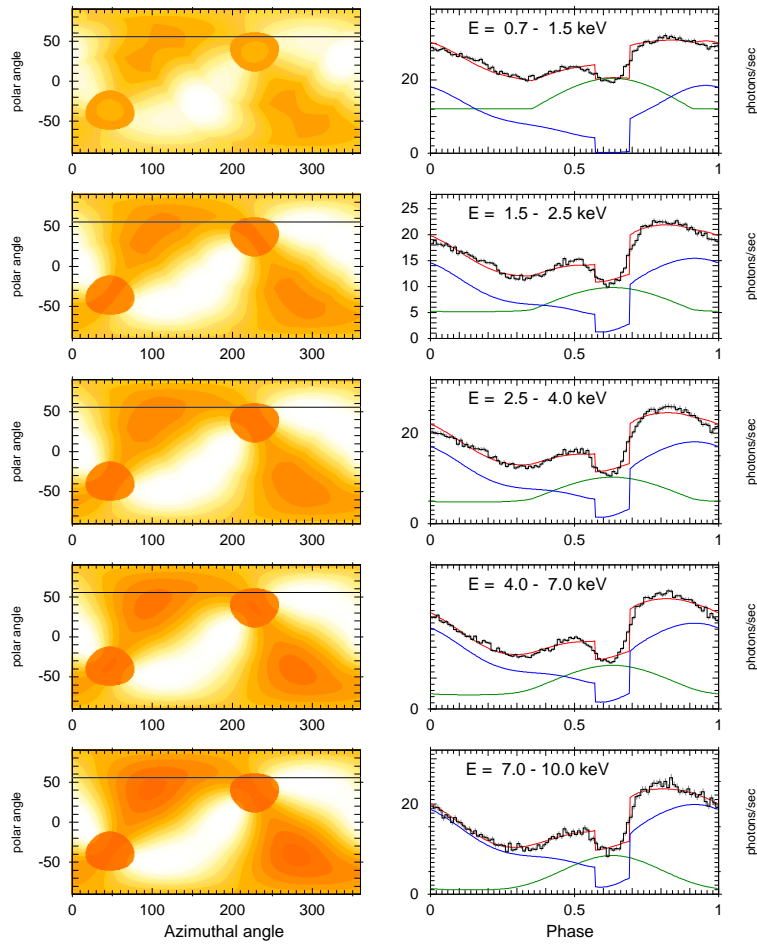


**Figure 11.10:** Left: density plot of the total emission of a pencil-beam and a fun-beam like emission model from the *NS* accretion column (x-axis phase, y axis observing direction), the horizontal line indicates the observing angle of the system. Right: best fit model of the pulse profile based on a combination of pencil like (green lines) and fun-beam like (blue lines) emission.

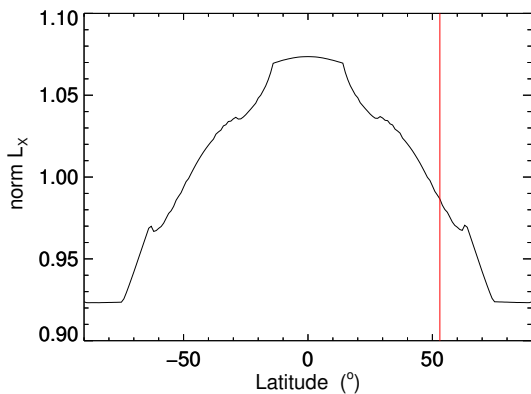


**Figure 11.11:** Observed normalised phase averaged isotropic luminosity for an observer at a random latitude angle. The angle is measured from the equator plane of the spinning *NS*. Vertical line marks the observer orientation for the best fit solution of LXP 8.04.

## LXP 38.55: October 2014 outburst

**I**n this chapter we report on the results of a  $\sim 40$  d multi-wavelength monitoring of the Be X-ray binary system IGR J05007-7047 (LXP 38.55). During that period the system was monitored in the X-rays using the *Swift* telescope and in the optical with multiple instruments. When the X-ray luminosity exceeded  $10^{36}$  erg s $^{-1}$  we triggered an *XMM-Newton* ToO observation. Timing analysis of the photon events collected during the *XMM-Newton* observation reveals coherent X-ray pulsations with a period of 38.551(3) s ( $1\sigma$ ), making it the 17<sup>th</sup> known high-mass X-ray binary pulsar in the LMC. During the outburst, the X-ray spectrum is fitted best with a model composed of an absorbed power law ( $\Gamma = 0.63$ ) plus a high-temperature black-body (kT  $\sim 2$  keV) component. By analysing  $\sim 12$  yr of available OGLE optical data we derived a 30.776(5) d optical period, confirming the previously reported X-ray period of the system as its orbital period. During our X-ray monitoring the system showed limited optical variability while its IR flux varied in phase with the X-ray luminosity, which implies the presence of a disk-like component adding cooler light to the spectral energy distribution of the system.

## 12.1 Analysis and results of X-ray observations

### 12.1.1 X-ray observations

We used *Swift*/XRT to monitor the most promising BeXRBs candidate systems of the MCs (for most recent catalogues see: [Haberl and Sturm 2016](#); [Antoniou and Zezas 2015](#)) to search for an X-ray outburst. We detected IGR J05007-7047 on 2014 October 26, at an X-ray Luminosity of  $\sim 2 \times 10^{36}$  erg s $^{-1}$  in the 0.3-10.0 keV band. We continued monitoring the system with *Swift*/XRT for a period of 40 days to achieve an X-ray coverage of about one orbital period (30.771 d, see §12.2.3). During the maximum X-ray luminosity we triggered one of our granted *XMM-Newton* anticipated ToO (PI: R. Sturm) that was performed on 2014 November 20. Looking at archival data, the system was detected during an *XMM-Newton* slew ([Saxton et al. 2008](#)) on 2006 November 29 (XMMSL1 J050045.3-704441) at an angular distance of 4.7'' (error 7.7'') from the *XMM-Newton* ToO position (see §12.1.2). Moreover, the system was also observed with Chandra on 2005 June 16. The results of the Chandra observation were published in [Sazonov et al. \(2005\)](#), but the derived luminosities were based on a power-law model with photon index characteristic of an AGN ( $\Gamma = 1.4$ ). Thus, we re-analysed the Chandra observation in order to calculate the luminosity of the system at the given time. The complete log of the *Swift*, *XMM-Newton* and Chandra observations obtained and analysed for the current work is summarised in Table 12.1. The X-ray, optical and near IR light curves of the system during our monitoring are presented in Fig. 12.1.

### 12.1.2 X-ray position

The position of LXP 38.55 was determined from the *XMM-Newton* ToO observation that provided the best statistics. X-ray images were created from all the EPIC cameras

## 12. LXP 38.55: OCTOBER 2014 OUTBURST

#	OBS-ID	Instrument <sup>a</sup>	T <sub>start</sub> MJD [d]	orbital phase <sup>b</sup>	exposure <sup>c</sup> [s]	count rate <sup>d</sup> cts s <sup>-1</sup>	UVOT filter <sup>e</sup>	AB magnitudes <sup>f</sup>
<i>XMM-Newton</i>								
1	Slew	EPIC-pn	54068.2	0.87	6.6	1.05±0.3 <sup>g</sup>	–	–
2	0743910301	EPIC-pn	56981.611	0.54	22039	1.337±0.009	–	–
		EPIC-MOS1	56981.611	0.54	23701	0.469±0.006	–	–
		EPIC-MOS2	56981.611	0.54	23672	0.442±0.005	–	–
<i>Swift</i>								
1	00031846004	XRT	56956.025	0.71	662	0.068±0.014	u	14.46±0.02
2	00031846005	XRT	56966.903	0.06	1086	0.022±0.006	uvwm2	14.46±0.02
3	00031846006	XRT	56968.232	0.10	869	0.019±0.007	u	14.45±0.02
4	00031846008	XRT	56972.560	0.25	1251	0.033±0.007	u	14.42±0.02
5	00031846009	XRT	56974.555	0.32	1036	0.038±0.008	uvwm2	14.57±0.02
6	00031846010	XRT	56976.810	0.38	1076	0.087±0.012	u	14.44±0.02
7	00031846011	XRT	56978.474	0.44	1061	0.140±0.015	uvwm2	14.44±0.02
8	00031846012	XRT	56980.671	0.50	966	0.130±0.017	u	14.41±0.02
9	00031846013	XRT	56982.233	0.56	167	0.14 ±0.04	uvwm2	14.48±0.02
10	00031846014	XRT	56984.545	0.64	1900	0.098±0.009	u	14.44±0.02
							uvw2	14.46±0.02
11	00031846015	XRT	56986.661	0.70	1286	0.069±0.010	uvwm2	14.52±0.02
12	00031846017	XRT	56988.077	0.75	1179	0.076±0.011	u	14.48±0.02
13	00031846018	XRT	56990.520	0.83	867	0.032±0.008	uvwm2	14.43±0.02
14	00031846019	XRT	56992.583	0.90	1011	0.026±0.007	u	14.43±0.02
15	00031846020	XRT	56994.658	0.96	4821	0.021±0.009	uvwm2	14.44±0.02
16	00031846021	XRT	56996.444	0.02	1284	0.016±0.005	u	14.43±0.02
<i>Chandra</i>								
1	6271	ACIS-I	53537.125	0.61	3415	0.200±0.008 <sup>f</sup>	–	–

<sup>a</sup> Observation setup: For the *XMM-Newton* ToO, full-frame mode was used for all EPIC instruments, while medium filter was used for the EPIC/MOS cameras and thin filter for the EPIC/PN. For *Swift*/XRT the photon-counting mode (PC) was used.  
<sup>b</sup> The zero orbital phase is selected to match Fig. 12.1 as MJD – 56965 d.  
<sup>c</sup> Exposure time for *XMM-Newton* EPIC cameras, Chandra/ACIS, or total *Swift*/XRT exposure time of all snapshots taken within the duration of the obs-id.  
<sup>d</sup> Vignetting corrected count rate in the 0.3–10.0 keV energy band.  
<sup>e</sup> UVOT filter used during the *Swift*/UVOT integration.  
<sup>f</sup> *Swift*/UVOT AB magnitudes, not corrected for extinction.  
<sup>g</sup> count rate of the slew survey is given in the 0.2–12 keV band.

**Table 12.1:** X-ray observations log of LXP 38.55.

## 12.1 Analysis and results of X-ray observations

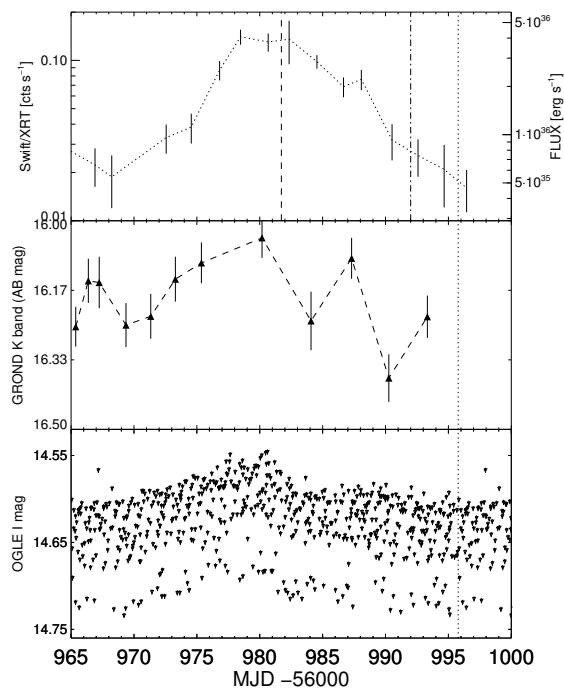


**Figure 12.1:** Multi-wavelength light curve of LXP 38.55 during a moderate outburst that resulted in a trigger of an *XMM-Newton* ToO. Top panel shows the *Swift*/XRT light curve during the November 2014 outburst, middle panel shows the GROND K band light curve during the same period. Bottom panel shows the total OGLE-IV I band light curve, folded for a period of  $\sim 30.775$  d. In all the panels the time between MJD 56965 and the vertical dotted line denotes one  $\sim 30.775$  d optical period. In the top panel the vertical dashed line indicates the time of the *XMM-Newton* ToO. The dash-dotted line indicates the phase at which the *XMM-Newton* slew survey detection was made.

using the *XMM-Newton* standard energy sub-bands (Watson et al. 2009). Source detection was performed simultaneously on all the images using the SAS task `edetect_chain`. The source position was determined to R.A. =  $05^{\text{h}}00^{\text{m}}46.^{\text{s}}06$  and Dec. =  $-70^{\circ}44'37''.4$  (J2000), with a  $1\sigma$  statistical uncertainty of  $0.04''$ . The total  $1\sigma$  positional error, however, is dominated by the remaining systematic uncertainty assumed to be  $0.5''$  (see section 4.3 of Sturm et al. 2013a).

### 12.1.3 Timing analysis

We used the SAS task `barycen` to correct the *XMM-Newton* EPIC event arrival times to the solar-system barycentre. To search for a periodic signal we used an epoch folding technique (Davies 1990; Larsson 1996). We initially searched for a periodic signal in the EPIC-pn event data. The detected signal was longer than the frame time of the EPIC-MOS instrument (2.6 s), thus in order to increase the signal-to-noise ratio we used the merged event list of EPIC-pn and EPIC-MOS with the common good-time intervals for our timing analysis<sup>1</sup>. Additionally, we computed the Lomb-Scargle (LS) periodogram (Scargle 1982; Horne and Baliunas 1986) of the binned X-ray light curve, while performing Monte Carlo white noise simulations to calculate the significance of the derived period. Based on 10000 simulated light curves we conclude that the measured period is significant at a larger than  $3\sigma$  level. In Fig. 12.2, we present the inferred power density spectrum of LS method and the results of the epoch folding phase dispersion minimization statistical test. To improve the result of our initial estimation and to estimate the uncertainty of our solution, we followed Haberl et al. (2008a). Based on a Bayesian periodic signal detection method introduced by Gregory and Loredo (1996), we determined the pulse period with its  $1\sigma$  uncertainty to  $38.551 \pm 0.003$  s.

By using the five standard energy bands (0.2-0.5, 0.5-1.0, 1.0-2.0, 2.0-4.5, 4.5-10 keV), we can define four hardness ratios as  $HR_i = (R_{i+1} - R_i)/(R_{i+1} + R_i)$ , with  $R_i$  denoting the background-subtracted count rate in energy band  $i$ . The period-folded pulse profiles in the EPIC standard energy bands, together with the hardness ratios derived from the pulse profiles in two adjacent energy bands, are plotted in Fig. 12.3.

### 12.1.4 Spectral analysis

We used `xspec` (version 12.8.2, Arnaud 1996) to perform the X-ray spectral analysis. The *XMM-Newton*/EPIC cameras provided a total of  $\sim 35$ k counts enabling us to use  $\chi^2$  statistics in the fitting procedure. The three spectra were fitted simultaneously with the same model with the addition of a scaling factor to account for instrumental differences. For the EPIC-pn we fixed the scaling factor at 1, while for both EPIC-MOS, we obtained values of  $C_{MOS1} = 1.03 \pm 0.02$  and  $C_{MOS2} = 0.97 \pm 0.02$ , which is consistent with the expected values (see Stuhlinger et al. 2006, or the latest version of the *XMM-Newton* calibration manual<sup>2</sup>). The X-ray absorption was modelled using the `tbnew`

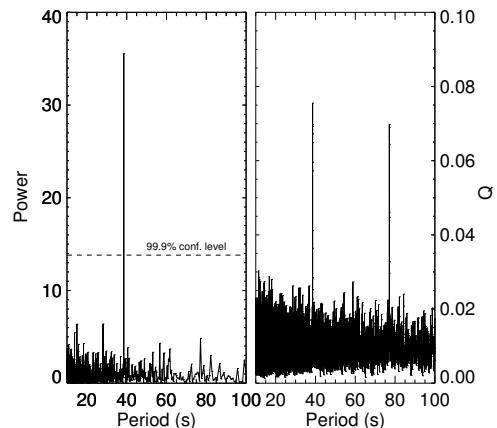


**Figure 12.2:** *Left:* LS power density spectrum created from the merged EPIC data in the 0.2-10.0 keV energy band. The time binning of the input light curve was 0.1 s. The best-fit period 38.551 s (frequency  $\omega \sim 0.02594$  Hz) is easily distinguished in the plot. The horizontal line denotes the 99.9% confidence level of the simulated light-curves. *Right:* Results of the phase dispersion minimization test (ep-fold). The epoch-folding test statistics  $Q$  is defined as in Leahy et al. (1983a). The second peak corresponds to a value two times of the best fit period.

<sup>1</sup>For the analysis the photon arrival times are randomised over the frame time of each instrument.

<sup>2</sup>[http://xmm2.esac.esa.int/external/xmm\\_sw\\_cal/calib/cross\\_cal/](http://xmm2.esac.esa.int/external/xmm_sw_cal/calib/cross_cal/)

## 12.1 Analysis and results of X-ray observations

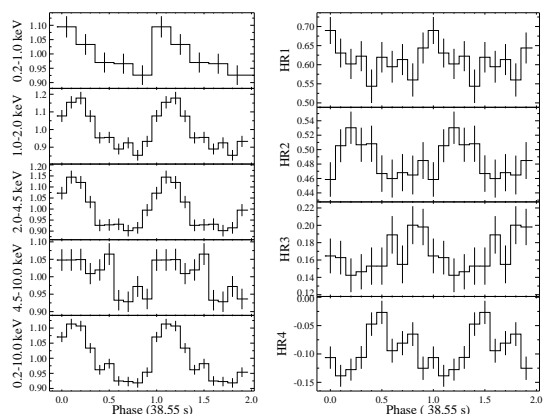


**Figure 12.3:** *Left:* Pulse profiles of IGR J05007-7047 obtained from the merged EPIC data in different energy bands. (For better statistics the first two standard energy bands were combined in the top panel, while the bottom panel shows all five energy bands combined). The profiles are background-subtracted and normalised to the average count rate (from top to bottom: 0.182, 0.426, 0.597, 0.493 and 1.70  $\text{cts s}^{-1}$ ). *Right:* Hardness ratios derived from the pulse profiles in two neighbouring standard energy bands as a function of pulse phase.

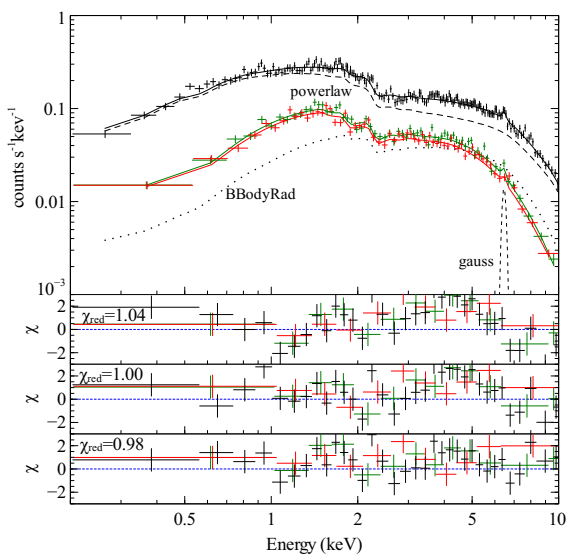


**Figure 12.4:** Pulse-phase averaged EPIC spectra of LXP 38.55. The top panel shows the EPIC-pn (black), EPIC-MOS1 (red) and EPIC-MOS2 (green) spectra, together with a best-fit model (solid lines) composed of an absorbed power law with photon index  $\Gamma = 0.63$ , a black body with 2.04 keV temperature (dotted line), and a Gaussian line at 6.46 keV. The second panel shows the residuals of an absorbed power law model ( $\Gamma = 0.58$ ). The third panel shows the residuals for the fitted model of an absorbed power law ( $\Gamma = 0.64$ ) plus multi-temperature disc black body model ( $kT = 0.1$  keV). Bottom panel shows the residuals of the best fit model plotted in the top panel. The residuals were rebinned for clarity while the spectra in the top panel show the binning used for the spectral fit. We note that residuals at  $\sim 2.2$  keV are an instrumental feature, related to the Au layer on the mirrors.

code, a new and improved version of the X-ray absorption model `tbabs` (Wilms et al. 2000), while the Atomic Cross Sections were adopted from Verner et al. (1996). The photo-electric absorption was modelled as a combination of Galactic foreground absorption and an additional column density accounting for both the interstellar medium of the LMC and the intrinsic absorption of the source. For the Galactic photo-electric absorption we used a fixed column density of  $N_{\text{H,GAL}} = 0.847 \times 10^{21} \text{ cm}^{-2}$  (Dickey and Lockman 1990a), with abundances according to Wilms et al. (2000). We note that  $N_{\text{H,GAL}}$  was not fixed to the value provided by the Leiden/Argentine/Bonn (LAB) Survey of Galactic HI ( $1.35 \times 10^{21} \text{ cm}^{-2}$ , Kalberla et al. 2005), since this value corresponds to the total Galactic and LMC column density due to the filter used in the survey. The LMC intrinsic column density  $N_{\text{H,LMC}}$  was left as a free parameter with abundances of 0.49 for elements heavier than helium (Rolleston et al. 2002). All the uncertainties were calculated based on a  $\Delta\chi^2$  statistic of 2.706, equivalent to a 90% confidence level for one parameter of interest.

The spectra are well fitted by an absorbed power law (photon index  $\Gamma \sim 0.58$ ,  $\chi^2_{\text{red}} = 1.05$ ), however the addition of an additional component can improve the fit at low energies and smooth out the residuals at higher energies (Fig. 12.4). It is not

## 12. LXP 38.55: OCTOBER 2014 OUTBURST

uncommon for HMXBs to show an additional component in their X-ray spectrum. [Hickox et al. \(2004\)](#) provided several interpretations for the origin of such emission that they refer to as soft excess. In the case of intermediate X-ray luminosity systems like LXP 38.55, this excess can be a result of reprocessing of hard X-rays from the NS by optically thick accreting material located at the inner edge of the accretion disk, by photo-ionized or collisionally heated diffuse gas, or thermal emission from the NS surface. Moreover, [La Palombara et al. \(2013c\)](#) showed that many X-ray pulsars show a spectral feature that can be interpreted as black body emission from a small region, most likely the polar cap of the NS. Multiple components may contribute to the spectrum of LXP 38.55. Although the simple power-law fit is already acceptable and the statistical quality of the EPIC spectra does not require additional model components, we test if emission components which are expected to exist, improve the spectral fit. We restrict the model to a maximum of two continuum components, i.e. a combination of the power law with a thermal component. We found two solutions which improve the fit at a) low energies (mainly below  $\sim 1.5$  keV) and b) higher energies (above  $\sim 2$  keV).

For case a) both a single-temperature black-body (e.g. `BBodyRad` in `xspec`) or a multi-temperature accretion disc (e.g. `EzdiskBB` in `xspec`) with temperature ( $\sim 0.1$  keV) provide the same improvement in fit quality. It is however important to note that each of the models implies a different physical origin for the radiation process. As the normalization parameter of both components translates to an emission region with radius<sup>1</sup> of  $\sim 200$  km, it is more physical to attribute the emission originating from a region close to the inner radius of an accretion disc rather than a hot accretion column that reaches the NS surface. The statistical improvement of the fit compared to an absorbed power-law model was estimated with the `f-test` (probability for a value drawn from the F-distribution) and was found to be  $\sim 8 \sigma$ .

The best fit is provided by the combination of an absorbed power-law plus a high-temperature black-body component with temperature  $\sim 2.04$  keV (case b). This model improves significantly the residuals of the fit at higher energies and provides a statistical improvement above a  $3.5 \sigma$  level compared the low temperature black-body plus power law model. There is clear evidence of an emission line present at 6.4 keV that originates from neutral Fe ( $K_\alpha$  line). The width of the line ( $\sigma \sim 10^{-5}$  keV) was found to be bounded by the spectral resolution of the

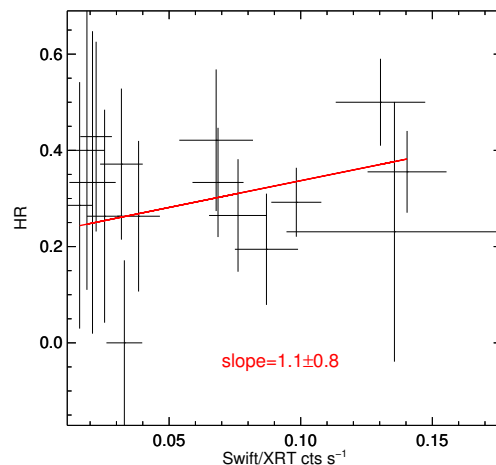


**Figure 12.5:** X-ray HR vs *Swift*/XRT count rate (0.3-10 keV). HR was computed based on the total counts in the low (0.3-2.0 keV) and high (2.0-10 keV) energy band for the duration of the monitoring. HR is defined again as the ratio of the differences over the sum of the two energy bands, i.e.  $HR = (R_h - R_l)/(R_h + R_l)$ .

<sup>1</sup> $R = \sqrt{Norm / \cos i} * Dist * f^2$ , where  $R$  is the inner radius of the disc in km,  $Dist$  is the distance to the source in units of 10 kpc,  $i$  is the inclination, and  $f = 1.4$  is the color to effective temperature ratio

instrument, thus we fixed the width of the line to zero since an exact value could not be resolved. The parameters for the models described above are given in Table 12.2.

We note that both the low and high temperature black-body components improve the residuals on different parts of the X-ray spectrum and account for different physical processes, thus in principle they could co-exist in the system. However, modelling the spectrum with a combination of three continuum components is not statistically justified. Moreover, the use of three continuum components together with the column density as free parameter adds degeneracy to the solution. While we cannot exclude the existence of more components in the spectrum, the available statistics does not justify the use of a more complicated spectral model.

The *Swift*/XRT observations could not provide sufficient statistics for modelling the X-ray spectrum, we were however able to derive values for the hardness of the spectrum in two adjacent energy bands (0.3-2.0 keV vs. 2.0-10 keV) and compare this quantity along the evolution of the burst. There was no significant evidence for a monotonous change in the hardness of the spectrum with luminosity along the  $\sim 40$  day monitoring cycle (see Fig.12.5), but a rather weak trend of the system becoming harder with increasing luminosity.

## 12.2 Analysis and results of optical data

### 12.2.1 SWIFT UVOT

Our *Swift* monitoring enabled us to measure the UV magnitudes (using the *Swift* UV/Optical Telescope, UVOT). We used the default filter of the day for the *Swift*/UVOT instrument setup. This resulted in nine observations performed with the U filter (central wavelength 3465 Å), seven with the UVM2 (2246 Å) and one with the UVW2 (1928 Å). To derive the systems UV magnitudes we used the `uvotsource` tool. A 5'' radius was used for performing aperture photometry for all filters. No significant variation was measured in any of the filters; the mean values for the derived magnitudes were:  $14.23 \pm 0.02$  for the U,  $14.12 \pm 0.05$  for the UVM2 and  $14.166 \pm 0.06$  for the UVW2 filter.

### 12.2.2 GROND

LXP 38.55 was observed thirteen times between 2014 November 4 and December 2 with the Gamma-Ray Burst Optical/Near-Infrared Detector (GROND; Greiner et al. 2008) at the MPI/ESO 2.2 m telescope (La Silla, Chile). Seven bands were used, providing a coverage in both optical (g', r', i' and z') and near-IR (J, H and K<sub>s</sub>) wavelengths. Each individual observation consists of 24 dithered exposures of 10 s in the near-IR and 4 dithered exposures in the optical with various exposure times (35 s in the eight first epochs and 66 s in the five last epochs), taken at a mean airmass of 1.3 and a mean seeing of 1.4".

Single dithered exposures were reduced (bias subtraction, flat-fielding, distortion cor-

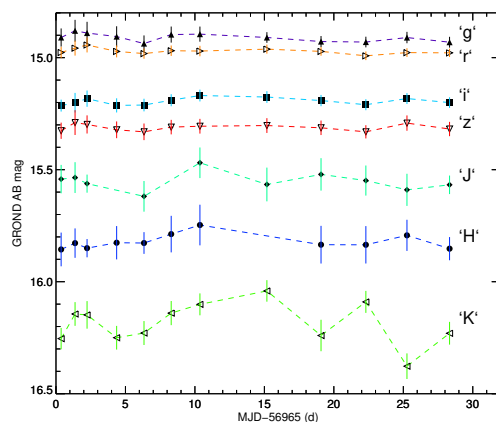


Figure 12.6: GROND light curves in seven filters.

## 12. LXP 38.55: OCTOBER 2014 OUTBURST

Component	Parameter	Value	units
Power-law plus High Energy Black body (T>1 keV)			
tbnew*tbnew*(gaussian + bbodyrad + powerlaw)			
tbnew	nH	$0.033^{+0.021}_{-0.018}$	$10^{22} \text{ cm}^{-2}$
gaussian	LineE	$6.46^{+0.04}_{-0.04}$	keV
	EqWidth	$0.047^{+0.04}_{-0.10}$	keV
bbodyrad	$kT$	$2.04^{+0.28}_{-0.3}$	keV
	norm	$0.020 \pm 0.005$	
	R	$0.7^{+0.08}_{-0.09}$	km
powerlaw	PhoIndex	$0.63^{+0.12}_{-0.08}$	
	Flux/Norm <sup>a</sup>	$(7.7^{+1.0}_{-1.3})$	$10^{-12} \text{ erg cm}^{-2} \text{ s}^{-1}$
Observed Flux <sup>b</sup>		$1.03 \times 10^{-11}$	$\text{erg cm}^{-2} \text{ s}^{-1}$
Unabsorbed Luminosity <sup>c</sup>		$3.03 \pm 0.08 \times 10^{36}$	$\text{erg s}^{-1}$
$\chi^2/\text{DOF}$		0.98/1174	
Power-law plus Low Energy Black body (T<1 keV)			
tbnew*tbnew*(gaussian + bbodyrad + powerlaw)			
tbnew	nH	$0.31 \pm 0.06$	$10^{22} \text{ cm}^{-2}$
gaussian	LineE	$6.46^{+0.04}_{-0.04}$	keV
	EqWidth	$0.047^{+0.04}_{-0.10}$	keV
bbodyrad	$kT$	$0.088^{+0.007}_{-0.006}$	keV
	norm	$2300^{+2500}_{-1300}$	
	R	$240^{+100}_{-80}$	km
powerlaw	PhoIndex	$0.60 \pm 0.03$	
	Flux/Norm <sup>a</sup>	$(10.92 \pm 0.15)$	$10^{-12} \text{ erg cm}^{-2} \text{ s}^{-1}$
Observed Flux <sup>b</sup>		$1.05 \times 10^{-11}$	$\text{erg cm}^{-2} \text{ s}^{-1}$
Unabsorbed Luminosity <sup>c</sup>		$3.38^{+0.11}_{-0.13} \times 10^{36}$	$\text{erg s}^{-1}$
$\chi^2/\text{DOF}$		1.00/1174	
Power-law plus low Energy multi-temperature disc Black body (T<1 keV)			
tbnew*tbnew*(gaussian + EzdiskBB + powerlaw)			
tbnew	nH	$0.34^{+0.05}_{-0.08}$	$10^{22} \text{ cm}^{-2}$
gaussian	LineE	$6.46^{+0.04}_{-0.04}$	keV
	EqWidth	$0.047^{+0.04}_{-0.10}$	keV
EzdiskBB	$kT_{\text{max}}$	$0.099^{+0.011}_{-0.006}$	keV
	norm	$340^{+300}_{-210}$	
	inner R	$215 \mp 80$	km
powerlaw	PhoIndex	$0.605 \pm 0.03$	
	Flux/Norm <sup>a</sup>	$(10.92 \pm 0.16)$	$10^{-12} \text{ erg cm}^{-2} \text{ s}^{-1}$
Observed Flux <sup>b</sup>		$1.05 \times 10^{-11}$	$\text{erg cm}^{-2} \text{ s}^{-1}$
Unabsorbed Luminosity <sup>c</sup>		$3.48^{+0.12}_{-0.13} \times 10^{36}$	$\text{erg s}^{-1}$
$\chi^2/\text{DOF}$		1.00/1174	

<sup>a</sup> Unabsorbed flux of the power-law component in the 0.3-10. keV energy band.

<sup>b</sup> Absorbed flux of the fitted model in the 0.3-10. keV energy band.

<sup>c</sup> Unabsorbed Luminosity of the fitted model in the 0.3-10. keV energy band, for a distance of 50 kpc (Pietrzyński et al. 2013).

**Table 12.2:** results of the X-ray spectral modelling

rection) and stacked using standard IRAF<sup>1</sup> tasks implemented in the GROND pipeline (Krühler et al. 2008; Yoldaş et al. 2008). The astrometry calibration was computed on single exposures against stars selected from the USNO-B1.0 catalogue (Monet et al. 2003) in the optical bands and the 2MASS catalogue (Skrutskie et al. 2006) in the near-IR bands, yielding an accuracy of 0.3" with respect to the chosen reference frame. The photometric calibration in the optical was computed against a close-by field from the Sloan Digital Sky Survey (York et al. 2000) at  $\delta = -10$  deg. This was observed five times over the entire observation run (including the first night) under photometric conditions. From the calibrated images we extracted a grid of secondary photometric calibrators for direct on-the-frame calibration on the subsequent nights. In the near-IR, the photometric calibration was computed against 2MASS stars identified in the GROND field of view. The accuracy of the absolute photometry calibration was 0.03 mag in  $g'$ ,  $r'$ ,  $i'$  and  $z'$ , 0.07 mag in J and H, and 0.05 mag in  $K_s$ . The seven band light curves derived from the GROND observation is presented in Fig. 12.6.

Having simultaneously obtained the photometry of the optical companion from NIR to optical, we can construct its SED and look for an IR excess. As BeXRBs are intrinsically variable in the optical, having both orbital and super-orbital variability, GROND data offer us the unique opportunity to study the SED of such systems. Moreover, since our *Swift*/UVOT fluxes showed no significant variability (compared to the NIR fluctuations) we can supplement the GROND magnitudes with the UV data from *Swift*, constructing an SED with (quasi-)simultaneous observations. To de-redden the optical observations, we used the extinction curve given by Misselt et al. (1999), which is most appropriate for the LMC. The foreground Galactic reddening was set to  $E(B - V)_{\text{Gal}} = 0.1062$  mag (Schlafly and Finkbeiner 2011). We used the Kurucz models of stellar atmospheres (Kurucz 1979; Castelli et al. 1997) to fit the observed photometry, while constraining the metallicity to that of the LMC ( $[\text{Fe}/\text{H}] = -0.5$ ).

The spectral types of the optical counterparts of BeXRBs in the SMC are reported to be in the range between O5 and down to B9 (Coe et al. 2005). However, in the new compilation of spectral types by Haberl and Sturm (2016) only stars with uncertain classification may have types as late as B5. There are no B6, B7 or B8 counterparts and only one B9 which may cast doubts on the spectral classification or the correct identification. This makes the spectral type distribution more similar to that of the

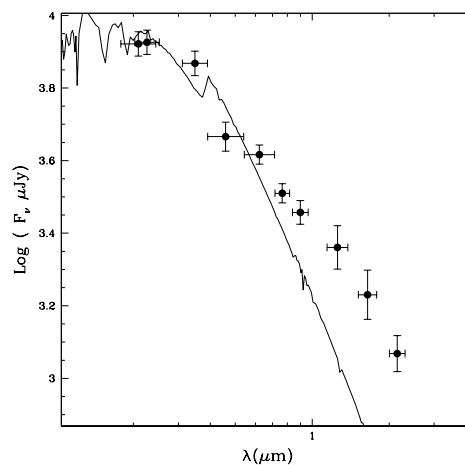


**Figure 12.7:** Spectral energy distribution of LXP 38.55. From left to right the three *Swift*/UVOT and the seven GROND optical and NIR fluxes are plotted. The plotted line corresponds to the Kurucz model with  $T=22000$  K,  $\log z = -0.05$  and  $\log g = 3.5$ .

<sup>1</sup>IRAF is distributed by the National Optical Astronomy Observatories, which are operated by the Association of Universities for Research in Astronomy, Inc., under cooperative agreement with the National Science Foundation.

## 12. LXP 38.55: OCTOBER 2014 OUTBURST

filter	central wavelength Å	$F_{\text{observed}}/F_{\text{template}}^a$	$F_{\text{excess}}$ $\mu Jy$
i	7640.0	$1.24^{+0.08}_{-0.07}$	$582^{+180}_{-170}$
z	8989.3	$1.42^{+0.10}_{-0.10}$	$779^{+190}_{-180}$
G	12560.9	$1.88^{+0.25}_{-0.22}$	$988^{+290}_{-250}$
H	16467.1	$2.14^{+0.32}_{-0.28}$	$848^{+240}_{-210}$
K	21512.4	$2.20^{+0.24}_{-0.21}$	$625^{+120}_{-110}$

**Table 12.3:** NIR excess attributed to the Be disk.

Galaxy which seems to end at B3. A B2 III star, like our system in study, is expected to have a temperature of  $\sim 21500$  K (Cox 2000), thus we limit the temperature parameter to the range of 20000-24000 K. We note that the decretion disc of a Be star can account up to 50% of its total luminosity (de Wit et al. 2006), thus stellar atmosphere models are expected to generally produce poor fits to the variable SED of those systems. A brute force fit of a stellar atmosphere model to our data without accounting for any prior knowledge of the systems properties (spectral type or distance) produces questionable results. This method delivers a best fit model of a much cooler than expected star ( $T \sim 10000$  K) and at a much closer distance than that of the LMC. By limiting the temperature parameter search grid to the range of 20000-24000 K, and by excluding the optical and NIR GROND data from the fit we can achieve a good fit, where the normalization and the radius of the star describe our prior assumptions. The best derived model was that of a star with temperature of 22000 K and surface gravity  $\log g = 3.5$ . The fitted SED of the system is presented in Fig. 12.7. From the fitted model it is clear that the contribution of the disc is not restricted to the NIR magnitudes but affects the optical emission of the system as well.

To stress the importance of UV measurements to the SED fitting we repeated the above exercise by using only the GROND magnitudes. We then get a best fit model of a star with a temperature range of 8500-9500 K, with a normalization pointing to a source located much closer than the LMC distance. This suggests the presence of a cool disc that contributes to the SED of the B star. Further investigation of the contribution of the disc in the SED of the star lies beyond the scope of the present work as it requires precise modelling of the decretion disk.

### 12.2.3 OGLE

The Optical Gravitational Lensing Experiment (OGLE) started its initial observations in 1992 (Udalski et al. 1992) and continues observing till today (OGLE IV, Udalski et al. 2015). Observations were made with the 1.3 m Warsaw telescope at Las Campanas Observatory, Chile. Images are taken in the V and I filter pass-bands, while the data reduction is described in Udalski et al. (2015). OGLE photometric magnitudes are calibrated to the standard VI system.

In the present work, we used the OGLE I and V band magnitudes for the counterpart of LXP 38.55 that were taken between Modified Julian dates (MJD) 52166 and 57275. The latest I and V band light curves are shown in Fig. 12.8. The photometric data can be downloaded from the OGLE-IV real time monitoring of X-ray sources web-

page<sup>1</sup> (Udalski 2008). For the OGLE I band magnitudes we computed periodograms by using the Lomb-Scargle algorithm (see Fig. 12.9). We searched for periodicities up to half of the total OGLE observing period, which at the time of the analysis was  $\sim 5108$  d.

By using the  $\sim 14$  year of available OGLE observations in the I band we were able to derive a refined orbital period of  $30.776 \pm 0.005$  d (see Fig. 12.9). Additionally, a  $410 \pm 18$  d super-orbital quasi-periodic modulation can be seen in the data. We note that the super-orbital modulation should not be treated as a periodic signal like the orbital modulation, its nature is probably related to the precession of the Be disk. Period uncertainties were computed using the bootstrap method and repeating the calculations for 10000 light curves. Both orbital and super-orbital modulations are confirmed well above a 99% confidence level by performing 10000 white and red noise (using REDFIT, Schulz and Mudelsee 2002)<sup>2</sup> simulations. Due to the limited OGLE coverage ( $\sim 12$  super-orbital periods) and the gaps in the light curve the uncertainty on the super-orbital solution is high. Following equation 14 of Horne and Baliunas (1986) we estimate an uncertainty of about  $\sim 40$  d for the super-orbital solution. This value is different from the uncertainty computed by the bootstrap method and is only used as an estimator of the effect of the length of the data to the determination of the periodic solution. Observations spanning over a  $N$  times larger interval would decrease this uncertainty by a factor of  $\sim N^{3/2}$ , e.g. by doubling the coverage we would only improve the uncertainty to 14 d. The shape of the  $\sim 410$  d fundamental peak of the Lomb-Scargle periodogram is affected by both the length of the data set (see Fig. 6 & 7 of Rajoelimanana et al. 2011) and the 365 d yearly periodicity that is expected to be found in the OGLE data. The final super-orbital period was derived by performing Monte Carlo simulations and fitting the fundamental peak of the Lomb-Scargle periodogram with a Gaussian profile. During the OGLE-III phase (MJD < 55000 d) the system exhibits high long term variability in addition to its orbital and super-orbital periodicities. By analysing data from multiple epochs (1-2 y intervals) we conclude that there has been no statistically significant change in the orbital period within the investigated time intervals. We note that the orbital period is detected during the OGLE-III phase only at a low significance level ( $\sim 50\%$  confidence level) and it can be easily dismissed by automatic detection algorithms.

Figure 12.10 indicates that the system becomes redder when brighter. This colour modulation can be attributed to the presence of a decretion disc around the Be star, as a face-on configuration of the disc is expected to cause this modulation (for similar examples see Rajoelimanana et al. 2011).

## 12.3 Discussion

By monitoring the BeXRBS system IGR J05007-7047 we were able to promptly trigger an *XMM-Newton* ToO. Timing analysis of the photon events collected during the *XMM-Newton* ToO reveals coherent X-ray pulsations (see Fig. 12.2) with a period of  $38.551(3)$  s ( $1\sigma$ ), making LXP 38.55 the 17<sup>th</sup> known HMXB pulsar in the LMC (see Antoniou and Zezas 2015, and references therein). During the outburst, the X-ray spectrum is well represented by an absorbed power law ( $\Gamma = 0.85$ ), however we argue

<sup>1</sup>XROM: <http://ogle.astrouw.edu.pl/ogle4/xrom/xrom.html>

<sup>2</sup>REFFIT: <http://www.ncdc.noaa.gov/paleo/softlib/redfit/redfit.html>

## 12. LXP 38.55: OCTOBER 2014 OUTBURST

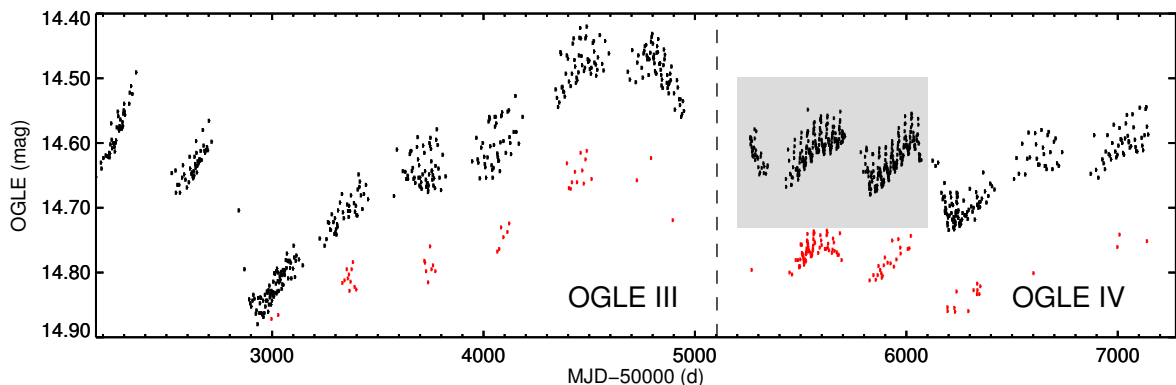


**Figure 12.8:** OGLE I (black) & V (red) band light curves. Data obtained during the OGLE-III and IV phases are separated by the vertical dashed line. The grey shaded area marks the first 900 d of the OGLE-IV phase when the system was observed more frequently. The  $\sim 30.77$  d period is clearly seen within this interval.

for the presence of additional components that can both improve the residuals of the fit and account for known physical processes resulting in X-ray emission from BeXRBs systems. Our analysis indicates that a model composed of an absorbed power-law plus a high-temperature black-body ( $kT \sim 2$  keV) model (Fig. 12.4) improves the fit. A model composed by an absorbed power law ( $\Gamma = 0.6$ ) and a multi-temperature low-temperature disc black body ( $kT \sim 0.1$  keV) provides an acceptable fit but only improves the residuals at lower energies. The tested models can help us to study different emission mechanisms and understand the physical properties of different regions in the binary system, like the accretion column towards the magnetic poles of the neutron star, or the inner edge of the accretion disc at the outer parts of the magnetosphere.

The normalization of the best fit model with a high-energy black-body component yields an accretion region with a radius of 0.7 km, and can be interpreted as emission from a polar cap. The normalization of the multi-temperature black-body component translates to an emitting region with a size of  $\sim 200$  km, which could be the inner region of an accretion disc around the NS. Another possible explanation is that this low temperature multi-temperature black-body component originates from reprocessing of X-rays in the inner part of the accretion disk. Hard X-rays originating from the NS can illuminate an area at distance  $R_{ir}$  under a solid angle  $\Omega$ . This radius is different than the one computed from the normalization of the black-body and can be calculated from  $R_{ir} = (4\pi\sigma T_{BB}^4/L_X)^{-1/2}$  (Hickox et al. 2004), where  $L_X$  is the total X-ray luminosity and  $T_{BB}$  is the temperature of the black-body. From fitted parameters we calculate a radius of  $\sim 600$  km.

Expressing  $L_X$  in terms of mass accretion rate we find  $\dot{M} = 3.5 \times 10^{-10} M_\odot \text{ year}^{-1}$  using a typical accretion efficiency value of 0.2 (Sibgatullin and Sunyaev 2000). Assuming the magnetospheric radius of the NS has the same size as the accretion disc inner radius we can make an order of magnitude estimation of the magnetic field strength of the NS. Following Frank et al. (2002), for an X-ray luminosity of  $4 \times 10^{36} \text{ erg s}^{-1}$ , a magnetospheric radius of 200 km and typical values for the mass and radius ( $M_{NS} = 1.4 M_\odot$  and  $R_{NS} = 12.5 \text{ km}$ ) we derive a magnetic field strength of  $10^{10}$  G. Moreover, we note that the magnetospheric radius is much smaller than the corotation radius of the NS,

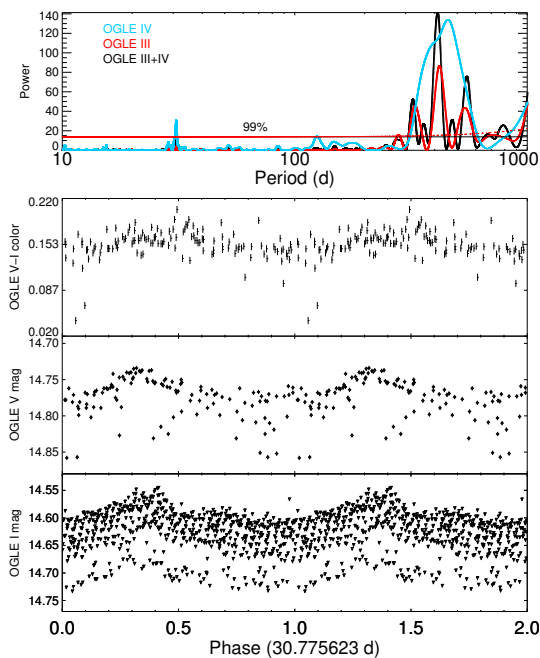


**Figure 12.9:** Upper panel: Lomb-Scargle periodogram of the OGLE III and IV I band photometric data of LXP 38.55. Horizontal lines indicate the 99% confidence level for significant periods. Bottom three panels: OGLE V-I, V & I band phase folded light curves. In order to avoid confusion only data from OGLE-IV epoch were used. Throughout the current study all folded light curves are produced with a the same folded period as in this plot ( $\sim 30.776$  d) and zero phase of 56965 d.

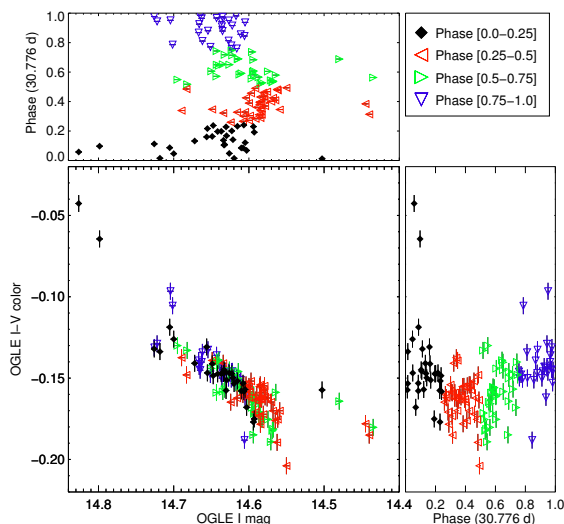


**Figure 12.10:** LXP 38.55 OGLE colour magnitude diagram. For comparison the phase folded I-V colour light curve is plotted on the right, while the phase folded I band light curve is plotted on top of the plot. Both light curves are folded for the  $\sim 30.776$  d period. The group of observations performed between “MJD 56100” and “MJD 56500” when the optical luminosity of the system was at its lowest stage follows the same modulation in lower luminosities, see group of points with I mag  $> 14.68$  on the left of the main plot.

which is  $R_{co} = (G M_{NS} P_{\text{spin}}^2 \pi^{-2}/4)^{1/3} = 1.9 \times 10^4$  km, where  $P_{\text{spin}}$  is the spin period of the NS. If we assume that the accretion originates from a Keplerian disc with inner radius  $r$  where the velocity of the disc exceeds the spin angular velocity of the NS, we conclude that the interaction between the Keplerian disc and the NS results in a spin-up of the system (accretor regime).

The 30.77 d optical modulation can be attributed to the orbital period of the NS-Be star system. This modulation is associated to the truncation of the Be disc due to gravitational interaction with the NS during an orbital revolution. The colour modulation –redder when brighter– is also a result of changes in the decretion disc around the Be star. A face-on geometry of the disc is expected to cause the above behaviour (Rajoelimanana et al. 2011). Similar behaviour has been encountered in numerous BeXRBs systems, like XMMU J010743.1-715953 (Coe et al. 2012), LXP 168.8 (Maggi et al. 2013), LXP 8.04 (Vasilopoulos et al. 2014a) or isolated Be Stars in the

SMC (de Wit et al. 2006). The disc adds cooler light to the stellar emission of the B Star without obscuring the star itself (face-on geometry), while variations in the disc size or radius within the binary orbit result in a variable SED. This is also noticeable in the GROND observations where the optical part of the SED (dominated by the B star) is much less variable than the IR (larger contribution from the Be disk).

The long term optical variability (super-orbital) is believed to be related to the formation and depletion of the circumstellar disc around the Be star (Rajoelimanana et al. 2011). The  $\sim 30.77$  d orbital modulation was still present in all the available data, and the same colour modulation –redder when brighter– was detected (see Fig. 12.10). During the OGLE-III phase the system exhibited high long-term variability evident of a variable Be disk. There is no evidence for significant changes in the size of the disc during the OGLE-IV epoch, where the amplitude of orbital modulation in the optical band is comparable to the long term variability of the system. Multi-epoch observations in the X-ray and optical would allow for a comparison between the long term X-ray and optical variability, unfortunately all the available X-ray observations were performed when the OGLE I band magnitude of the system was between 14.55 and 14.7.

By comparing the available X-ray observations that were performed on times separated by more than one orbital period, but correspond to the same orbital phase we can advocate about the long term X-ray variability of the system. The *XMM-Newton* slew detection was performed at a phase when only *Swift* observations were available (phase 0.87 of Fig. 12.1 & 12.9). By comparing their fluxes we derive that at the time of the *XMM-Newton* slew detection the luminosity of the system was higher by a factor of  $3.3 \pm 1.0$  compared to the one measured with *Swift*. The Chandra observation of the system was performed on MJD  $\sim 53537.1$  d corresponding to phase 0.61. The luminosity of the system was found to be  $\sim 2.6 \times 10^{36}$  erg s $^{-1}$  in the 0.3-10.0 keV band. By comparing the reported luminosity to the *Swift* luminosity corresponding to the same orbital phase we found that the system was brighter by a factor of  $\sim 1.1$  during the *Swift*/XRT monitoring performed on November 2014. Our data confirm the findings of D’Aì et al. (2011) that the systems long term X-ray emission is persistent within a variability factor of  $\sim 3$ -4, which is lower than the orbital variability (variability factor  $\sim 10$ ).

Our *Swift*/XRT monitoring was performed when the average OGLE I band magnitude of the system was  $\sim 14.65$ . Based on the SED modelling we found that in the I band the system has an excess of  $\sim 24\%$  compared to the template flux of a B star with same temperature (see Tab. 12.3). Interestingly this translates to a difference of  $\sim 0.23$  in magnitude, which is exactly the difference between the average I magnitude during our monitoring and the lowest flux level observed in the OGLE I band; I mag of 14.88 at MJD 52930 d. This might be evident of an epoch where the Be disc was almost completely depleted.

D’Aì et al. (2011) reported the system as a possible wind fed X-ray system, but our results reveal the presence of a cooler component in the SED of the companion star suggesting that this is a NS pulsar with a Be companion. Moreover, the hot thermal excess in the X-ray spectrum adds to the population of BeXRBs systems sharing this feature. Recently La Palombara et al. (2013b) reported a population of long spin ( $>200$  s), low luminosity ( $L \sim 10^{34}$  erg s $^{-1}$ ), X-ray persistent Galactic BeXRBs systems showing

this characteristic feature. A similar hot thermal excess was also found in the X-ray spectra of other **BeXRBS** in the Magellanic Clouds during moderate outbursts with  $L \sim 10^{36}$  erg  $s^{-1}$  (Vasilopoulos et al. 2013a; Bartlett et al. 2013a). LXP 38.55 is likely another example of such a system, showing evidence of a hot black-body component at higher X-ray luminosity, suggesting the black-body component is more common and not limited to the population originally proposed by La Palombara et al. (2013b). It is not clear if this feature is model dependent, but the physical parameters derived from such a phenomenological spectral treatment where the degeneracy of the fitted parameters is significant should be treated as order of magnitude approximations. Yet the study of such systems in the Magellanic Clouds has the major advantage of the low column density in the line of sight, thus through the study of these systems we are able to improve the modelling of their X-ray spectrum and derive stringent constraints on our findings.

The position of LXP 38.55 in the Corbet diagram (Knigge et al. 2011) lies close to the best fit line derived from the population of confirmed MC pulsars (see Fig. 12.11). Looking at the properties of other **BeXRBS** systems located near LXP 38.55 in the  $P_{\text{spin}}$  vs.  $P_{\text{orbit}}$  diagram, we found no notable similarities between them and the newly reported system. Most of these systems show much larger long term X-ray variability, with variability factors  $\sim 1000$ , as expected for such short-spin systems (Haberl and Sturm 2016). However since LXP 38.55 is a newly discovered system, future observations might reveal a higher variability factor. Moreover, the lack of deep X-ray observations during their peak luminosity prohibits us from comparing their X-ray spectral properties. SXP 25.55 (Haberl et al. 2008b) with an orbital period of 22.5 d (Rajoelimanana et al. 2011) is an SMC **BeXRBS** pulsar located very close to the position of LXP 38.55 in the Corbet diagram. An *XMM-Newton* spectrum is available for this system, but its peak luminosity is about 30 times smaller than that of LXP 38.55, while its spectrum is affected by stronger absorption. LXP 28.28 (Şahiner et al. 2016) is the closest LMC system having an orbital period of  $\sim 27.1$  d. (Coe et al. 2015).

## 12.4 Conclusions

A triggered *XMM-Newton* ToO observation of the candidate **BeXRBS** system IGR J05007-7047 located in the LMC revealed coherent X-ray pulsations with a period of 38.551(3) s. The X-ray spectrum of the system can be described by an absorbed power-law ( $\Gamma \sim 0.63$ ) plus a hot black body component ( $\sim 2.04$  keV) that can be interpreted as black body emission from a small region, most likely the polar cap of the NS. Addi-

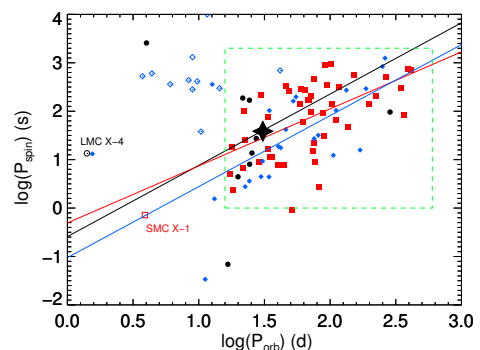


**Figure 12.11:** Corbet diagram of the LMC (black circles), SMC (red squares), and Milky Way (blue diamonds) HMXB pulsars. Open symbols denote SG-XRB systems while filled indicate **BeXRBS** systems. The black star points to the position of LXP 38.55. The green box indicates the locus where most of the **BeXRBS** pulsars are found. The best fit lines of the three groups are produced from points within this area and have slopes of  $\sim 1.5$ ,  $\sim 1.2$  and  $\sim 1.5$  respectively.

## 12. LXP 38.55: OCTOBER 2014 OUTBURST

---

tionally there is a statistically significant evidence for a soft excess that can originate from a region close to the magnetospheric radius and is a result of reprocessing of hard X-rays emitted by the accretion column of the NS. Analysis of optical data confirms the 30.776(5) d orbital period that was previously reported. By using simultaneously obtained optical and NIR data we constructed the SED of the binary system that reveals the presence of a decretion disc around the massive optical companion of the NS. Our analysis confirms LXP 38.55 as the 17<sup>th</sup> HMXB pulsar in this star forming galaxy.

## SXP 2.16: November 2015 outburst

**I**n this chapter we present the temporal and spectral properties of IGR J01217-7257 as determined by an *XMM-Newton* ToO observation that was triggered during a major outburst. In addition to the *XMM-Newton* observation, we monitored the system during the X-ray outburst using *Swift*/XRT, which allowed us to constrain the magnetic field strength of the NS. We investigated the long-term behaviour of the system using the  $\sim 6.3$  yr optical light curve as obtained from the Optical Gravitational Lensing Experiment (OGLE, Udalski et al. 2015), and the  $\sim 2.5$  yr X-ray light curve as observed by *Swift*/BAT.

### 13.1 XMM-Newton observations during the November 2015 outburst

The *XMM-Newton* ToO observation (obsid: 0763590401) was performed on November 7, 2015 (MJD 57333.6 d), using the full frame thin filter set-up for the EPIC-pn detector (Strüder et al. 2001), and full frame medium filter for both EPIC-MOS detectors (Turner et al. 2001). *XMM-Newton* SAS 15.0.0<sup>1</sup> software was used for data processing. We checked for background contamination of the data due to flaring activity by applying background thresholds of 8 and 2.5 counts ks<sup>-1</sup> arcmin<sup>-2</sup> in the 7.0–15.0 keV band for the EPIC-pn and EPIC-MOS detectors, respectively. The light curves were affected by only a few short, relatively weak flares, resulting in net exposure times of 22.0, 23.7, and 23.6 ks for pn, MOS1, and MOS2 after flare removal. Source event extraction was performed using a circular region around the source, while background events were extracted from a nearby area free of point sources. The radii of the source extraction regions were optimised for signal-to-noise ratio using the SAS task `eregionanalyse`. The MOS frame time in full frame mode is too long to resolve the short pulsations discovered in IGR J01217-7257. In addition differences in calibration between the detectors make comparison between phase resolved spectra (EPIC-pn) and phase averaged (EPIC-pn and EPIC-MOS) more difficult. Therefore, we considered only EPIC-pn data in the timing and spectral analysis presented here. For the EPIC-pn spectra and light curves, we selected single- and double-pixel events (`PATTERN`  $\leq 4$ ) with highest-quality flag (`FLAG = 0`). Spectra and response files for the spectral analysis were created by using the SAS task `especget`. Spectra were binned to achieve a minimum signal-to-noise ratio of fifteen for each bin for both phase-averaged and phase resolved spectra. The spectra from the Reflection Grating Spectrometer (RGS, den Herder et al. 2001) were extracted with `rgsproc`, the RGS1 and RGS2 spectra were combined using the task `rgscombine`.

#### 13.1.1 X-ray position

The position of the source was determined by performing a maximum-likelihood source detection analysis on the EPIC images. In total fifteen images were created from the three EPIC cameras in the five standard energy bands:  $1 \rightarrow (0.2 - 0.5)$  keV,

<sup>1</sup>Science Analysis Software (SAS), <http://xmm.esac.esa.int/sas/>

### 13. SXP 2.16: NOVEMBER 2015 OUTBURST

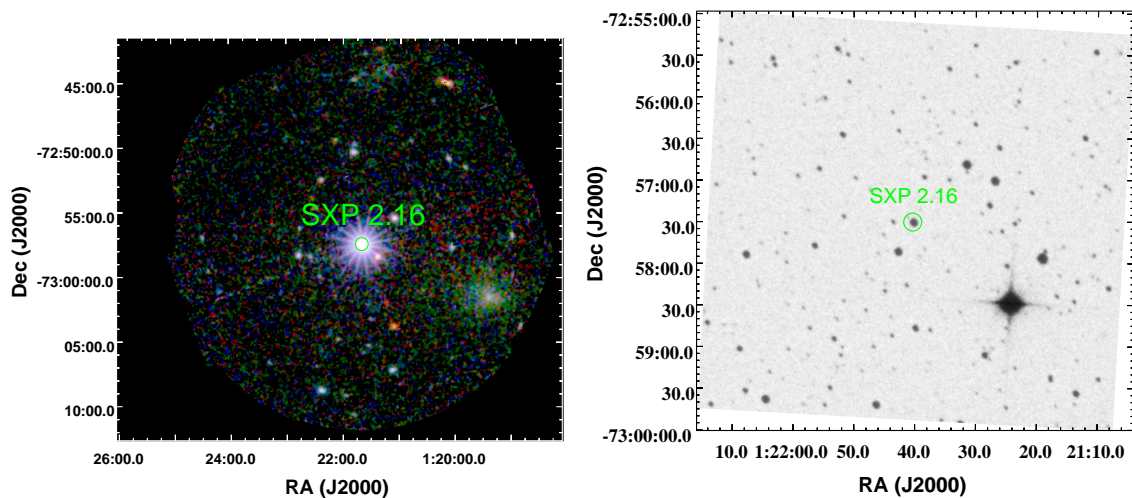


**Figure 13.1:** *Left:* *XMM-Newton* X-ray image of SXP 2.16. For the colours three energy bands were used, red $\rightarrow$ (0.2-1.0) keV, green $\rightarrow$ (1.0-2.0) keV and blue $\rightarrow$ (2.0-4.5) keV. The *XMM-Newton* X-ray position is marked with a green region. *Right:* optical R band image of SXP 2.16. The circle size does not represent the error circle ( $\sim 1''$ ) but has been rescaled ( $\sim 6''$ ) for plotting purposes.

2  $\rightarrow$  (0.5 – 1.0) keV, 3  $\rightarrow$  (1.0 – 2.0) keV, 4  $\rightarrow$  (2.0 – 4.5) keV, 5  $\rightarrow$  (4.5 – 10.0) keV (Watson et al. 2009; Sturm et al. 2013a). Source detection was performed on all the images simultaneously using the SAS task `edetect_chain`, resulting in a position for IGR J01217-7257 of R.A. =  $01^{\text{h}}21^{\text{m}}40.^{\text{s}}54$  and Dec. =  $-72^{\circ}57'32''.6$  (J2000), with a  $1\sigma$  statistical uncertainty of  $0.02''$ . However, the positional error is dominated by systematic astrometric uncertainties, which can reach several arc seconds (Sturm et al. 2013a). Our derived X-ray position agrees within  $1.7''$  with 2MASS J01214061-7257309 which corresponds to the proposed optical counterpart AzV 503 = [MA93] 1888 (Meyssonnier and Azzopardi 1993) and confirms the association. In Fig. 13.1 we present the X-ray image of SXP 2.16 created from the *XMM-Newton* data, together with an optical finding chart in the R band (Guibert 1992; Bonnarel et al. 2000).

#### 13.1.2 X-ray timing analysis

We searched for a periodic signal in the EPIC-pn event arrival time series by using an epoch folding technique (Davies 1990; Larsson 1996). The method uses a set of trial periods within a predefined range and performs a  $\chi^2$  test based on the constant signal hypothesis. If the data are folded with an arbitrary period the result will be a flat signal, and any deviation will be consistent with Poisson statistics. If the real period is used the pulse profile will significantly diverge from a flat profile (constant signal hypothesis). Thus, a large value of the  $\chi^2$  indirectly supports the presence of a periodic signal. A disadvantage of this method is that it lacks proper determination of the period uncertainty. Normally, the full width at half maximum of the  $\chi^2$  distribution gives an order of magnitude estimate for the uncertainty, but this value only improves with the length of the time series and not with the number of events (Gregory and Loredo 1996). In order to have a better estimate for both the period and its error, we applied the Gregory-Loredo method of Bayesian Periodic Signal Detection (Gregory and Loredo 1996), using the prior knowledge of the existence of a period around the range predicted

by the epoch folding method. From the Bayesian analysis we detect coherent pulsations in the 0.3-10.0 keV energy band and derive a period of 2.1650122(17) s. We have repeated the analysis for the five *XMM-Newton* standard energy bands individually. The resulting most probable values of 2.165005(10) s (0.2-0.5 keV), 2.165016(3) s (0.5-1.0 keV), 2.165010(3) s (1.0-2.0 keV), 2.165011(4) (2.0-4.5 keV) and 2.165010(4) (4.5-10.0 keV) for the period all agree within their statistical uncertainties. The phase-folded light curve profiles for the five energy bands and the full band are shown in Fig. 13.2. The pulse profile in the full energy band is complex with multiple peaks of different width and strength.

Based on the five energy bands, we defined four hardness ratios ( $i = 1-4$ ) as  $HR_i = (R_{i+1} - R_i)/(R_{i+1} + R_i)$ , with  $R_i$  denoting the background-subtracted count rate in the  $i^{\text{th}}$  energy band. In Fig. 13.2 we present the phase resolved hardness ratios that correspond to the phase-folded light curves of Fig. 13.2. As can be seen the profile strongly varies with energy. To better visualise the spectral changes with pulse phase we produced a 2D-histogram for the number of events as function of energy and phase (top panel of Fig. 13.3). The histogram of the events covers a large dynamic range due to the strongly varying efficiency of the camera and telescope with energy. To produce an image where features are easier recognised we normalised the histogram by the phase-averaged count rate in each energy bin (middle panel, Fig. 13.3). Finally we further normalise by the energy-averaged count rate in each phase bin (bottom panel, Fig. 13.3). If the X-ray spectrum would not vary in shape then the resulting image would be a smooth single-colour plot.

Despite of the complexity of the pulse profiles, several features can be recognised in Figs. 13.2 and 13.3:

- (i) The two major peaks in the pulse profile around phases 0.2 and 0.7 in Fig. 13.2 originate from low-energy emission ( $< 2.0$  keV), while the two weaker peaks at phases 0.4 and 0.55 are produced by emission at higher energies.
- (ii) In the 2D-histogram a pattern with reverse “Y” ( $\Lambda$ ) shape appears in the normalised images, with the profile gradually changing from a broad single peak with maximum at phase 0 (or 1) at very low energies ( $< 0.5$  keV) to a double peak profile at medium energies ( $\sim 0.5-3$  keV) and finally to a broader single peak (although with some structure) with maximum near phase 0.4 at the higher energies.

### 13.1.3 Spectral analysis

For the spectral analysis we used the X-ray spectral-fitting program `XSPEC` version 12.9.0 (Arnaud 1996). Given the available source counts ( $\sim 10^5$ ) we used  $\chi^2$  statistics for the fitting procedure, with all the uncertainties calculated based on a  $\Delta\chi^2$  statistic of 2.706, equivalent to a 90% confidence level for one parameter of interest.

The data were fitted by several combinations of absorbed models. The X-ray absorption was modelled using the `tbnew`<sup>1</sup> code, a new and improved version of the X-ray absorption model `tbabs` (Wilms et al. 2000), while the Atomic Cross Sections were adopted from Verner et al. (1996). The photo-electric absorption was modelled as a combination of Galactic foreground absorption and an additional column density accounting for both the interstellar medium of the SMC and the intrinsic absorption of the source. For the Galactic photo-electric absorption we used a fixed column density

---

<sup>1</sup><http://pulsar.sternwarte.uni-erlangen.de/wilms/research/tbabs/>

### 13. SXP 2.16: NOVEMBER 2015 OUTBURST

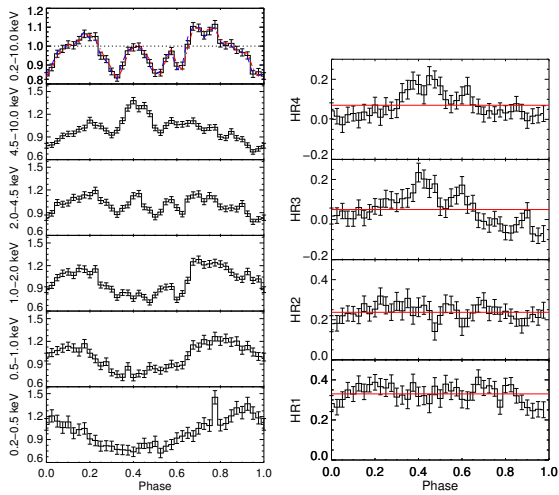


**Figure 13.2:** Left: Phase-folded pulse profile of IGR J01217-7257 obtained from EPIC-pn data in the *XMM-Newton* 0.2–10 keV energy band, and the five sub-bands. The histogram and data points with error bars are derived using the highest-likelihood period. For the 0.2–10 keV energy band, blue and red lines indicate the profiles for the lower and upper  $1\sigma$  confidence limits of the period. The profiles are background subtracted and normalised to their average count rate (from top to bottom: 4.735, 0.34, 0.68, 1.1, 1.2 and 1.40 cts s<sup>-1</sup>) Right: Hardness ratios derived from the pulse profiles in two neighbouring standard energy bands (see left) as a function of pulse phase. The red lines mark the pulse-phase average values for each quantity.

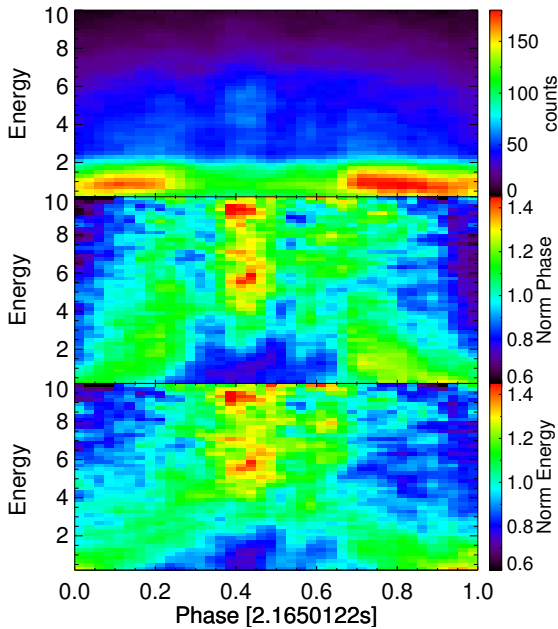


**Figure 13.3:** Phase dependent spectral heat map, obtained by binning the EPIC-pn source counts to 40 phase and 50 energy bins. Top: Colours are proportional to the number of counts per bin. Middle: Data normalised by the phase-averaged number of counts in each energy bin. Bottom: Data normalised a second time using the energy-average of each phase bin.

of  $N_{\text{H,GAL}} = 4.3 \times 10^{20} \text{ cm}^{-2}$  (Dickey and Lockman 1990a), with abundances according to Wilms et al. (2000).

While the average distance of the SMC is well measured (62.1 kpc, Graczyk et al. 2014), recent studies provide accurate distances to individual Cepheids in the galaxy, which confirms that the SMC is tilted and elongated towards the observer. This results in a distance uncertainty of up to  $\sim 30\%$  (Scowcroft et al. 2016). Using their results, we find that for the position of SXP 2.16 in the Eastern Wing the distance to the pulsar can be up to 6 kpc shorter than the average, yielding a minimum value of  $\sim 56$  kpc. In our calculations we will use the average distance of the SMC, but we note that quantities like the luminosity of the system can be up to 23% overestimated compared to the ones assuming the minimum distance of 56 kpc.

### Phase-averaged spectrum

We first investigated the phase-averaged spectrum with different combinations of models which were used in the past to fit the X-ray spectra of BeXRBs (Table 13.1). The fit with an absorbed power-law model was unacceptable with large systematic deviations over the whole energy band. The residuals show a large deviation from a normal distribution (see residual method; Andrae et al. 2010). To improve the fit at low energies, we added soft components like black-body or disc black-body emission. These components do not aim to represent seed photons of the accreting column, their use was to model the low energy excess in general. However, if we just use a phenomenological parametrization the accretion column should have a gradient in its temperature, thus the disc black-body could provide a better fit as it has a wider spectral energy distribution than the black-body. On the other hand the seed photons are going to be comptonised so the resulting spectrum can change significantly (West et al. 2017b; Becker and Wolff 2007a). A prominent feature in the residuals remained at high energies due to a turn-over in the spectrum. An acceptable fit with power law as basic model could only be achieved by adding a soft component and modifying the power law at high energies (see model 5 in Table 13.1).

Alternatively, we investigated a thermal comptonisation model (`nthcomp` in XSPEC; Zdziarski et al. 1996; Życki et al. 1999), a model with intrinsic curvature at higher energies. In this model, the high energy cut-off is determined by the electron temperature. Additionally, it incorporates the low energy roll-over parametrized by the seed photon temperature. The general shape of the model is set by the electron temperature and the electron scattering optical depth and can be parametrized by an asymptotic power law with index  $\Gamma$  (Sunyaev and Titarchuk 1980).

The comptonisation model provides the best fit among the models summarised in Table 13.1 over the total spectrum, without the need of additional components. Moreover, it provides a set of physical parameters (e.g. electron temperature, energy of seed photons) in contrast to the phenomenological approach of the power-law model. Thus, following Occams razor principle we use the most physical and simple model for our more detailed analysis. The best fit parameters are presented in Table 13.2, and the EPIC-pn spectrum with best fit thermal comptonisation model is presented in Fig. 13.4.

### Phase-resolved spectra

We created spectra from ten phase intervals of equal length and fitted them simultaneously with the thermal comptonisation model which yielded the best fit to the phase-averaged spectrum. Based on the flat HR1 and HR2 profiles (see Fig. 13.2) we

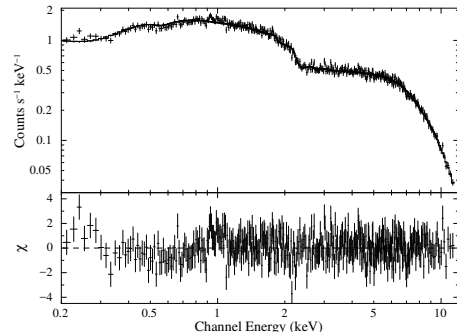


**Figure 13.4:** Pulse-phase averaged EPIC-pn spectrum of SXP 2.16. The top panel shows the spectrum together with the best-fit model composed of an absorbed thermal comptonisation component. The second panel shows the residuals in units of  $\sigma$ .

### 13. SXP 2.16: NOVEMBER 2015 OUTBURST

No.	XSPEC model	$\chi^2$	$\chi_r^2$	dof
1	tbnew*powerlaw	875.3	2.26	387
2	tbnew*powerlaw*highcut	873.6	2.27	385
3	tbnew*(bbody + powerlaw)	566.3	1.47	385
4	tbnew*(diskbb + powerlaw)	465.5	1.21	385
5	tbnew*(diskbb + powerlaw)*highcut	403.6	1.05	383
6	tbnew*nthcomp	379.8	0.99	385

For all models an additional absorption component is applied to account for the Galactic foreground absorption (see text).

**Table 13.1:** Analysis of the phase-averaged EPIC-pn spectrum with different models

Phase	$N_H$ ( $10^{20} \text{ cm}^{-2}$ )	Photon index	$kT_e$ (keV)	$kT_{bb}$ (eV)	$F_{\text{observed}}^a$ ( $\text{erg cm}^{-2} \text{ s}^{-1}$ )	$L^{a,b}$ ( $\text{erg s}^{-1}$ )
0.0 - 1.0	0.16 (<0.44)	1.160±0.003	3.61±0.09	3 (<56)	$4.30 \times 10^{-11}$	$2.01 \times 10^{37}$
0.0 - 0.1	0.26 (<0.57) <sup>c</sup>	1.203±0.008	3.55±0.10 <sup>c</sup>	4 (<55) <sup>c</sup>	$3.56 \times 10^{-11}$	$1.67 \times 10^{37}$
0.1 - 0.2		1.180±0.007			$4.21 \times 10^{-11}$	$1.97 \times 10^{37}$
0.2 - 0.3		1.148±0.006			$4.44 \times 10^{-11}$	$2.07 \times 10^{37}$
0.3 - 0.4		1.122±0.005			$4.32 \times 10^{-11}$	$2.01 \times 10^{37}$
0.4 - 0.5		1.099±0.004			$5.04 \times 10^{-11}$	$2.34 \times 10^{37}$
0.5 - 0.6		1.136±0.006			$4.20 \times 10^{-11}$	$1.95 \times 10^{37}$
0.6 - 0.7		1.146±0.006			$4.37 \times 10^{-11}$	$2.03 \times 10^{37}$
0.7 - 0.8		1.191±0.007			$4.32 \times 10^{-11}$	$2.02 \times 10^{37}$
0.8 - 0.9		1.208±0.008			$3.83 \times 10^{-11}$	$1.80 \times 10^{37}$
0.9 - 1.0		1.223±0.009			$3.34 \times 10^{-11}$	$1.57 \times 10^{37}$

<sup>a</sup> 0.2 – 10 keV.

<sup>b</sup> Source intrinsic luminosity corrected for absorption. Assumed distance 62.1 kpc.

<sup>c</sup> The spectral parameters for each phase-resolved spectrum were tied together. Thus, the same best-fit value is determined by the combined fit for each phase-resolved spectrum. For clarity we only list the value for the first phase bin.

**Table 13.2:** Spectral fit results for the thermal comptonisation model

can exclude spectral variation to be a result of changes in the column density. The ten spectra were fitted simultaneously with the same model. Within the fitting procedure some of the model parameters are tied to their equivalent values for each phase-resolved spectrum, meaning these parameters were free but were forced to have the same values for each spectrum. Other parameters were allowed to be free for each spectrum. As a first step all parameters for each spectrum were tied together and only the normalisations of the spectra were allowed to vary independently, while all other parameters were free in the fit, but forced to be the same for the spectra. This resulted in a reduced  $\chi^2$  of 1.36 with residuals clearly showing differences in the slopes of the spectra. Allowing in addition individual photon indices improves the fit to 1.0 (see Table 13.2). The EPIC-pn spectra are presented in Fig. 13.5, while the models corresponding to the phase-resolved spectra are plotted in Fig. 13.5. In statistical terms the  $\chi^2$  value of the fit was improved from  $\chi^2=4825$  (for 3553 DOF) to  $\chi^2=3587$  (for 3544 DOF), or equivalently  $\sim 31\sigma$  (F-test; Bevington 1969). To further demonstrate the improvement

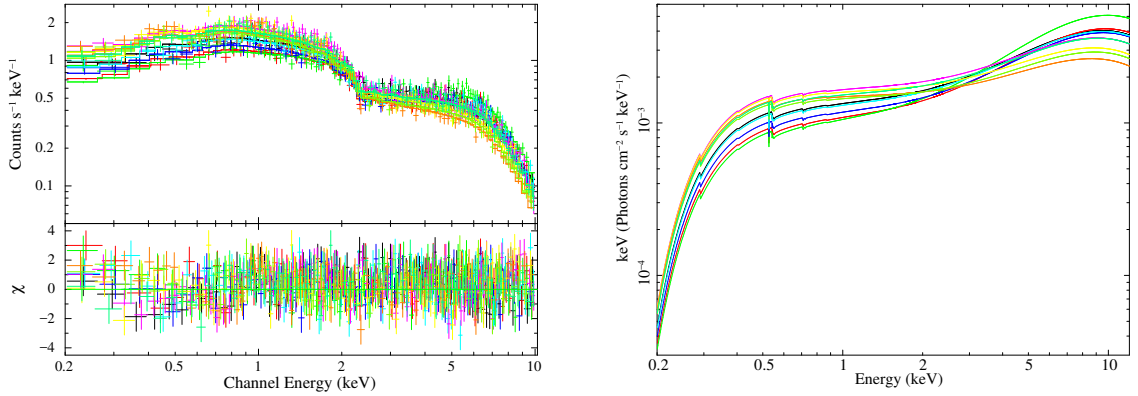


**Figure 13.5:** Left: Pulse-phase resolved EPIC-pn spectra of SXP 2.16. The top panel shows the spectra from the 10 phase intervals together with the best-fit thermal comptonisation model. The bottom panel shows the residuals in units of sigma. The model was fitted simultaneously to the spectra, only allowing normalisation and photon index to vary between the spectra. Right: Pulse-phase resolved spectral models derived from the fitted EPIC-pn spectra of SXP 2.16 shown in the left panel.

of the fit we used the residual method (Andrae et al. 2010). In simple terms the  $\chi^2$  method assumes that the distribution of the residuals follows a Gaussian distribution, thus by performing a Kolmogorov-Smirnov test (Kolmogoroff 1933; Smirnov 1948) to the residual distribution we can assess the goodness of the fitted model. This method rejected the assumption that the residual distribution is described by a normal distribution at a  $\sim 11\sigma$  significance when only the normalisation is left as a free parameter for the different phases, while it cannot reject the hypothesis when both the normalisation and  $\Gamma$  are left free. The photon index of the comptonisation model decreases, i.e. the spectrum hardens, with increasing flux during the X-ray pulse profile (see Fig. 13.6). Following Sunyaev and Titarchuk (1980) we can compute the electron optical depth as a function of the fitted photon index  $\Gamma$  and electron temperature  $T_e$ .

$$\tau = \frac{3}{2} \left( 1 + \sqrt{1 + \frac{4}{3} \frac{m_e c^2 / k T_e}{(\Gamma + 3/2)^2 - 9/4}} \right) \quad (13.1)$$

With the values of Table 13.2 we compute the optical depth as a function of spin phase. This yields a variable optical depth between 10.8 and 11.4 for the softest and hardest phase-resolved spectra respectively. Given that the optical depth is unavoidably model-dependent we just present the photon index as function of spin phase in Fig. 13.7.

### RGS spectroscopy

XMM-Newton RGS provided 4647 counts for 1<sup>st</sup> order and 1724 for 2<sup>nd</sup> order events. This allowed us to search for emission/absorption line features in the 0.33 to 2.0 keV energy range. The continuum is well fitted by an absorbed power-law model, and additional Gaussian components were fitted whenever a pattern was visible in the residuals of the fitted data. Three emission lines were identified with significance above  $3\sigma$  at energies of 500 eV, 572 eV and 653 eV. We can ascribe these features to

### 13. SXP 2.16: NOVEMBER 2015 OUTBURST

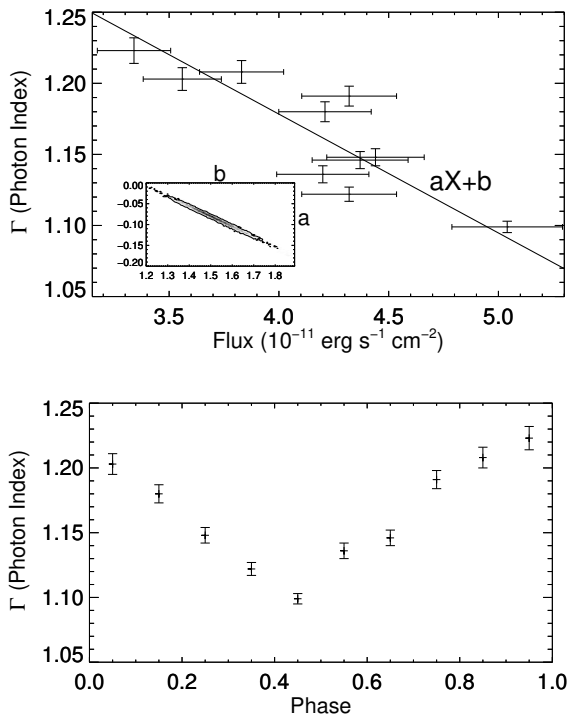


**Figure 13.6:** Photon index versus observed flux derived from the combined fit of the thermal comptonisation model to the phase-resolved spectra. The solid line shows the best fit of a linear function based on the median values of the posterior distribution of 10000 MCMC simulations (Kelly 2007) (Slope  $a = -0.085^{+0.021}_{-0.024}$ , in plot units). The  $3\sigma$  contour plot of the MCMC simulations is shown inset plot.

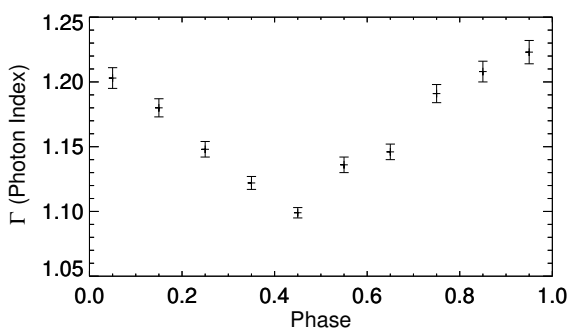


**Figure 13.7:** Photon index versus pulse phase derived from the combined fit of the thermal comptonisation model to the phase-resolved spectra.

the  $\text{Ly}\alpha$  line of N VII, the He-like triplet of O VII, and the  $\text{Ly}\alpha$  of O VIII, respectively. At energies below 450 eV the data had low signal to noise thus could not constrain the existence of any emission lines. A broad emission feature is seen at energies around 1 keV in the EPIC-pn data, but despite the RGS high resolution capabilities we were not able to resolve any feature in this range. This feature can be due to blended Fe emission lines and a radiation recombination continuum from O VIII or Ne IX. The RGS Spectra are shown in Fig. 13.8 while most prominent lines are listed in Table 13.3.

### 13.2 Swift/XRT X-ray light curve

Following the discovery of the new outburst in October 2015, we monitored IGR J01217-7257 with *Swift*/XRT. The data were processed using the standard analysis methods described in Evans et al. (2007). For a more detailed description of the outburst we binned the events per *Swift*/XRT snapshot. For the non-detections we estimated the  $3\sigma$  upper limits using the Bayesian method introduced by Kraft et al. (1991). The

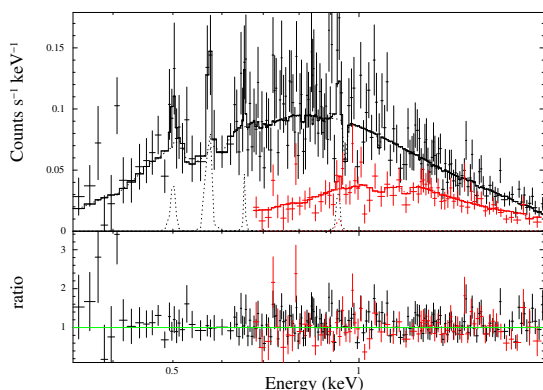


**Figure 13.8:** Best fit model for RGS spectra (0.33-2.0 keV). The continuum can be modelled by a simple power-law. Gaussian components were used to account for the presence of three major emission lines at 500 eV, 572 eV and 653 eV corresponding to the rest energies of N VII, O VII and O VIII respectively.

Gaussian line rest-frame (eV)	E eV	Equivalent Width eV	Luminosity $10^{34} \text{ erg s}^{-1}$
N VII - Ly $\alpha$ (500)	$500^{+5}_{-6}$	$6.7^{+2.7}_{-5.7}$	$0.71^{+0.5}_{-0.4}$
O VII (He-like triplet)	$572.0^{+2.5}_{-2.5}$	$16^{+5.6}_{-6.6}$	$1.7^{+0.8}_{-0.7}$
O VIII - Ly $\alpha$ (654)	$652.8^{+5}_{-8}$	$3.3^{+2.7}_{-2.7}$	$0.45^{+0.25}_{-0.23}$
Fe blended ??	$926.2^{+8}_{-6}$	$6.2^{+3.8}_{-3.7}$	$1.1^{+0.4}_{-0.4}$

Table 13.3: RGS spectroscopy

X-ray light curve is presented in the upper plot of Fig. 13.9. To search for spectral changes we computed hardness ratios for each *Swift*/XRT observation. No statistically significant change in the spectral shape was found, but we note that the results were limited by low statistics especially at higher energies. Thus, assuming the best-fit model found for the phase-averaged EPIC-pn spectrum and no spectral variability during the outburst, we converted the *Swift*/XRT count rates to luminosity by using a conversion factor of  $\sim 2.4 \times 10^{37} \text{ erg s}^{-1}/(c/s)$  (0.3-10 keV band). A sudden drop in the X-ray light curve is seen between MJD  $\sim 57360$  d and  $\sim 57363$  d (last detection during the burst). Between the *XMM-Newton* observation (at a luminosity of  $2 \times 10^{37} \text{ erg s}^{-1}$ ) and the last *Swift*/XRT detection the source brightness dropped by a factor of about 110 to a luminosity of  $\sim 1.8 \times 10^{35} \text{ erg s}^{-1}$ .

### 13.3 Optical/X-ray Variability

Our derived *XMM-Newton* position confirms the optical counterpart of IGR J01217-7257 suggested by Coe et al. (2014). To confirm the proposed 84 d for the orbital period of the BeXRB-system, we analysed the publicly available long-term X-ray (*Swift*/BAT) and optical (OGLE IV) light curves. We downloaded the OGLE-IV I band photometric data that are available online through the OGLE XROM<sup>1</sup> web page (Udalski 2008). The *Swift*/BAT and OGLE-IV light curves are shown in Fig. 13.9.

To search for periodicities we computed the Lomb-Scargle (LS) periodogram (Scargle 1982; Horne and Baliunas 1986) of the OGLE light curve. We searched for periodicities up to half of the total OGLE observing period, which at the time of the analysis was  $\sim 2262$  d. No significant ( $> 3\sigma$ ) period was found, while for the shorter periods ( $< 200$  d) the peak with the highest significance was located at  $\sim 167$  d. However, in the light-curve regular outbursts with about half that period are clearly visible in the OGLE-IV light curve (Fig. 13.9). We detrended the OGLE light curve by fitting the original data with a high-order polynomial and subtracting the best fit from the data (see middle panel in Fig. 13.9). Applying the LS algorithm to the detrended light curve yielded the detection of a  $83.6 \pm 0.2$  d period above the 99.99% significance level. The uncertainties were estimated via bootstrapping the data (10000 iterations) while using different polynomials for detrending the data.

*Swift*/XRT observations performed after the Oct./Nov. 2015 outburst suggest that

<sup>1</sup>XROM: OGLE-IV real time monitoring of X-ray variables: <http://ogle.astrouw.edu.pl/ogle4/xrom/xrom.html>

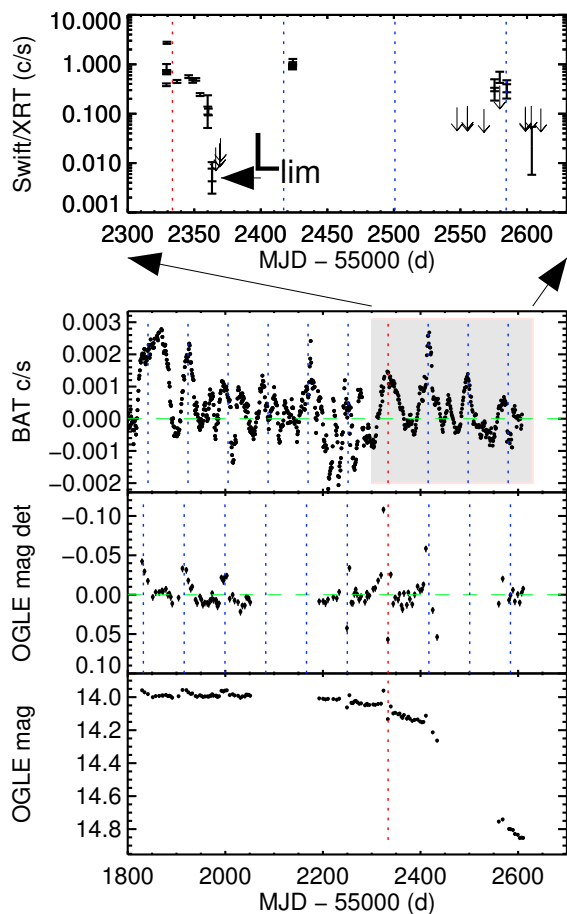


**Figure 13.9:** *Bottom plot - Bottom panel:* OGLE I band light curve of SXP 2.16 between May 2010 and August 2016. Magnitude uncertainties are plotted and comparable to the size of the data points ( $\sim 0.003$  mag). *Middle panel:* De-trended OGLE I-band light curve. Vertical dotted lines are separated by 83.58 d. *Top panel:* *Swift*/BAT light curve of SXP 2.16. The light curve was smoothed and no errors are shown for a clearer presentation. Vertical lines are separated by 81.78 d. In all panels the time of the *XMM-Newton* ToO is marked with a red dotted vertical line, all other vertical lines are in phase with the *XMM-Newton* ToO. *Upper plot:* *Swift*/XRT X-ray light curve during and after the Oct./Nov. 2015 outburst of SXP 2.16. For the pointings with no detection we plotted  $3\sigma$  upper limits using downward arrows. Vertical lines are spaced according to the period derived from the OGLE data. The horizontal arrow marks the minimum detection after a sudden drop in source flux during the Oct./Nov. 2015 outburst. The range of the plot covers the grey shaded area on the bottom plot.

IGR J01217-7257 went into outburst again at times roughly corresponding to the optical maxima (Fig. 13.9). To investigate the X-ray long-term variability, we analysed the available *Swift*/BAT data (upper panel of Fig. 13.9). Again, we used the LS algorithm on 10000 bootstrapped light curves and found a most probable period at  $82.0 \pm 0.3$  d. This is significantly different from the period derived from the optical with the  $3\sigma$  confidence regions for the two data sets not overlapping (see Fig. 13.10).

At the time of writing we became aware of a detailed long-term study focusing on the analysis of the OGLE and *Swift*/BAT light curves (Boon et al. 2017). Their results are consistent with our values for the OGLE optical period. Moreover, by back-processing archival *Swift*/BAT data covering a period of  $\sim 3300$  d they computed an improved X-ray period of  $82.5 \pm 0.7$  d. Their analysis also confirms that the X-ray data available from the *Swift*/BAT Hard X-ray Transient Monitor<sup>1</sup> (Krimm et al. 2013) covering the latest  $\sim 1000$  d of monitoring yield an X-ray period shorter than the optical period.

## 13.4 Discussion

The EPIC-pn data of IGR J01217-7257 revealed X-ray pulsations with a period of 2.1650122(17) s. The pulse period is very close to that of the transient XTE J0119-

<sup>1</sup><http://swift.gsfc.nasa.gov/results/transients/>

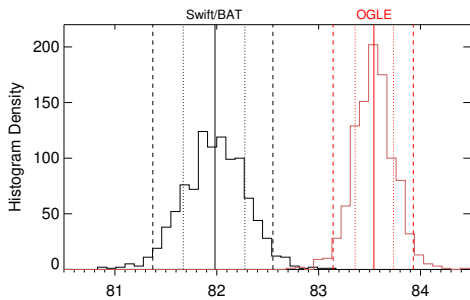


**Figure 13.10:** Histograms of the period distributions derived from the two samples of bootstrapped light curves (*Swift*/BAT in black and OGLE in red). Vertical lines mark the best derived period (solid), the  $1\sigma$  (dotted) and the  $2\sigma$  uncertainties.

731 (2.1652(1) s), discovered by Corbet et al. (2003a) in RXTE data from January 5, 2003. The reported RXTE position is  $\sim 19'$  away from the *XMM-Newton* position reported in this paper, as in previous cases the RXTE positional error ( $2'$  in R.A. and  $3.7'$  in Dec.) was underestimated. This strongly suggests that IGR J01217-7257 and XTE J0119-731 are the same source, that has shown little net change of the spin period of the neutron star over 12.8 years. The position derived from the EPIC images confirms the optical counterpart suggested for IGR J01217-7257 (Coe et al. 2014), the emission-line star AzV 503 = [MA93] 1888 with spectral type B0-5Ile (2dF survey, Evans et al. 2004) and radial velocity of  $146 \pm 3$  km/s. Below, we discuss the results of our analysis. We first comment on the orbital period as measured from *Swift*/BAT and OGLE light curves, then we discuss the X-ray light curve during the outburst as observed by *Swift*/XRT, and finally we discuss the shape of the pulse profile in the context of the phase resolved spectroscopy.

### 13.4.1 Optical period

Analysis of the OGLE-IV data of the optical counterpart revealed a period of  $\sim 83.6$  d confirming the reported period by Coe et al. (2014). We additionally found that the *Swift*/BAT X-ray light curve shows evidence of a  $\sim 82.0$  d period, which is statistically different to the optical period. The LS algorithm used for period search is optimized to identify sinusoidal-shaped periodic signals in time-series data, which in our case is a fundamentally mistaken prior. Especially for the *Swift*/BAT data the shape of the light-curve for each cycle can vary significantly. This behaviour is not uncommon with several systems reported in the literature of BeXRB pulsars to have different X-ray and optical periods (Haberl and Sturm 2016; Bird et al. 2012), while there are cases where systems share the same optical and X-ray period (e.g. the 30.77 d period of LXP 38.55, Vasilopoulos et al. 2016b; D’Aì et al. 2011). This difference can be interpreted as a result of Be disc precession or its density profile. The periodic Type-I X-ray outbursts are a result of the interaction of the NS with the Be disk, the outburst reaches its maximum luminosity around periastron where the separation of the system becomes smaller, thus mass accretion becomes larger. But there can be cases where the maximum accretion does not happen exactly at periastron. This can be explained in terms of a non-axisymmetrical equatorial disc in which a one-armed perturbation (a zone in the disc with higher density) propagates around the star in the same direction as the nearly Keplerian orbits of the disc material (Telting et al. 1994). Disk precession in BeXRBs can be probed by studying the variability of the  $H\alpha$  line emission: as the Be disc orientation changes so does the double-peaked  $H\alpha$  line profile (Hirata 2007).

In some extreme cases a synchronization of line variations with the orbital periods occurs, but it is not clear under which conditions this can take place (Štefl et al. 2007). Nevertheless it is possible that the morphology or the precession of the Be disc can cause the difference in the X-ray and orbital period. We note that in case the disc precession had a period smaller than the observed length of the X-ray time series then this effect should smear out, thus it is possible with more future observations to find time intervals where the X-ray period is larger than the optical. To conclude, it is generally accepted that both X-ray and optical variability should originate from interactions of the NS with the decretion disc (e.g. Reig et al. 2010). However, in short time scales this correlation is not always clear (Reig and Fabregat 2015). Since the X-ray light curve presented here and by Boon et al. (2017) have a shorter coverage than the OGLE data, we argue that the optical period of SXP 2.16 should be considered as the orbital period of the system.

### 13.4.2 Propeller transition

*Swift*/XRT monitoring of the outburst started around the time the system reached the maximum X-ray luminosity and continued until its flux dropped below detection limit. A plausible explanation for the sudden drop seen in the *Swift*/XRT light curve is that the system is entering its propeller phase (Illarionov and Sunyaev 1975b; Campana et al. 2002). This luminosity jump mainly depends on the spin period of the NS ( $\propto P_{NS}^{2/3}$ ), and can be estimated to  $\sim 224$  in the case of SXP 2.16. Henceforth, we assumed a  $1.4 M_{\odot}$  NS with 12.5 km radius.

Using the detected minimum luminosity as observed by *Swift*, before the source became undetectable, we can estimate the magnetic field strength (B) of the NS. By using equation 3.5 and the observed limiting luminosity of the 2015 outburst of SXP 2.16 (upper plot of Fig. 13.9) we estimate a magnetic field strength of  $2.0 \times 10^{11}$  G for SXP 2.16. Based on the uncertainties of the NS mass-radius as well as the model uncertainties we can set an acceptable range for the magnetic field strength of  $\sim 1 - 4 \times 10^{11}$  G.

We note, that due to the spread of the monitoring observations of the system the limiting luminosity before the system enters the propeller phase should be regarded as upper limit. Recently Christodoulou et al. (2016) have traced the lowest propeller limit of BeXRB pulsars located in the MCs. They showed that most of the known pulsars measured fluxes lie in a loci limited by a lower dipole magnetic momentum of  $\mu = 3 \times 10^{29} \text{ G cm}^3$  ( $B \sim 3 \times 10^{11}$  G), our estimated values are close to that limit supporting the assumption that the system was caught by *Swift* near its transition phase. When the system enters the propeller phase the mass trapped within the magnetosphere should be accreted to the NS within a fraction of a second; this is comparable to the free fall time from that distance. Following this fact, it is generally assumed, that transition between the two phases should be equally fast, thus the transition between the two regimes would only be detectable by luck if the observation was performed during the transition. This has been the case for SMC-X2 a system with similar spin period outside our Galaxy (Lutovinov et al. 2017), when only upper limits were determined for its luminosity in the propeller regime after the accretor-propeller transition has been observed during a *Swift*/XRT monitoring. For SXP 2.16 the X-ray luminosity of the system dropped by a factor of  $\sim 17$  between the latest two *Swift*/XRT detections that were separated by about 3 days (MJD  $\sim 57360-3$  d).

An important consequence of a magnetic field of this order is the prediction of cyclotron resonance scattering features (CRSF, Schönherr et al. 2007a) within the energy range of the *XMM-Newton*/EPIC instruments. Following the equation  $E_{CRSF} = 11.57 \times B_{12}(1+z)^{-1}$  keV which stands as  $B \ll B_{cri}$ <sup>1</sup>, one predicts the presence of cyclotron absorption lines at energies close to 1-4 keV. In the literature there have been cases where even cyclotron emission features have been resolved from the spectra of low luminosity pulsars (Sguera et al. 2010; Nelson et al. 1995). In the case of SXP 2.16 we have found no clear evidence of features that can be associated with cyclotron resonance scattering. This might be an indication of the presence of multipolar magnetic field components near the surface of the NS, that would be responsible for higher magnetic field strength (Asseo and Khechinashvili 2002) thus producing cyclotron lines outside the *XMM-Newton* energy range. Interestingly, this is the second SMC pulsar with a magnetic field estimate based on the propeller limiting luminosity which is not confirmed by the detection of cyclotron resonance scattering feature, with SMC X-3 being the other one (Tsygankov et al. 2017).

### 13.4.3 X-ray spectral and temporal properties

RGS spectra reveal the presence of a few emission lines of N VII, O VIII and O VII. Similar lines have been measured in other BeXRB systems during outburst and their presence could be associated with the circum-source photo-ionized material within the inner disc (e.g. SMC X-2 La Palombara et al. 2016). SMC X-2, a system with similar spin period (2.37 s) and higher magnetic field strength ( $2-3 \times 10^{12}$  G Jaisawal and Naik 2016; Lutovinov et al. 2017) was observed with *XMM-Newton* during its 2015 outburst at a luminosity about ten times higher than SXP 2.16 (La Palombara et al. 2016). Interestingly the equivalent widths of the N VII and O VIII lines for SXP 2.16 were a factor of two smaller than those from SMC X-2, while for the O triplets was about two times higher (though the uncertainties were higher). Thus, there seems to be a connection between the luminosity of the system and the line emission, thus the ionization states of the material. This is also indicated by comparing the centroid of the O VII triplet, which is found to be at 572 eV for SXP 2.16 and 557 eV in SMC X-2. The latter is more dominated by the forbidden (z) line at 561, while in our case we have higher contribution from the 574 eV resonance (w) line. As the forbidden to resonance line is roughly the electron temperature-sensitive "G-ratio", there is also an effect of the photo-ionising temperature (Porquet and Dubau 2000) as evidenced by the difference of the O VII triplet centroid energy of the two systems. Thus, we can conclude that the photo-ionising source in SXP 2.16 (whatever it is) has higher  $T_e$  than in SMC X-2.

The pulse profile obtained from EPIC-pn data in the 0.2 - 10.0 keV energy band is complex with four major peaks. This leads to a power spectrum with the first (the strongest), second and third harmonics being stronger than the fundamental frequency at 0.46189 Hz. The spectral evolution with pulse phase (Fig. 13.3) revealed a characteristic change in the pulse shape with energy. Our phase resolved spectral analysis indicates that the change in the pulse profile can be explained by changes in source flux and spectral slope and does not require a change of the intrinsic column density

<sup>1</sup> $B_{cri} = (m^2 c^3)/(e\hbar) \sim 4.414 \times 10^{13}$  G, the magnetic field strength where the de Broglie radius of plasma electrons becomes comparable to its Larmor radius, thus quantum mechanical treatment of the electrons motion is required (Mészáros 1992)

### 13. SXP 2.16: NOVEMBER 2015 OUTBURST

---

responsible for soft X-ray absorption. Moreover, source flux and spectral slope are correlated in a way that the spectrum becomes flatter (harder) with increasing flux.

Phase averaged spectra could be explained by a simple comptonisation model with seed photons taken from a black-body distribution. The high energy cut-off of the spectrum provides a good constraint on the electron temperature that remains constant with spin phase. The temperature of the seed photons could not be well constrained since it is related to the low energy roll-off of the spectrum, the later falls near the lower energy range of *XMM-Newton*. Nevertheless this parameter does not affect the electron temperature and the optical depth of the comptonisation model. Among the models we tested (see Table 13.1), any combination containing a simple black-body component does not fit the data as well as a model containing a disc black-body component with similar temperature. Only if the black-body temperature is  $\sim 3.7$  keV the fit is statistically “good” (i.e.  $\chi^2_{\text{red}} \approx 0.99$ ) but then the black-body component contributes more to the higher energies ( $>5$  keV) than the PL, while the PL contributes to the lower energies. This model was rejected and is not included in Table 13.1 as it does not represent a physical mechanism. Additionally, it is not straight forward to compare the temperature of the thermal BB components used and the `nthcomp` seed photon temperature, due to the model parameters degeneracies.

Phase resolved spectral analysis (Table 13.2 and Fig. 13.6) shows that the change in the pulse profile can be explained by the comptonisation model with phase variable normalisation and slope. Based on the luminosity level of the system during the *XMM-Newton* observation and the NS properties ( $P_{\text{spin}}$ , B) we expect an accretion column to have been created (Mushtukov et al. 2015a,b). At any case, the high anisotropy of photon-electron cross-section in the presence of high magnetic fields (Lodenquai et al. 1974) can lead to anisotropic emission from the accretion column, thus we can expect moderate variations in the spectral shape with spin phase. Moreover, theoretical predictions put the source near the transition limit between the fan beam and pencil beam emission pattern regime, as the systems luminosity lies near the critical limit for shock creation (Basko and Sunyaev 1976; Schönherr et al. 2007a). The extra information needed to probe the emission pattern comes from the pulse profile itself. Pencil-beam emission is usually associated with single peak profiles, that tend to be more complex due to gravitational and obscuration effects (Mészáros 1992). Double peaked profiles yield a fan-beam dominated emission (Koliopanos and Gilfanov 2016; Rea et al. 2004; Paul et al. 1997). BeXRB in major outbursts have been known to have complex pulse profiles that combine both these patterns (Sasaki et al. 2012; Kraus et al. 1996), but most of the pulsed profiles studied in these cases did not include energies below 3 keV. The pulse profile of SXP 2.16 seems complex (Fig. 13.2) but our phase resolved analysis showed that the flux varies smoothly within the spin phase (Table 13.2 and Fig. 13.6) which is indicative of a pencil beam profile. If radiation was isotropically emitted by a hot spot, this would result only in a variable normalisation as the observing angle of the region changed with phase. But, in the heat map of SXP 2.16 (Fig. 13.3) we see that the spectrum becomes harder and softer with phase in a more or less continuous manner (reverse “Y” ( $\lambda$ ) shape). This show that the phase resolved variability is not only a product of a change of normalisation, but also due to anisotropic emission mechanism.

For all the models used for fitting the phase average spectra containing a PL com-

ponent (e.g. `diskbb+powerlaw`) the photon index is smaller compared to the `nthcomp`. However, if we use a PL component instead of the `nthcomp` for the phase resolved spectroscopy, then for the values of the PL slope we find the same trend in their evolution with phase as the ones found for the asymptotic slope of the comptonisation model.

#### 13.4.4 Limitations - Motivation for future observations

Although the thermal comptonisation model provides a good fit to the spectra of SXP 2.16, some of the model parameters take unphysical values. Namely the seed photon temperature appears to be too low, assuming the photons are produced at the base of the accretion column where a shock is formed. But accounting for the seed photon distribution is a much more complex problem, the distribution of the black-body photons might then resemble more a multi-temperature black-body, while one should account for the bremsstrahlung radiation produced by electrons below the shock. The optical depth luminosity dependence should also be treated as a qualitative result, as the electron scattering cross-section has a dependence on the magnetic field properties. A thorough treatment of accretion onto a magnetised NS has been presented by [Becker and Wolff \(2007a\)](#) while a model has been developed for `xspec` to treat the detailed model ([Farinelli et al. 2016](#)). Unfortunately this treatment would require broader X-ray spectra, since the model parameters cannot be sufficiently constrained within the *XMM-Newton* band. [West et al. \(2017b\)](#) focused on modelling the spectra of accretion powered NS by offering a detailed analysis of the hydrodynamic and thermodynamic structure of the accretion column. In their study they mimic the phase averaged spectra by assuming emission originating from different parts of the accretion column. Again their results could be implemented on bright sources with broader X-ray coverage, while additional assumptions about extra emission components were needed (e.g. accretion disk, Gaussian emission lines). Future X-ray observations during a similar moderate outburst of SXP 2.16 could offer the opportunity for combined observations with *XMM-Newton* and NuSTAR that could provide the broad band coverage needed for a more detailed treatment using adaptations of the above models.

### 13. SXP 2.16: NOVEMBER 2015 OUTBURST

---

## SXP 15.6: June 2016 outburst

**I**n this chapter we report on the X-ray spectral and temporal properties of the Be/X-ray binary system XMMU J004855.5-734946 located in the Small Magellanic Cloud. The system was monitored by *Swift*/XRT during a moderate outburst in July 2016, while an unanticipated Chandra target of opportunity observation was triggered when the luminosity of the system was greater than  $10^{36}$  erg s<sup>-1</sup> allowing a detailed study of the systems X-ray properties. Specifically, its X-ray spectrum, as observed during the outburst, is well modelled by an absorbed power law ( $\Gamma = 0.58$ ). Timing analysis of the collected photon events revealed coherent X-ray pulsations with a period of  $\sim 15.64$  s, thus confirming XMMU J004855.5-734946 as a high-mass X-ray binary pulsar. By analyzing archival *XMM-Newton* observations we determined the long term spin period evolution of the neutron star, showing that the compact star has spun-up by  $\dot{P} \sim -0.0028$  s yr<sup>-1</sup>. By modelling the X-ray pulsed emission as detected by Chandra we set constraints on the inclination of the magnetic and rotation axis of the neutron star, as well to its compactness (i.e.  $(M/M_{\odot})/(R/\text{km}) = 0.095 \pm 0.007$ ).

### 14.1 General information about the system

XMMU J004855.5-734946 is a **BeXRB** in the SMC (source XMM 1859 in the catalogue of [Haberl and Sturm 2016](#)) with a 36.432(9) d orbital period measured from optical photometry ([McBride et al. 2017](#); [Coe et al. 2016](#)). The optical counterpart of the system has been proposed to have a spectral type of O9 IIIe2 ([Lamb et al. 2016](#)), while [McBride et al. \(2017\)](#) have determined its spectral type to be B0 IV-Ve. Recently coherent X-ray pulsations have been reported ([Vasilopoulos et al. 2016a](#)), while in this study we expand upon the findings of the initial announcement by presenting a thorough analysis and review of the X-ray spectral and temporal properties of the system based on a large collection of new and archival X-ray data (i.e. Chandra, *Swift*, *XMM-Newton*).

The system was detected in June-July 2016 during the *Swift* SMC Survey (S-CUBED) monitoring program ([Kennea et al. 2016b](#)), at a luminosity level between  $10^{36}$  erg s<sup>-1</sup> and  $10^{37}$  erg s<sup>-1</sup> (a flux to luminosity conversion factor of  $\sim 4.6 \times 10^{47}$  cm<sup>2</sup> based on a 62 kpc distance is used throughout this study; [Graczyk et al. 2014](#)). Following the first detection of the system we requested *Swift*/XRT monitoring of the system to follow the evolution of the outburst, and a Chandra ToO to search for X-ray pulsations. The Chandra ToO revealed a spin period of  $15.6398 \pm 0.0009$  s, thus making XMMU J004855.5-734946 the 64<sup>th</sup> known HMXB pulsar in the SMC (for a most recent catalogue see [Haberl and Sturm 2016](#)). We suggest the alternative name SXP 15.6, following the nomenclature introduced by [Coe et al. \(2005\)](#) for the **BeXRB** pulsars in the SMC. Since SXP 15.6 has a known orbital period, by measuring its spin period we raise the number of systems where both the orbital and spin period is known to 49 ([Haberl and Sturm 2016](#)). Apart from the available Chandra and *Swift* data collected during the June-July 2016 event, we analysed the available archival *XMM-Newton* observations from 2006 and 2007. Thus, we were able to study the change in the temporal and spectral properties of SXP 15.6 over a period of ten years and over a luminosity

## 14. SXP 15.6: JUNE 2016 OUTBURST

---

range of almost two orders of magnitude.

The X-ray observations and their results are presented in §14.2. Data extraction and analysis are described in §14.2.1. The temporal analysis of the X-ray event time of arrivals is presented in §14.2.2, while the phase-averaged spectral analysis is reported in §14.2.3. The phase-resolved spectral analysis is shown in §14.2.4, and in the same section we present a basic modelling of the pulse profile of the neutron star by assuming that the X-ray flux of a pulsar originates from one or two antipodal polar caps. This in turn allows us to put constraints on the geometric properties of the system and compare them with basic models proposed for the equation of state of a NS. In §14.3 we discuss the results of the spectral and temporal properties of the system, and put the source in context of SMC pulsars by comparing its properties to other known systems.

### 14.2 Observations and data analysis of SXP 15.6

SXP 15.6 was detected in June-July 2016 during the *Swift* SMC Survey (S-CUBED) monitoring program (Kennea et al. 2016b), a wide-area and short-exposure ( $\sim 40$  s) survey of the SMC in X-rays with *Swift*/XRT (Burrows et al. 2005). On June 16, 2016 a marginal detection (upper limit,  $L_X < 5 \times 10^{36}$  erg s $^{-1}$ ) was made during the S-CUBED monitoring. On June 24, 2016 a short (37 s) *Swift*/XRT observation yielded a detection at an X-ray luminosity  $\sim 10^{37}$  erg s $^{-1}$  (Evans et al. 2016). A follow-up 1ks *Swift*/XRT ToO (obsid:00034599001 ; PI: G. Vasilopoulos) triggered by us and performed on June 29 measured an X-ray luminosity of  $L_X = 8.3 \times 10^{36}$  erg s $^{-1}$ , thus confirming the onset of a moderate outburst. This provided a unique opportunity to measure the spin period of one of the few BeXRBs in the SMC with known orbital period but unknown spin period. A Chandra ToO (DDT time; ObsID 18885; PI: G. Vasilopoulos) was performed on July 7, 2016, while our *Swift*/XRT monitoring was continued until July 12, 2016.

#### 14.2.1 X-ray data analysis

##### *Swift*/XRT data

The *Swift*/XRT data were analysed following the instructions described in the *Swift* data analysis guide<sup>1</sup>. We used `xrtpipeline` to generate the *Swift*/XRT products, while events were extracted by using the command line interface `xselect` available through HEASoft FTOOLS (Blackburn 1995)<sup>2</sup>. The `xrtmkarf` command was invoked to produce the auxiliary response files. For the analysis the latest response matrix was used, as provided by the *Swift* calibration database `caldb`.

##### Chandra data

For the Chandra observation of XMMU J004855.5-734946 a special instrument setup was used. Specifically the Chandra/ACIS instrument was used in a 1/4 sub-array mode which yields a readout time of 0.84104 s, which allows the detection of pulsations as fast as double the readout time, while it reduces the effect of pileup. XMMU J004855.5-734946 was projected on the S3 CCD, while a 4' offset was applied in order to mitigate the effect of pile up in case the luminosity was comparable or higher than that measured by *Swift*/XRT. Data reduction was performed with the CIAO v4.8.1 software (Fruscione

---

<sup>1</sup><http://www.swift.ac.uk/analysis/xrt/>

<sup>2</sup><http://heasarc.gsfc.nasa.gov/ftools/>

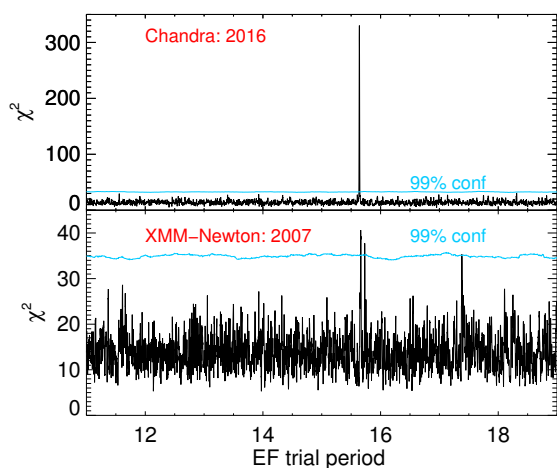


**Figure 14.1:** Results of period search using epoch folding method in the events collected from the Chandra ToO (upper panel) and the 2007 *XMM-Newton* observation. Confidence levels are determined from the results of the same method on 1000 simulated light curves.

et al. 2006). The source and the background events were extracted from circular regions with  $6''$  and  $21''$  radius, respectively. The CIAO script `specextract` was used to extract the source spectrum and create the appropriate response matrix files and ancillary response files used in the spectral analysis. We used the FTOOLS task `fcalc` in order to prepare the events for timing analysis. The event arrival times were randomized within the readout time-frame (i.e. 0.84104 s). This step was taken in order to remove artificial periodic signal and mitigate the aliasing due to the instrument readout time-frame. Barycentric corrections were applied to the randomized arrival times of the photons to account for the difference in photon arrival times as the Earth and Chandra move around the Sun.

### *XMM-Newton* data

*XMM-Newton* had performed two observations in the direction of the system in 2006 and 2007. Both observations were included in the analysis for the *XMM-Newton* point source catalogue of the SMC (Sturm et al. 2013a), where the first detection and classification of SXP 15.6 as a BeXRB candidate was reported. We analysed the available observations using *XMM-Newton* SAS 14.0.0<sup>1</sup> for the data processing, and selected source and background events from circular regions of  $24''$  and  $50''$  radius respectively. The first observation ( $\sim 20$  ks performed on March 19 2006; obsid: 0301170501), was highly affected by background flares that hampered in turn the source detection and estimation of flux level for SXP 15.6. The second observation was performed on October 28 2007 ( $\sim 20$  ks, obsid: 0503000201), with the same instrument set-up as the first one, and was not affected by background flares. For the 2006 observation a detection with a signal-to-noise ratio of 1.4 was possible, yielding a count rate of  $0.010 \pm 0.007$  c/s or a  $3\sigma$  upper limit of 0.03 c/s. For the second “flare free” observation, SXP 15.6 was the brightest source in the field of view of the *XMM-Newton*/EPIC camera, and  $\sim 1000$  counts were extracted from the EPIC detectors with  $\sim 13\%$  background contribution, resulting in a background/vignetting/PSF corrected count rate of  $0.081 \pm 0.003$  c/s for the EPIC-pn detector.

### 14.2.2 X-ray timing analysis

Only observations with a high number of events can be used for search of a periodic signal at a significant level ( $> 3\sigma$ ). From the available data sets, only events collected by Chandra ( $\sim 8500$  counts) and *XMM-Newton* (combined EPIC events  $\sim 1400$ ) provide enough number of counts for a period search.

A common tool used for X-ray timing analysis and search for periodic signal is the Fast Fourier transform (FFT), which is implemented through `powspec`, a tool provided by the HEASoft `XRONOS` package. Although this method provided a good estimate of the periodic signal present in the Chandra data, it failed to provide a significant detection in the archival *XMM-Newton* data, which is possibly the reason why a pulse period was not reported earlier.

To search for a periodic signal in both the *XMM-Newton* and Chandra data we used the epoch folding (EF) technique (Davies 1990; Larsson 1996). The EF method uses a set of trial periods within a predefined range and performs a  $\chi^2$  test based on the constant signal hypothesis. Thus, a maximization of the  $\chi^2$  indirectly supports the presence of a periodic signal. To determine the significance of any detection we created 1000 event files with random arrival times and applied the EF algorithm, the results were used to estimate a baseline for the maximum  $\chi^2$  value we would expect from a non periodic time series. For the Chandra data the EF method revealed the presence of a strong signal, while for the 2007 *XMM-Newton* observation a signal was revealed just above the 99% confidence limit. The results of our search for pulsations with the EF technique are shown in Fig. 14.1, for simplicity we restricted the plotting range around the determined period.

On the other hand, the Gregory-Loredo method (GL; Gregory and Loredo 1992) has several advantages over the FFT and EF algorithms for the search of a periodic signal in event arrival time data (Gregory and Loredo 1996). The GL method has been extensively used for the detection of BeXRB pulsars (e.g. Haberl et al. 2008a; Vasilopoulos et al. 2013a, 2014a, 2016b). A major advantage is that while the period's uncertainty of the EF method depends mainly on the length of the observation, in the GL method the uncertainty improves with the number of events. One should not confuse the uncertainty of the period with the strength of the detection, which for both methods increases with

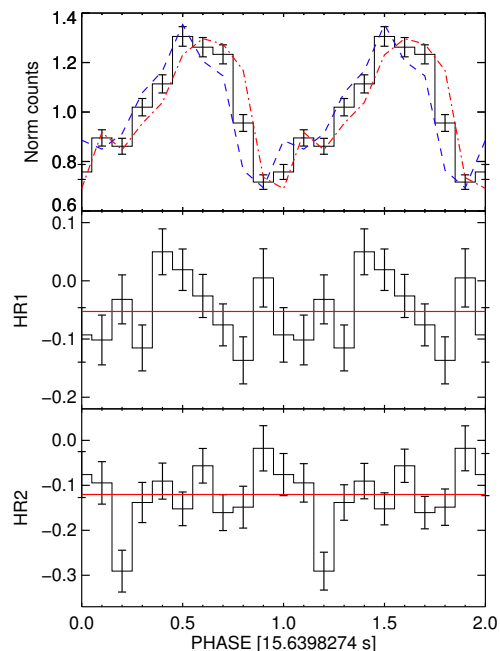


**Figure 14.2:** *Top:* Folded pulse profile obtained by folding the Chandra events to the best determined spin period (15.6398274 s), normalized at average count rate 0.340627 c/s, with lower and upper  $1\sigma$  errors of period in blue and red, respectively. *Middle-bottom:* Phase resolved hardness ratio profile in the [0.5-2.0:2.0-4.0] keV band (middle) and the [2.0-4.0:4.0-10.0] keV band (bottom). The red lines show the phase average values.

<sup>1</sup>Science Analysis Software (SAS), <http://xmm.esac.esa.int/sas/>

the available number of events. The GL method, being Bayesian, allows the inclusion of a prior on the period of the pulsar. Generally, the search can be limited between the minimum time resolution of the data and half the exposure duration. In our case we invoked the GL algorithm to have the best estimation of the pulse period and its uncertainty, and we restricted the search to the interval around the period derived from the EF method. Based on the GL algorithm, the presence of pulsations in the Chandra observation with a period of  $15.6398 \pm 0.0009$  s ( $1\sigma$  error) is confirmed at a larger than 99.9% significance level.

Based on the derived period we have constructed the X-ray pulse profile of SXP 15.6, shown at the top panel of Fig. 14.2. In the plot, the same number of bins has been used as in the GL analysis. The solid histogram represents the pulse profile based on the best fit period, the dashed lines represent the pulse profile folded with the  $1\sigma$  upper (blue) and lower (red) limits of the best fit period.

By using three different energy bands (0.5-2.0, 2.0-4.0, 4.0-10.0 keV), we can define two hardness ratios as  $HR_i = (R_{i+1} - R_i)/(R_{i+1} + R_i)$ , with  $R_i$  denoting the background-subtracted count rate in the energy band  $i$ . The middle and bottom panels of Fig. 14.2 show the soft ( $HR_1$ ) and hard ( $HR_2$ ) hardness ratios. The HR plots indicate no significant spectral variability over the pulse profile with the exception of a decrease in  $HR_2$  at phase  $\sim 0.2$ . This variation coincides with a minor second peak in the pulse profile, as seen in the top panel of Fig. 14.2. Nevertheless, the pulse profile of SXP 15.6 is consistent with a single peak shape, owing its variability mostly to changes in the intensity of the pulsed emission.

From the pulse profiles we can compute the pulsed fraction (PF) as the ratio between the difference and the sum of the maximum and minimum count rates over the pulse profile (i.e.  $PF = (F_{max} - F_{min})/(F_{max} + F_{min})$ ). For the total energy range 0.3-10.0 keV we get  $PF = 0.29 \pm 0.02$ , while for the three energy bands used for the HRs we get  $PF_{0.5-2.0} = 0.35 \pm 0.04$ ,  $PF_{2.0-4.0} = 0.33 \pm 0.04$  and  $PF_{4.0-10.0} = 0.36 \pm 0.04$ , thus there are no significant changes in the PF over the entire spectrum.

Initial timing analysis of the Oct. 2007 *XMM-Newton*/EPIC events with the FFT method (e.g. `powspec` task) did not yield any significant peak in the power spectrum. By applying the GL method and by using our prior knowledge of the existence of the period (e.g. 15-16 s) we confirmed the presence of pulsations at a larger than 99.9% significance. By using the same bin size for the folded data as in the Chandra events, the best period was measured to be  $15.664 \pm 0.004$  s ( $1\sigma$  error).

### 14.2.3 X-ray spectral analysis

The X-ray spectral analysis was performed with `xspec` (version 12.8.2, Arnaud 1996). A total of 8402 event photons were extracted from the Chandra/ACIS detector allowing us the use of  $\chi^2$  statistics in the fitting procedure. The data were successfully fitted by an absorbed power-law model. The X-ray absorption was modelled using the `tbnew` code, a new and improved version of the X-ray absorption model `tbabs` (Wilms et al. 2000), while the atomic cross sections were adopted from Verner et al. (1996). For separating the foreground and intrinsic absorption we used a combination of Galactic foreground absorption ( $N_{H,GAL}$ ) and an additional column density accounting for both the interstellar medium of the SMC and the intrinsic absorption of the source ( $N_{H,SMC}$ ). The column density of the Galactic component was fixed to a value of  $N_{H,GAL} = 3.99 \times 10^{20}$  cm<sup>-2</sup> (weighted average value, Dickey and Lockman 1990a), with

## 14. SXP 15.6: JUNE 2016 OUTBURST

abundances according to [Wilms et al. \(2000\)](#). We note that  $N_{\text{H,GAL}}$  was not fixed to the value provided by the Leiden/Argentine/Bonn (LAB) Survey of Galactic HI ( $2.56 \times 10^{21} \text{ cm}^{-2}$ , [Kalberla et al. 2005](#)), since this value corresponds to the total Galactic and SMC column density due to the filter used in the survey. The SMC intrinsic column density  $N_{\text{H,SMC}}$  was left as a free parameter with metal abundances of  $0.2 Z_{\odot}$  for elements heavier than helium ([Russell and Dopita 1992](#)). All the uncertainties were calculated based on a  $\Delta\chi^2$  statistic of 2.706, equivalent to a 90% confidence level for one parameter of interest. The best-fit model parameters are given in [Table 14.1](#), while the X-ray spectrum is presented in [Fig. 14.3](#).

For the *XMM-Newton* archival data, the combined EPIC spectra of the 2007 observation yielded best-fit values of  $N_{\text{H,SMC}} = 0.14^{+0.20}_{-0.14} \times 10^{22} \text{ cm}^{-2}$  and  $\Gamma = 0.77 \pm 0.12$  consistent with the *XMM-Newton* spectral properties reported by [Haberl and Sturm \(2016\)](#). Based on the best fit values of the *XMM-Newton* spectra we calculated an unabsorbed source luminosity of  $2.53^{+0.23}_{-0.24} \times 10^{35} \text{ erg s}^{-1}$  for the 2007 observation and a  $3 \sigma$  upper limit of  $0.9 \times 10^{35} \text{ erg s}^{-1}$  for the 2006 non detection. We note that the spectral shape as derived from the *XMM-Newton* observation ( $\Gamma = 0.77 \pm 0.12$ ) is marginally softer compared to the Chandra ToO ( $\Gamma = 0.58 \pm 0.04$ ). This is not unusual for different luminosity levels of the same system. Nevertheless, due to calibration uncertainties and the low count rate that does not justify spectral fitting with more complex models, thus we cannot claim a significant change in the spectral properties of the X-ray source.

For the *Swift*/XRT spectra, X-ray spectral analysis provided no strong constraints on the X-ray spectral evolution of the outburst due to the low count rate. In fact, by calculating the hardness ratios in the soft (0.3-2.0 keV) and hard (2.0-10.0 keV) energy bands we do not find any statistically significant indication of changes in the X-ray spectrum.

### 14.2.4 Phase-resolved properties

To further study the spin phase-resolved properties of SXP 15.6 we split the observed events into ten phase bins. The ten spectra had between 600 and 1200 counts, thus we used C-statistics ([Cash 1979](#)) for the fitting procedure. We fitted the spectra using the best-fit phase averaged model and tying the absorption to be the same for all spectra, but letting both the normalization and  $\Gamma$  parameters free between the different spectra. The best-fit model delivered a combined fit statistic of 472 for 482 degrees of freedom (equivalent test statistics: reduced  $\chi^2 = 0.93$ ). The results of the phase-resolved spectroscopy are presented in [Fig. 14.4](#). There is an indication that the spectral shape is changing with pulse-phase, with a general trend of the spectrum becomes harder when brighter. The unabsorbed X-ray luminosity changes by a factor of  $\sim 1.95$  between the off and on pulse phase, which is consistent with the PF that was determined by

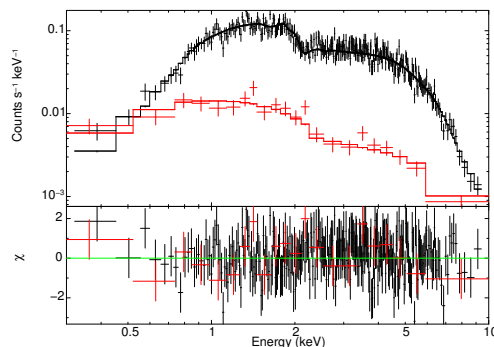


**Figure 14.3:** The X-ray phase averaged spectrum of SXP 15.6 from the Chandra observation together with the best fit model of an absorbed power-law. The *XMM-Newton* EPIC-pn spectrum of obtained by the archival 2007 observation is plotted with red color for comparison.

## 14.2 Observations and data analysis of SXP 15.6

model: tbnew_gas * tbnew * powerlaw				
Component	Parameter	Value		units
		CXO	XMM	
tbnew_gas <sup>a</sup>	N <sub>H</sub>	0.0399		10 <sup>22</sup> cm <sup>-2</sup>
tbnew	N <sub>H</sub>	0.06 <sup>+0.07</sup> <sub>-0.06</sub>	0.14 <sup>+0.20</sup> <sub>-0.14</sub>	10 <sup>22</sup> cm <sup>-2</sup>
power-law	Γ	0.58 <sup>+0.04</sup> <sub>-0.04</sub>	0.77 <sup>+0.13</sup> <sub>-0.12</sub>	
	norm <sup>b</sup>	8.67 <sup>+0.25</sup> <sub>-0.25</sub>	0.55 <sup>+0.08</sup> <sub>-0.04</sub>	10 <sup>-12</sup> erg cm <sup>-2</sup> s <sup>-1</sup>
Flux <sup>c</sup>		8.52	0.52	10 <sup>-12</sup> erg cm <sup>-2</sup> s <sup>-1</sup>
Luminosity <sup>d</sup>		3.99±0.12	0.25±0.03	10 <sup>36</sup> erg s <sup>-1</sup>
	χ <sup>2</sup> /DOF	0.90/275	1.13/33	

<sup>a</sup> Galactic foreground absorption, fixed with solar metallicity values.

<sup>b</sup> Unabsorbed flux of the power-law component in the 0.3-10.0 keV energy band.

<sup>c</sup> Observed (absorbed) flux in the 0.3-10.0 keV band.

<sup>d</sup> Unabsorbed luminosity (0.3-10.0 keV) for the distance of the SMC (62 kpc; Graczyk et al. 2014).

**Table 14.1:** Results of the X-ray spectral modelling

the pulsed profile.

For the X-ray luminosity of SXP 15.6 during the Chandra observation, an extended accretion column is not expected to have been created (Mushtukov et al. 2015a,b). Most of the emission should therefore originate from a region very close to the NS surface. In this case, the emission should form a pencil beam pattern (Basko and Sunyaev 1976). This claim is also supported by the single peaked pulse profile (Mészáros 1992), while double peaked pulse profiles are usually associated with fan-beam emission patterns and higher luminosity systems (e.g. Sasaki et al. 2012; Rea et al. 2004). Although a precise modelling of the emission pattern is beyond the scope of this paper, useful insights can be gained by the following calculations. We can model the pulse profile by adopting a basic model for the pulsar’s emission. The observed pulse profile can be modeled by assuming two symmetric regions located on the magnetic poles whose emission is gravitationally bent by the gravity of the NS (Beloborodov 2002). This model only depends on three free parameters, the angle  $i$  between the observer’s line of sight and the rotation axis of the NS, the angle  $\theta$  between the NS magnetic and rotation axis, and the ratio of the NS Schwarzschild radius ( $r_g$ ) and radius ( $R$ ). The fitting method was based on the Levenberg-Marquardt algorithm (Moré and Wright 1993; Moré 1978), using an adaptation of the IDL<sup>1</sup> procedure MPFIT (Markwardt 2009). The results of the pulse profile fitting are presented in Fig. 14.4. The best-fit model parameters and their  $1\sigma$  uncertainties are;  $i = 25 \pm 6$   $\theta = 52 \pm 4$  and  $r_g/R = 0.28 \pm 0.02$ . We note that there is a degeneracy between the two calculated angles, i.e. solutions with reversed angle values (e.g.  $[i,\theta]=[\theta,i]$ ) produce the same pulse profiles. We note that similar values were derived by applying the model to the normalised phase-folded pulse profile

<sup>1</sup>IDL®, a product of Exelis Visual Information Solutions, Inc., a subsidiary of Harris Corporation (Exelis VIS)

## 14. SXP 15.6: JUNE 2016 OUTBURST

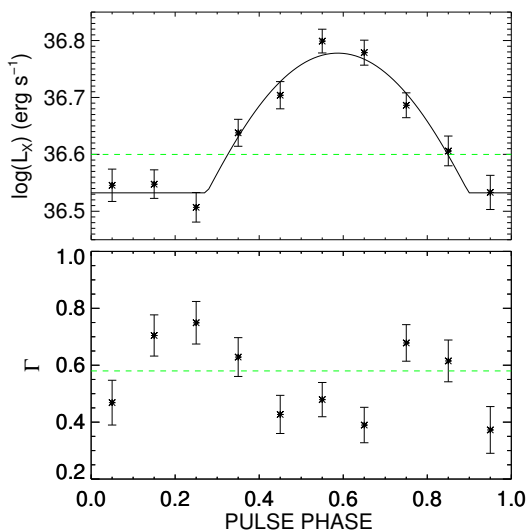


**Figure 14.4:** Results of the phase resolved spectral modelling of the events collected by Chandra during the 2016 outburst, all errorbars denote the  $1\sigma$  uncertainties. In both panels, the horizontal dashed line indicates the values of the phase-averaged spectrum. *Upper panel:* The unabsorbed luminosity (0.3-10 keV) of the system for each of the 10 spectral phase bins. The solid line shows the best-fit pulse profile model following Beloborodov (2002), and for the parameter values described in the text. *Lower panel:* Evolution of the power-law slope with spin phase.

(Fig. 14.2) or the phase-resolved derived X-ray luminosity (Fig. 14.4), as it is expected for a system without strong spectral changes within its spin pulse phase.

### 14.2.5 X-ray and optical light curve of the outburst

The optical counterpart of SXP 15.6 has been regularly monitored by the Optical Gravitational Lensing Experiment (OGLE, Udalski et al. 2015). The OGLE-IV I band photometric data are publicly available online through the OGLE XROM<sup>1</sup> web page (Udalski 2008). In order to compare the X-ray and the optical light curves we downloaded the OGLE-IV I band data from the above portal. The optical light curve of SXP 15.6 for a period of  $\sim 500$  d is presented in Fig. 14.5. The proposed orbital period of the 36.432(9) d (McBride et al. 2017) is marked with vertical lines in the same plot.

By combining the *Swift*/XRT observations performed during June-July 2016 and adopting the spectral parameters from the X-ray spectral analysis of the Chandra data we construct an X-ray light-curve of the outburst (see Fig. 14.6). For that purpose the *Swift*/XRT count rates were converted into luminosity values assuming the best fit model from the Chandra observation, which for the *Swift*/XRT instrument yields a count-rate to luminosity (0.3-10 keV band) conversion factor  $4.2259 \times 10^{37}$  erg s<sup>-1</sup>/(c/s). For the S-CUBED pointings with exposure times less than 50 s, and for detections with less than 8 counts, we estimated the  $3\sigma$  upper limits using a Bayesian method introduced by Kraft et al. (1991). Comparing the optical and X-ray light curves in Fig. 14.6 we find that the peak in the X-ray light curve lags the optical maximum by  $\sim 6$  d, although this number should be taken with high caution due to the sparse optical coverage and the large uncertainties in the luminosity values derived from the *Swift*/XRT S-CUBED pointings.

<sup>1</sup>XROM: OGLE-IV real time monitoring of X-ray variables: <http://ogle.astrouw.edu.pl/ogle4/xrom/xrom.html>

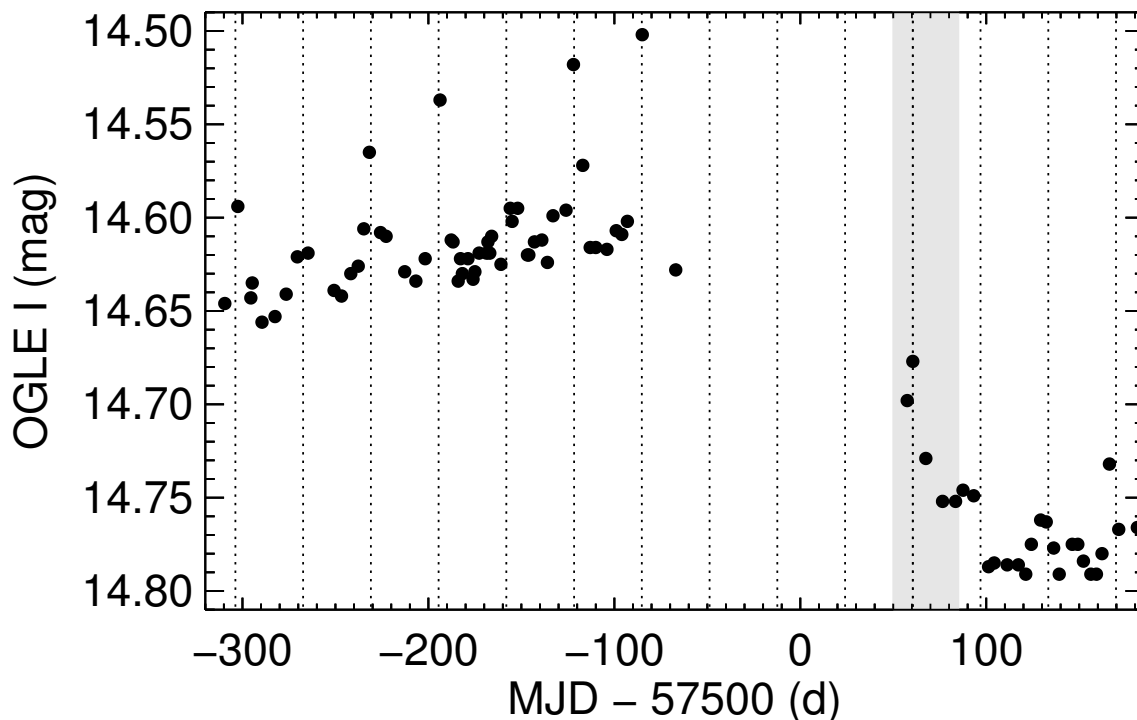


**Figure 14.5:** OGLE I band light curve of the optical counterpart of SXP 15.6 as presented by McBride et al. (2017), vertical lines mark the 36.432 d orbital period reported by the same authors. Gray shaded area marks a 35 d interval ( $\sim 1$  orbit) around the 2016 X-ray outburst. A zoom in of this region is seen in Fig. 14.6

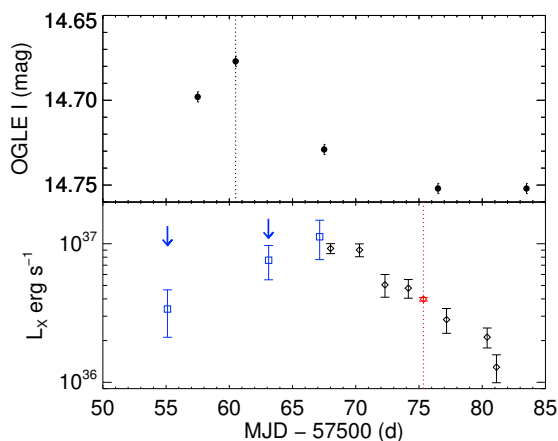


**Figure 14.6:** *Upper panel:* Optical light curve during the 2016 X-ray outburst of SXP 15.6, magnitudes are taken from the publicly available OGLE data in the I band. The vertical line represents the optical maximum based on the complete optical light curve and the 36.432 d orbital period. *Lower panel:* X-ray light curve of the 2016 outburst of SXP 15.6. Black diamond points indicate the *Swift*/XRT observations of our monitoring, blue squares indicate the *Swift*/XRT pointings of S-CUBED and are based on very low detected counts (2, 5, 10 events). For the two pointings with the lowest statistics we plotted the  $3\sigma$  upper limit using blue downward arrows. The luminosity inferred from the Chandra observation is plotted with a red diamond. A vertical red dotted line has been plotted at the date of the Chandra observation to guide the eye.

### 14.3 Discussion

From the analysis of the available X-ray observations of SXP 15.6 during the June–July 2016 outburst and during quiescence we were able to infer the basic spectral and temporal properties of this BeXRB system.

The X-ray spectrum of SXP 15.6 is well described by an absorbed power-law model with photon index of 0.58 (Table 14.1), which is on the hard side of the typical range 0.6 to 1.4 reported by Haberl et al. (2008a). Although in many BeXRB systems there is indication of residual structure in their spectrum that requires spectral fitting with additional components like a combination of a power-law and a soft black-body (e.g. Vasilopoulos et al. 2016b, 2014a, 2013a; Sturm et al. 2014b; La Palombara et al. 2013b,a; Bartlett et al. 2013a), in our case there is no statistical justification for using a more complicated model. The analysis of the *XMM-Newton* archival data provided a detection at a luminosity of  $2.53 \times 10^{35}$  erg s<sup>-1</sup> (0.3–10.0 keV) in the 2007 *XMM-Newton* observation while the 2006 *XMM-Newton* pointing yielded an upper-limit of  $0.9 \times 10^{35}$  erg s<sup>-1</sup> (0.3–10.0 keV). Based on the fitted Chandra and *XMM-Newton* X-ray spectra of the system and the *Swift*/XRT hardness ratios there is marginal spectral change through the 2016 outburst and its lower luminosity state during the 2007 observation. Considering the maximum X-ray luminosity of the system during our *Swift*/XRT monitoring and the upper limit estimated by the *XMM-Newton* 2007 non-detection the total X-ray variability of the system is at least a factor of 100 ( $\sim 10^{37}/10^{35}$ ). High X-ray variability is not uncharacteristic of BeXRBs, as it has been shown that all of the known BeXRB pulsars in the SMC with spin period less than 20 s show X-ray variability larger than this value (see Fig. 5 of Haberl and Sturm 2016).

Timing analysis of the *XMM-Newton* and Chandra data revealed a statistically significant change in the spin period of the NS over a period of about 10 yr. Specifically, within 3175 d the NS has spun-up by 0.024 s, or an average of  $\dot{P} = -8.8 \times 10^{-11}$  s s<sup>-1</sup> ( $-0.0028$  s yr<sup>-1</sup>). Our estimate does not account for orbital motion corrections which at the moment remain unknown. Nevertheless, the detected NS spin period can be altered up to  $\pm 0.0025$  s due to Doppler effect for a typical BeXRB system (Townsend et al. 2011). The derived spin-up value is comparable to the estimated values of other SMC BeXRB pulsars (Klus et al. 2014). In particular SMC X-2 (SXP 2.37), one of the brightest and fastest spinning pulsars in the SMC, has a spin-down rate of  $-0.0037$  s yr<sup>-1</sup>, while two systems with similar spin period as SXP 15.6, namely SXP 15.3 and SXP 16.6 have reported values of  $0.007$  s yr<sup>-1</sup> (spin-down) and  $-0.0131$  s yr<sup>-1</sup> (spin-up) respectively (Klus et al. 2014).

The 2016 outburst ( $L_X > 10^{36}$  erg s<sup>-1</sup>) lasted for more than 25 d, thus 70% of the orbital period, which is more than the typical value reported for type I outbursts of BeXRBs but not uncommon ( $< 50\%$  for most systems; Kretschmar et al. 2012). By integrating the X-ray light curve of Fig. 14.6 (using only detections and not upper limits), we find that within the 25 d period the total energy released was  $1.1 \times 10^{43}$  erg translating to a total accreted mass of  $6.2 \times 10^{-12}$  M<sub>⊙</sub> (assuming an efficiency of 1).

Transient events of BeXRB systems can provide a laboratory for studying the luminosity dependent processes of accreting NS, while providing information about the magnetosphere of the highly magnetised objects (Poutanen et al. 2013). The basic idea while studying interactions between the magnetosphere and in-falling material during X-ray outbursts of BeXRBs is that the gravitational pressure of the accreted

matter can change the size of the magnetospheric radius. Depending on how this radius compares with the corotation radius, the system might be in the accretion or propeller phase. For systems where the corotation and magnetospheric radii are close, the system can rapidly change between the two phases, thus entering a phase-off state where the luminosity is rapidly decreasing. Illarionov and Sunyaev (1975a) have set the basic principles of such interactions, showing that this limit is basically a function of the accretion rate as well as the spin period and magnetic moment of the NS. It has been evident that in many NS pulsars the corotation radius is comparable to the magnetospheric radius even in active accretion phases (e.g., 4U 1626-67; Koliopanos and Gilfanov 2016). While in other cases the rapid decline and fade out of a NS binary pulsar outburst has been used to constrain the size of the magnetosphere (e.g., SMC X-2; Lutovinov et al. 2017), the x-ray light curve of SXP 15.6 does not extend long enough to show if the system completely turns off. However, there is evidence for a sharp decline in the luminosity at MJD 57581 (Fig. 14.6). This sharp decline could be either the result of the NS leaving the dense region of the Be star disc around periastron and/or the onset of the propeller effect (Campana et al. 2002; Stella et al. 1986; Corbet 1996). For this we use the critical mass accretion rate that would put the magnetospheric radius at the corotation radius (D’Angelo and Spruit 2012). Moreover, we assume that the energy release during accretion is equal to the Newtonian gravitational potential for the NS surface (Campana et al. 2002), thus  $\sim 16\%$  of the infalling rest mass energy. From the above, we can estimate the critical luminosity for the onset of the propeller effect (e.g. Vasilopoulos et al. 2017b; Tsygankov et al. 2016; Campana et al. 2002; Stella et al. 1986):

$$L_{lim} \simeq \frac{GM\dot{M}_{lim}}{R_{NS}} \simeq 5.6 \times 10^{37} \eta P^{-7/3} M_{1.4}^{-2/3} R_6^5 B_{12}^2 \text{ erg s}^{-1} \quad (14.1)$$

where  $P$  is the NS period  $M_{1.4}$  the NS mass in units of  $1.4M_{\odot}$ ,  $R_6$  the NS radius in units of  $10^6$  cm,  $B_{12}$  is the NS magnetic field strength in units of  $10^{12}$  G, and  $\eta$  is a factor yielding the relative strength of the generated magnetic field toroidal component ( $\eta \equiv B_{\phi}/B_z$ ) and has typical values of the order of  $\sim 0.1$  (D’Angelo and Spruit 2012; Spruit and Taam 1993). Given that we did not observe the accretor to propeller transition in the 2016 outburst, it is more appropriate to use the minimum luminosity of the system as detected in 2007 (i.e.  $2.5 \times 10^{35}$  erg s $^{-1}$ ). This yields a magnetic field strength of  $\lesssim 5.2 \times 10^{12}$  G, which is within the typical range observed for the BeXRB pulsar population in the SMC (Christodoulou et al. 2017b).

Phase-resolved analysis of the X-ray spectrum showed that it can be modelled by a power law with variable normalisation and slope. In Fig. 14.4 we see evidence that the system becomes harder when brighter. Limited statistics did not allow us to test models with multiple components without over-fitting the data ( $\chi_{red}^2 < 1$ ), thus we are not able to argue against a two component model with two separate components (e.g. black-body and power-law) with normalisations exhibiting different dependence with spin phase.

By modelling the pulsed emission of the system using the analytical approximation introduced by Beloborodov (2002), we were able to set constraints on the inclination between the magnetic and rotation axis of the NS (see §14.2.4). Given the degeneracy of the solution this can be either  $32^\circ$  or  $52^\circ$ . From the fit to the pulse profile, we also estimated the ratio  $r_g/R$  to be  $0.28 \pm 0.02$ . This translates to a compactness

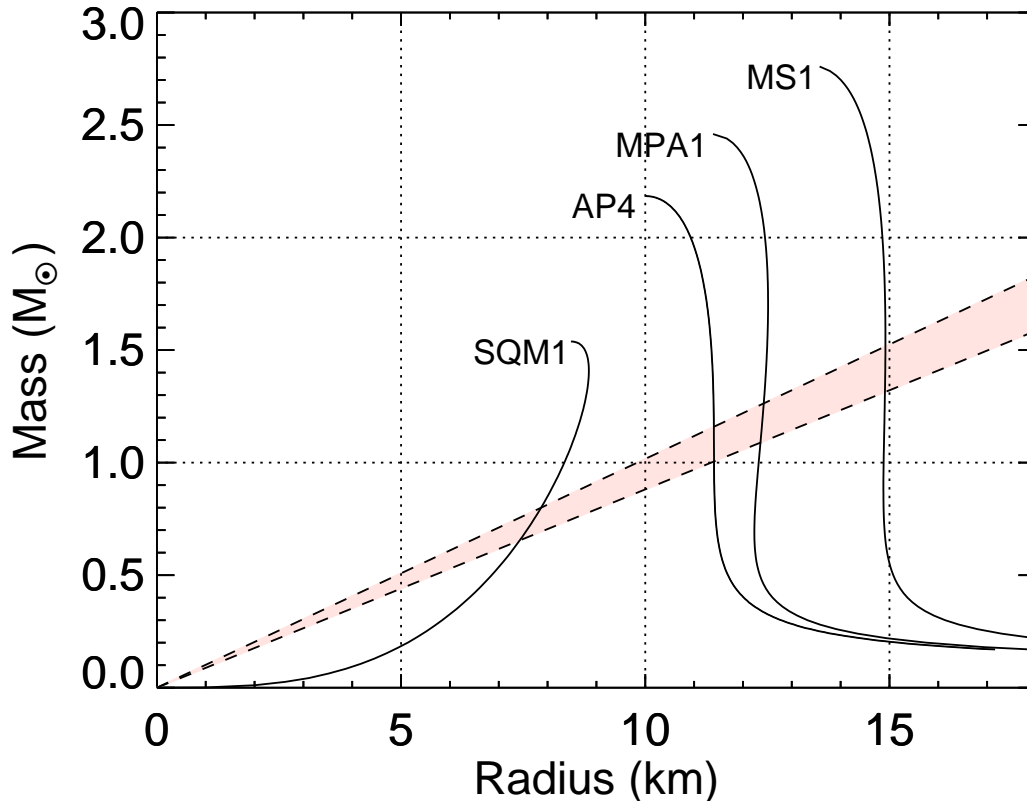


**Figure 14.7:** Mass-radius curves predicted for different equations of state for NS matter proposed for the interiors of neutron stars (Özel and Freire 2016) with naming conventions introduced in the same paper (SQM1: Prakash et al. (1995), AP4: Akmal et al. (1998), MPA1: Mütter et al. (1987), MS1: Müller and Serot (1996)). Filled area is produced by the fitted value of the  $r_g/R$  ratio.

of the system defined as  $(M/M_\odot)/(R/\text{km}) = 0.095 \pm 0.007$ . This methodology has been applied to pulse profiles of accreting millisecond pulsars (e.g. Poutanen and Gierliński 2003), quiescent low-mass X-ray binary systems (Özel and Freire 2016) and BeXRB systems (Bartlett et al. 2013a). Moreover, it is interesting to notice that the compactness of SXP 15.6 can be comparable or marginally smaller to that of isolated NS (e.g.  $0.105 \pm 0.002$  for RX J0720.4-3125; Hambaryan et al. 2017). We can use this result to set some constraints on the equation of state for NS matter (Özel and Freire 2016). Although, in general either the NS mass or radius needs to be known from independent measurements (e.g. black-body radius or orbital motion Stiele et al. 2016; Özel et al. 2016), in our case we can use the same principles and define the loci of possible NS mass and radius (see Fig. 14.7). Thus, a wider study of accreting NS during low luminosity outbursts can provide additional insight on the NS properties. This can also be implemented with current and future X-ray missions (e.g. NICER; Özel et al. 2016).

Finally, we comment on the assumptions that affect the estimated uncertainties,

as well as the limitations of the above methodology. Most of the simplifications come from the treatment of the properties and geometry of the emission region. X-rays originate from the NS magnetic polar cap which is assumed to be the surface of the NS. As shown by Mushtukov et al. (2015b) for the luminosity level of SXP 15.6 the size of the accretion column should only be a small fraction of the NS radius (e.g.  $< 2\%$ ), so the size and geometry of the accretion column should have only a small effect on the analytic solution of Beloborodov (2002). The magnetic axis is fixed to go through the centre of the NS. Nevertheless, an off-centre magnetic axis is known to produce asymmetric pulse profiles (Bogdanov et al. 2007). Moreover, different size of the two emitting regions can cause asymmetry in the pulse profile. For SXP 15.6 an asymmetry is present in the pulse profile but it is ignored by the fitted model. The above are affecting the shape of the pulse profile, thus mainly affecting the values of the angles derived from the fit. The  $r_g/R$  ratio value is mainly derived from the ratio of the maximum and minimum pulsed flux. However, the constant pulse fraction in different energy bands, supports the assumption that the X-ray emission is originating from a single region and it is not significantly contaminated by un-pulsed emission from regions away from the NS (e.g. accretion disk).

## 14.4 Conclusions

By analysing data from a Chandra ToO we confirm the detection of coherent pulsations ( $P = 16.6398 \pm 0.0009$ ), thus identifying SXP 15.6 as a new HMXB pulsar in the SMC. Its X-ray spectrum is well described by an absorbed power-law ( $\Gamma = 0.58 \pm 0.04$ ). By comparing the available Chandra and *XMM-Newton* archival data we conclude there is no indication for significant spectral variation for luminosities between  $2.5 \times 10^{35}$  erg  $s^{-1}$  and  $9 \times 10^{36}$  erg  $s^{-1}$ . There is an indication of spectral change with the pulse phase, making the system appear harder when brighter. Pulse profile modelling of the X-ray emission was used to put constraints on the angle between the NS rotational and magnetic axis, and the compactness of the NS ( $(M/M_\odot)/(R/\text{km}) = 0.095 \pm 0.007$ ).

## 14. SXP 15.6: JUNE 2016 OUTBURST

---

## SMC X-2: September 2015 outburst

**I**n this chapter I report on the X-ray spectral and temporal properties of SMC X-2 as derived from the analysis of three *XMM-Newton* observations performed during the 2015 major outburst of the system. Deep observations were obtained at different luminosity levels, from  $3 \times 10^{38}$  erg s<sup>-1</sup> down to  $7.8 \times 10^{37}$  erg s<sup>-1</sup>, enabling detailed modelling of the X-ray emission and its evolution. I discovered that the X-ray emission can be described by a power-law like component that is probably originating from the accretion column, and a soft component contributing at lower energies (<0.8 keV). The intensity of the power-law like component varies with phase and is reproducing most of the observed pulsed emission above 1 keV, while the soft component is non-pulsating. My analysis revealed that the non-pulsating soft excess could originate from both optically thick and optically thin material, that can be attributed to an inflated accretion disk. At lower luminosities the intensity of the pulses significantly drops to a pulsed fraction of 0.1 compared to 0.45 at the highest luminosity.

### 15.1 Historic X-ray activity of SMC X-2

SMC X-2 is a known [BeXRB](#) pulsar in the [SMC](#). The binary system consists of a [NS](#) with a spin period of 2.37 s ([Corbet et al. 2001](#)), orbiting around a massive emission-line star ([McBride et al. 2008](#)). SMC X-2 was first discovered in 1977, when it underwent a major outburst, reaching an X-ray luminosity of  $\sim 10^{38}$  erg s<sup>-1</sup> ([Clark et al. 1978](#)). The outburst lasted  $\sim 30$  d ([Clark et al. 1979](#)) and was followed by a prolonged quiescent phase, until its next major X-ray outburst in early 2000 ([Corbet et al. 2001](#)). It was during this second outburst that the first constraints on its orbital parameters were placed (i.e. 18.4 d orbital period [Schurch et al. 2008](#); [Townsend et al. 2011](#)). After a period of  $\sim 15$  years during which SMC X-2 was in an X-ray quiescence state, a new outburst occurred in September 2015 ([Kennea et al. 2015](#)). During the peak of the outburst the luminosity of the system exceeded  $10^{38}$  erg s<sup>-1</sup> in the 0.3-10.0 keV energy band. In this study we present the results of these *XMM-Newton* [ToO](#) observations that were obtained during the recent outburst. The first observation was carried out at the start of the burst and during its brightest phase (2015-09-29), the second on 2015-10-08 and the third observation was performed (2015-10-24) when the X-ray luminosity had dropped by a factor of  $\sim 4.2$ .

### 15.2 Observations and data analysis

#### 15.2.1 X-ray data analysis

Our first *XMM-Newton* [ToO](#) observation was performed having EPIC-pn ([Strüder et al. 2001](#)) in timing mode, EPIC-MOS1 ([Turner et al. 2001](#)) in full frame mode and EPIC-MOS2 in timing mode. The timing mode was preferred as at the given flux level it delivers detailed X-ray spectra in the 0.7-10.0 keV band without being affected by pile-up features. For the second *XMM-Newton* [ToO](#) the EPIC-pn small window mode was preferred for the given luminosity that delivers excellent quality spectra in the 0.3-10.0 keV energy band. In both observations one of the EPIC cameras was in Full frame

## 15. SMC X-2: SEPTEMBER 2015 OUTBURST

#	OBS-ID	Instrument	T_start MJD [d]	exposure <sup>a</sup> [ks]
1	0770580701	EPIC-pn	57294.96	7.7
		EPIC-MOS1/MOS2		9.7/9.4
		RGS1/RGS2		9.9/9.9
2	0770580801	EPIC-pn	57303.89	29.7
		EPIC-MOS1/MOS2		29.9/29.9
		RGS1/RGS2		30.1/30.1
3	07705807901	EPIC-pn	57319.58	30.6
		EPIC-MOS1/MOS2		30.9/30.6
		RGS1/ RGS2		31.031.0

<sup>a</sup> Exposure time for each *XMM-Newton* instrument.

**Table 15.1:** X-ray observation log of SMC X-2.

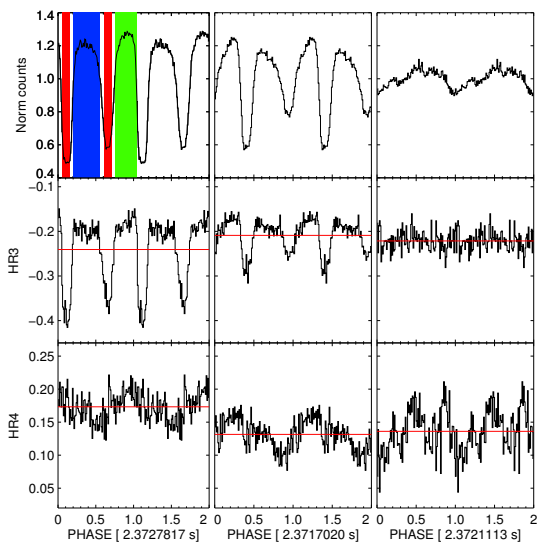


**Figure 15.1:** Left: Pulse profile (0.7-10.0 keV) obtained from the merged EPIC data (obsid: 0770580701). HRs are derived from the (0.7-2.0) keV, (2.0-4.0) keV, (4.0-10.0) keV energy bands. There is evidence of a soft excess during fainter pulse phases. Colour shaded regions indicate the phase intervals used for the phase-resolved spectroscopy. Middle: Pulse profile obtained from the merged EPIC data (obsid: 0770580801). Right: Pulse profile obtained from the merged EPIC data (obsid: 0770580901). No evidence for a soft excess during fainter pulse phases is seen.

mode to detect possible other X-ray sources in the *XMM-Newton* field of view. The complete observing log is presented in Table 15.1. We used *XMM-Newton* SAS 14.0.0<sup>1</sup> for the data processing.

For the EPIC-pn spectra and light curves, we selected single-pixel and double-pixel events (`PATTERN`≤4). To Search for background flare events, we defined a threshold of 2.5 counts ks<sup>-1</sup> arcmin<sup>-2</sup> using the EPIC-MOS1 detector. The event files were created with the SAS task `epproc`. Spectra were extracted using the task `evselect` from 30 pixel columns (timing mode) or a circular region with 30" radius (small window mode). The SAS task `barycen` was used to correct the *XMM-Newton* EPIC-pn event arrival times to the solar-system barycentre. The EPIC-pn spectra were binned to achieve a minimum signal-to-noise ratio of five for each bin. The spectra from the Reflection Grating Spectrometer (RGS, [den Herder et al. 2001](#)) were extracted with `rgsproc`, the RGS1 and RGS2 spectra were combined using the task `rgscombine`.

### 15.2.2 X-ray timing analysis

To search for a periodic signal in the EPIC-pn data we used an [EF](#) technique. Based on the best derived pulse periods for the three *XMM-Newton* observations we computed

<sup>1</sup>Science Analysis Software (SAS), <http://xmm.esac.esa.int/sas/>

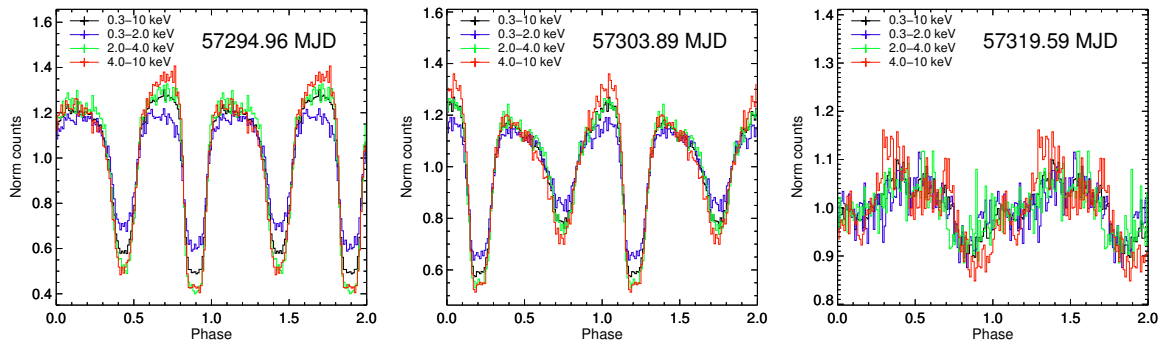


**Figure 15.2:** Pulse-profile for different energy bands

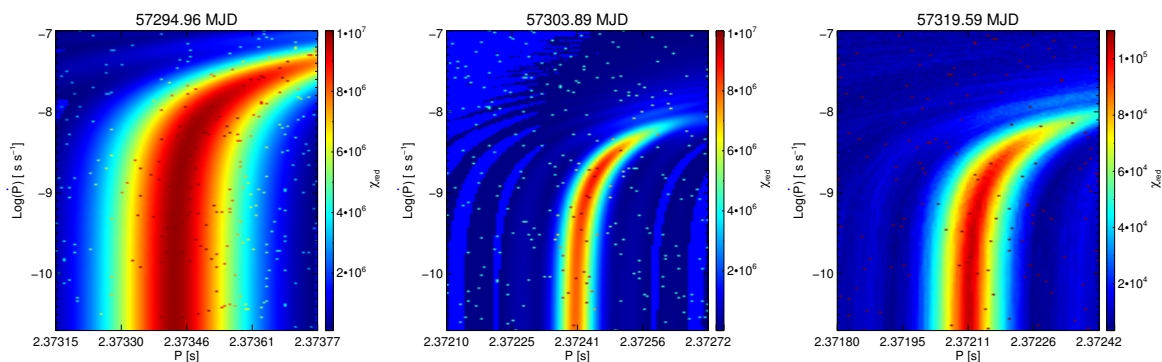


**Figure 15.3:** Reduced  $\chi^2$  in the  $P$  vs  $\dot{P}$  plane for all 3 *XMM-Newton* observations. Event times were corrected for heliocentric barycentre and binary solution (Townsoed et al. in prep.). From 1st to 2nd observation  $\dot{P} = -1.36 \times 10^{-9}$  or  $\log(|\dot{P}|) = -8.87$ . From 2nd to 3rd observation  $\dot{P} = -1.47 \times 10^{-10}$  or  $\log(|\dot{P}|) = -9.83$ .

the period-folded pulse profiles that are plotted in the top panels of Fig. 15.1. To search for spectral variability we can look for changes in the HR within the pulsed period. By using the three energy bands (0.7-2.0, 2.0-4.0, 4.0-10 keV), we can define four HRs. The HRs derived from the pulse profiles in two adjacent energy bands, are plotted in the middle and bottom panels of Fig. 15.1.

In Fig. 15.2 we plot the pulse profile in different energy bands for the three *XMM-Newton* ToO observations. There are several features that can be distinguished and worth mentioning. The pulse profile changes from double peak to a single peak profile. For this transition to occur one of the two dips seen in the first pulse profile, gradually “fills-up” till the two peaks are not distinguishable. Moreover, during the off-pulse phase of the most luminous stages the spectrum becomes significantly softer at lower energies, this is consistent with a non-pulsating soft component that mainly emits below 2.0 keV.

Since SMC X-2 is one of the few BeXRB systems with known orbital solution we can put further constraints on the spin evolution of the system. Moreover, due to the magnitude of the major outburst we were able to improve and provide updated values of the binary solution. By using the ephemeris of the orbital solution of the binary system (Townsend et al. in prep, private communication Townsend et al. 2011), we can constrain both the pulse period ( $P$ ) and its first derivative ( $\dot{P}$ ) during each of the

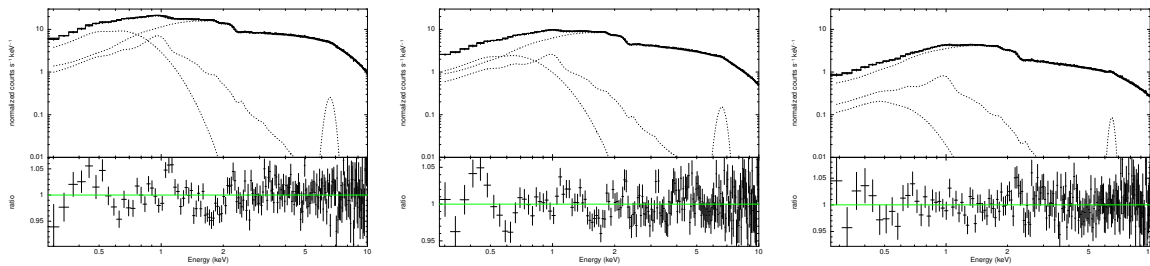


**Figure 15.4:** Pulse-phase averaged EPIC spectra from obsids 0770580701 (left), 0770580801 (middle) and 0770580901 (right). The same model was used for all observations and is composed of a Comptonised component that describes the hard continuum, and a combination of optically thick and optically thin emission that contribute at low energies (see text for more details).

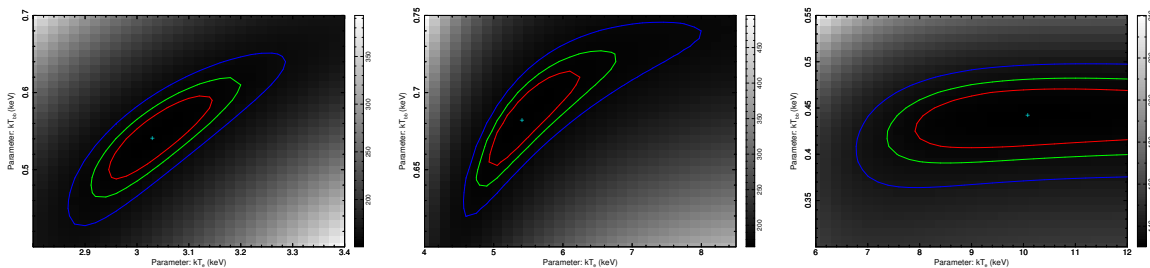


**Figure 15.5:** Pulse-phase averaged contour plots for the fitted parameters (electron energy vs. seed photon energy) of the Comptonised emission (nthcomp model) as derived from the EPIC spectra (2.0-10 keV) from obsid: 0770580701 (left), 0770580801 (middle) and 0770580901 (right). At lower  $L_X$  (right plot) the electron energy becomes unconstrained while at higher energy the electron energy can be well constrained.

*XMM-Newton* observations. Another condition that allows us to do this is that the luminosity of the system remained constant during these observations so the accreting material should be in-falling with a steady rate. To investigate the P- $\dot{P}$  parameter space we used the [accelerated epoch folding \(AEF\)](#) method. The reduced  $\chi^2$  values computed for the search grid are plotted in Fig. 15.3. We note that the event arrival times have been corrected for the binary solution thus the P values refer to the [NS](#) system and not the observer as in Fig. 15.1. The maximum  $\chi^2$  values (dark red colour) are indicative of the amplitude of the pulse and the statistics of each *XMM-Newton* observation, e.g the values drop with time as the pulse profile changes from double to single peak.

### 15.2.3 X-ray phase-averaged spectral analysis

The spectral analysis was performed with [xspec](#) ([Arnaud 1996](#)) version 12.8.0. We used  $\chi^2$  statistics for the fitting procedure, while all the uncertainties were calculated based on a  $\Delta\chi^2$  statistic of 2.706, equivalent to a 90% confidence level for one parameter of interest.

The *XMM-Newton* EPIC phase averaged spectra were fitted simultaneously using the same model parameters with an additional scaling factor to account for instrumental differences. The scaling factor for the EPIC-pn model was fixed at 1. Each of the three *XMM-Newton* observations was fitted with the same model. In particular the model was composed of:

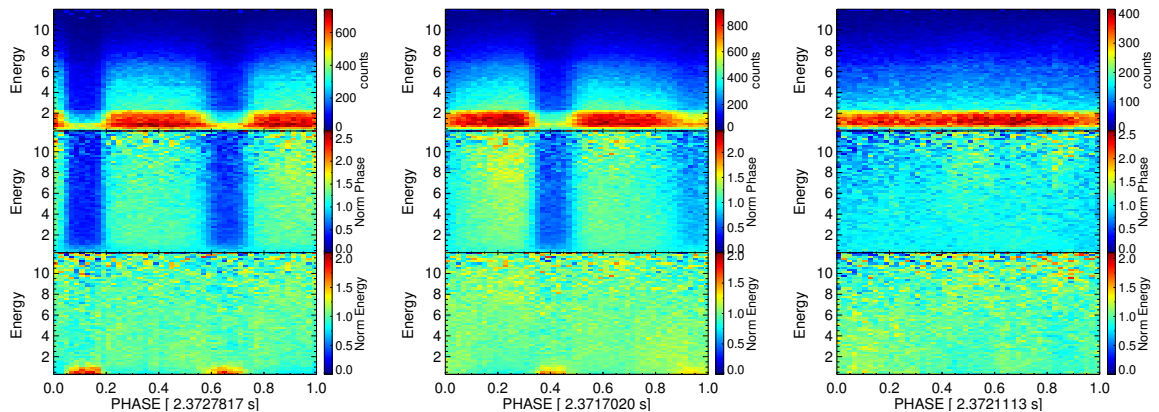


**Figure 15.6:** Phase dependent spectral heat-map (left to right obsids: 0770580701, 0770580801 and 0770580901), obtained by binning the EPIC-pn source counts to 50 phase bins and 50 energy channels. Top panel: colours are proportional to the number of counts per bin, middle-panel: data were normalized by the phase averaged number of counts in the same energy bin, bottom-panel: data were again normalized according to the energy averaged count rate of each phase bin.

(i) Two absorption components: a Galactic foreground absorption and an additional column density accounting for both the interstellar medium of the SMC and the intrinsic absorption of the source. The Galactic column density was fixed to  $N_{\text{H,GAL}} = 6 \times 10^{20} \text{ cm}^{-2}$  (Dickey and Lockman 1990a), with abundances according to Wilms et al. (2000).

(ii) A sum of three continuum components: a black-body (bbodyrad), a thermal plasma component (vmekal) and a thermal Comptonisation component (nthcomp). We note that the thermal plasma model could be replaced by a simple Gaussian component as it mainly improves the fit around 1 keV.

(iii) A Gaussian component to describe emission from neutral-ionised Fe ( $K_{\alpha}$  lines). For the description of the continuum, a different combination of components can provide similar goodness of the fit to the data, e.g. broken power law, or cut-off power law instead of the Comptonisation component. But all these combinations would only give a phenomenological description and their parameters would be less easily translated to physical quantities. To minimize degeneracies to the solution, we proceeded fitting the data into two steps, first we ignored emission below 2.0 keV and fitted the data with only the use of the absorbed Comptonisation component plus a Gaussian. Then we fixed the parameters of the Comptonisation and Gaussian components and fitted the total spectrum with the complete model. To ensure the best fit is reached we then fitted the model with all the parameters free, we note that this did not change any of the fitted model values. Best-fit parameters are given in Table 15.2, while best-fit models are plotted in Fig. 15.4.

During the three observations we find a progressively higher energy cut-off (when using a cut-off power-law (PL) fit) in their spectra. Within the Comptonisation model, the cut-off energy of the spectrum is related to the average electron energy. While this parameter is well constrained in the first observation, in the following two we have higher uncertainties as the energy goes closer to the limiting range of the detector, see Fig. 15.5.

## 15. SMC X-2: SEPTEMBER 2015 OUTBURST

Component	Parameter	Values			units
obsid		701	801	901	
<i>tbnew(fixed) * tbnew(vmekal + bbodyrad + gaussian + nthComp)</i>					
tbnew	nH	$0.14^{+0.02}_{-0.02}$	$0.085^{+0.014}_{-0.013}$	$0.0787^{+0.025}_{-0.023}$	$10^{22} \text{cm}^{-2}$
bbodyrad	$kT$	$0.121^{+0.007}_{-0.007}$	$0.146^{+0.009}_{-0.008}$	$0.097^{+0.024}_{-0.04}$	keV
	norm	$13000^{+7000}_{-4000}$	$1300^{+600}_{-400}$	$600^{+4000}_{-400}$	
vmekal	$kT$	$0.93^{+0.03}_{-0.04}$	$1.04^{+0.03}_{-0.03}$	$0.958^{+0.07}_{-0.08}$	keV
	<i>norm</i>	$0.017^{+0.003}_{-0.003}$	$0.0069^{+0.0010}_{-0.0009}$	$0.0020^{+0.0006}_{-0.0005}$	
nthcomp <sup>a</sup>	Gamma	$1.246^{+0.015}_{-0.011}$	$1.276^{+0.006}_{-0.011}$	$1.13^{+0.04}_{-0.08}$	
	$kT_e$	$3.03^{+0.12}_{-0.10}$	$5.4^{+0.9}_{-0.5}$	$10.0^{+8}_{-2.3}$	keV
	$kT_{BB}$	$0.54^{+0.06}_{-0.06}$	$0.68^{+0.03}_{-0.03}$	$0.44^{+0.03}_{-0.04}$	keV
	norm	$0.0131^{+0.0010}_{-0.0008}$	$0.00723^{+0.00023}_{-0.00021}$	$0.00044^{+0.0003}_{-0.00023}$	
gaussian <sup>a</sup>	LineE	$6.59^{+0.12}_{-0.12}$	$6.634^{+0.07}_{-0.07}$	$6.49^{+0.06}_{-0.06}$	keV
	sigma	$0.26^{+0.12}_{-0.09}$	$0.28^{+0.07}_{-0.06}$	$0.156^{+0.07}_{-0.06}$	keV
	EqWidth	$0.037^{+0.005}_{-0.005}$	$0.0532^{+0.0005}_{-0.0005}$	$0.0408^{+0.0005}_{-0.0005}$	keV
Observed Flux <sup>b</sup>		6.25	3.6	1.25	$10^{-10} \text{erg cm}^{-2} \text{s}^{-1}$
Unabsorbed Luminosity <sup>c</sup>		$29.36^{+0.14}_{-0.16}$	$16.7^{+0.04}_{-0.1}$	$7.81^{+0.02}_{-0.09}$	$10^{37} \text{erg s}^{-1}$
$\chi^2/\text{DOF}$		1.61/168	1.33/127	1.02/127	

<sup>a</sup> model was fitted to the 2.0-10 keV energy range and parameters were fixed for the 0.3-10 keV fit.

<sup>b</sup> Absorbed flux of the fitted model in the 0.3-10 keV energy band.

<sup>c</sup> Unabsorbed Luminosity of the fitted model in the 0.3-12 keV energy band, for a distance of 62 kpc (Graczyk et al. 2014).

**Table 15.2:** results of the X-ray spectral modelling

### 15.2.4 Phase-resolved spectroscopy

On the pulse profile of the different energy bands presented in Fig. 15.2 we see evidence of spectral variations with energy. To better understand the spectral changes in the pulse profile and help select an appropriate model for the X-ray fit we produced a 2D intensity histogram over event energy and phase (see Fig. 15.6). The non-normalised histogram of the detector events is dominated by features caused by the detector efficiency. To produce an image where features are easier recognised first we normalised by the phase-averaged count rate in each energy bin. Finally, to emphasize variations with energy and phase we normalise again by the energy-averaged count rate on each phase bin. If the system had no spectral variability (e.g. only normalisation would vary) the image would result in a single colour map.

In the 1<sup>st</sup> and 2<sup>nd</sup> observation we identify the presence of a strong spectral feature at soft X-rays (< 1.5 keV). In contrast, in the third observation we see only weak indications of spectral variability that are consistent with the statistical error of each point. This is also consistent with the pulse profiles and the spin-phase resolved HR shown in Fig. 15.1.

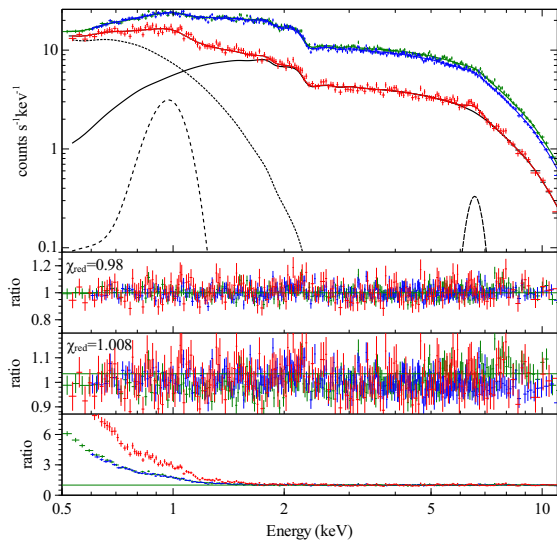


**Figure 15.7:** Top: Pulse-resolved EPIC-pn spectra of observation 0770580701, colours are based on Fig. 15.1. Second panel: data-to-model ratio for a model with normalizations of diskBB and Gauss-1keV line is the same for the three spectra, PL photon index and normalization vary. Third panel: as above, but PL photon index and normalizations of diskBB and Gauss-1keV line is the same for the three spectra. PL normalization is the only different parameter between the three different phases. It is clear that there is a small change in the photon index or cutoff energy, as residuals of the spectra of the two peaks alternate in the lower and upper energy range. Lower panel: normalizations of BB and Gaussian set to zero.

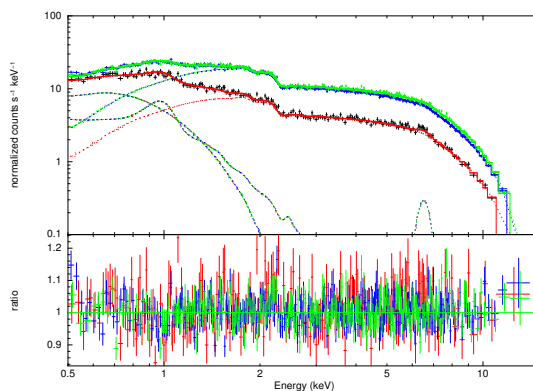


**Figure 15.8:** Upper panel: Same as in Fig. 15.7, but for the tested continuum a thermal plasma component was used instead of the wide Gaussian to model the excess at  $\sim 1$  keV. Lower panel: data-to-model ratio for the best fit model, i.e. only PL photon index and normalization vary with phase.

For the phase-resolved spectroscopy, only EPIC-pn data from the first *XMM-Newton* ToO observation were used, while the events were grouped for different phases of the pulse profile. In particular three different phase intervals were used to group the data, one for each of the two peaks of the double-peaked phase folded light curve and one for the dips of the light curve (see colour-shaded regions in Fig. 15.1). We fitted the phase-resolved spectra with a similar model as used for the phase averaged spectrum. Our analysis shows that the properties of the soft excess have a very weak dependence on phase. As it is shown in Fig. 15.7 (and Fig. 15.8) the on-pulse and off-pulse spectra are fitted perfectly by only letting the properties of the hard continuum vary with phase. Moreover, the data-to-model ratio plots show (Fig. 15.7) that apart from the normalization of the pulsating component, its slope/hardness also changes with phase.

### 15.2.5 RGS spectroscopy

The RGS data were used to search for narrow line features in the soft energy band. The RGS spectra were not binned and fitted employing Cash statistics (Cash 1979). A simple PL model sufficiently describes the continuum spectrum in the RGS energy band.

We searched the RGS spectra for emission and absorption lines by a blind search for Gaussian features. The spectra are searched by adding the Gaussian with a fixed

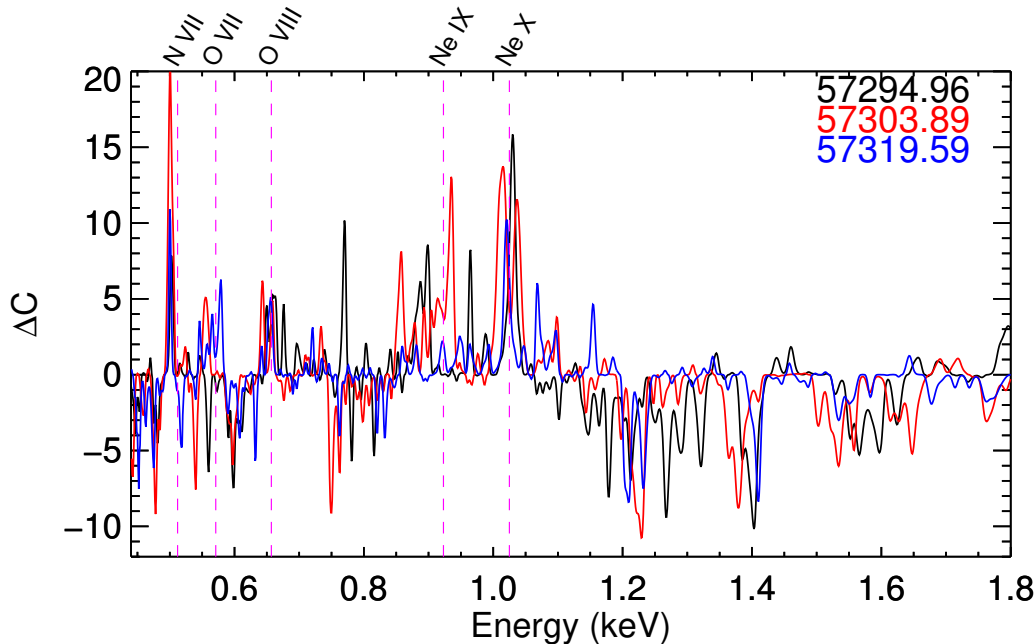


**Figure 15.9:** Results of the line search in the RGS spectra, the  $3\sigma$  significance corresponds to  $\Delta C \sim 10$ .

width to the continuum and performing a fit by letting only the normalization of the line to vary. The fit was repeated multiple times by using a 1 eV step for the line central energy, while each time the resulting  $\Delta C$  was recorded. To estimate the significance of the line we simulated 1000 spectra based on the continuum model and repeated the process of line-search using the fixed-width Gaussian. The results are plotted in Fig. 15.9, while for comparison we mark the characteristic energies of several lines.

### 15.3 Discussion

It is challenging for high luminosity [HMXBs](#) to find the correct interpretation for their soft X-ray emission. However, outbursts of systems located in the [MCs](#) where the foreground column density is low, allow modern observatories like *XMM-Newton* to collect spectra with unprecedented quality/statistics down to 0.3 keV. Deviations from a simple power-law model are now a ubiquitous signature in the soft X-ray spectra of most high-luminosity [HMXB](#) systems. [Hickox et al. \(2004\)](#) provided several interpretations for the origin of such emission that they refer to as soft excess. In the case of near Eddington X-ray luminosity systems like SMC X-2, this excess can be a result of reprocessing of hard X-rays from the [NS](#) by optically thick accreting material located at the inner edge of the accretion disk, by photo-ionized or collisionally heated diffuse gas, or thermal emission from the [NS](#) surface. Both the phase-resolved [HR](#) and the detailed phase-resolved spectroscopy have shown the presence of a non-pulsating soft excess that is well described by two components. Interestingly, the relative ratio of the components changes with accretion rate, with the optically thick component becoming stronger with increasing luminosity (see Fig. 15.4). Another interesting feature is the

Gaussian line	701	801	901
E (eV)	$1023.^{+6}_{-5}$	$1029^{+4}_{-4}$	$1059^{+15}_{-14}$
$\sigma$ (eV)	$20^{+6}_4$	$18^{+5}_{-4}$	$51^{+14}_{-10}$
E (eV)	$964.2^{+1.3}_{-0.9}$	$936^{+0.8}_{-0.7}$	$926^{+4}_{-4}$
$\sigma$ (eV)	$-^+_{-}$	$0.8^+_{-}$	$6.8^{+4}_{-3}$
E (eV)	$659^{+4}_{-5}$	$651^{+7}_{-7}$	$657^{+2}_{-4}$
$\sigma$ (eV)	$6^{+6}_{-2}$	$8.3^{+4}_{-3}$	$4.4^{+3.2}_{-1.6}$
E (eV)	$503.0^{+1.6}_{-1.3}$	$500.5^{+1.0}_{-1.1}$	$501.7^{+0.6}_{-1.2}$
$\sigma$ (eV)	$3.6^{+1.6}_{-1.8}$	$5.3^{+1.6}_{-0.9}$	$2.3^{+1.2}_{-0.7}$

**Table 15.3:** RGS spectroscopy: using multiple lines

presence of absorption and emission line features in the grating spectra. The most prominent and easily recognised emission lines are the N VII, O VIII and the oxygen triplet O VII, however there are several emission lines present in the 0.8-1.1 keV energy range, and a forest of absorption features between 1.1 and 1.5 keV. Given the high density of lines within these two regions it is not possible to identify them. It is possible that many of the emission lines originate from the hot material around the magnetosphere. On the other hand the absorption features could originate from a fast outflow, thus they could be blue shifted in wavelength.

**15. SMC X-2: SEPTEMBER 2015 OUTBURST**

---

## SMC X-3: June 2016 outburst

The 2016 major outburst of SMC X-3 offers a rare opportunity to study accretion physics onto a highly magnetised NS during an episode of high mass accretion. SMC X-3 was one of the earliest X-ray systems to be discovered in the SMC in 1977 by the SAS 3 satellite at a luminosity level of about  $10^{38}$  erg s<sup>-1</sup> (Clark et al. 1978). The pulsating nature of the system was revealed more than two decades later when 7.78 s pulsations were measured (Corbet et al. 2003b) using data from the Proportional Counter Array on board the Rossi X-ray Timing Explorer (PCA, RXTE Jahoda et al. 2006), and a proper association was possible due to analysis of archival Chandra observations (Edge et al. 2004a). By investigating the long term optical light-curve of the optical counterpart of SMC X-2, Cowley and Schmidtke (2004) reported a 44.86 d modulation that they interpreted as the orbital period of the system. McBride et al. (2008) have reported a spectral type of B1-1.5 IV-V for the BeXRB’s donor star.

The event was reported by MAXI (Negoro et al. 2016) and is estimated to have started around June 2016 (Kennea et al. 2016a), while lasted for more than seven binary orbital periods thus can be classified as one of the longest ever observed for any BeXRB system. Since the outburst was reported the system has been extensively monitored in the X-rays by *Swift* with short visits, while deeper observations have been performed by NuSTAR, Chandra and *XMM-Newton*. Townsend et al. (2017) have reported a 44.918 d period as the true orbital period of the system by modeling the pulsar period evolution during the 2016 outburst with data obtained by *Swift*/XRT and by analyzing the optical light-curve of the system, obtained from the Optical Gravitational Lensing Experiment (OGLE, Udalski et al. 2015). The maximum luminosity obtained by *Swift*/XRT imposes an above-average maximum magnetic field strength at the NS surface ( $> 10^{13}$  G), as does the lack of any cyclotron resonance feature in the high energy X-ray spectrum of the system (Pottschmidt et al. 2016; Tsygankov et al. 2017). On the other hand, the lack of a transition to the propeller regime, during the evolution of the 2016 outburst suggests a much weaker magnetic field at the magnetospheric radius. According to Tsygankov et al. (2017) this apparent contradiction could be resolved if there was a significant non-bipolar component of the magnetic field close to the NS surface.

Following the evolution of the outburst I was involved in a non anticipated *XMM-Newton* ToO observation (PI: F. Koliopanos) in order to perform a detailed study of the soft X-ray spectral characteristics of the system. In the following sections I describe the X-ray data, and introduce a toy model constructed to phenomenologically explain the evolution of the spectral properties the system.

### 16.1 Spectral and temporal properties

Following the standard tools described in the previous chapters I obtained the pulse profile of the system (Fig. 16.1). Moreover, I constructed the phase resolved heat-map to visualize the spin-phase resolved spectral evolution of the pulsar (Fig. 16.2, left panel). Motivated by the features of the heat-map I performed phase resolved spectroscopy using a model similar to the case of LXP 8.04 and SMC X-2. The model

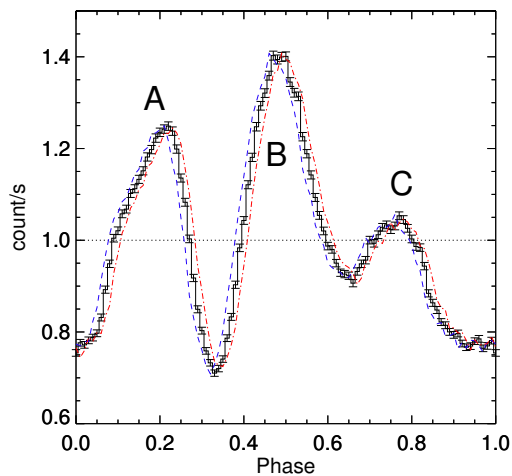


**Figure 16.1:** Phase folded pulse profile of SMC X-3 derived from the best fit period of 7.7720059. Profile is normalized at an average count rate of  $44.49 \text{ cts s}^{-1}$ . Red and blue lines correspond to the derived pulse profile for a period shifted by  $\pm 5 \times 10^{-5} \text{ s}$  which is  $\sim 1000$  times larger than the derived period uncertainty. This was chosen to demonstrate the accuracy of the derived period. Three peaks are clearly distinguished.

is composed by a power-law that accounts for most of the pulsating emission and a thermal component that contributes at the soft energies (Fig. 16.2, right panel). From the above it is clear that the source of the pulsations can be phenomenologically described by a power-law component. I note that both the shape and the normalization of the component changes with spin-phase. The soft component can be described by a weakly or non-pulsating thermal component.

To report on the longterm evolution of spectral properties throughout the 2016 outburst all available *Swift*/XRT data were used. For each *Swift* visit we extracted the source events and computed the two *HR* for 3 energy bands. *HR soft* using the 0.5-2.0 keV and 2.0-4.5 keV bands, and *HR hard* using the 2.0-4.5 keV and 4.5-10.0 keV bands. To compare the long term spectral evolution with the phase resolved, the same calculation was performed for the SMC X-3 *XMM-Newton* events. In particular *HR* values were calculated for 40 phase intervals. The results are plotted in Fig. 16.3.

## 16.2 Pulse profile evolution

Using all available *Swift*/XRT observations throughout the burst one can follow the pulse profile evolution at different luminosity levels. For each XRT snapshot I computed the *NS* spin period using the *EF* method, and then computed the pulsed profile and *PF*. The evolution of *PF* with *Swift*/XRR count-rate (i.e. Luminosity) is shown in Fig. 16.4.

The 0.01-12 keV luminosity of SMC X-3 during the *XMM-Newton* observation is estimated at  $1.45 \pm 0.01 \times 10^{38} \text{ erg/s}$  for a distance of  $\sim 62 \text{ kpc}$ . The corresponding mass accretion rate, assuming an efficiency of  $\xi = 0.21$  (e.g. Sibgatullin and Sunyaev 2000), is  $\dot{M} \sim 1.2 \times 10^{-8} M_{\odot}/\text{yr}$ , which places the source well within the fan-beam regime (Basko and Sunyaev 1976; Nagel 1981). Furthermore, the shape of the pulse profile (Fig. 16.1), indicates a more complex emission pattern, comprised of the primary fan beam and a secondary, reflected polar beam as was proposed in Trümper et al. (2013) and briefly presented in Section 3.4. The energy resolved pulse profiles and the phase resolved hardness ratios presented in Fig. 16.2 strongly indicate that the pulsed emission is dominated by hard-energy photons, while the smooth single-color appearance of the

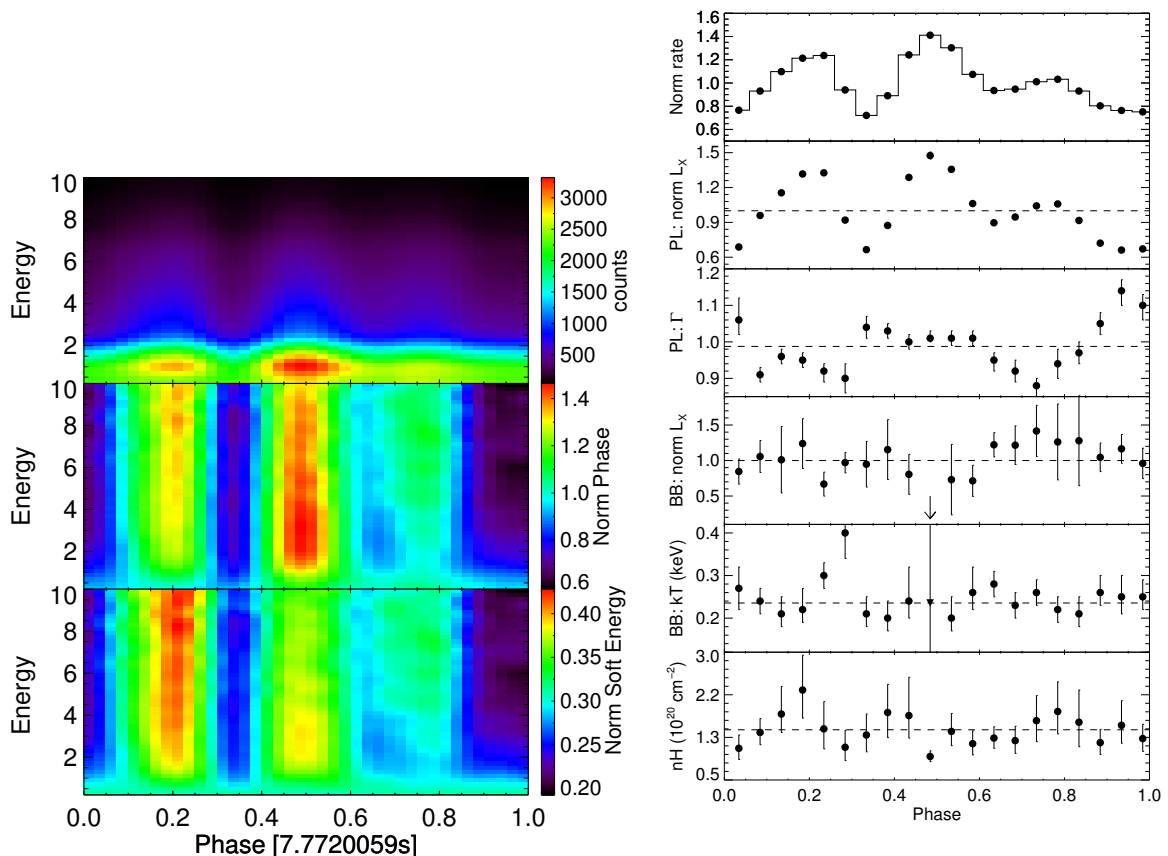


**Figure 16.2:** Left: Phase dependent spectral heat map, obtained by binning the EPIC-pn source counts to 40 phase and 50 energy bins. Top: Colors are proportional to the number of counts per bin. Middle: Data rates are corrected for the EPIC-pn response matrix efficiency and normalised by the phase-averaged number of counts in each energy bin. Bottom: Data normalised a second time using the rate average of each phase bin for the soft X-ray band (0.2-0.6 keV) Right: Evolution of spectral parameters for the phase resolved spectroscopy.

0.2-0.6 keV energy range in the lower bin of the heat-map indicates the presence of a soft spectral component that is not pulsating.

Using our toy-model for the emission of the accretion column, we were able to explore the evolution of the PF with the  $F_{\text{Polar}}/F_{\text{Fan}}$  ratio, assuming a broad range of observer viewing angles. Interestingly the resulting PF vs  $F_{\text{Polar}}/F_{\text{Fan}}$  ratio (Fig. 16.5), qualitatively resembles the evolution of the PF, with increasing source count-rate, as presented in Fig. 16.4, using *Swift*/XRT data. Following the paradigm of Basko and Sunyaev (1975) and Basko and Sunyaev (1976) we expect the emission pattern of the accretion column to shift from a pencil to a fan-beam pattern as accretion rate increases. Namely, below  $\sim 1$  cts/sec the emission is dominated by the

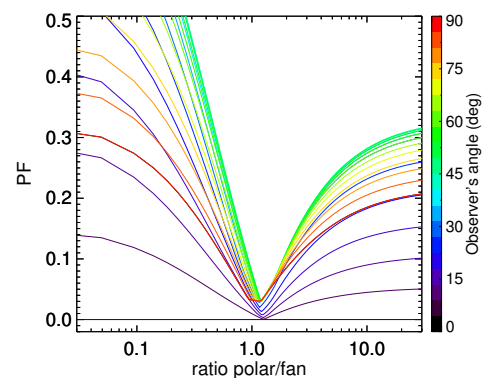


**Figure 16.5:** PF versus intensity between fan and pencil beam.

## 16. SMC X-3: JUNE 2016 OUTBURST

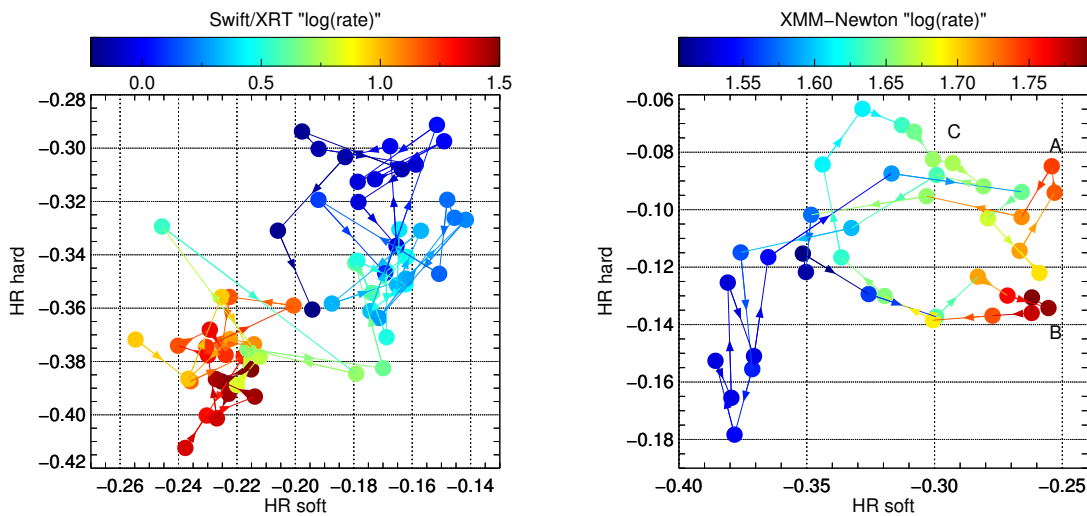


**Figure 16.3:** *Left:* Hardness ratio evolution of the average X-ray spectrum of SMC X-2 as estimated for all *Swift*/XRT observations. Calculations were made using three bands 0.5-2.0 keV, 2.0-4.5 keV and 4.5-10.0 keV. HR soft was estimated using the 2 former energy bands, while HR hard was estimated for the later two. Colors are representative of the average count rate of each observation, while arrows connect observations in a chronological order. *Right:* Hardness ratio evolution of the phase resolved X-ray spectrum of SMC X-2 based on the *XMM-Newton* observation. HR were defined as in the left plot, while 40 phase bins were used. Colors are representative of the average count rate of each phase bin, while arrows connect observations based on their phase evolution. Labels “A”, “B” and “C” represent the three peaks in Fig. 16.1

pencil beam (which is qualitatively similar to the polar beam). This regime is defined by  $F_{\text{Polar}}/F_{\text{Fan}} > 2$ . As the luminosity increases<sup>1</sup>, the radiation of the accretion column starts to be emitted in a fan beam, which is accompanied by the secondary polar beam, corresponding to  $0.7 \lesssim F_{\text{Polar}}/F_{\text{Fan}} \lesssim 2$ . This is the era during which the *XMM-Newton* observation was conducted. As accretion rate continued to increase, the accretion column grew larger, the height of emitting region increased and the emission started to become dominated by the fan-beam, as the reflected component decreases, yielding a smaller value of the  $F_{\text{Polar}}/F_{\text{Fan}}$  ratio. Nevertheless, in Fig. 16.4 it is evident that the PF does not readily increase, as the fan beam becomes more predominant (i.e. above  $\sim 7$  cts/s). This indicates that the height of the accretion column is limited to moderate values (e.g., as argued by Poutanen et al. 2013; Mushtukov et al. 2015b) and therefore a considerable contribution from the polar beam is always present.

The presence of the polar beam is also indicated by the shape of the pulse profile and its spectral evolution (Fig. 16.2). The pulse profile features three distinct peaks, which we label “A”, “B” and “C”, from left to right in Fig. 16.1. The analysis presented here reveals that the pulse peaks are dominated by harder emission. A closer inspection, indicates that peak B is “softer” than the other two peaks, and is still present (albeit much less pronounced) in the lower energy bands. This finding is further supported by our study of the HR evolution of the sources throughout the *XMM-Newton* observation, presented in Fig. 16.3 (right panel). In this representation, it is clearly demonstrated

<sup>1</sup>This only refers to the X-axis of Fig. 16.4 and does not imply chronological order. The chronological evolution is indicated with arrows in Fig. 16.3

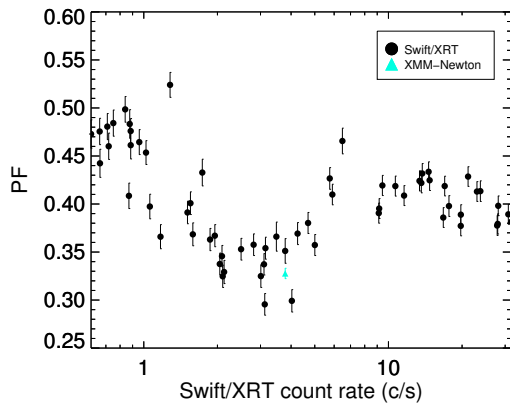


**Figure 16.4:** PF evolution of SMC X-3. Errors are computed based on the poisson uncertainty of the pulse profile, and do not include calculations based on the period uncertainties, as systematic uncertainty of 0.01 was added to the estimated *Swift*/XRT PF.

that the source is harder during high flux intervals (namely the peaks of the pulse profile), but also that peak B is distinctly softer than peaks A and C. We argue that these findings indicate a different origin of the three peaks. More specifically, we surmise that the softer and more prominent peak B originates mostly from the fan beam, while the two harder peaks (A,C) are dominated by the polar beam emission, which is expected to be harder than the fan beam. This is because only the harder incident photons (of the fan beam) will be “reflected” (i.e. backscattered) off the NS atmosphere, while the softer ones will be absorbed (e.g. Trümper et al. 2013; Postnov et al. 2015a).

## 16.3 Conclusions

The above section partially summarizes the findings extensively discussed by Koliopoulos and Vasilopoulos (2018). In the complete study, we have analyzed, the high quality *XMM-Newton* observation of SMC X-2, during its 2016 outburst. The *XMM-Newton* data were complimented with *Swift*/XRT observations, which were used to study the long-term behavior of the source. By carrying out a detailed temporal and spectral analysis (including phase resolved spectroscopy) of the source emission, we find that its behavior and temporal and spectral characteristics adhere to the theoretical expectations and the previously noted observational traits of accreting highly magnetised NS at high accretion rates. More specifically, we find indications of a complex emission pattern of the primary, pulsed radiation, which most likely involves a combination of a “fan” beam emission component directed perpendicularly to the magnetic field axis and a secondary “polar” beam component reflected off the NS surface and directed perpendicularly to the primary, fan beam (as discussed in e.g. Basko and Sunyaev 1976; Wang and Frank 1981 and more recently Trümper et al. 2013).

The spectroscopic analysis of the source, further reveals the presence of optically thick material located at approximately the boundary of the magnetosphere. The reprocessing region has an angular size (as viewed from the NS), that is large enough to reprocess a considerable fraction of the primary, beamed emission which is remitted in the form of a soft thermal-like component that contributes very little to the pulsed emission. These findings are in agreement with previous works on XRP (e.g. Endo et al. 2000; Hickox et al. 2004), but also the theoretical predictions for highly super-Eddington accretion onto highly magnetised NS (e.g. King et al. 2017; Mushtukov et al.

## 16. SMC X-3: JUNE 2016 OUTBURST

---

2017b; Koliopoulos et al. 2017), where it is argued that this reprocessing region grows to the point that it may reprocess the entire pulsar emission.

## Part V

# Neutron stars powering ultraluminous X-ray sources



## Highly magnetised accreting neutron stars powering ultraluminous X-ray sources

**I**n the previous chapters I focused on the properties of [BeXRBs](#) that were observed during major X-ray outbursts. Although each system can uniquely stand-out of the group, there are multiple features that they have in common. In this chapter I will summarise the main properties of these intriguing systems and build up a physical picture that can explain most of the properties of [ULX](#) systems in the context of accreting [NSs](#).

Concerning the spectral properties, the soft excess is maybe the most prominent feature. The identification of this feature is best seen in the better calibrated instruments like *XMM-Newton*/EPIC cameras, while in spectra with low statistics (e.g. *Swift*/XRT) its presence can be smeared out. Soft excess can be mainly identified through residual structure in a [PL](#) fit. However, although phenomenologically a fit can be improved by the inclusion of different thermal components, the physical properties of the system should be the ones dictating our selection. In low-luminosity systems, the soft excess cannot originate from an accretion disk, as the disk is truncated at very large distances, but it can be attributed to thermal emission from the [NS](#) surface, and specifically from the polar cap (e.g. *Swift* J053041.9-665426). In intermediate-luminosity systems the pulsating hard emission from the accretion column can dominate the X-ray emission and the soft excess can be lost as it is swamped by the accretion column emission (e.g. SXP 15.6, SXP 2.16). In luminous systems, the soft excess can originate from the inner part of the accretion disk (e.g. SMC X-2, SMC X-3, LXP 8.04), but its properties do not describe a typical thin disk. Specifically, the disc temperature, size and luminosity evolution with the global pulsar luminosity does not follow the typical disc truncated at  $R_M$ . This is clearly seen in SMC X-2 where we have multiple high resolution observations available from *XMM-Newton*. The disc temperature in SMC X-2 through the brightest stages of the outburst seems to remain constant, while its size significantly changes. All this can be explained by a toy model where the disc luminosity is a result of reprocessing of hard X-rays that originate from the accretion column of the [NS](#). In this explanation the inner disc can gradually be inflated and thus occupy a larger solid angle with respect to the [NS](#). Another characteristic of the brightest [BeXRBs](#) is the presence of emission and absorption lines in their X-ray spectra. The emission lines occupy energies close to their rest frame, but some of the strongest candidate absorption features are blue-shifted, thus must be produced in some outflow. This is in agreement with simulations of [NS](#) magnetospheres where large outflows are seen to originate from regions where reconnection occurs from the opening of magnetic field lines ([Parfrey and Tchekhovskoy 2017](#); [Parfrey et al. 2016b](#)).

We can start painting a picture of the environment around the [NS](#) that is responsible for the radiative transfer processes that result in the observed spectrum. As material is trapped by the magnetic field, an optically thick structure is formed inside the pulsar magnetosphere, which (for a range of viewing angles) covers the primary source, partially reprocessing its radiation. The optically thick region is expected to have an angular size of the order of a few tens of degrees and to be centered at the latitudinal

## 17. HIGHLY MAGNETISED ACCRETING NEUTRON STARS POWERING ULTRALUMINOUS X-RAY SOURCES

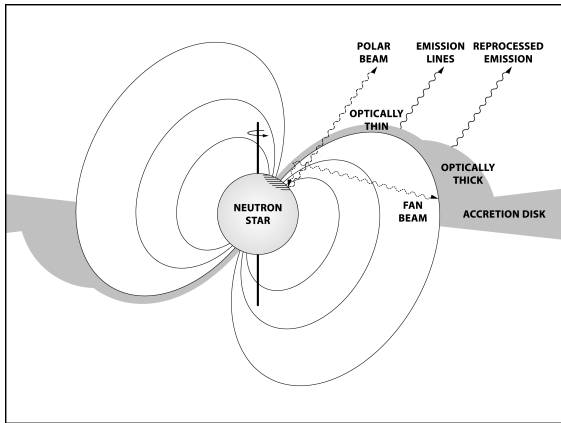


**Figure 17.1:** A schematic representation of the proposed structural configuration of X-ray pulsars at the moderately high accretion regime. The (possibly inflated) accretion disc is truncated at approximately the magnetosphere and a combination of optically thick and thin plasma, is trapped at the magnetospheric boundary. The optically thick material (and the inner disc edge) partially cover the primary emission source and reprocess its emission. At higher latitudes the material remains optically thin, the emission lines originate from this region. The source of the primary emission is located at a some height above the NS pole, inside the accretion column. (Credit: Cheryl Woynarski)

position of the accretion disk. At higher latitudes and closer to the accretion column, the trapped plasma, remains optically thin, producing the observed emission lines. At high accretion rates, the size of the reprocessing region becomes large enough to reprocess a measurable fraction of the primary emission. This is due to the increase in the accreting material getting trapped by the pulsar’s magnetosphere and the increase in the thickness of the accretion disc due to a higher radiation pressure (e.g. [Shakura and Sunyaev 1973](#); [Poutanen et al. 2007](#); [Dotan and Shaviv 2011](#); [Chashkina et al. 2017b](#)). The proposed configuration is schematically represented in Fig. 17.1. I note that an observer at a specific angle would observe pulsations from the main component that originates from the NS accretion column while components originating from the outer magnetosphere would be weakly or non-pulsating.

The schematic representation (Fig. 17.1) of the environment around BeXRBs describes well their observed properties during major outbursts (i.e.  $L_X \sim 10^{38-39}$  erg  $s^{-1}$ ). An intriguing question is if this paradigm still holds at even higher accretion rates. The best candidate systems to explore this idea are ULXs that host NSs as their central engine. We can be confident for the NS nature of the compact object of a ULX system only if we observe pulsations; currently, we are aware of only four ULXPs systems. However, even for these systems there is a debate in the scientific community if they indeed host a NS that accretes at super-Eddington rate or their unusual high luminosity is an effect of extreme beaming.

Before focusing on pulsating systems, I will briefly describe the scientific census around typical ULXs. Prior to the discovery of ULXPs, the most commonly accepted scenario for ULXs was that they host intermediate-mass BHs ([Colbert and Mushotzky 1999](#)). Recent observations of the hard spectra of common ULXs revealed that their properties are inconsistent with known sub-Eddington accretion modes, as would be expected for an intermediate-mass BH, but instead support the notion ([Poutanen et al. 2007](#)) that they are powered by super-Eddington accretion onto stellar-mass BHs ([Gladstone et al. 2009](#); [Roberts et al. 2016](#)). The most widely accepted interpretation of the spectral curvature of ULXs invokes the presence of strong, optically thick winds. Namely, under the assumption that ULXs are accreting BHs in the super-Eddington regime, then the spectral shape of the emission may be strongly influenced by the presence of massive, optically thick outflows. [King and Pounds \(2003\)](#) and [Poutanen](#)

## 17.1 Accretion funnels and envelopes around neutron stars during extreme accretion

---

et al. (2007) argued that the curvature of the spectra of (at least some) **ULXs** can be interpreted in terms of reprocessing of the primary emission in the optically thick wind. In this scenario the soft thermal emission is associated with the wind itself, and the hard emission is also thermal and originates in the hot, innermost parts of an accretion disk.

**ULXPs** show similar spectral properties to non-pulsating **ULXs** systems and to **BeXRBs**, as all systems show hard X-ray spectra with similar shape (Pintore et al. 2017). Nevertheless, focusing just on pulsating systems, **ULXPs** have some striking differences to **BeXRBs**: they have a much lower cut-off energy in their spectrum and their pulse profile is smooth and single peaked. These features are very different to what we see from **BeXRBs** during major outbursts, where we generally observe complicated emission patterns (e.g. double peak fan-beam; Cappallo et al. 2017). Moreover, the nearly sinusoidal single-peaked pulse profiles of **ULXPs** (e.g. NGC 7793 P13: Israel et al. 2017b) suggest the absence of strong beaming (Kaaret et al. 2017), as it is also the case for **BeXRBs** (see results on LXP 8.04; Fig. 11.11). I note that although there have been cases of **BeXRBs** with low cut-off energies and single peaked pulse profiles, these two properties are shared among **ULXPs** (Kaaret et al. 2017).

In what follows, I will describe the basic characteristics of the accretion flow onto a highly magnetised **NS** in the regime of super-Eddington accretion, and I will demonstrate the basic characteristic spectral signatures expected from these systems. I will then focus on the spectral properties of the population of non-pulsating **ULXs** showing that they are compatible with super-Eddington accretion onto a **NS**, thus demonstrating that a large fraction of these systems host **NS** and not **BHs**.

## 17.1 Accretion funnels and envelopes around neutron stars during extreme accretion

The first key in understanding the observed differences between **BeXRBs** and **ULXPs** is the accretion funnel, or the environment between the top of the accretion column and the inner disc radius. In Fig. 17.1 we describe this region as an optically thin accretion curtain that can emit like hot plasma. We argue that in cases of high accretion rates this curtain will be filled by material forming an optically thick envelope that can absorb and reprocess most of the radiation from the accretion column. In fact this envelope can become large enough and result in the loss of the pulsating signal.

Below, we revisit the proposed model of accretion envelopes in order to apply its basic principles to **ULXPs** and illustrate why this model is very likely to describe their observed characteristics. We note that the basis of this model has already been used to successfully explain the spectra of non-pulsating **ULX** (Koliopanos et al. 2017) while in parallel to our work a similar study has appeared in the literature (Mushtukov et al. 2017a).

We calculate the magnetospheric radius following Lai (2014). We assume that the total X-ray luminosity is equal to the rate at which gravitational energy of the in-falling matter is released ( $L_X \simeq GM\dot{M}/R_{NS}$ ), and that accreting matter follows the direction of the last closed magnetic field line (i.e.  $R_m$ ). Matter is then confined in a space defined by adjacent lines, this can be a small fraction of  $R_m$ . At the base of the accreted flow a cylindrical accretion column is formed. Through diffusion processes the width of the accretion column can be broadened, but this does not affect our calculations especially

## 17. HIGHLY MAGNETISED ACCRETING NEUTRON STARS POWERING ULTRALUMINOUS X-RAY SOURCES

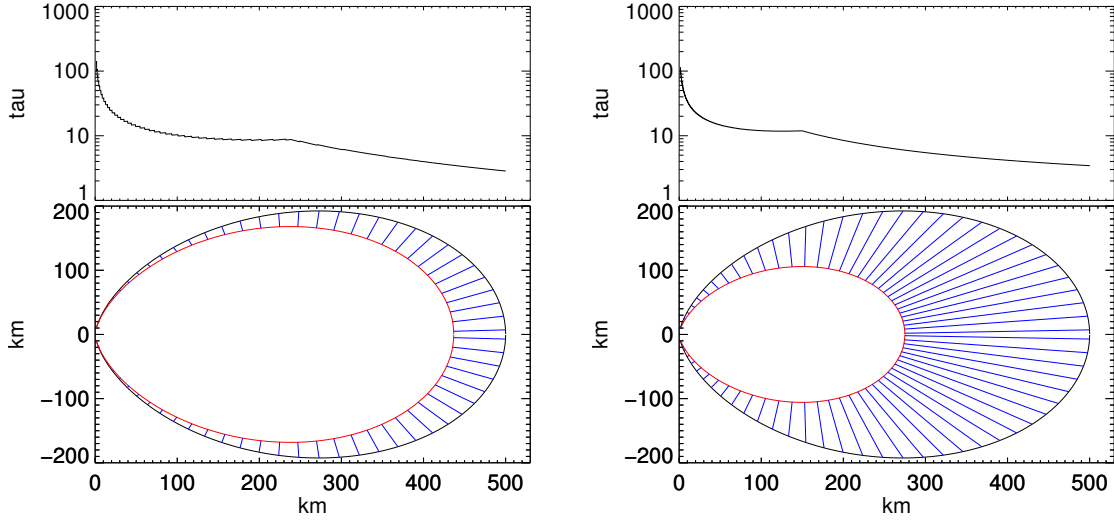


**Figure 17.2:** Schematic structure of the accretion envelope where the optical depth is given as a function of distance from the NS. Across the envelope the optical depth has been computed based on the minimum separation of the two confining lines. The separation of the lines at the base of the accretion column has been selected to be 100 m (left) and 300 m (right) wide. Wider accretion columns can be expected due to diffusion processes as matter is accreted towards the NS. Still, there should be an upper limit on the area between the lines that can be occupied by matter at larger radii.

away from the NS. The equation of a dipole magnetic field line can be expressed in terms of its largest radius (e.g.  $R_m$ ) and its angular coordinate ( $\theta$ ) from the equatorial plane:  $R(\theta) = R_m \cos^2 \theta$ . For the last closed field line at the surface of the NS this corresponds to  $\cos(\theta_{\text{NS}}) = \sqrt{R_{\text{NS}}/R_m}$  or  $\theta_{\text{NS}} \sim 82^\circ$ . Thus, we can express any magnetic line based on their trace on the NS surface by using the relation:

$$R(\theta) = R_{\text{NS}} \frac{\cos^2 \theta}{\cos^2 \theta_{\text{NS}}} \quad (17.1)$$

As a next step we need to calculate the size or width of the envelope at a given radius, and its minimum optical depth as a function of radius. By following two “parallel” closed field lines from the NS surface towards the magnetosphere we can calculate the surface area between them based on their minimum separation ( $d_{\text{R,min}}$ ) at a given point (see West et al. 2017a, for more details about the described configuration). Moreover, we calculate the surface area  $S_{\text{D,R}}$  of this conical frustum that is defined by the orientation of  $d_{\text{R,min}}$  assuming axial symmetry around the magnetic axis (see Fig. 17.2). The opacity of the envelope in the direction of the minimum width can then be calculated as a function of radius (see also eq. 3 in Mushtukov et al. 2017a):

$$\tau(R) = \frac{\kappa_e \dot{M} d_{\text{R,min}}}{2S_{\text{D,R}} v(R)}, \quad (17.2)$$

where  $\kappa_e$  is the Thomson electron scattering opacity, and  $v(R)$  is the local velocity of the in-falling matter, which cannot be larger than the free fall velocity. We note that at a given distance from the rotation axis, the separation of two close field lines can only

be a fraction of that distance thus the free fall velocity can vary by less than a factor of two within the range of the conical frustum. In Fig. 17.2 we plot an example of a formed envelope assuming different line configurations at the NS surface as well as the opacity derived by solving eq. 17.2. From these calculations – based on fundamental principles – it becomes apparent that for mass accretion rates that correspond to an observed luminosity greater than  $10^{39}$  erg s<sup>-1</sup>, the accretion shell formed by the material following the magnetic field lines becomes partially or fully optically thick.

We further note that in the case of oblique rotators, where the magnetic and rotation axis do not align, a fully closed envelope could be difficult to maintain its structure for many dynamical times. Most of the time material should fall onto the polar cap from the direction where magnetic lines are closer to the inner disc radius, as indicated by simulations (Parfrey and Tchekhovskoy 2017). This would result in an envelope that covers only a fraction of the sphere around the NS. For example if the envelope covers only half the sphere around the pole, the same amount of material would be confined inside an envelope with half the maximum size, and the optical depth at a given radius would be double. Thus, the optical depth plotted in Fig. 17.2 should only be considered as a lower limit. Pulsations would then naturally arise from the rotation of the accretion funnel, as the observing angle of its surface would change with pulse phase.

### 17.1.1 Accretion column in high accretion rates

The optical thick accretion envelope (or funnel in the case of oblique rotator) does not contradict the physics of the accretion column (Becker and Wolff 2007a; Farinelli et al. 2016; West et al. 2017a) but it is a natural expansion of the accretion column environment. In the literature there is a surprising lack in the application of physics-based models for the X-ray spectra of BeXRBS. However there is a variety of *ad hoc* functional forms that are used to fit the observed spectra, with some of them being (I) a power-law with high energy cut-off, (II) a power-law with Fermi-Dirac cutoff (Mihara 1995), or (III) a sum of two power-law functions with positive and negative slopes and exponential cutoff (Mihara 1995).

The physics behind the above power-law like models with some cut-off has been explained by Becker and Wolff (2007a) (see also §3.3). The accretion column is a complex structure. At the base of the column there is a thermal mound with size  $\sim 1$  km and high temperatures (few keV). This mound produces thermal seed photons to the accretion column. The top of the accretion column can be approximated by the point where the in-falling flow becomes subsonic. Below the subsonic point electrons produce bremsstrahlung and cyclotron radiation. In the first approximation by Becker and Wolff (2007a) the size (height) of the accretion column was assumed to be a few km which is appropriate for most typical X-ray pulsars. In a more recent work (West et al. 2017a) it has been shown that the accretion column can extend to much larger radii for high accretion rates. By following the basic equations for radiation and ram pressure equilibrium we can estimate the size (height) of the accretion column as a function of accretion rate and magnetic field strength of the NS. It should be noted that in order to accurately calculate the height of the accretion we should account for the mixed polarisation states and the energy dependence of the scattering cross-section at energies below the local cyclotron energy for a given magnetic field strength. These effects will not strongly affect the height of the accretion column at large accretion

## 17. HIGHLY MAGNETISED ACCRETING NEUTRON STARS POWERING ULTRALUMINOUS X-RAY SOURCES

---

rates, but greatly affect the critical luminosity at which the accretion column is formed (Mushtukov et al. 2015a). For the ordinary polarisation mode, the electron scattering cross-section is given by:

$$\sigma_s = \sigma_T[(1 - \mu^2) + \mu^2 f_s] \begin{cases} f_s = 1, E \geq E_{cyc} \\ f_s = (E/E_{cyc})^2, E \leq E_{cyc} \end{cases} \quad (17.3)$$

where  $\sigma_T$  is the Thomson cross-section,  $\mu = \sin \theta$  is the angle with respect to the magnetic field, and  $E_{cyc} = 11.6 B_{12}$  keV is the cyclotron energy for the corresponding local  $B$ . In general, the size of the accretion column will increase with increasing accretion rate. However, in this approximation the maximum length of the column is bound by a strict geometrical limit. This is the dipole turnover radius  $r_{turn}$ , which is approximately  $\sim 2/3R_m$ . Following the basic equation introduced by West et al. (2017a) the upper surface of the accretion column is found to be:

$$r_{top} = \left[ r_{turn}^{-3/2} + \frac{3(m_e + m_i)(2GM_{NS})^{1/2}\Omega_{NS}}{2\sigma_{\parallel}\dot{M}R_{NS}} \right]^{-2/3} \quad (17.4)$$

where  $m_e + m_i$  denotes the total particle mass, assuming the accreting gas is composed of fully ionized hydrogen. Since plasma accretes along the magnetic field lines, the accretion column has a curved shape, thus for large accretion columns it is more appropriate to use the term length and not height to describe its extend along the magnetic field lines. In Fig. 17.3 I plot the calculated size of the accretion column as function of observed  $L_X$  assuming typical efficiency (i.e. 20%). For comparison, I also plot the size of a BB with luminosity equal to the accretion column. It is clear that for  $L_X > 10^{39}$  erg s<sup>-1</sup> the size of the accretion column can be of the order of 100 km. Moreover, by comparing Figs. 17.3 and 17.2 we can see that the accretion column and the surrounding flow is optically thick for much larger distances. In comparison, for  $L_X \lesssim 10^{38}$  erg s<sup>-1</sup> the optical depth at the top of the accretion column can be smaller than 1 for typical  $B$  values.

To conclude, the size and the optical depth inside and around the accretion column during extreme accretion provide the basic physical tools needed to explain the spectral properties of ULXPs as a natural continuation of the model introduced by Becker and Wolff (2007a). In sub-Eddington rates the seed bremsstrahlung and cyclotron photons are scattered by in-falling electrons and produce the spectrum observed in BeXRBs (see West et al. 2017b). For the typical densities in the accretion flow, the escaping photons can maintain some of the spectral information of the seed spectra. However, for extreme optical depths like in the case of ULXPs, due to repeated Compton scattering the escaping photons will have a broad peak around  $3kT/h$  (Wien spectra; Rybicki and Lightman 1979). Nevertheless, the escaping spectrum could be a superposition of regions along the accretion column, but its characteristic signature would be the Wien cut-off at the maximum electron temperature.

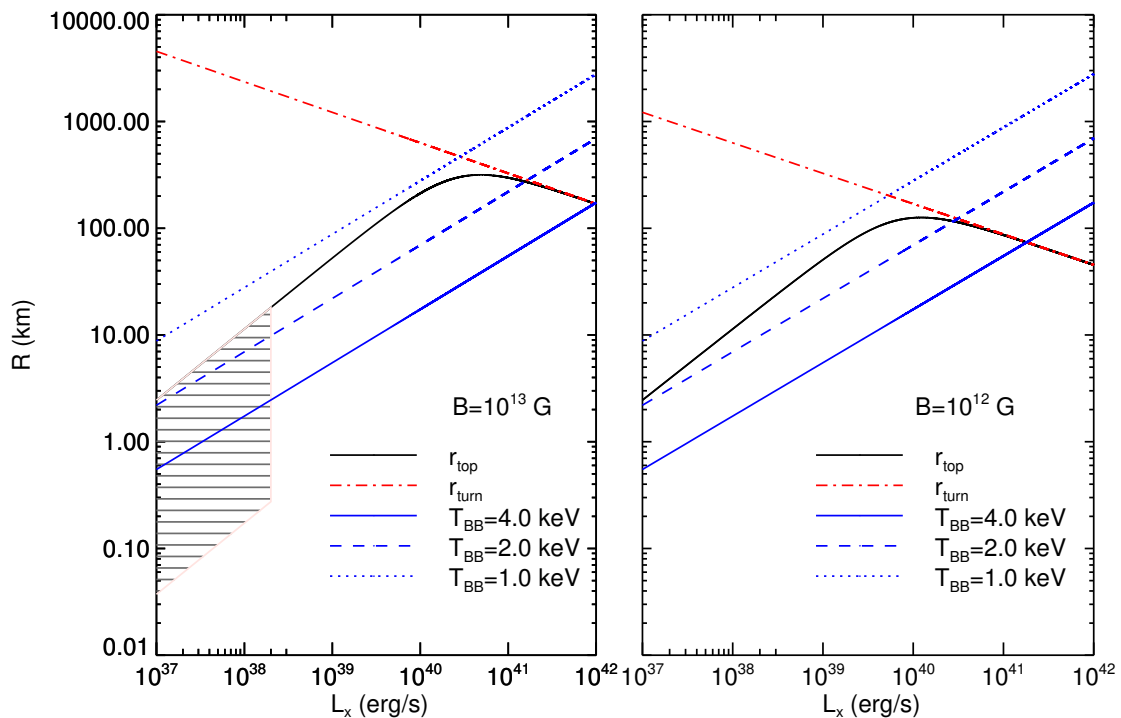


**Figure 17.3:** Accretion column length (black lines) as estimated by eq. 17.4 for a magnetic field of  $10^{13}$  G (left) and  $10^{12}$  G (right). Shaded area denotes the region where  $\sigma_{\perp} < \sigma_T$  due to  $E_{cyc}$  being larger from the typical photon energy (i.e 5 keV). The dashed-dotted line marks the turn-point of the magnetic lines a fundamental geometrical restriction of the column size. Blue lines note the size of a pure BB with luminosity equal to the accretion column (see text) and  $T_{BB}$  1.0 keV, 2.0 keV and 4.0 keV.

## 17.2 ULX spectra

In accordance with the predictions for the formation of optically thick accretion envelopes around super-Eddington accreting, highly magnetised NSs (see also; Mushukov et al. 2017b) we can fit the spectral continuum of ULXs with a combination of two multi-temperature components (MTC) and a power-law high energy tail. This is what we did in Koliopanos et al. (2017). The soft MTC is expected to originate in an accretion disc truncated approximately at the magnetospheric radius of the NS. The values for the best fit model for each system are listed in Table 17.1. It should be noted that this is used as a rough approximation of the multi-temperature disk, as most likely the disc will be geometrically thick (Chashkina et al. 2017a; Koliopanos et al. 2017). Similarly the second (hot) MTC is an approximate description for the multicolour BB emission of the accretion envelope. In addition to the two MTC components the fit also required the presence of a hard non-thermal tail, which we model using a power-law distribution. This component accounts for a small fraction of the accretion column photons that are up-scattered by the free falling material within the accretion funnel.

The use of a double thermal spectral model successfully describes the spectra of ULXs and the unusual high-energy roll-over of the ULX spectra can be re-interpreted as the Wien tail of a hot (multicolour) black-body component. It should be noted that

## 17. HIGHLY MAGNETISED ACCRETING NEUTRON STARS POWERING ULTRALUMINOUS X-RAY SOURCES

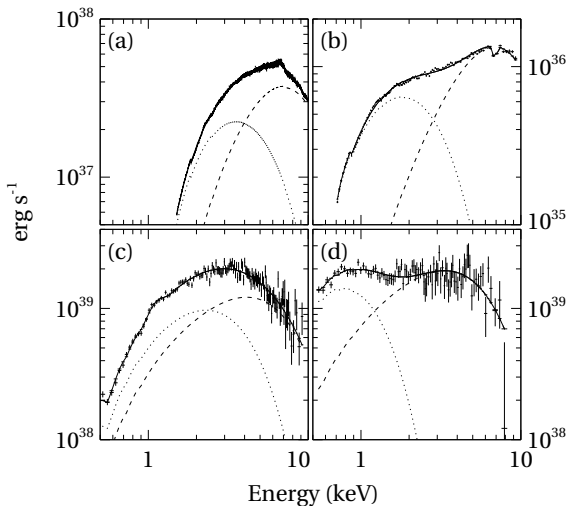


**Figure 17.4:** Example, unfolded spectra of two ULXs from this study and two well known NS-XRBs in the soft state. (a) 4U 1705-44, during a soft state. (b) Double thermal spectrum from NS-LMXB 4U 1916-05. (c) Apparent, dual thermal emission from ULX M81 X-6, at similar temperatures as 4U 1705-44. (d) Similarly shaped spectrum from NGC 4559 X-1.

the temperatures derived for the double thermal spectrum bares similarities with those of NS-XRBs in the soft state. For comparison, we have analysed the spectra of NS-XRBs 4U 1916-05 and 4U 1705-44 with the dual thermal model. For 4U 1916-05 the hot thermal component has a size of  $\sim 1$  km and a temperature of  $1.75 \pm 0.01$  keV, while the soft thermal component has a size of  $\sim 13$  km and a temperature of  $0.66 \pm 0.01$  keV. For 4U 1705-44 the hot thermal component has a size of  $\sim 5$  km and a temperature of  $1.76 \pm 0.01$  keV, while the soft thermal component has a size of  $\sim 12$  km and a temperature of  $1.14 \pm 0.03$  keV. From the derived sizes of the hot and cold component it is clear that for NS-XRBs in the soft state the accretion disc has reached NS surface (see Fig. 3.1). The similarities between the spectral morphology of ULXs and those of NS-XRBs in the soft state are illustrated in Figure 17.4. We have plotted the *XMM-Newton* spectra of two known NS-XRBs (4U 1916-05 and 4U 1705-44) along with the spectra of two (non pulsating) ULXs that were analysed for this study. Dotted lines correspond to the dual thermal model (in this example it is an absorbed MCD plus black-body model) which – in the case of the two NS-XRBs – is used to model emission from the boundary layer and the thin accretion disk.

By using the two-MTC model I have successfully fitted the spectra of non-pulsating and pulsating ULX system. Assuming that all these ULXs are hosting a highly magnetised NS, the soft MTC component should have the characteristic size of the magnetosphere. Thus, the size of this thermal component provides a way of estimating the magnetic field of the NS. By applying the accretion envelope model to the spectra of ULX systems I have computed the magnetic field strength of the NS (see Fig. 17.5). Most of these values (i.e. those  $< 10^{13}$  G) are comparable with the typical values derived for NSs in BeXRB (cyclotron absorption features: Maitra and Paul 2013; Doroshenko et al. 2017; Tendulkar et al. 2014) and XRB systems (Müller et al. 2013;

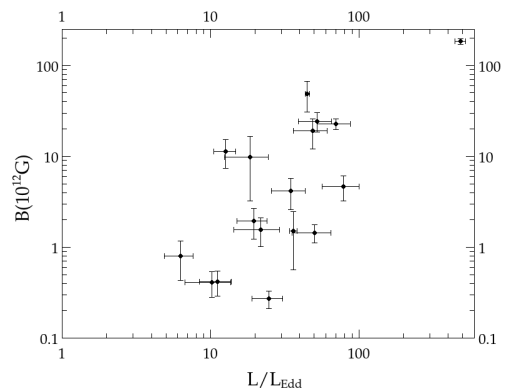


**Figure 17.5:** Polar magnetic field strength vs. luminosity for the accretion envelope model for the ULX system listed in Table 17.1. All values are also given in the same table.

(Mushtukov et al. 2014) and demonstrate the similarities of the two populations. We note that the average values of  $B$  in Fig. 17.5 are somewhat larger than the typical values derived by measuring the cyclotron absorption feature in the X-ray spectra of BeXRBs. However, the cyclotron features in magnetised NSs could originate from a region several NS radii away from the pulsar’s surface (Tiengo et al. 2013), and they do not reflect the surface magnetic field strength which should be higher. Thus, the above toy model provides a natural explanation for the major characteristics of ULX systems and their connection with BeXRBs.

Source	nH [ $\times 10^{21}$ cm $^{-2}$ ]	kT $_{\text{in}}$ K	R $_{\text{in}}$ [km]	kT $_{\text{bb}}$ K	R $_{\text{bb}}$ km	R $_{\text{sph}}^a$ km	$\chi^2_{\text{red}}/\text{dof}$
Ho II X-1	0.40 $^b$	0.57 $^{+0.02}_{-0.01}$	724 $^{+76.5}_{-62.1}$	1.26 $^{+0.17}_{-0.18}$	93.5 $^{+28.3}_{-22.7}$	974 $^{+297}_{-247}$	1.25/137
Ho IX X-1	0.33 $^{+0.10}_{-0.08}$	0.91 $^{+0.04}_{-0.03}$	198 $^{+38.3}_{-42.2}$	1.95 $^{+0.27}_{-0.25}$	59.2 $^{+18.8}_{-17.7}$	1120 $^{+384}_{-310}$	1.06/156
IC 342 X-1	7.42 $^{+0.44}_{-0.41}$	0.61 $\pm 0.05$	302 $^{+61.1}_{-52.5}$	1.66 $^{+0.14}_{-0.10}$	72.8 $^{+23.0}_{-19.8}$	304 $^{+135}_{-104}$	1.05/101
M33 X-8	0.82 $^{+0.03}_{-0.02}$	0.70 $^{+0.06}_{-0.07}$	202 $^{+51.8}_{-41.0}$	1.11 $^{+0.16}_{-0.18}$	62.1 $^{+50.2}_{-44.5}$	155 $^{+125}_{-108}$	1.01/121
M81 X-6	1.61 $^{+0.16}_{-0.12}$	1.03 $^{+0.33}_{-0.42}$	155 $^{+20.8}_{-22.2}$	1.51 $^{+0.46}_{-0.35}$	38.2 $^{+8.12}_{-6.78}$	346 $^{+91.4}_{-80.1}$	1.13/124
M83 ULX	0.39 $^b$	0.38 $^{+0.10}_{-0.08}$	482 $^{+86.8}_{-91.8}$	0.83 $^{+0.09}_{-0.11}$	88.3 $^{+20.0}_{-16.3}$	87.2 $^{+22.5}_{-19.4}$	0.95/44
NGC 55 ULX	2.16 $^{+0.58}_{-0.51}$	0.33 $^{+0.03}_{-0.02}$	986 $^{+108}_{-201}$	0.65 $^{+0.16}_{-0.15}$	128 $^{+18.3}_{-17.7}$	153 $^{+32.1}_{-29.8}$	1.11/89
NGC 253 ULX2	2.35 $^{+0.33}_{-0.51}$	0.95 $^{+0.14}_{-0.12}$	121 $^{+302}_{-257}$	1.39 $^{+0.16}_{-0.15}$	51.8 $^{+14.3}_{-15.7}$	258 $^{+105}_{-84.8}$	1.05/120
NGC 253 XMM2	1.09 $^{+0.19}_{-0.21}$	0.65 $^{+0.09}_{-0.10}$	218 $^{+64.3}_{-47.6}$	1.17 $^{+0.11}_{-0.09}$	54.2 $^{+22.0}_{-16.6}$	142 $^{+61.4}_{-49.0}$	1.14/108
NGC 1313 X-1	1.83 $^{+0.18}_{-0.17}$	0.44 $^{+0.21}_{-0.20}$	778 $^{+156}_{-133}$	1.39 $^{+0.54}_{-0.43}$	52.8 $^{+22.0}_{-22.8}$	730 $^{+225}_{-186}$	1.09/113
NGC 1313 X-2	1.70 $\pm 0.11$	0.86 $^{+0.11}_{-0.08}$	261 $^{+43.2}_{-35.6}$	1.66 $^{+0.06}_{-0.05}$	54.6 $^{+19.1}_{-15.8}$	700 $^{+244}_{-204}$	1.01/144
NGC 4190 ULX1	0.56 $^{+0.32}_{-0.31}$	0.87 $^{+0.42}_{-0.38}$	256 $^{+208}_{-120}$	1.51 $^{+0.17}_{-0.19}$	85.0 $^{+10.2}_{-6.06}$	505 $^{+31.8}_{-30.1}$	1.06/112
NGC 4559 X-1	0.15 $^b$	0.43 $^{+0.04}_{-0.05}$	1133 $^{+528}_{-412}$	1.04 $^{+0.12}_{-0.10}$	169 $^{+21.5}_{-18.1}$	626 $^{+22.2}_{-22.7}$	1.07/84
NGC 4736 ULX1	0.86 $^{+0.33}_{-0.31}$	0.61 $^{+0.22}_{-0.18}$	269 $^{+209}_{-122}$	0.99 $\pm 0.06$	76.6 $^{+11.3}_{-10.7}$	272 $^{+73.9}_{-62.2}$	1.12/68
NGC 4861 ULX	1.15 $^{+0.92}_{-0.81}$	0.33 $^{+0.11}_{-0.08}$	2398 $^{+728}_{-687}$	0.93 $^{+0.31}_{-0.25}$	205 $^{+44.7}_{-35.5}$	176 $^{+35.2}_{-29.7}$	1.10/22
NGC 5204 X-1	0.14 $^b$	0.43 $^{+0.09}_{-0.12}$	1262 $^{+308}_{-295}$	0.99 $^{+0.18}_{-0.15}$	152 $^{+41.0}_{-39.1}$	681 $^{+211}_{-174}$	1.15/65
NGC 5907 ULX	6.04 $^{+3.01}_{-2.52}$	0.74 $\pm 0.11$	608 $^{+133}_{-101}$	1.38 $^{+0.12}_{-0.09}$	224 $^{+49.3}_{-57.7}$	6740 $^{+554}_{-571}$	1.09/83
NGC 7793 P13	0.66 $\pm 0.14$	0.63 $\pm 0.04$	251 $^{+108}_{-115}$	1.70 $\pm 0.05$	59.7 $^{+22.0}_{-19.1}$	483 $^{+148}_{-122}$	1.10/141

<sup>a</sup> Spherisation radius (e.g. King and Lasota 2016):  $R_{\text{sph}} = 27/4\dot{m}R_g$ , where  $R_g = GM/c^2$  and  $\dot{m} = \dot{M}/\dot{M}_{\text{Edd}}$ .

<sup>b</sup> Parameter frozen at total galactic HI column density (Dickey and Lockman 1990a).

**Table 17.1:** Best fit parameters of the MCD plus black-body model for the *XMM-Newton* observations. All errors are in the  $1\sigma$  confidence range.

## 17.3 Conclusions

In the previous section, I have presented an alternative interpretation of the X-ray spectra of eighteen well-known ULXs, which provides physically meaningful spectral parameters. More specifically, from the analysis of the *XMM-Newton* and NuSTAR spectra, I conclude that the curvature above  $\sim 5$  keV – found in the spectra of most ULXs (pulsating and non-pulsating) – is consistent with the Wien tail of thermal emission ( $kT > 1$  keV). Furthermore, the high-quality *XMM-Newton* spectra confirm the presence of a secondary, cooler thermal component ( $kT < 1$  keV) that can be attributed to the presence of a hot accretion disk. These observational findings are in agreement with previous studies (e.g. Walton et al. 2014, 2015; Luangtip et al. 2016), but the physical interpretation we propose is very different. In contrast to the accepted paradigm for accretion in low magnetised NS, we propose that the dual thermal spectrum may be the result of accretion onto a highly magnetised NS, as predicted in recent theoret-

## 17. HIGHLY MAGNETISED ACCRETING NEUTRON STARS POWERING ULTRALUMINOUS X-RAY SOURCES

---

ical models ([Mushtukov et al. 2017b](#)) in which the hot thermal component originates from an optically thick envelope that engulfs the entire NS at the boundary of the magnetosphere, and the soft thermal component originates in an accretion disc that becomes truncated at approximately the magnetospheric radius. This finding offers an additional and compelling argument in favour of magnetised NSs as more suitable candidates for powering ULXs, as has been recently suggested ([King and Lasota 2016](#); [King et al. 2017](#)). In light of this interpretation, the ultraluminous state classification put forward by [Sutton et al. \(2013\)](#) can be re-interpreted in terms of different temperatures and relative flux contribution of the two thermal components, which result in the different spectral morphologies.

## NGC 300 ULX1: A test case for accretion torque theory

NGC 300 ULX1 is a newly identified ULX pulsar (Carpano et al. 2018), located in NGC 300 at a distance of 1.88 Mpc (Gieren et al. 2005). The system became active in X-rays and optical in May 2010, when its luminosity rapidly increased causing it to exhibit what was classified as a supernova impostor event (SN 2010da, Binder et al. 2011; Lau et al. 2016). Remarkably, while it is typical for accreting XRPs to be observed having spin periods ( $P$ ) near equilibrium (Ho et al. 2014) where they are expected to remain for many years ( $P/\dot{P} \gtrsim 100$  y), the spin period of NGC 300 ULX1 has dramatically changed within only 4 years. In the following sections, I will compare the evolution of the spin period of the NS in this unique system with predictions of standard accretion theories and I will comment on its derived properties that make NGC 300 ULX1 such an exciting case study among ULXPs. The study of the accretion torque through the spin evolution of NGC 300 ULX1 provides an independent way to probe the accretion rate of the system and confirms the super-Eddington accretion rate onto the NS, thus providing strong evidence that the high X-ray luminosity of ULXPs is not an effect of beaming.

### 18.1 Observational data

After its X-ray brightening in 2010, NGC 300 ULX1 has been monitored by most of the modern X-ray observatories, *Swift*, *XMM-Newton*, NuSTAR and Chandra. I was involved in successful proposals (PI: G. Vasilopoulos) that requested additional *Swift* and Chandra ToO observations in order to measure the most recent spin-up rate and X-ray luminosity of the system. A NuSTAR ToO observation was performed closely with our 2018 Chandra observations (Bachetti et al. 2018). For all available X-ray observations standard products were extracted using the latest available software packages and instrument calibration files. For details about *XMM-Newton* and NuSTAR data reduction I refer the reader to Carpano et al. (2018). Chandra data reduction was performed with CIAO v4.9 software (Fruscione et al. 2006), while *Swift*/XRT data were processed with the standard xrtpipeline v0.13.3 software.

The X-ray spectra were fitted using the *xspec* (v12.9.0) spectral fitting package (Arnaud 1996). For the fit I used a phenomenological model that best described the high

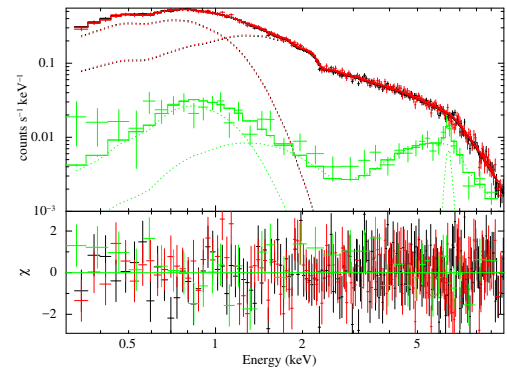


**Figure 18.1:** Simultaneous spectral fit of NGC 300 ULX1 using the *XMM-Newton*/EPIC-pn spectra together with the residuals. Data from two 2016 observations that were performed continuously are shown in black and red colours, while the 2010 data are marked with green colour. Best fit model is composed by a disc BB and a PL with cut-off. The two different epochs can be explained by only letting the partial absorption component vary. Credit: Carpano et al. (2018)

## 18. NGC 300 ULX1: A TEST CASE FOR ACCRETION TORQUE THEORY

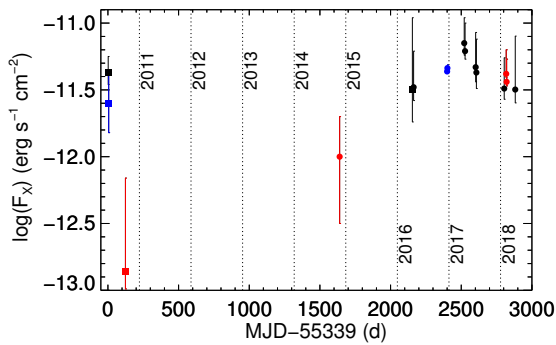


**Figure 18.2:** Absorption corrected X-ray flux (0.3–10.0 keV) of the hard component of NGC 300 ULX1 using the available X-ray data from *Swift* (black points), *XMM-Newton* (blue) and *Chandra* (red). The NS spin period was detected in observations performed after 2014.

quality X-ray spectra obtained during three *XMM-Newton* observation performed on 2010 and 2016 (Carpano et al. 2018). For this model, the continuum consists of a power-law with a high-energy cutoff ( $\sim 6$  keV) and a disc black-body component that account for emission from the accretion disc (i.e. soft excess). Absorption is modelled by a partially coverage component and a normal absorption component. As noted by Carpano et al. (2018), in the early 2010 observations the spectrum of the system was greatly affected by partial absorption, while in the 2016 spectrum optical depth of the partial absorption component greatly decreases (see Fig. 18.1). I found that between 2010 and 2018 the X-ray luminosity of the system has not changed much and the difference in the observed flux is a result of changes in the absorption of the spectrum (see Fig. 18.2).

ULXPs are systems with very high accretion rate, thus the acting torque can result in extreme spin-up rates that significantly alter the spin period of the NS within the duration of typical X-ray exposures. To take into account this effect, I performed an AEF test (Leahy et al. 1983b) to derive the ephemeris of NGC 300 ULX1. The complete list of observations and the derived temporal properties of the system are listed in Table 18.1. Throughout the study I also made use of already published X-ray data for other ULXPs. Their properties are also listed in Table 18.1.

### 18.2 Results

The basic principles for the interaction between the NS and the accretion disc are given in §3.1. I remind that the differential eq. 3.2 connects observable quantities (i.e.  $L_X$ ,  $P$ ,  $\dot{P}$ ) with  $B$ , since the other parameters are well constrained by theory (i.e.  $\xi$ ,  $M_{NS}$ ,  $R_{NS}$ ):

$$-\frac{\dot{P}}{P} = \frac{P}{I_{NS}2\pi} n(\omega_{fast}) L_X \frac{R_{NS}}{GM_{NS}} \sqrt{GM_{NS}R_M} \quad (18.1)$$

For the observed properties (i.e.  $L_X$ ,  $P$ ,  $\dot{P}$ ) of NGC 300 ULX1 one can estimate  $B$  by using eq. 18.1. For both the 2016 and 2018 sets of measurements we calculated an equatorial magnetic field of  $B \sim 6 \times 10^{12}$  G, and typical NS mass and radius values. Using the various torque models we find  $B_{12} = 3 - 11$ . The largest magnetic field strength ( $B_{12} = 11$ ) is derived considering the torque model of Parfrey et al. (2016a), while the polar magnetic field could be larger by a factor of 2. It is also interesting to perform the same calculation for the other three known ULXPs. The results are shown in Fig. 18.3. The plot clearly shows that NGC 300 ULX1 is still away from the equilibrium period, which when reached will be less or around 1 s, depending on  $\dot{M}$  at

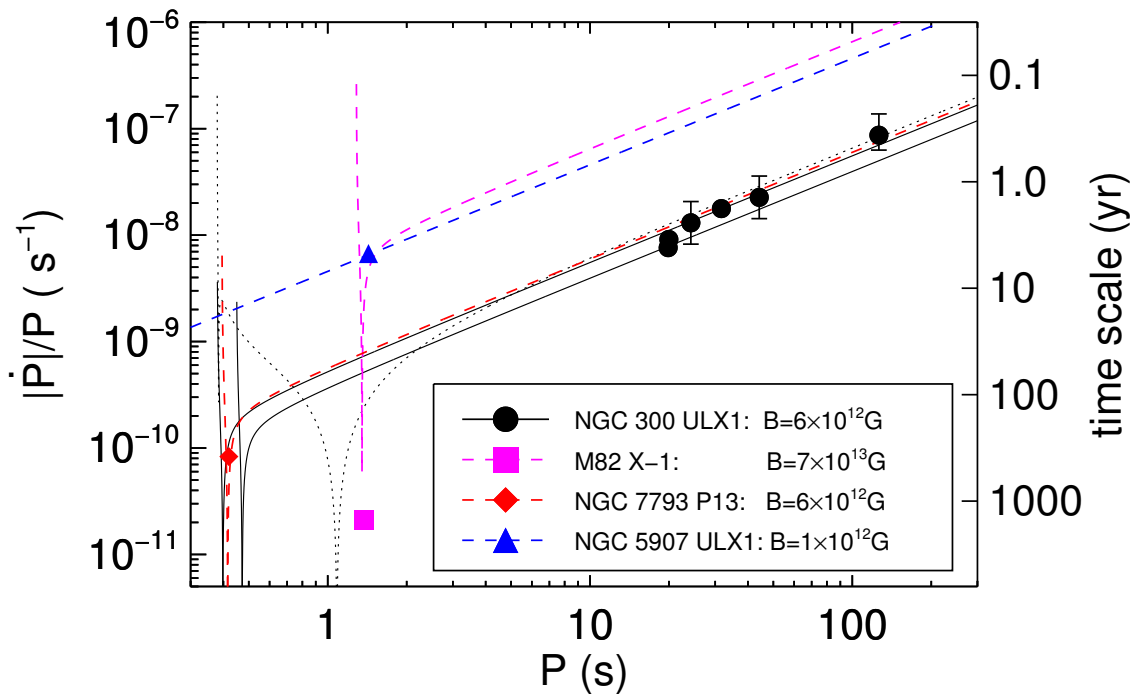


**Figure 18.3:**  $|\dot{P}|/P$  vs.  $P$  for the four ULXPs discussed in the text. Solid black and coloured dashed lines denote the solution using the approximation of Wang (1995) while assuming a constant luminosity and standard efficiency ( $n_{\text{eff}} = 0.2$ ). For NGC 300 ULX1 we plot two solutions based on the  $P$ ,  $\dot{P}$  and  $L_X$  measurements obtained from the 2016 *XMM-Newton* and the 2018 Chandra observations (see Table 18.1). The solution based on the Ghosh and Lamb (1979) model is plotted for comparison (black dotted line) only for NGC 300 ULX1.

that epoch.

Having an estimate on the magnetic field of the NS we can numerically solve eq. 18.1 backwards (and forward) in time from the latest spin-period measurement. The only assumption is the history of the luminosity of the system (i.e.  $\dot{M}$ ). From the observed spectra it is clear that the intrinsic luminosity of the system only varied by a relatively moderate factor (Fig. 18.2) and the large deviation in the observed flux is mainly caused by a change in absorption (see also Carpano et al. 2018). Small fluctuations are expected to occur due to orbital variations and variability of the donor star. The theoretical prediction can then be compared with the observed data. In Fig. 18.4 we compare the observed spin periods with the theoretical period evolution for a range of  $L_X$  values in order to account for variations of  $\dot{M}$ .

Assuming nearly constant accretion, which started with the SN 2010da event, the only way to explain the spin-period evolution is that an accretion disc was formed rotating retrograde with respect to the NS spin. Thus, initially the NS was spinning down and at some point the rotation was stopped and the NS has started to rotate in the opposite direction (Fig. 18.4). The formation of retrograde accretion discs has also been proposed to explain the long-term evolution of spin periods in X-ray binaries (Nelson et al. 1997; Christodoulou et al. 2017a). A particularly interesting system is the Galactic low mass X-ray binary GX 1+4 where a retrograde disc has been proposed

## 18. NGC 300 ULX1: A TEST CASE FOR ACCRETION TORQUE THEORY

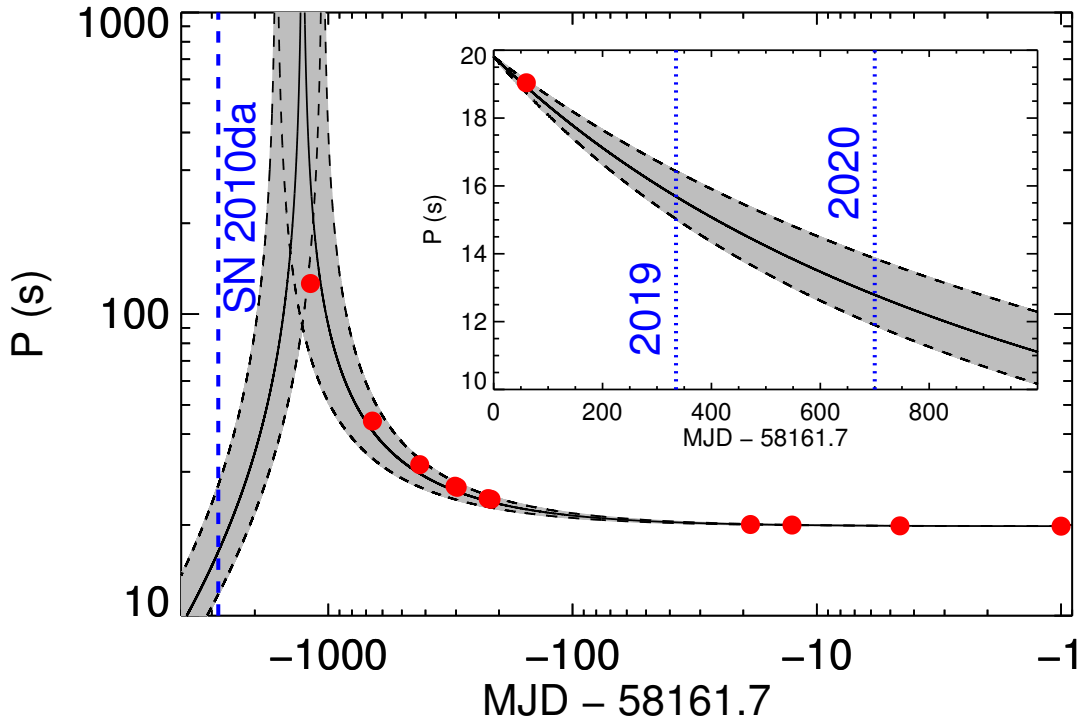


**Figure 18.4:** Evolution of the NS spin period of NGC 300 ULX1 since the SN 2010da event (blue vertical dashed line). The black solid line denotes the theoretical prediction assuming a constant accretion rate and stellar torque from disc-magnetosphere interactions (Wang 1995) with efficiency = 0.2,  $B = 5 \times 10^{12}$  G and  $L_X = 4 \times 10^{39}$  erg s $^{-1}$ . The gray shaded area marks the evolution path for a range of luminosities, i.e.  $3\text{--}5 \times 10^{39}$  erg s $^{-1}$ . The inset plot shows the predicted evolution of the spin period for the next years with the most recent *Swift* measurement shown for better visibility of the period change.

to explain the spin-down of the system (González-Galán et al. 2012). However, we note that the spin-period evolution of the symbiotic system GX 1+4 could also be explained in terms of quasi-spherical accretion (Shakura et al. 2012), where the equilibrium period is a function of mass accretion rate (see eq. 4 of Vasilopoulos et al. 2018). The latter is also consistent with the change of the decrease of the X-ray luminosity of the system during the period when the torque reversal occurred (i.e.  $\sim 1984$  Shakura et al. 2012), and the enhanced activity near periastron passage of the NS (Iłkiewicz et al. 2017).

In general, there are multiple ways to maintain the necessary  $\dot{M}$  to fuel ULXPs. For systems fueled by Roche Lobe overflow accretion carries the angular momentum of the orbit, thus it is implausible for a disc to switch between retrograde and prograde rotation (Chakrabarty et al. 1997). Any change between retrograde and prograde rotation of the NS disc system needs to be due to a change in the direction of the NS rotation. Thus, for NGC 300 ULX1 it is more probable that the accretion mechanism was drastically altered during the SN 2010da event, prior of which the NS could have been fueled via wind accretion. A possible explanation for such a phase transition to occur can be an episode of thermal-timescale mass transfer (King et al. 2001). In that case the donor star has a radiative envelope and fills its Roche lobe as it expands across the Hertzsprung gap after the wind-fed X-ray phase ends.

However, Roche lobe overflow is not the only way to explain such high accretion rates. Supergiant systems and luminous blue variables (LBV) can also exhibit mass loss rates in excess of  $10^{-6} M_{\odot} \text{ yr}^{-1}$  (Smith 2014), thus for a binary system in a moderately close orbit the compact object can capture enough matter to sustain super-Eddington accretion. An LBV is also most probable according to Binder et al. (2016) while other authors have ruled out this classification as inconclusive (Lau et al. 2016; Villar et al. 2016). We note that many of the arguments used in the classification of the optical counterpart were based on the decay of the X-ray luminosity of the system within the first two months of *Swift*/XRT observations. However, this might not be the case as the initial reports did not properly account for the change in X-ray absorption (Carpano et al. 2018).

It is interesting to note the striking confluence between the epoch when the absorption decreased and the expected epoch when the reversal of the NS should have happened. Thus, we can pose the question: is there any connection between retrograde accretion discs and the increased absorption? In principle an outflow with mass loss rate comparable ( $\sim 50\%$ ) to the accreting  $\dot{M}$  starting close to  $R_M$  and a velocity similar to the Keplerian one, can obtain in a column density similar to the observed one ( $10^{24} \text{ cm}^{-2}$ , Carpano et al. 2018). Modelling the interaction of a compact object with a retrograde accretion disc is challenging. In the case of black holes, this mechanism has been proposed to power bright jets (e.g. Middleton et al. 2014), while numerical simulations have shown that retrograde discs can more effectively produce outflows due to the opening of magnetic field lines and reconnection events (Parfrey et al. 2015). Since there is more angular velocity shear between the event horizon and a given magnetic field line's footpoint in the disc in the retrograde case, field lines are more prone to open up and form a jet or stronger mass-loaded outflows. The latter might also be the case for retrograde discs around NSs as it is simply an issue of angular velocity mismatch. An outflow with mass-loss rate being a fraction of the accretion rate (e.g. 30%) is possible to explain the increased absorption in the X-ray spectrum of the system prior to 2015. As strong outflows have been suggested from observations of non-pulsating ULXs (Kosec et al. 2018), it is interesting to further explore the idea of retrograde discs and enhanced outflows in ULX systems. Finally, it is worth considering the possibility of a warped or misaligned disc. Due to the extreme and continuous mass transfer the rotation axis of the NS should be progressively aligned with the binary plane, thus the warping of the accretion disc should be higher within the first years of activity. The effects of a warped disc in the observed  $F_X$  should be similar to that in other known systems (e.g. 35 d ON-OFF cycle Her X-1 Petterson 1975).

## 18.3 Conclusions

I have studied the spin period evolution of NGC 300 ULX1, the most extreme spin-up system powered by an accretion disc. By obtaining multiple precise measurements of  $P$  and  $\dot{P}$  we have tested standard theoretical models of accretion theory. Even though many of the models assume a geometrically thin disc we find that in the current regime of the system ( $\omega_{\text{fast}} < 1$ ) all of them can explain its evolution fairly well. Given the fast spin-up of the NS, future observations performed close to spin equilibrium will be of major importance to test different accretion models. However, given the time scale of the period evolution of the NS at the current accretion rate it might take close to

## 18. NGC 300 ULX1: A TEST CASE FOR ACCRETION TORQUE THEORY

hundred years for the system to reach equilibrium. Finally, we argued that according to theoretical predictions and given the observable properties of the system, the NS has probably exhibited a spin reversal prior to 2014.

Target	Observatory/ ObsID <sup>(a)</sup>	T <sub>obs</sub> <sup>(b)</sup> MJD	T <sub>Zero</sub> <sup>(c)</sup> MJD-T <sub>obs</sub>	P <sub>Zero</sub> <sup>(d)</sup> s	Log(  $\dot{P}$  ) <sup>(e)</sup> s/s	PF <sup>(f)</sup>	log( $F_x$ ) <sup>(g)</sup> erg s <sup>-1</sup> cm <sup>-2</sup>
NGC300 ULX1							
	S-00031726001	55341	–	–	–	–	–11.37 <sup>+0.12</sup> <sub>-0.09</sub>
	X-0656780401	55344.6	–	–	–	–	–11.60 <sup>+0.24</sup> <sub>-0.22</sub>
	C-12238	55463.1	–	–	–	–	–12.86 <sup>+0.7</sup> <sub>-0.13</sub>
	C-16029	56978.6	–	126.28±0.3 <sup>(*)</sup>	–4.94±0.20 <sup>(*)</sup>	0.64±0.154	–12.0 <sup>+0.3</sup> <sub>-0.5</sub>
	S-00049834002	57493	–	–	–	–	–11.50 <sup>+0.54</sup> <sub>-0.24</sub>
	S-00049834005	57502	–	44.18±0.1 <sup>(*)</sup>	–6.0±0.2 <sup>(*)</sup>	0.75±0.2	–11.48 <sup>+0.27</sup> <sub>-0.10</sub>
	N-30202035002	57738	0.65661582	31.718 ±0.001	–6.257±0.005	0.746±0.008	–
	X-0791010101	57739	0.39833581	31.683±0.001	–6.25±0.01	0.607±0.005	–11.362 <sup>+0.015</sup> <sub>-0.013</sub>
	X-0791010301	57741	0.39280867	31.588±0.001	–6.25±0.01	0.613±0.007	–11.337 <sup>+0.024</sup> <sub>-0.017</sub>
	S-00049834008	57860	–	26.87±0.1 <sup>(*)</sup>	–6.34±0.02 <sup>(*)</sup>	0.61±0.12	–11.15 <sup>+0.19</sup> <sub>-0.09</sub>
	S-00049834010	57866	–	26.65±0.1 <sup>(*)</sup>	–6.4±0.4 <sup>(*)</sup>	0.64±0.07	–11.21 <sup>+0.21</sup> <sub>-0.06</sub>
	S-00049834013	57941	–	24.24±0.1 <sup>(*)</sup>	–6.8±0.4 <sup>(*)</sup>	0.7±0.12	–11.33 <sup>+0.26</sup> <sub>-0.11</sub>
	S-00049834014	57946	–	24.22±0.1 <sup>(*)</sup>	–6.5±0.4 <sup>(*)</sup>	0.79±0.2	–11.37 <sup>+0.25</sup> <sub>-0.12</sub>
	S-00049834015	58143	–	20.06±0.1 <sup>(*)</sup>	–6.5±0.4 <sup>(*)</sup>	0.79±0.2	–11.49 <sup>+0.23</sup> <sub>-0.08</sub>
	N-90401005002	58149	0.05840888	19.976±0.002	–6.74±0.02	0.66±0.02	–
	C-20965	58157	0.12920876	19.857±0.002	< –6.7	0.69±0.03	–11.38 <sup>+0.18</sup> <sub>-0.03</sub>
	C-20966	58160	0.69721163	19.808±0.002	< –6.7	0.66±0.03	–11.44 <sup>+0.17</sup> <sub>-0.03</sub>
	C-20965/20966	58157	0.12920876	19.857±0.002	–6.82±0.02	0.68±0.02	–
	S-00049834019	58221	–	19.046±0.01 <sup>(*)</sup>	–6.6±0.6 <sup>(*)</sup>	0.75±0.1	–11.5 <sup>+0.4</sup> <sub>-0.1</sub>
Other ULXP systems <sup>(h)</sup>							log( $L_X$ ) [erg/s]
M82 X-2	NuSTAR <sup>(h)</sup>	56696	–	1.3725443	–10.537065	–	40.6
NGC 5907 ULX1	X-0145190201	52690	0.94776199	1.427579(5)	–8.02(5)	–	41.0
NGC 5907 ULX1	X-0729561301	56847	0.94776199	1.13742(2?)	–8.35(2)	–	–
NGC 7793 P13	X-0693760401	56621	–	0.4197119(2)	–	–	39.7
NGC 7793 P13	X-0748390901	57001	–	0.4183891(1)	–10.4 (“secular”)	–	–
NGC 7793 P13	X-0781800101	57528	–	0.4169512(1)	–10.5 (“secular”)	–	–

<sup>(a)</sup> Observation ID for *XMM-Newton* (X), *Chandra* (C) and *Swift* (S). <sup>(b)</sup> T<sub>obs</sub> : Start day of observation. <sup>(c)</sup> T<sub>Zero</sub> : reference time for calculated P<sub>Zero</sub> and  $\dot{P}$  using millisecond accuracy. <sup>(d)</sup> Pulse period derived using the accelerated epoch folding algorithm. <sup>(e)</sup> Spin-up of the pulsar. Data sets with low statistics or large dead time intervals are marked with star (\*), for those a unique solution could not be established thus the given uncertainty denotes the characteristic spread between multiple solutions. For some ULXP systems we only derived a long term (“secular”) spin up rate based on two observations. <sup>(f)</sup> Pulsed fraction ( $PF = (F_{max} - F_{min}) / (F_{max} + F_{min})$ ) derived from the folded pulse profile using 10 phase bins, we treated uncertainties in phase bins with low numbers of counts by following [Gehrels \(1986\)](#). <sup>(g)</sup> Absorption corrected X-ray Flux (0.3–10.0 keV) of the hard component as derived from the distributions of the marginalised parameters using the Bayesian framework described in the text. Given value denotes the median of the distribution, while error values the 5% and 95% percentiles. <sup>(h)</sup> M82 X-2 ([Bachetti et al. 2014](#)), NGC 5907 ULX1 ([Israel et al. 2017a](#)), NGC 7793 P13 ([Israel et al. 2017b](#)).

**Table 18.1:** Properties of the ULXP systems discussed in the current study.

**Part VI**  
**Summary**



## Conclusions and outlook

### 19.1 Summary and conclusions

The initial target of my PhD was the study of the [HMXB](#) population of the [LMC](#) by utilising the data collected by the *XMM-Newton* very large survey of this nearby galaxy. I was quickly fascinated by the transient nature of the systems in study and I became involved in a relentless hunt of new outbursting systems. However, my research goals evolved as new scientific breakthroughs were made in the area of observational high-energy astrophysics; the discovery of pulsating ultra luminous X-ray sources and their physical similarities with [HMXBs](#) motivated my involvement in their study. In the following paragraphs I summarise the topics that have been extensively covered in this dissertation.

#### HMXB population of the LMC

For the study of the [HMXB](#) population of the [LMC](#), I used all existing *XMM-Newton* observations towards the galaxy. I performed point source detection on the available data and constructed an X-ray point source catalogue of almost 10000 detections. I identified new candidate [HMXB](#) systems based on their X-ray spectral properties and their spatial correlation with massive stars. I combined the available archival catalogues with the new candidate systems to compile an updated catalogue of [HMXBs](#) in the [LMC](#). I was involved in the optical follow-up of 25 poorly studied [HMXB](#) candidate systems. I obtained and analysed their optical light-curves ([OGLE](#) data) and identified the better candidates based on the existence of long-term variability or periodic signal that confirms the binary nature of the optical system. Moreover, our team obtained spectroscopic observations of the same systems in order to perform spectral classification of the donor stars and look for evidence of the Be nature of the massive star (i.e. emission lines). This provided crucial information for the proper clarification of the systems and the construction of an up-to-date census of the [HMXB](#) population of the [LMC](#). In total there are 60 confirmed or good candidate [HMXBs](#). For 19 of these systems there is now proof that they host a [NS](#) as a compact object. Out of the 4 [NS-SgXRBs](#) half have measured pulsations, while I have discovered the first confirmed extragalactic [SFXT](#) system.

In contrast to the [LMC](#), the [SMC](#) contains only one [SgXRB](#) system. The [HMXB](#) population of the [LMC](#) is more abundant of younger systems despite all the observational biases that would favour the opposite (i.e. deeper and longer X-ray observations). To further investigate this aspect I performed a correlation analysis between the local [SFH](#) and of the locations of the confirmed [LMC HMXBs](#). The recent star formation rate (i.e. ages younger than 10 Myr) in regions containing [HMXB](#) pulsars is about 4 times higher than the [LMC](#) average. If only [SgXRBs](#) are considered this difference is even higher, as the recent star formation rate can be up to 12 times higher. I note that there is about 1% probability that these results are due to chance coincidence.

### Hunting BeXRB outbursts in the MCs

Having obtained an updated census of [HMXBs](#) in the [LMC](#), I requested a series of follow up observations with *Swift*/XRT. These observations were performed either (i) around the periods of expected outbursts for systems with known orbital parameters (i.e. NS periastron passage), or (ii) at random times as *Swift* fill-in targets. Moreover, I complimented the monitoring observations by daily analysing all *Swift*/XRT observations that were performed in the direction of the [MCs](#). This task was performed by automated scripts and resulted in the detection of X-ray outbursts from several X-ray systems. In total our team obtained high-quality observations from about 8 [BeXRB](#) outbursts. For most of these systems we complemented our study with multi-wavelength data during the outbursts. Some of the highlights of each discovered system are the following.

**LXP 28.77:** The system was observed during a low-luminosity outburst ( $\sim 5 \times 10^{35}$  erg s<sup>-1</sup>). I discovered X-ray pulsations and by performing phase-resolved spectroscopy I showed that the X-ray spectrum of the pulsar can be best described by a combination of a power-law and a black-body component with temperature of  $\sim 1.5$  keV and size  $\sim 800$  m. As it is seen in other persistent low-luminosity pulsars the thermal component originates from the [NS](#) hot spot.

**LXP 38.55:** This [BeXRB](#) pulsar exhibits regular optical and X-ray outbursts at periastron. I obtained X-ray observations distributed over a full  $\sim 30$  d binary orbit where the peak  $L_X$  was  $\sim 4 \times 10^{36}$  erg s<sup>-1</sup>. Analysis of the X-ray spectra revealed the presence of a soft excess that can be attributed to a hot thermal component at the [NS](#) surface. Analysis of the long-term optical data reveals that the colour of the system becomes redder when brighter during the X-ray outbursts. This modulation can be attributed to excess radiation from the Be disc - which is colder than the star - during the outbursts.

**SXP 15.6:** To follow up the X-ray outburst of the system that was serendipitously detected from our automatic alert pipeline, I obtained a Chandra [ToO](#) observation. Phase-resolved spectroscopy and pulse-profile modelling provided constraints on the angle between the magnetic and rotation axis as well as the compactness of the system. Our novel approach has demonstrated that we can use accreting [NS](#) pulsars to measure  $r_g/R$  and thus provide constraints for the equation of state of the more massive [NSs](#) and compare them with that of the isolated pulsars.

**SXP 2.16:** The pulsar was monitored during an outburst that reached a luminosity level of  $\sim 10^{38}$  erg s<sup>-1</sup>. By following the decline of the outburst I identified the propeller transition of the pulsar, thus obtaining an estimate of its magnetic field strength. The most intriguing feature of this pulsar is its pulse profile that appears to have 4 peaks in the 0.3-10.0 keV band. By performing detailed spectral analysis I showed that the complex pulse profile can be explained by a componentised component. Within the pulse both the normalisation and the hardness of the component change following a sinusoidal modulation. The spectrum becomes harder when brighter, thus when the flux is low (high) the pulse profile peaks at low (high) energies. This unique configuration provides insight into the

anisotropic emission of the accretion column as we can connect the spectral and temporal properties of the system with the optical depth of the accretion column.

**LXP 8.04:** This is the first system that I observed at super-Eddington luminosity level. Perhaps the most fascinating result is that by implementing a pulsar modelling scheme developed by collaborators, I have reconstructed the 3D emission pattern of the pulsar. This finding suggests that in both the observer’s and system’s rest frame the total emitting luminosity is above the Eddington limit. Moreover, I have shown that this system and probably most [BeXRB](#) pulsars do not show highly beamed emission patterns. Specifically, for LXP 8.04 by considering all possible directions the ratio of maximum to minimum X-ray flux only varies by a factor of 2.

**SMC X-2:** The system was observed multiple times with *XMM-Newton* during a major outburst. The superb effective area and spectral resolution of the *XMM-Newton*/EPIC cameras allowed us to perform phase-resolved spectroscopy during different luminosity levels. My analysis demonstrated the presence of a non-pulsating soft excess (i.e at energies  $< 2$  keV) that originates from the inflated inner disc radius. The soft excess consists of two separate components, emission from optically thick plasma (i.e. black-body like) and emission lines from optically thin plasma. The optically thick emission becomes dominant with increased luminosity.

**SMC X-3:** Multiple X-ray observatories followed the evolution of the major 2016 outburst of the system. By using *XMM-Newton* data I studied the nature of the soft-excess. I confirmed the presence of a non-pulsating soft component that can be attributed to an irradiated disc. In addition, I have demonstrated that the evolution of the pulsed fraction with luminosity can be explained by a toy-model where the ratio of the fan-to-pencil beam intensity changes with luminosity.

Considering all the spectral properties of the systems that were observed at different luminosity levels, the soft excess is maybe the most prominent feature. In *low-luminosity* systems, observed below the critical limit for the formation of the accretion column, the soft excess cannot originate from an accretion disc, as the disc is truncated at very large distances, but it can be attributed to thermal emission from the [NS](#) surface, and specifically the polar cap (e.g. LXP 28.77). In *intermediate-luminosity* systems (where the accretion column has been formed) the pulsating hard emission from the accretion column can dominate the X-ray emission and the soft excess can be lost as it is swamped by the accretion column emission (e.g. SXP 15.6, SXP 2.16). In *luminous systems* (close to the Eddington limit), the soft excess can originate from the inner part of the accretion disc (e.g. SMC X-2, SMC X-3, LXP 8.04), but its properties do not describe a typical thin disc. Specifically, the disc temperature, size and luminosity evolution with the global pulsar luminosity does not follow the typical disc truncated at  $R_M$ . This is clearly seen in SMC X-2 where we have multiple high resolution observations available from *XMM-Newton*. The disc temperature in SMC X-2 through the brightest stages of the outburst seems to remain constant, while its size significantly changes. All this can be explained by a model where the disc luminosity is a result of reprocessing of hard X-rays that originate from the accretion column of

## 19. CONCLUSIONS AND OUTLOOK

---

the **NS**. In this explanation the inner disc can gradually be inflated and thus occupy a larger solid angle with respect to the **NS**.

Finally, bright **BeXRBs** show evidence for the presence of emission and absorption lines in their X-ray spectra (see SMC X-3). The emission lines occupy energies close to their rest frame, but some of the strongest absorption features could be associated with blue-shifted lines, thus must be produced in some outflow. This interpretation is in agreement with simulations of **NS** magnetospheres where large outflows are seen to originate from regions where reconnection occurs from the opening of magnetic field lines.

### Super Eddington accretion onto magnetised NS

The study of **BeXRBs** at different luminosity levels provides a detailed picture of the environment around an accreting **NS**. At lower luminosity levels the accretion disc does not contribute at all to the observed X-ray spectrum of the pulsar. However, as mass accretion increases, the disc is responsible for a non-pulsating soft excess in the spectrum of the system. At super-Eddington rates the disc becomes inflated and can engulf a large portion of the sphere around the **NS**, thus it can reprocess a significant fraction of the pulsed radiation. This picture provides significant information for understanding the elusive **ULXPs**. I have demonstrated that above a luminosity of  $10^{39}$  erg s<sup>-1</sup> the free-falling material around the accretion column becomes optically thick ( $\tau > 10 - 100$ ). The optical depth around the base of the accretion column can be higher than 100 and gradually decrease as we follow the last closed magnetic field lines towards the inner accretion disc. Thus, in the super-Eddington regime the spectrum of an accreting highly magnetised **NS** can be approximated by two thermal components, one hot component that describes the envelope around the accretion column and a soft that originates from the inner accretion disc. I have successfully applied this model to the spectra of all known **ULX** systems (for which high quality observations are available) and have demonstrated that a significant fraction of them can contain an **NS** and not a **BH** as a central engine.

The newly discovered ultra-luminous X-ray pulsar NGC 300 ULX1 provided an ideal laboratory to test accretion theories. I have shown that its spectrum can be fitted by a two component model, a non-pulsating soft component and a pulsating hard component. Although the nature of the hard component is debatable it can be both fitted by a power-law like component with cutoff around 6 keV or a thermal component with peak flux at the same energy. By performing detailed spectral analysis I have shown that the intrinsic luminosity of the system remained almost constant between 2010 and 2018. Moreover, by performing detailed temporal analysis I was able to measure the observed spin period evolution of the system between 2014 and 2018. My analysis has reproduced the spin period evolution of the **NS**. The importance of my result is that I have demonstrated beyond any doubt that the spin evolution of the system requires accretion rates that highly exceed the Eddington limit, thus the observed luminosity is by no means an effect of beaming. Finally, I have shown that according to theoretical predictions and given the observable properties of the system, the **NS** has probably exhibited a spin reversal prior to 2014.

## 19.2 Outlook

The current work provides a state-of-the-art study of accretion onto magnetised **NSs** at different accretion regimes. However, our understanding of these systems is far from complete. There are still several outstanding questions, such as: What is the structure of the accretion column in accreting magnetised **NSs**? Are the cyclotron absorption lines produced within the accretion column, or from reflection onto the **NS** surface? How does the accretion column geometry change with accretion rate? What are the properties of hot plasma in the vicinity of the **NS**? Are there relativistic outflows from accreting **NSs** in **HMXBs**, and how do they compare with those reported in **ULXs**? Within the next years we will be given the opportunity to further enrich our knowledge of those systems, in terms of detailed study of radiative transfer in extreme environments and binary population studies.

Current X-ray observatories can provide high quality observations to further study multiple aspects of accreting **NS**. Combined *XMM-Newton* and NuSTAR observations can be used to follow up outbursts of bright systems and study the phase resolved spectra of **XRPs** with more physically motivated models. Furthermore, a detailed study of the temporal properties of the same systems can be based on NICER observations. It has already been demonstrated that constraints for the equation of state of **NSs** can be obtained even for **XRBs** systems that are observed at low X-ray luminosities (e.g. SXP 15.6). NICER can also be used to follow-up major outbursts of **BeXRBs** (and **XRBs** in general). These observations can be used to study the pulse profiles of the accreting pulsars at different luminosity levels and help eliminate any degeneracy between model parameters that should be constant (i.e. geometrical configuration of magnetic, rotation axis and observer orientation). Interestingly, study of the evolution of spectral properties (i.e. spectral hardness, absorption cyclotron lines) of **BeXRBs** during outbursts have revealed interesting features like, hysteresis between the cyclotron line energy and/or spectral hardening with the outburst luminosity. These features have been attributed to different accretion column geometries during the rise and the decay phase of the outburst, that could be related to changes in the accretion disc size or intrinsic magnetic field decay of the **NS** due to matter accumulated to the **NS** surface. The high sensitivity of NICER can enable a detailed study of the evolution of the pulse profile and look for similar behaviour in the temporal properties of the systems and provide further insights.

Furthermore, the study of outbursts can be accommodated by several all-sky surveys like *Swift*/BAT, FERMI/GBM, or MAXI all sky monitoring program. These instruments have enough sensitivity to provide triggers for Galactic systems. Moreover, dedicated X-ray monitoring campaigns of nearby star-forming galaxies (i.e. **MCs**) can be used to obtain a more complete census of the **HMXB** population and better constrain their formation efficiency. In the same respect, the eROSITA survey will cover the **MCs** several times per year, allowing the detection of systems in outburst with  $L_X \gtrsim 10^{35} \text{ erg s}^{-1}$ . A pilot *Swift*/XRT campaign dedicated to such scientific goals was the quasi-biweekly campaign of the **SMC**, that scanned the nearby galaxy for a period of half year and provided triggers for outbursts of systems studied in this thesis.

Future missions, like the X-ray Astronomy Recovery Mission (XARM, launched in 2021), will provide sensitive detectors (X-ray calorimeter) that would allow us to study the properties of the hot plasma around the magnetosphere through emission lines, and

## 19. CONCLUSIONS AND OUTLOOK

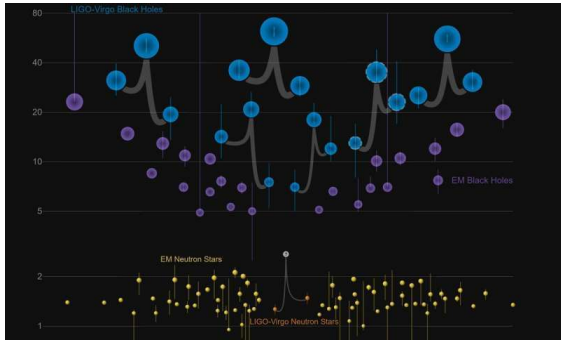


**Figure 19.1:** BH and NS masses compared. The masses of stellar remnants are measured in many different ways. This graphic shows the masses for black holes detected through electromagnetic observations (purple); the BHs measured by gravitational-wave observations (blue); NSs measured with electromagnetic observations (yellow); and the masses of the NSs that merged in an event called GW170817, which were detected in gravitational waves (orange). GW170608 is the lowest mass of the LIGO/Virgo black holes shown in blue. The vertical lines represent the error bars on the measured masses. Credit: LIGO-Virgo/Frank Elavsky/Northwestern

relativistic outflows powered by reconnection events and strong radiative driven winds. These are features that we have now just started exploring with grating detectors, but still require unrealistic large exposures to identify for most BeXRB and ULX systems.

Regarding the X-ray binary population of nearby galaxies, we should still plan observational campaigns to identify additional systems, and possible new pulsars. It is not simply enough to quote the number of identified pulsars in the MCs (i.e.  $\sim 80$ ) and argue that discovery of a new system would not be as important. It is as important to establish stringent constraints for non-pulsating systems, this would be the only way to identify XRBs hosting BHs, or NS systems with aligned magnetic and rotation axis, systems that are important for binary evolution models. We can argue that we are at crossroad where we are no longer looking for confirmation to the rule, but for possible exceptions. Moreover, it is important to understand that in a few years, X-rays might not be the optimal tool to identify massive binary systems, as gravitational wave detectors are expected to detect hundreds of BH and NS binary systems. Given that HMXBs are the progenitors of these systems, we will possibly be able to perform comparison between the different populations. Will there be a confluence of the population properties and their distributions? Given that all the BH mergers detected by gravitational waves so far only probe massive stellar BHs, it is important to understand if this is just a case due to observational biases and sensitivity limits, or there is a deeper cause. Within a few years we will know if there is a statistical difference between the masses of stellar remnants (see Fig. 19.1) detected by gravitational waves or their electromagnetic signatures. If the two populations are different, this would mean that the typical HMXBs are not progenitors of the massive binaries detected with gravitational waves, which in turn would be of great importance for stellar formation and evolution studies, that could involve further binary evolution in dense stellar environments. In this sense, our interest in HMXBs should increase, as we should now be looking for close binary systems hosting massive BHs, and what better candidates are out there than the elusive ULXs.

## Future projects

Motivated by the open questions in the field of [XRBs](#), I describe below some of the future projects I plan to pursue.

***A comprehensive study of the optical light-curves of the optical counterparts of the confirmed and candidate [HMXBs](#) in the [MCs](#).*** The majority of the [HMXB](#) population of the [MCs](#) has a Be counterpart. The transient nature of [BeXRBs](#) hinders their discovery and challenges their study. The [SMC](#) pulsars are currently the best studied population of [HMXBs](#) ([Haberl and Sturm 2016](#)) of a galaxy, while the study of the [LMC](#) counterparts is gaining momentum in the past years. Most of the [MCs](#) X-ray pulsars have been discovered during major outbursts, thus systems with lower luminosity and variability are far less studied ([Haberl and Sturm 2016](#)). One major observational bias of [HMXB](#) systems is the lack of a homogeneous study in the optical band. Specifically, a study of the variability of the optical companion of the [NS](#) has only been performed for confirmed pulsars and for limited samples of systems. The optical variability of a [HMXB](#) can provide insights into multiple properties of the system. Periodic variability attributed to orbital motion (5-1000 days) or non-radial pulsations ( $\sim 1$  d) of the massive star can be easily detected in the optical data. Non periodic variability can be connected to changes in the Be stars decretion disc. Study of the evolution of the colour versus magnitude can reveal systems where the decretion disc faced is observed under an edge-on orientation (bluer when brighter [Rajaelimanana et al. 2011](#)).

From such a study I will answer questions like: Are there any population differences between [HMXB](#) pulsars, and non-pulsating systems? Do the later systems exhibit larger average orbital separations or lower eccentricities? What is the fraction of them with little or none orbital modulation?

This can be achieved by a multi-step process that will improve the understanding of [HMXB](#) systems and decrease observational biases due to limiting X-ray coverage. I will (i) search for evidence of orbital variability in the existing optical data (OGLE project) of all non-pulsating [HMXBs](#) in the [MCs](#), (ii) perform X-ray monitoring observations using *Swift* phased around the epoch of enhanced optical emission (i.e. periastron passage), (iii) perform X-ray monitoring of regions of the [LMC](#) with enhanced recent [SFH](#), and (iv) trigger *XMM-Newton* target of opportunity observations during X-ray outburst that will allow to discover new pulsating systems and establish a [BeXRB](#) sample where only stringent upper limits for pulsations can be derived (i.e. [BH](#) candidates).

An intriguing aspect of such a study is the identification of a [BH-BeXRB](#) population in the [SMC](#) and its implication for binary evolution scenarios. There is evidence that the mass distribution of [NSs](#) has a cut-off around  $2.1 M_{\odot}$  ([Özel and Freire 2016](#); [Alsing et al. 2017](#)). Although there are numerous [NS](#) with masses close to that limit, there are very few [low-mass black holes \(LMBH\)](#) with confirmed masses below  $5 M_{\odot}$ . Being the evolutionary product of accreting [NS](#), the [LMBH](#) population should have comparable numbers as the high-mass [NS](#) population. The typical [BH-BeXRB](#) population should share common features with the [NS-BeXRBs](#). They should exhibit outbursts during the periastron passage, but also their X-ray luminosity should be smaller than a typical [NS BeXRB](#). The non-pulsating [BeXRBs](#) in the [SMC](#) seem to share this basic property (i.e. lower X-ray variability and average luminosity; [Haberl and Sturm 2016](#)) Their population offers an ideal sample to search for the missing [LMBHs](#) and a more

## 19. CONCLUSIONS AND OUTLOOK

---

systematic study of their population could yield exciting new results.

*A comprehensive study of the X-ray spectral and temporal properties of ULX systems.* The presence of pulsations and the spectral properties of ULXs is consistent with accretion into a NS. ULXs have now more in common with HMXBs than any other category of systems. However, there has been no systematic study of their temporal properties in the context of magnetospheric accretion. For this purpose, I will investigate ULX systems during different luminosity levels. From the study of their X-ray spectra one can test if their properties are consistent with the presence of an envelope around an NS. I will test if the size, temperature, and luminosity of this feature are consistent with the proposed model and in which fraction of ULXs. I will study the temporal properties of their X-ray emission in the context of accretion from a disc, truncated at the magnetospheric radius. So far, the temporal properties (i.e. QPOs) of ULXs have been only investigated in the context of intermediate mass black holes. I will search for the presence of QPO-like features in their power density spectra, and investigate if these features are consistent with the properties derived from the spectra. Such study will offer concrete evidence in favour of (or against) the scenario where most of the ULXs are powered by accreting NS.

## Acknowledgments

Finally, I would like to express my gratitude to everyone who contributed to the success of my PhD studies.

After many years of working on it I could not possibly come up with a full list of all the people who had helped, but I take comfort that you all know who you are and that this work could not have been possible without you. However, I would like to personally thank those who contributed the most.

First, I would like to express my sincere gratitude to my supervisor Frank Haberl for giving me the opportunity of working at MPE and starting my scientific career, but also for his patient guidance and encouragement. I would also like to thank all my co-authors, that made all our publications possible. Furthermore, I would like to thank the members of the MPE's High Energy Group, but especially Konrad Dennerl for all his help on the projects we worked together and I would advise him to watch out for Greek drivers on his bicycle tours in Rodos or in other places, and Vadim Burwitz for giving me the opportunity to enjoy the night in the telescope and for sharing many interesting stories. I would like to also thank Jochen Greiner, for helping with the preparation of the thesis and for providing advice through my PhD.

Here, I also have to thank Harald Baumgartner for his flawless IT support and for constantly expanding my storage space, and Birgit Boller for administrative support.

Moreover, I would like to thank my former professors from the University of Athens, and especially Despina Hatzidimitriou and Apostolo Mastichiadi, for all their "remote" guidance and advice.

I would like to extend my gratitude to Dimitri Giannio for hosting me as a visitor at Purdue University, and for all his help while being there.

I would also like to thank my friends Filippo, Myriam, Tyrone, Cheryl, Pierre, Florian, Sotiri, Apostolo (and other) for making this a fun trip. I will avoid sharing information on official documents... but you all know what you did.

A special thank goes to my family, for being supportive and enabling me to follow my dreams. I also wish to my younger brother Alexandro to do the same and follow the path that he is passionate about.

Last, but not least, I would like to thank my wife Maria for her support and encouragement. You were there in all the good and bad steps of this journey and I could not have finished it without you.

## 19. CONCLUSIONS AND OUTLOOK

---

## References

- A. Akmal, V. R. Pandharipande, and D. G. Ravenhall. Equation of state of nucleon matter and neutron star structure. *Physical Review C*, 58:1804–1828, September 1998. doi: 10.1103/PhysRevC.58.1804. [154](#)
- C. Alcock, R. A. Allsman, D. R. Alves, et al. Calibration of the MACHO Photometry Database. *PASP*, 111:1539–1558, December 1999. doi: 10.1086/316469. [78](#)
- J. Alsing, H. O. Silva, and E. Berti. Evidence for a maximum mass cut-off in the neutron star mass distribution and constraints on the equation of state. *ArXiv e-prints: 1709.07889*, September 2017. [199](#)
- R. Andrae, T. Schulze-Hartung, and P. Melchior. Dos and don'ts of reduced chi-squared. *ArXiv e-prints*, December 2010. [29](#), [53](#), [131](#), [133](#)
- V. Antoniou and A. Zezas. Star-formation history and X-ray binary populations: the case of the Large Magellanic Cloud. *Monthly Notices of the Royal Astronomical Society; submitted*, 2015. [111](#), [121](#)
- V. Antoniou and A. Zezas. Star formation history and X-ray binary populations: the case of the Large Magellanic Cloud. *Monthly Notices of the Royal Astronomical Society*, 459:528–553, June 2016. doi: 10.1093/mnras/stw167. [21](#), [38](#), [39](#), [40](#), [41](#), [42](#), [45](#), [47](#), [50](#)
- V. Antoniou, A. Zezas, D. Hatzidimitriou, and V. Kalogera. Star Formation History and X-ray Binary Populations: The Case of the Small Magellanic Cloud. *Astrophysical Journal Letters*, 716:L140–L145, June 2010. doi: 10.1088/2041-8205/716/2/L140. [5](#), [21](#), [45](#), [47](#)
- V. Antoniou, A. Zezas, and V. Kalogera. Young X-ray Binary Populations in Low Metallicity Star-Forming Galaxies. In *American Astronomical Society Meeting Abstracts 218*, page 228.29, May 2011. [79](#)
- K. A. Arnaud. XSPEC: The First Ten Years. In G. H. Jacoby and J. Barnes, editors, *Astronomical Data Analysis Software and Systems V*, volume 101 of *Astronomical Society of the Pacific Conference Series*, page 17, 1996. [53](#), [70](#), [85](#), [98](#), [114](#), [129](#), [147](#), [160](#), [185](#)
- E. Asseo and D. Khechinashvili. The role of multipolar magnetic fields in pulsar magnetospheres. *Monthly Notices of the Royal Astronomical Society*, 334:743–759, August 2002. doi: 10.1046/j.1365-8711.2002.05481.x. [139](#)
- W. A. Baan and A. Treves. On the Pulsation of X-Ray Sources. *Astronomy & Astrophysics*, 22:421, February 1973. [14](#), [16](#)
- M. Bachetti. Ultraluminous X-ray sources: Three exciting years. *Astronomische Nachrichten*, 337:349, May 2016. doi: 10.1002/asna.201612312. [8](#)
- M. Bachetti, F. A. Harrison, D. J. Walton, et al. An ultraluminous X-ray source powered by an accreting neutron star. *Nature*, 514:202–204, October 2014. doi: 10.1038/nature13791. [8](#), [97](#), [190](#)
- M. Bachetti, B. W. Grefenstette, D. J. Walton, et al. NuSTAR timing of NGC 300 ULX-1 / Supernova Impostor SN2010da. *The Astronomer's Telegram*, 11282, February 2018. [185](#)
- E. S. Bartlett, M. J. Coe, and W. C. G. Ho. XMM-Newton observation of the highly magnetized accreting pulsar Swift J045106.8-694803: evidence of a hot thermal excess. *Monthly Notices of the Royal Astronomical Society*, 436:2054–2062, December 2013a. doi: 10.1093/mnras/stt1711. [55](#), [91](#), [125](#), [152](#), [154](#)
- E. S. Bartlett, M. J. Coe, and W. C. G. Ho. XMM-Newton observation of the highly magnetised accreting pulsar Swift

## REFERENCES

---

- J045106.8-694803: Evidence of a hot thermal excess. *Monthly Notices of the Royal Astronomical Society submitted*, 2013b. [80](#)
- M. M. Basko. Iron line emission from the Alfvén shell in X-ray binaries. *Astronomy & Astrophysics*, 87:330–338, July 1980. [107](#)
- M. M. Basko and R. A. Sunyaev. Radiative transfer in a strong magnetic field and accreting X-ray pulsars. *Astronomy & Astrophysics*, 42:311–321, September 1975. [6](#), [16](#), [17](#), [18](#), [107](#), [169](#)
- M. M. Basko and R. A. Sunyaev. The limiting luminosity of accreting neutron stars with magnetic fields. *Monthly Notices of the Royal Astronomical Society*, 175:395–417, May 1976. [17](#), [107](#), [108](#), [140](#), [149](#), [168](#), [169](#), [171](#)
- P. A. Becker and M. T. Wolff. Thermal and Bulk Comptonization in Accretion-powered X-Ray Pulsars. *Astrophysical Journal*, 654:435–457, January 2007a. doi: 10.1086/509108. [16](#), [131](#), [141](#), [179](#), [180](#)
- P. A. Becker and M. T. Wolff. Thermal and Bulk Comptonization in Accretion-powered X-Ray Pulsars. *Astrophysical Journal*, 654:435–457, January 2007b. doi: 10.1086/509108. [6](#), [14](#)
- A. M. Beloborodov. Gravitational Bending of Light Near Compact Objects. *Astrophysical Journal Letters*, 566:L85–L88, February 2002. doi: 10.1086/339511. [17](#), [18](#), [19](#), [149](#), [150](#), [153](#), [155](#)
- K. Beuermann, V. Burwitz, and K. Reinsch. A new soft X-ray spectral model for polars with an application to AM Herculis. *Astronomy & Astrophysics*, 543:A41, July 2012. doi: 10.1051/0004-6361/201219217. [18](#)
- P. R. Bevington. *Data reduction and error analysis for the physical sciences*. 1969. [132](#)
- B. Binder, B. F. Williams, A. K. H. Kong, et al. Chandra Detection of SN 2010da Four Months After Outburst: Evidence for a High-mass X-Ray Binary in NGC 300. *Astrophysical Journal Letters*, 739:L51, October 2011. doi: 10.1088/2041-8205/739/2/L51. [185](#)
- B. Binder, B. F. Williams, A. K. H. Kong, et al. Recurring X-ray outbursts in the supernova impostor SN 2010da in NGC 300. *Monthly Notices of the Royal Astronomical Society*, 457:1636–1643, April 2016. doi: 10.1093/mnras/stw119. [189](#)
- A. J. Bird, M. J. Coe, V. A. McBride, and A. Udalski. On the periodicities present in the optical light curves of Small Magellanic Cloud Be/X-ray binaries. *Monthly Notices of the Royal Astronomical Society*, 423:3663–3678, July 2012. doi: 10.1111/j.1365-2966.2012.21163.x. [7](#), [137](#)
- A. J. Bird, A. Bazzano, A. Malizia, et al. The IBIS Soft Gamma-Ray Sky after 1000 Integral Orbits. *Astrophysical Journal Suppl. Ser.*, 223:15, March 2016. doi: 10.3847/0067-0049/223/1/15. [7](#)
- J. K. Blackburn. FTOOLS: A FITS Data Processing and Analysis Software Package. In R. A. Shaw, H. E. Payne, and J. J. E. Hayes, editors, *Astronomical Data Analysis Software and Systems IV*, volume 77 of *Astronomical Society of the Pacific Conference Series*, page 367, 1995. [144](#)
- P. Blay, I. Negueruela, and V. Reglero. Supergiant Fast X-ray Transients: an INTEGRAL view. *MmSAI*, 83:251, 2012. [61](#)
- S. Bogdanov, G. B. Rybicki, and J. E. Grindlay. Constraints on Neutron Star Properties from X-Ray Observations of Millisecond Pulsars. *Astrophysical Journal*, 670:668–676, November 2007. doi: 10.1086/520793. [155](#)
- A. Z. Bonanos, D. L. Massa, M. Sewilo, et al. Spitzer SAGE Infrared Photometry of Massive Stars in the Large Magel-

- lanic Cloud. *Astronomical Journal*, 138: 1003–1021, October 2009. doi: 10.1088/0004-6256/138/4/1003. [27](#), [76](#)
- A. Z. Bonanos, D. J. Lennon, F. Köhlinger, et al. Spitzer SAGE-SMC Infrared Photometry of Massive Stars in the Small Magellanic Cloud. *Astronomical Journal*, 140:416–429, August 2010. doi: 10.1088/0004-6256/140/2/416. [27](#), [76](#)
- A. Z. Bonanos, N. Castro, L. M. Macri, and R.-P. Kudritzki. The Distance to the Massive Eclipsing Binary LMC-SC1-105 in the Large Magellanic Cloud. *Astrophysical Journal Letters*, 729:L9, March 2011. doi: 10.1088/2041-8205/729/1/L9. [77](#)
- F. Bonnarel, P. Fernique, O. Bienaymé, et al. The ALADIN interactive sky atlas. A reference tool for identification of astronomical sources. *Astronomy & Astrophysics Supplement*, 143:33–40, April 2000. doi: 10.1051/aas:2000331. [128](#)
- C. M. Boon, A. J. Bird, M. J. Coe, et al. Multiwavelength observations of the Be/X-ray binary IGR J01217-7257 (=SXP 2.16) during outburst. *Monthly Notices of the Royal Astronomical Society*, 466:1149–1159, April 2017. doi: 10.1093/mnras/stw3169. [60](#), [136](#), [138](#)
- E. Bozzo, M. Falanga, and L. Stella. Are There Magnetars in High-Mass X-Ray Binaries? The Case of Supergiant Fast X-Ray Transients. *Astrophysical Journal*, 683:1031-1044, August 2008. doi: 10.1086/589990. [8](#)
- E. Bozzo, L. Oskinova, A. Feldmeier, and M. Falanga. Clumpy wind accretion in supergiant neutron star high mass X-ray binaries. *Astronomy & Astrophysics*, 589: A102, May 2016. doi: 10.1051/0004-6361/201628341. [8](#)
- R. Buccheri, K. Bennett, G. F. Bignami, et al. Search for pulsed gamma-ray emission from radio pulsars in the COS-B data. *Astronomy & Astrophysics*, 128: 245–251, November 1983. [52](#)
- J. Buchner, A. Georgakakis, K. Nandra, et al. X-ray spectral modelling of the AGN obscuring region in the CDFS: Bayesian model selection and catalogue. *Astronomy & Astrophysics*, 564:A125, April 2014. doi: 10.1051/0004-6361/201322971. [30](#)
- D. N. Burrows, J. E. Hill, J. A. Nousek, et al. The Swift X-Ray Telescope. *Space Science Reviews*, 120:165–195, October 2005. doi: 10.1007/s11214-005-5097-2. [144](#)
- Ş. Şahiner, M. M. Serim, A. Baykal, and S. Ç. İnam. RXTE and Swift Observations of SWIFT J0513.4-6547. *Monthly Notices of the Royal Astronomical Society*, 456:845–852, February 2016. doi: 10.1093/mnras/stv2775. [125](#)
- S. Campana, L. Stella, G. L. Israel, et al. The Quiescent X-Ray Emission of Three Transient X-Ray Pulsars. *Astrophysical Journal*, 580:389–393, November 2002. doi: 10.1086/343074. [10](#), [11](#), [12](#), [138](#), [153](#)
- S. Campana, L. Stella, S. Mereghetti, and D. de Martino. A universal relation for the propeller mechanisms in magnetic rotating stars at different scales. *ArXiv e-prints*, November 2017. [9](#)
- K. Cananzi, R. Augarde, and J. Lequeux. An Atlas of Balmer Lines - H-Delta and H-Gamma. *Astronomy & Astrophysics Supplement*, 101:599, November 1993. [57](#)
- R. Cappallo, S. G. T. Laycock, and D. M. Christodoulou. On the Geometry of the X-Ray Emission from Pulsars. I. Model Formulation and Tests. *PASP*, 129(12): 124201, December 2017. doi: 10.1088/1538-3873/aa8dee. [177](#)
- S. Carpano, F. Haberl, C. Maitra, and G. Vasilopoulos. Discovery of pulsations from NGC 300 ULX1 and its fast period evolution. *Monthly Notices of the Royal Astronomical Society*, 476:L45–L49, May 2018. doi: 10.1093/mnras/sly030. [8](#), [185](#), [186](#), [187](#), [189](#)

## REFERENCES

---

- J. Casares, P. G. Jonker, and G. Israelian. X-ray Binaries. *ArXiv e-prints*, January 2017. [5](#)
- W. Cash. Parameter estimation in astronomy through application of the likelihood ratio. *Astrophysical Journal*, 228:939–947, March 1979. doi: 10.1086/156922. [148](#), [163](#)
- F. Castelli, R. G. Gratton, and R. L. Kurucz. Notes on the convection in the ATLAS9 model atmospheres. *Astronomy & Astrophysics*, 318:841–869, February 1997. [119](#)
- D. Chakrabarty, L. Bildsten, M. H. Finger, et al. On the Correlation of Torque and Luminosity in GX 1+4. *Astrophysical Journal Letters*, 481:L101–L105, June 1997. doi: 10.1086/310666. [188](#)
- P. A. Charles, A. Rajoelimanana, and T. J. Maccarone. Swift J053041.9-665426, the new LMC X-ray transient, has a variable optical counterpart. *The Astronomer's Telegram*, 3751:1, November 2011. [69](#)
- A. Chashkina, P. Abolmasov, and J. Poutanen. Super-Eddington accretion on to a magnetized neutron star. *Monthly Notices of the Royal Astronomical Society*, 470:2799–2813, September 2017a. doi: 10.1093/mnras/stx1372. [9](#), [12](#), [106](#), [181](#)
- A. Chashkina, P. Abolmasov, and J. Poutanen. Super-Eddington accretion onto a magnetized neutron star. *ArXiv e-prints*, March 2017b. [176](#)
- S. Chaty. Obscured Sources and Supergiant Fast X-ray Transients: New Classes of High Mass X-ray Binaries. *Chinese Journal of Astronomy and Astrophysics Supplement*, 8:197–201, October 2008a. [61](#)
- S. Chaty. INTEGRAL sources: from obscured high mass X-ray binaries to supergiant fast X-ray transients. *ArXiv e-prints*, September 2008b. [61](#)
- Z.-Q. Cheng, Y. Shao, and X.-D. Li. On the Spin Period Distribution in Be/X-Ray Binaries. *Astrophysical Journal*, 786:128, May 2014a. doi: 10.1088/0004-637X/786/2/128. [44](#)
- Z.-Q. Cheng, Y. Shao, and X.-D. Li. On the Spin Period Distribution in Be/X-Ray Binaries. *Astrophysical Journal*, 786:128, May 2014b. doi: 10.1088/0004-637X/786/2/128. [6](#)
- J. Choi, A. Dotter, C. Conroy, et al. Mesa Isochrones and Stellar Tracks (MIST). I. Solar-scaled Models. *Astrophysical Journal*, 823:102, June 2016. doi: 10.3847/0004-637X/823/2/102. [58](#)
- D. M. Christodoulou, S. G. T. Laycock, J. Yang, and S. Fingerman. Tracing the Lowest Propeller Line in Magellanic High-mass X-Ray Binaries. *Astrophysical Journal*, 829:30, September 2016. doi: 10.3847/0004-637X/829/1/30. [138](#)
- D. M. Christodoulou, S. G. T. Laycock, and D. Kazanas. Retrograde Accretion Disks in High-Mass Be/X-ray Binaries. *ArXiv e-prints*, April 2017a. [44](#), [187](#)
- D. M. Christodoulou, S. G. T. Laycock, J. Yang, and S. Fingerman. Determination of the magnetic fields of Magellanic X-ray pulsars. *Research in Astronomy and Astrophysics*, 17:059, May 2017b. doi: 10.1088/1674-4527/17/6/59. [153](#)
- G. Clark, R. Doxsey, F. Li, J. G. Jernigan, and J. van Paradijs. On two new X-ray sources in the SMC and the high luminosities of the Magellanic X-ray sources. *Astrophysical Journal Letters*, 221:L37–L41, April 1978. doi: 10.1086/182660. [157](#), [167](#)
- G. Clark, F. Li, and J. van Paradijs. Deep X-ray survey of the Small Magellanic Cloud. *Astrophysical Journal*, 227:54, January 1979. doi: 10.1086/156702. [157](#)
- J. S. Clark, E. S. Bartlett, P. S. Broos, et al. The VLT-FLAMES Tarantula survey. XX. The nature of the X-ray bright emission-line star VFTS 399. *Astronomy & Astrophysics*, 579:A131, July 2015. doi: 10.1051/0004-6361/201424427. [45](#)

- M. J. Coe. An estimate of the supernova kick velocities for high-mass X-ray binaries in the Small Magellanic Cloud. *Monthly Notices of the Royal Astronomical Society*, 358:1379–1382, April 2005. doi: 10.1111/j.1365-2966.2005.08857.x. [79](#), [94](#)
- M. J. Coe, I. Negueruela, D. A. H. Buckley, N. J. Haigh, and S. G. T. Laycock. Optical studies of two Large Magellanic Cloud X-ray transients: RX J0544.1-7100 and RX J0520.5-6932. *Monthly Notices of the Royal Astronomical Society*, 324:623–627, June 2001. doi: 10.1046/j.1365-8711.2001.04327.x. [83](#)
- M. J. Coe, W. R. T. Edge, J. L. Galache, and V. A. McBride. Optical properties of Small Magellanic Cloud X-ray binaries. *Monthly Notices of the Royal Astronomical Society*, 356:502–514, January 2005. doi: 10.1111/j.1365-2966.2004.08467.x. [85](#), [119](#), [143](#)
- M. J. Coe, F. Haberl, R. Sturm, et al. The XMM-Newton survey of the Small Magellanic Cloud: XMMU J010633.1-731543 and XMMU J010743.1-715953, two new Be/X-ray binary systems. *Monthly Notices of the Royal Astronomical Society*, 424:282–292, July 2012. doi: 10.1111/j.1365-2966.2012.21193.x. [93](#), [123](#)
- M. J. Coe, A. J. Bird, V. A. McBride, et al. Detection of an X-ray outburst by INTEGRAL from a previously unknown SMC source IGR J01217-7257. *The Astronomer’s Telegram*, 5806, January 2014. [135](#), [137](#)
- M. J. Coe, M. Finger, E. S. Bartlett, and A. Udalski. Swift J0513.4-6547 = LXP 27.2: a new Be/X-ray binary system in the Large Magellanic Cloud. *Monthly Notices of the Royal Astronomical Society*, 447:1630–1637, February 2015. doi: 10.1093/mnras/stu2562. [125](#)
- M. J. Coe, V. McBride, F. Haberl, A. Bird, and A. Udalski. The optical counterpart to XMMU J004855.5-734946. *The Astronomer’s Telegram*, 9198, June 2016. [143](#)
- E. J. M. Colbert and R. F. Mushotzky. The Nature of Accreting Black Holes in Nearby Galaxy Nuclei. *Astrophysical Journal*, 519:89–107, July 1999. doi: 10.1086/307356. [8](#), [176](#)
- R. Corbet, C. B. Markwardt, F. E. Marshall, et al. XTE J0119-731. *IAU Circ.*, 8064, February 2003a. [137](#)
- R. H. D. Corbet. Be/neutron star binaries - A relationship between orbital period and neutron star spin period. *Astronomy & Astrophysics*, 141:91–93, December 1984. [6](#), [44](#), [94](#)
- R. H. D. Corbet. Transient X-Ray Sources, Luminosity Gaps, and Neutron Star Densities. *Astrophysical Journal Letters*, 457:L31, January 1996. doi: 10.1086/309890. [153](#)
- R. H. D. Corbet, F. E. Marshall, M. J. Coe, S. Laycock, and G. Handler. The Discovery of an Outburst and Pulsed X-Ray Flux from SMC X-2 Using the Rossi X-Ray Timing Explorer. *Astrophysical Journal Letters*, 548:L41–L44, February 2001. doi: 10.1086/318929. [157](#)
- R. H. D. Corbet, W. R. T. Edge, S. Laycock, et al. Periodic Recurrent Outbursts from a 7.8s Pulsar in the SMC. In *AAS/High Energy Astrophysics Division #7*, volume 35 of *Bulletin of the American Astronomical Society*, page 629, March 2003b. [167](#)
- A. P. Cowley and P. C. Schmidtke. The Orbital Period of SMC X-3 from Optical Photometry. *Astronomical Journal*, 128:709–711, August 2004. doi: 10.1086/422025. [167](#)
- A. N. Cox. *Allen’s astrophysical quantities*. 2000. [120](#)
- S. M. Crawford, M. Still, P. Schellart, et al. PySALT: the SALT science pipeline. In *Society of Photo-Optical Instrumentation*

## REFERENCES

---

- Engineers (SPIE) Conference Series*, volume 7737 of *Society of Photo-Optical Instrumentation Engineers (SPIE) Conference Series*, July 2010. doi: 10.1117/12.857000. [103](#)
- R. M. Cutri and et al. WISE All-Sky Data Release (Cutri+ 2012). *VizieR Online Data Catalog*, 2311:0, April 2012. [76](#)
- R. M. Cutri, M. F. Skrutskie, S. van Dyk, et al. 2MASS All-Sky Catalog of Point Sources (Cutri+ 2003). *VizieR Online Data Catalog*, 2246:0, March 2003. [74](#), [76](#)
- R. M. Cutri, M. F. Skrutskie, S. van Dyk, et al. 2MASS 6X Point Source Working Database / Catalog (Cutri+ 2006). *VizieR Online Data Catalog*, 2281:0, February 2012. [76](#)
- A. D’Aì, V. La Parola, G. Cusumano, et al. The Swift-BAT survey reveals the orbital period of three high-mass X-ray binaries. *Astronomy & Astrophysics*, 529:A30, May 2011. doi: 10.1051/0004-6361/201016401. [124](#), [137](#)
- C. R. D’Angelo and H. C. Spruit. Episodic accretion on to strongly magnetic stars. *Monthly Notices of the Royal Astronomical Society*, 406:1208–1219, August 2010. doi: 10.1111/j.1365-2966.2010.16749.x. [8](#)
- C. R. D’Angelo and H. C. Spruit. Accretion discs trapped near corotation. *Monthly Notices of the Royal Astronomical Society*, 420:416–429, February 2012. doi: 10.1111/j.1365-2966.2011.20046.x. [11](#), [153](#)
- R. E. Davies and J. E. Pringle. Spindown of neutron stars in close binary systems. II. *Monthly Notices of the Royal Astronomical Society*, 196:209–224, July 1981. doi: 10.1093/mnras/196.2.209. [6](#), [45](#)
- R. E. Davies, A. C. Fabian, and J. E. Pringle. Spindown of neutron stars in close binary systems. *Monthly Notices of the Royal Astronomical Society*, 186:779–782, March 1979. doi: 10.1093/mnras/186.4.779. [6](#)
- S. R. Davies. An improved test for periodicity. *Monthly Notices of the Royal Astronomical Society*, 244:93–95, May 1990. [28](#), [52](#), [114](#), [128](#), [146](#)
- D. de Martino, G. Matt, T. Belloni, F. Haberl, and K. Mukai. BeppoSAX observations of soft X-ray intermediate polars. *Astronomy & Astrophysics*, 415:1009–1019, March 2004. doi: 10.1051/0004-6361:20034160. [18](#)
- W. J. de Wit, H. J. G. L. M. Lamers, J. B. Marquette, and J. P. Beaulieu. The remarkable light and colour variability of Small Magellanic Cloud Be stars. *Astronomy & Astrophysics*, 456:1027–1035, September 2006. doi: 10.1051/0004-6361:20065137. [78](#), [92](#), [120](#), [124](#)
- J. W. den Herder, A. C. Brinkman, S. M. Kahn, et al. The Reflection Grating Spectrometer on board XMM-Newton. *Astronomy & Astrophysics*, 365:L7–L17, January 2001. doi: 10.1051/0004-6361:20000058. [26](#), [127](#), [158](#)
- J. M. Dickey and F. J. Lockman. H I in the Galaxy. *Ann. Rev. Astron. Astrophys.*, 28:215–261, 1990a. doi: 10.1146/annurev.aa.28.090190.001243. [53](#), [54](#), [71](#), [78](#), [86](#), [98](#), [115](#), [130](#), [147](#), [161](#), [183](#)
- J. M. Dickey and F. J. Lockman. H I in the Galaxy. *Ann. Rev. Astron. Astrophys.*, 28:215–261, 1990b. doi: 10.1146/annurev.aa.28.090190.001243. [21](#)
- V. Doroshenko, S. S. Tsygankov, A. A. Mushtukov, et al. Luminosity dependence of the cyclotron line and evidence for the accretion regime transition in V 0332+53. *Monthly Notices of the Royal Astronomical Society*, 466:2143–2150, April 2017. doi: 10.1093/mnras/stw3236. [182](#)
- C. Dotan and N. J. Shaviv. Super-Eddington slim accretion discs with winds. *Monthly Notices of the Royal Astronomical Society*, 413:1623–1632, May 2011. doi: 10.1111/j.1365-2966.2011.18235.x. [176](#)

- A. Dotter. MESA Isochrones and Stellar Tracks (MIST) 0: Methods for the Construction of Stellar Isochrones. *Astrophysical Journal Suppl. Ser.*, 222:8, January 2016. doi: 10.3847/0067-0049/222/1/8. 58
- S. M. Dougherty, L. B. F. M. Waters, G. Burki, et al. Near-IR excess of Be stars. *Astronomy & Astrophysics*, 290, October 1994. 74
- B. T. Draine. *Physics of the Interstellar and Intergalactic Medium*. 2011. 14
- S. P. Drave, A. J. Bird, L. J. Townsend, et al. X-ray pulsations from the region of the supergiant fast X-ray transient IGR J17544-2619. *Astronomy & Astrophysics*, 539:A21, March 2012. doi: 10.1051/0004-6361/201117947. 62
- L. Ducci, V. Doroshenko, P. Romano, A. Santangelo, and M. Sasaki. Expected number of supergiant fast X-ray transients in the Milky Way. *Astronomy & Astrophysics*, 568:A76, August 2014. doi: 10.1051/0004-6361/201424215. 7
- W. R. T. Edge, M. J. Coe, R. H. D. Corbet, C. B. Markwardt, and S. Laycock. SMC X-3 Identified with RXTE 7.78s Pulsar from Archive Chandra Data. *The Astronomer's Telegram*, 225, January 2004a. 167
- W. R. T. Edge, M. J. Coe, J. L. Galache, and A. B. Hill. A major outburst from the X-ray binary RX J0520.5-6932. *Monthly Notices of the Royal Astronomical Society*, 349:1361–1364, April 2004b. doi: 10.1111/j.1365-2966.2004.07606.x. 83
- P. Eger and F. Haberl. XMM-Newton observations of the Small Magellanic Cloud: Long term evolution of frequently observed Be/X-ray binaries. *Astronomy & Astrophysics*, 491:841–849, December 2008. doi: 10.1051/0004-6361:200810809. 79
- R. F. Elsner and F. K. Lamb. Accretion by magnetic neutron stars. I - Magnetospheric structure and stability. *Astrophysical Journal*, 215:897–913, August 1977. doi: 10.1086/155427. 9
- D. Emmanoulopoulos, I. M. McHardy, and I. E. Papadakis. Generating artificial light curves: revisited and updated. *Monthly Notices of the Royal Astronomical Society*, 433:907–927, August 2013. doi: 10.1093/mnras/stt764. 28, 52
- T. Endo, F. Nagase, and T. Mihara. Pulse-Phase Resolved Spectroscopy of Hercules X-1 with ASCA. *Publications of the Astronomical Society of Japan*, 52:223, April 2000. doi: 10.1093/pasj/52.2.223. 15, 171
- C. J. Evans, I. D. Howarth, M. J. Irwin, A. W. Burnley, and T. J. Harries. A 2dF survey of the Small Magellanic Cloud. *Monthly Notices of the Royal Astronomical Society*, 353:601–623, September 2004. doi: 10.1111/j.1365-2966.2004.08096.x. 56, 57, 137
- C. J. Evans, J. T. van Loon, R. Hainich, and M. Bailey. 2dF-AAOmega spectroscopy of massive stars in the Magellanic Clouds. The north-eastern region of the Large Magellanic Cloud. *Astronomy & Astrophysics*, 584:A5, December 2015. doi: 10.1051/0004-6361/201525882. 56
- P. A. Evans, A. P. Beardmore, K. L. Page, et al. An online repository of Swift/XRT light curves of  $\gamma$ -ray bursts. *Astronomy & Astrophysics*, 469:379–385, July 2007. doi: 10.1051/0004-6361:20077530. 49, 134
- P. A. Evans, J. A. Kennea, and M. J. Coe. Swift detects an outburst from XMMU J004855.5-734946. *The Astronomer's Telegram*, 9197, June 2016. 144
- R. Farinelli, C. Ferrigno, E. Bozzo, and P. A. Becker. A new model for the X-ray continuum of the magnetized accreting pulsars. *Astronomy & Astrophysics*, 591:A29, June 2016. doi: 10.1051/0004-6361/201527257. 141, 179

## REFERENCES

---

- F. M. Fornasini, J. A. Tomsick, M. Bachetti, et al. An XMM-Newton and NuSTAR Study of IGR J18214-1318: A Non-pulsating High-mass X-Ray Binary with a Neutron Star. *Astrophysical Journal*, 841:35, May 2017. doi: 10.3847/1538-4357/aa6ff4. [55](#)
- J. Frank, A. King, and D. J. Raine. *Accretion Power in Astrophysics: Third Edition*. January 2002. [122](#)
- A. Fruscione, J. C. McDowell, G. E. Allen, et al. CIAO: Chandra's data analysis system. In *Society of Photo-Optical Instrumentation Engineers (SPIE) Conference Series*, volume 6270 of *Proceedings of the SPIE*, page 62701V, June 2006. doi: 10.1117/12.671760. [144](#), [185](#)
- F. Fürst, D. J. Walton, F. A. Harrison, et al. Discovery of Coherent Pulsations from the Ultraluminous X-Ray Source NGC 7793 P13. *Astrophysical Journal Letters*, 831:L14, November 2016. doi: 10.3847/2041-8205/831/2/L14. [8](#), [97](#)
- N. Gehrels. Confidence limits for small numbers of events in astrophysical data. *Astrophysical Journal*, 303:336–346, April 1986. doi: 10.1086/164079. [190](#)
- P. Ghosh and F. K. Lamb. Accretion by rotating magnetic neutron stars. III - Accretion torques and period changes in pulsating X-ray sources. *Astrophysical Journal*, 234:296–316, November 1979. doi: 10.1086/157498. [9](#), [187](#)
- P. Ghosh, C. J. Pethick, and F. K. Lamb. Accretion by rotating magnetic neutron stars. I - Flow of matter inside the magnetosphere and its implications for spin-up and spin-down of the star. *Astrophysical Journal*, 217:578–596, October 1977. doi: 10.1086/155606. [106](#)
- R. Giacconi, H. Gursky, E. Kellogg, E. Schreier, and H. Tananbaum. Discovery of Periodic X-Ray Pulsations in Centaurus X-3 from UHURU. *Astrophysical Journal Letters*, 167:L67, July 1971. doi: 10.1086/180762. [15](#)
- W. Gieren, G. Pietrzyński, I. Soszyński, et al. The Araucaria Project: Near-Infrared Photometry of Cepheid Variables in the Sculptor Galaxy NGC 300. *Astrophysical Journal*, 628:695–703, August 2005. doi: 10.1086/430903. [185](#)
- M. Gilfanov. Low-mass X-ray binaries as a stellar mass indicator for the host galaxy. *Monthly Notices of the Royal Astronomical Society*, 349:146–168, March 2004. doi: 10.1111/j.1365-2966.2004.07473.x. [49](#)
- M. Gilfanov, H.-J. Grimm, and R. Sunyaev. HMXB, ULX and star formation. *Nuclear Physics B Proceedings Supplements*, 132:369–375, June 2004. doi: 10.1016/j.nuclphysbps.2004.04.065. [8](#)
- J. C. Gladstone, T. P. Roberts, and C. Done. The ultraluminous state. *Monthly Notices of the Royal Astronomical Society*, 397:1836–1851, August 2009. doi: 10.1111/j.1365-2966.2009.15123.x. [176](#)
- K. Glatt, E. K. Grebel, and A. Koch. Ages and luminosities of young SMC/LMC star clusters and the recent star formation history of the Clouds. *Astronomy & Astrophysics*, 517:A50, July 2010. doi: 10.1051/0004-6361/201014187. [79](#)
- Y. N. Gnedin and R. A. Sunyaev. The Beaming of Radiation from an Accreting Magnetic Neutron Star and the X-ray Pulsars. *Astronomy & Astrophysics*, 25:233, 1973. [16](#), [17](#)
- A. González-Galán, E. Kuulkers, P. Kretschmar, et al. Spin period evolution of GX 1+4. *Astronomy & Astrophysics*, 537:A66, January 2012. doi: 10.1051/0004-6361/201117893. [188](#)
- D. Graczyk, G. Pietrzyński, I. B. Thompson, et al. The Araucaria Project. The Distance to the Small Magellanic Cloud from Late-type Eclipsing Binaries. *Astrophysical Journal*, 780:59, January 2014.

- doi: 10.1088/0004-637X/780/1/59. [21](#), [130](#), [143](#), [149](#), [162](#)
- P. C. Gregory and T. J. Loredo. A new method for the detection of a periodic signal of unknown shape and period. *Astrophysical Journal*, 398:146–168, October 1992. doi: 10.1086/171844. [146](#)
- P. C. Gregory and T. J. Loredo. Bayesian Periodic Signal Detection: Analysis of ROSAT Observations of PSR 0540-693. *Astrophysical Journal*, 473:1059, December 1996. doi: 10.1086/178215. [28](#), [74](#), [85](#), [114](#), [128](#), [146](#)
- J. Greiner, W. Bornemann, C. Clemens, et al. GROND-a 7-Channel Imager. *PASP*, 120:405, April 2008. doi: 10.1086/587032. [50](#), [117](#)
- E. D. Grundstrom, S. M. Caballero-Nieves, D. R. Gies, et al. Joint H $\alpha$  and X-Ray Observations of Massive X-Ray Binaries. II. The Be X-Ray Binary and Microquasar LS I +61 303. *Astrophysical Journal*, 656:437–443, February 2007. doi: 10.1086/510509. [57](#)
- J. Guibert. The MAMA Facility - a Survey of Scientific Programmes. In H. T. MacGillivray and E. B. Thomson, editors, *Digitised Optical Sky Surveys*, volume 174 of *Astrophysics and Space Science Library*, page 103, 1992. doi: 10.1007/978-94-011-2472-0\_14. [128](#)
- T. Güver and F. Özel. The relation between optical extinction and hydrogen column density in the Galaxy. *Monthly Notices of the Royal Astronomical Society*, 400:2050–2053, December 2009. doi: 10.1111/j.1365-2966.2009.15598.x. [78](#)
- F. Haberl. The X-ray properties of GX 301 - 2 (4U 1223 - 62). *Astrophysical Journal*, 376:245–255, July 1991. doi: 10.1086/170273. [60](#)
- F. Haberl and W. Pietsch. Variable X-ray sources in the LMC region observed by the ROSAT PSPC. *Astronomy & Astrophysics*, 344:521–532, April 1999. [83](#)
- F. Haberl and W. Pietsch. XMM-Newton observations of the Small Magellanic Cloud: X-ray outburst of the 6.85 s pulsar XTE J0103-728. *Astronomy & Astrophysics*, 484:451–455, June 2008. doi: 10.1051/0004-6361:20079308. [91](#)
- F. Haberl and R. Sturm. High-mass X-ray binaries in the Small Magellanic Cloud. *Astronomy & Astrophysics*, 586:A81, February 2016. doi: 10.1051/0004-6361/201527326. [6](#), [35](#), [44](#), [47](#), [59](#), [111](#), [119](#), [125](#), [137](#), [143](#), [148](#), [152](#), [199](#)
- F. Haberl, P. Eger, and W. Pietsch. XMM-Newton observations of the Small Magellanic Cloud: Be/X-ray binary pulsars active between October 2006 and June 2007. *Astronomy & Astrophysics*, 489:327–348, October 2008a. doi: 10.1051/0004-6361:200810100. [74](#), [80](#), [85](#), [87](#), [114](#), [146](#), [152](#)
- F. Haberl, P. Eger, W. Pietsch, R. H. D. Corbet, and M. Sasaki. XMM-Newton observations of the Small Magellanic Cloud: XMMU J004814.1-731003, a 25.55 s Be/X-ray binary pulsar. *Astronomy & Astrophysics*, 485:177–181, July 2008b. doi: 10.1051/0004-6361:200809540. [125](#)
- F. Haberl, R. Sturm, M. D. Filipović, W. Pietsch, and E. J. Crawford. SXP 1062, a young Be X-ray binary pulsar with long spin period. Implications for the neutron star birth spin. *Astronomy & Astrophysics*, 537:L1, January 2012a. doi: 10.1051/0004-6361/201118369. [45](#)
- F. Haberl, R. Sturm, M. D. Filipović, W. Pietsch, and E. J. Crawford. SXP 1062, a young Be X-ray binary pulsar with long spin period. Implications for the neutron star birth spin. *Astronomy & Astrophysics*, 537:L1, January 2012b. doi: 10.1051/0004-6361/201118369. [6](#)
- F. Haberl, G. L. Israel, G. A. Rodriguez Castillo, et al. EXTraS discovery of two pulsators in the direction of the LMC: a Be/X-ray binary pulsar in the LMC and a candidate double-degenerate polar

## REFERENCES

---

- in the foreground. *Astronomy & Astrophysics*, 598:A69, February 2017a. doi: 10.1051/0004-6361/201629744. [55](#)
- F. Haberl, G. L. Israel, G. A. Rodriguez Castillo, et al. EXTraS discovery of two pulsators in the direction of the LMC: a Be/X-ray binary pulsar in the LMC and a candidate double-degenerate polar in the foreground. *Astronomy & Astrophysics*, 598:A69, February 2017b. doi: 10.1051/0004-6361/201629744. [1](#), [36](#)
- V. Hambaryan, V. Suleimanov, F. Haberl, et al. The compactness of the isolated neutron star RX J0720.4-3125. *Astronomy & Astrophysics*, 601:A108, May 2017. doi: 10.1051/0004-6361/201630368. [154](#)
- R. J. Hamilton, F. K. Lamb, and M. C. Miller. Disk-accreting magnetic neutron stars as high-energy particle accelerators. *Astrophysical Journal Suppl. Ser.*, 90:837–839, February 1994. doi: 10.1086/191912. [107](#)
- J. Harris and D. Zaritsky. The Star Formation History of the Small Magellanic Cloud. *Astronomical Journal*, 127:1531–1544, March 2004. doi: 10.1086/381953. [21](#)
- J. Harris and D. Zaritsky. The Star Formation History of the Large Magellanic Cloud. *Astronomical Journal*, 138:1243–1260, November 2009. doi: 10.1088/0004-6256/138/5/1243. [21](#), [43](#), [47](#), [49](#)
- R. Haschke, E. K. Grebel, and S. Duffau. New Optical Reddening Maps of the Large and Small Magellanic Clouds. *Astronomical Journal*, 141:158, May 2011. doi: 10.1088/0004-6256/141/5/158. [57](#), [59](#)
- A. A. Henden, S. Levine, D. Terrell, and D. L. Welch. APASS - The Latest Data Release. In *American Astronomical Society Meeting Abstracts*, volume 225 of *American Astronomical Society Meeting Abstracts*, page 336.16, January 2015. [50](#)
- M. A. Hendry, S. J. Smartt, E. D. Skillman, et al. The blue supergiant Sher 25 and its intriguing hourglass nebula. *Monthly Notices of the Royal Astronomical Society*, 388:1127–1142, August 2008. doi: 10.1111/j.1365-2966.2008.13347.x. [57](#)
- R. C. Hickox, R. Narayan, and T. R. Kallman. Origin of the Soft Excess in X-Ray Pulsars. *Astrophysical Journal*, 614:881–896, October 2004. doi: 10.1086/423928. [15](#), [53](#), [72](#), [80](#), [91](#), [116](#), [122](#), [164](#), [171](#)
- R. W. Hilditch, I. D. Howarth, and T. J. Harries. Forty eclipsing binaries in the Small Magellanic Cloud: fundamental parameters and Cloud distance. *Monthly Notices of the Royal Astronomical Society*, 357:304–324, February 2005. doi: 10.1111/j.1365-2966.2005.08653.x. [70](#), [73](#)
- R. Hirata. Disk Precession in Pleione. In A. T. Okazaki, S. P. Owocki, and S. Stefl, editors, *Active OB-Stars: Laboratories for Stellar and Circumstellar Physics*, volume 361 of *Astronomical Society of the Pacific Conference Series*, page 267, March 2007. [137](#)
- W. C. G. Ho, H. Klus, M. J. Coe, and N. Andersson. Equilibrium spin pulsars unite neutron star populations. *Monthly Notices of the Royal Astronomical Society*, 437:3664–3669, February 2014. doi: 10.1093/mnras/stt2193. [185](#)
- W. C. G. Ho, C.-Y. Ng, A. G. Lyne, et al. Multiwavelength monitoring and X-ray brightening of Be X-ray binary PSR J2032+4127/MT91 213 on its approach to periastron. *Monthly Notices of the Royal Astronomical Society*, 464:1211–1219, January 2017. doi: 10.1093/mnras/stw2420. [6](#)
- J. Hoffman and B. T. Draine. Accurate Modeling of X-ray Extinction by Interstellar Grains. *Astrophysical Journal*, 817:139, February 2016. doi: 10.3847/0004-637X/817/2/139. [14](#)

- J. H. Horne and S. L. Baliunas. A prescription for period analysis of unevenly sampled time series. *Astrophysical Journal*, 302:757–763, March 1986. doi: 10.1086/164037. [29](#), [53](#), [60](#), [89](#), [114](#), [121](#), [135](#)
- N. R. Ikhsanov. The origin of long-period X-ray pulsars. *Monthly Notices of the Royal Astronomical Society*, 375:698–704, February 2007. doi: 10.1111/j.1365-2966.2006.11331.x. [6](#)
- K. Ikiewicz, J. Mikołajewska, and B. Monard. Variability of the symbiotic X-ray binary GX 1+4. Enhanced activity near periastron passage. *Astronomy & Astrophysics*, 601:A105, May 2017. doi: 10.1051/0004-6361/201630021. [188](#)
- A. F. Illarionov and R. A. Sunyaev. Why the Number of Galactic X-ray Stars Is so Small? *Astronomy & Astrophysics*, 39:185, February 1975a. [153](#)
- A. F. Illarionov and R. A. Sunyaev. Why the Number of Galactic X-ray Stars Is so Small? *Astronomy & Astrophysics*, 39:185, February 1975b. [6](#), [9](#), [138](#)
- L. Inno, N. Matsunaga, G. Bono, et al. On the Distance of the Magellanic Clouds Using Cepheid NIR and Optical-NIR Period-Wesenheit Relations. *Astrophysical Journal*, 764:84, February 2013. doi: 10.1088/0004-637X/764/1/84. [88](#)
- J. J. M. in’t Zand. Chandra observation of the fast X-ray transient IGR J17544-2619: evidence for a neutron star? *Astronomy & Astrophysics*, 441:L1–L4, October 2005. doi: 10.1051/0004-6361:200500162. [8](#)
- G. L. Israel, A. Belfiore, L. Stella, et al. An accreting pulsar with extreme properties drives an ultraluminous x-ray source in NGC 5907. *Science*, 355:817–819, February 2017a. doi: 10.1126/science.aai8635. [8](#), [97](#), [190](#)
- G. L. Israel, A. Papitto, P. Esposito, et al. Discovery of a 0.42-s pulsar in the ultraluminous X-ray source NGC 7793 P13. *Monthly Notices of the Royal Astronomical Society*, 466:L48–L52, March 2017b. doi: 10.1093/mnrasl/slw218. [177](#), [190](#)
- K. Jahoda, C. B. Markwardt, Y. Radeva, et al. Calibration of the Rossi X-Ray Timing Explorer Proportional Counter Array. *Astrophysical Journal Suppl. Ser.*, 163:401–423, April 2006. doi: 10.1086/500659. [167](#)
- G. K. Jaisawal and S. Naik. Detection of cyclotron resonance scattering feature in high-mass X-ray binary pulsar SMC X-2. *Monthly Notices of the Royal Astronomical Society*, 461:L97–L101, September 2016. doi: 10.1093/mnrasl/slw108. [139](#)
- P. Kaaret, H. Feng, and T. P. Roberts. Ultraluminous X-Ray Sources. *Ann. Rev. Astron. Astrophys.*, 55:303–341, August 2017. doi: 10.1146/annurev-astro-091916-055259. [8](#), [177](#)
- P. M. W. Kalberla, W. B. Burton, D. Hartmann, et al. The Leiden/Argentine/Bonn (LAB) Survey of Galactic HI. Final data release of the combined LDS and IAR surveys with improved stray-radiation corrections. *Astronomy & Astrophysics*, 440:775–782, September 2005. doi: 10.1051/0004-6361:20041864. [115](#), [148](#)
- A. D. Kaminker, V. N. Fedorenko, and A. I. Tsygan. A radiating accretion column as a model for an x-ray pulsar. *Soviet Ast.*, 20:436, August 1976. [17](#)
- A. Kathirgamaraju, R. Barniol Duran, and D. Giannios. Off-axis short GRBs from structured jets as counterparts to GW events. *Monthly Notices of the Royal Astronomical Society*, 473:L121–L125, January 2018. doi: 10.1093/mnrasl/slx175. [18](#)
- D. Kato, C. Nagashima, T. Nagayama, et al. The IRSF Magellanic Clouds Point Source Catalog. *Publications of the Astronomical*

## REFERENCES

---

- Society of Japan*, 59:615–641, June 2007. [74](#), [76](#)
- A. Kaufer, O. Stahl, S. Tubbesing, et al. Commissioning FEROS, the new high-resolution spectrograph at La-Silla. *The Messenger*, 95:8–12, March 1999. [50](#)
- B. C. Kelly. Some Aspects of Measurement Error in Linear Regression of Astronomical Data. *Astrophysical Journal*, 665:1489–1506, August 2007. doi: 10.1086/519947. [134](#)
- J. A. Kennea, D. N. Burrows, M. J. Coe, et al. Swift observations show MAXI J0051-736 is a new outburst of SMC X-2. *The Astronomer’s Telegram*, 8091, September 2015. [157](#)
- J. A. Kennea, M. J. Coe, P. A. Evans, et al. SMC X-3: S-CUBED detection of turn-on, brightening and identification with MAXI J0058-721. *The Astronomer’s Telegram*, 9362, August 2016a. [167](#)
- J. A. Kennea, P. A. Evans, and M. J. Coe. Swift detection of active X-ray transients in the SMC. *The Astronomer’s Telegram*, 9299, August 2016b. [143](#), [144](#)
- A. King and J.-P. Lasota. ULXs: Neutron stars versus black holes. *Monthly Notices of the Royal Astronomical Society*, 458:L10–L13, May 2016. doi: 10.1093/mnrasl/slw011. [183](#), [184](#)
- A. King, J.-P. Lasota, and W. Kluźniak. Pulsing ULXs: tip of the iceberg? *Monthly Notices of the Royal Astronomical Society*, 468:L59–L62, June 2017. doi: 10.1093/mnrasl/slx020. [171](#), [184](#)
- A. R. King. Masses, beaming and Eddington ratios in ultraluminous X-ray sources. *Monthly Notices of the Royal Astronomical Society*, 393:L41–L44, February 2009. doi: 10.1111/j.1745-3933.2008.00594.x. [8](#)
- A. R. King and K. A. Pounds. Black hole winds. *Monthly Notices of the Royal Astronomical Society*, 345:657–659, October 2003. doi: 10.1046/j.1365-8711.2003.06980.x. [176](#)
- A. R. King, M. B. Davies, M. J. Ward, G. Fabbiano, and M. Elvis. Ultraluminous X-Ray Sources in External Galaxies. *Astrophysical Journal Letters*, 552:L109–L112, May 2001. doi: 10.1086/320343. [188](#)
- H. Klus, W. C. G. Ho, M. J. Coe, R. H. D. Corbet, and L. J. Townsend. Spin period change and the magnetic fields of neutron stars in Be X-ray binaries in the Small Magellanic Cloud. *Monthly Notices of the Royal Astronomical Society*, 437:3863–3882, February 2014. doi: 10.1093/mnras/stt2192. [152](#)
- C. Knigge, M. J. Coe, and P. Podsiadlowski. Two populations of X-ray pulsars produced by two types of supernova. *Nature*, 479:372–375, November 2011. doi: 10.1038/nature10529. [6](#), [44](#), [94](#), [125](#)
- F. Koliopanos and M. Gilfanov. Luminosity-dependent change of the emission diagram in the X-ray pulsar 4U 1626-67. *Monthly Notices of the Royal Astronomical Society*, 456:3535–3541, March 2016. doi: 10.1093/mnras/stv2873. [6](#), [140](#), [153](#)
- F. Koliopanos and G. Vasilopoulos. Accreting, highly magnetized neutron stars at the Eddington limit: A study of the 2016 outburst of SMC X-3. *Monthly Notices of the Royal Astronomical Society; submitted*, 2017. [59](#)
- F. Koliopanos and G. Vasilopoulos. Accreting, highly magnetized neutron stars at the Eddington limit: A study of the 2016 outburst of SMC X-3. *ArXiv e-prints*, January 2018. [1](#), [30](#), [171](#)
- F. Koliopanos, G. Vasilopoulos, O. Godet, et al. ULX spectra revisited: Accreting, highly magnetized neutron stars as the engines of ultraluminous X-ray sources.

- Astronomy & Astrophysics*, 608:A47, December 2017. doi: 10.1051/0004-6361/201730922. [1](#), [8](#), [172](#), [177](#), [181](#)
- A. Kolmogoroff. Sulla determinazione empirica di una legge di distribuzione. *G. Ist. Ital. Attuari*, 4:83–91, 1933. [133](#)
- P. Kosec, C. Pinto, A. C. Fabian, and D. J. Walton. Searching for outflows in ultraluminous X-ray sources through high-resolution X-ray spectroscopy. *Monthly Notices of the Royal Astronomical Society*, 473:5680–5697, February 2018. doi: 10.1093/mnras/stx2695. [189](#)
- R. P. Kraft, D. N. Burrows, and J. A. Nousek. Determination of confidence limits for experiments with low numbers of counts. *Astrophysical Journal*, 374:344–355, June 1991. doi: 10.1086/170124. [49](#), [134](#), [150](#)
- U. Kraus, H.-P. Nollert, H. Ruder, and H. Riffert. Analyzing X-Ray Pulsar Profiles: Asymmetry as a Key to Geometry and Beam Pattern. *Astrophysical Journal*, 450:763, September 1995. doi: 10.1086/176182. [6](#), [16](#), [17](#)
- U. Kraus, S. Blum, J. Schulte, H. Ruder, and P. Meszaros. Analyzing X-Ray Pulsar Profiles: Geometry and Beam Pattern of Centaurus X-3. *Astrophysical Journal*, 467:794, August 1996. doi: 10.1086/177653. [140](#)
- P. Kretschmar, E. Nespoli, P. Reig, and F. Anders. The Be X-ray Binary Outburst Zoo. In *Proceedings of "An INTEGRAL view of the high-energy sky (the first 10 years)"*, page 16, 2012. [152](#)
- H. A. Krimm, S. T. Holland, R. H. D. Corbet, et al. The swift/bat hard x-ray transient monitor. *The Astrophysical Journal Supplement Series*, 209(1):14, 2013. [136](#)
- T. Krühler, A. Küpcü Yoldaş, J. Greiner, et al. The 2175 Å Dust Feature in a Gamma-Ray Burst Afterglow at Redshift 2.45. *Astrophysical Journal*, 685:376–383, September 2008. doi: 10.1086/590240. [119](#)
- M. Kuehnel, M. H. Finger, F. Fuerst, et al. Orbital parameters and spin evolution of RX J0520.5-6932. *The Astronomer's Telegram*, 5856:1, February 2014. [92](#), [93](#)
- R. L. Kurucz. Model atmospheres for G, F, A, B, and O stars. *Astrophysical Journal Suppl. Ser.*, 40:1–340, May 1979. doi: 10.1086/190589. [119](#)
- N. La Palombara and S. Mereghetti. XMM-Newton observation of the Be/neutron star system RX J0146.9+6121: a soft X-ray excess in a low luminosity accreting pulsar. *Astronomy & Astrophysics*, 455:283–289, August 2006. doi: 10.1051/0004-6361:20065107. [15](#), [18](#), [55](#), [80](#)
- N. La Palombara, L. Sidoli, P. Esposito, A. Tiengo, and S. Mereghetti. XMM-Newton observation of the persistent Be/NS X-ray binary pulsar RX J1037.5-5647 in a low luminosity state. *Astronomy & Astrophysics*, 505:947–954, October 2009. doi: 10.1051/0004-6361/200912538. [80](#)
- N. La Palombara, S. Mereghetti, L. Sidoli, A. Tiengo, and P. Esposito. The Hot-blackbody Spectral Excess in Low-luminosity High-Mass X-Ray Binaries. *Central European Astrophysical Bulletin*, 37:277–282, 2013a. [152](#)
- N. La Palombara, S. Mereghetti, L. Sidoli, A. Tiengo, and P. Esposito. Blackbody excess in persistent Be pulsars. *MmSAI*, 84:626, 2013b. [124](#), [125](#), [152](#)
- N. La Palombara, S. Mereghetti, L. Sidoli, A. Tiengo, and P. Esposito. Blackbody excess in persistent Be pulsars. *ArXiv e-prints*, January 2013c. [80](#), [91](#), [116](#)
- N. La Palombara, L. Sidoli, F. Pintore, et al. Spectral analysis of SMC X-2 during its 2015 outburst. *Monthly Notices of the Royal Astronomical Society*, 458:L74–L78, May 2016. doi: 10.1093/mnras/rlw020. [139](#)

## REFERENCES

---

- D. Lai. Theory of Disk Accretion onto Magnetic Stars. In *European Physical Journal Web of Conferences*, volume 64 of *European Physical Journal Web of Conferences*, page 01001, January 2014. doi: 10.1051/epjconf/20136401001. [9](#), [177](#)
- J. B. Lamb, M. S. Oey, D. M. Segura-Cox, et al. The Runaways and Isolated O-Type Star Spectroscopic Survey of the SMC (RIOTS4). *Astrophysical Journal*, 817:113, February 2016. doi: 10.3847/0004-637X/817/2/113. [143](#)
- G. Lanzuisi, G. Ponti, M. Salvato, et al. Active Galactic Nucleus X-Ray Variability in the XMM-COSMOS Survey. *Astrophysical Journal*, 781:105, February 2014. doi: 10.1088/0004-637X/781/2/105. [50](#)
- S. Larsson. Parameter estimation in epoch folding analysis. *Astronomy & Astrophysics Supplement*, 117:197–201, May 1996. [28](#), [52](#), [114](#), [128](#), [146](#)
- J.-P. Lasota. The disc instability model of dwarf novae and low-mass X-ray binary transients. *NAR*, 45:449–508, June 2001. doi: 10.1016/S1387-6473(01)00112-9. [5](#)
- R. M. Lau, M. M. Kasliwal, H. E. Bond, et al. Rising from the Ashes: Mid-infrared Re-brightening of the Impostor SN 2010da in NGC 300. *Astrophysical Journal*, 830:142, October 2016. doi: 10.3847/0004-637X/830/2/142. [185](#), [189](#)
- S. Laycock, R. Cappallo, K. Oram, and A. Balchunas. A Transient Supergiant X-Ray Binary in IC 10: An Extragalactic SFXT? *Astrophysical Journal*, 789:64, July 2014. doi: 10.1088/0004-637X/789/1/64. [8](#)
- D. A. Leahy, W. Darbro, R. F. Elsner, et al. On searches for pulsed emission with application to four globular cluster X-ray sources - NGC 1851, 6441, 6624, and 6712. *Astrophysical Journal*, 266:160–170, March 1983a. doi: 10.1086/160766. [114](#)
- D. A. Leahy, R. F. Elsner, and M. C. Weiskopf. On searches for periodic pulsed emission - The Rayleigh test compared to epoch folding. *Astrophysical Journal*, 272:256–258, September 1983b. doi: 10.1086/161288. [29](#), [186](#)
- D. J. Lennon. Revised spectral types for 64 B-supergiants in the Small Magellanic Cloud: metallicity effects. *Astronomy & Astrophysics*, 317:871–882, February 1997. [76](#)
- X.-D. Li and E. P. J. van den Heuvel. Could 2S 0114+650 Be a Magnetar? *Astrophysical Journal Letters*, 513:L45–L48, March 1999. doi: 10.1086/311904. [45](#)
- Q. Z. Liu, J. van Paradijs, and E. P. J. van den Heuvel. High-mass X-ray binaries in the Magellanic Clouds. *Astronomy & Astrophysics*, 442:1135–1138, November 2005. doi: 10.1051/0004-6361:20053718. [35](#)
- J. Lodenquai, V. Canuto, M. Ruderman, and S. Tsuruta. Photon Opacity in Surfaces of Magnetic Neutron Stars. *Astrophysical Journal*, 190:141–152, May 1974. doi: 10.1086/152858. [140](#)
- W. Luangtip, T. P. Roberts, and C. Done. The X-ray spectral evolution of the ultra-luminous X-ray source Holmberg IX X-1. *Monthly Notices of the Royal Astronomical Society*, 460:4417–4432, August 2016. doi: 10.1093/mnras/stw1282. [183](#)
- A. A. Lutovinov, S. S. Tsygankov, R. A. Krivonos, S. V. Molkov, and J. Poutanen. Propeller Effect in the Transient X-Ray Pulsar SMC X-2. *Astrophysical Journal*, 834:209, January 2017. doi: 10.3847/1538-4357/834/2/209. [138](#), [139](#), [153](#)
- Y. É. Lyubarskii. Saturated comptonization in a superstrong magnetic field. *Astrophysics*, 25:577–586, September 1986. doi: 10.1007/BF01006289. [16](#)
- Y. E. Lyubarskii and R. A. Syunyaev. Accretion Column Structure. *Soviet Astronomy Letters*, 14:390, September 1988. [16](#), [17](#)

- P. Maggi, F. Haberl, R. Sturm, et al. Discovery of a 168.8 s X-ray pulsar transiting in front of its Be companion star in the Large Magellanic Cloud. *Astronomy & Astrophysics*, 554:A1, June 2013. doi: 10.1051/0004-6361/201321238. 123
- P. Maggi, F. Haberl, P. J. Kavanagh, et al. The population of X-ray supernova remnants in the Large Magellanic Cloud. *Astronomy & Astrophysics*, 585:A162, January 2016. doi: 10.1051/0004-6361/201526932. 26
- C. Maitra and B. Paul. Pulse-phase-dependent Variations of the Cyclotron Absorption Features of the Accreting Pulsars A0535+26, XTE J1946+274, and 4U 1907+09 with Suzaku. *Astrophysical Journal*, 771:96, July 2013. doi: 10.1088/0004-637X/771/2/96. 182
- K. Makishima, A. Kubota, T. Mizuno, et al. The Nature of Ultraluminous Compact X-Ray Sources in Nearby Spiral Galaxies. *Astrophysical Journal*, 535:632–643, June 2000. doi: 10.1086/308868. 8
- G. Maravelias, A. Zezas, V. Antoniou, and D. Hatzidimitriou. Optical spectra of five new Be/X-ray binaries in the Small Magellanic Cloud and the link of the supergiant B[e] star LHA 115-S 18 with an X-ray source. *Monthly Notices of the Royal Astronomical Society*, 438:2005–2025, March 2014. doi: 10.1093/mnras/stt2302. 47
- C. B. Markwardt. Non-linear Least-squares Fitting in IDL with MPFIT. In D. A. Bohlender, D. Durand, and P. Dowler, editors, *Astronomical Data Analysis Software and Systems XVIII*, volume 411 of *Astronomical Society of the Pacific Conference Series*, page 251, September 2009. 149
- P. Massey. A UBVR CCD Survey of the Magellanic Clouds. *Astrophysical Journal Suppl. Ser.*, 141:81–122, July 2002. doi: 10.1086/338286. 50
- S. Mateos, A. Alonso-Herrero, F. J. Carrera, et al. Using the Bright Ultra-hard XMM-Newton survey to define an IR selection of luminous AGN based on WISE colours. *Monthly Notices of the Royal Astronomical Society*, 426:3271–3281, November 2012. doi: 10.1111/j.1365-2966.2012.21843.x. 51
- J. S. Mathis, W. Rumpl, and K. H. Nordsieck. The size distribution of interstellar grains. *Astrophysical Journal*, 217:425–433, October 1977. doi: 10.1086/155591. 14
- V. A. McBride, M. J. Coe, I. Negueruela, M. P. E. Schurch, and K. E. McGowan. Spectral distribution of Be/X-ray binaries in the Small Magellanic Cloud. *Monthly Notices of the Royal Astronomical Society*, 388:1198–1204, August 2008. doi: 10.1111/j.1365-2966.2008.13410.x. 157, 167
- V. A. McBride, A. González-Galán, A. J. Bird, et al. Confirmation of six Be X-ray binaries in the Small Magellanic Cloud. *Monthly Notices of the Royal Astronomical Society*, 467:1526–1530, May 2017. doi: 10.1093/mnras/stx181. 59, 143, 150, 151
- M. Meixner, K. D. Gordon, R. Indebetouw, et al. Spitzer Survey of the Large Magellanic Cloud: Surveying the Agents of a Galaxy’s Evolution (SAGE). I. Overview and Initial Results. *Astronomical Journal*, 132:2268–2288, December 2006. doi: 10.1086/508185. 76
- R. E. Mennickent, Z. Kołaczkowski, I. Soszyński, M. Cabezas, and H. Garrido. The SMC B-type supergiant AzV322: a g-mode pulsator with a circumstellar disc. *ArXiv e-prints*, October 2017. 58
- P. Mészáros. *High-energy radiation from magnetized neutron stars*. 1992. 16, 108, 139, 140, 149
- P. Meszaros and W. Nagel. X-ray pulsar models. II - Comptonized spectra and pulse shapes. *Astrophysical Journal*, 299:

## REFERENCES

---

- 138–153, December 1985. doi: 10.1086/163687. [6](#)
- N. Meyssonier and M. Azzopardi. A New Catalogue of H-Alpha Emission Line Stars and Small Nebulae in the Small Magellanic Cloud. *Astronomy & Astrophysics Supplement*, 102:451, December 1993. [128](#)
- M. J. Middleton, J. C. A. Miller-Jones, and R. P. Fender. The low or retrograde spin of the first extragalactic microquasar: implications for Blandford-Znajek powering of jets. *Monthly Notices of the Royal Astronomical Society*, 439:1740–1748, April 2014. doi: 10.1093/mnras/stu056. [189](#)
- T. Mihara. *Observational study of X-ray spectra of binary pulsars with Ginga*. PhD thesis, , Dept. of Physics, Univ. of Tokyo (M95), (1995), 1995. [179](#)
- K. A. Misselt, G. C. Clayton, and K. D. Gordon. A Reanalysis of the Ultraviolet Extinction from Interstellar Dust in the Large Magellanic Cloud. *Astrophysical Journal*, 515:128–139, April 1999. doi: 10.1086/307010. [119](#)
- D. G. Monet, S. E. Levine, B. Canzian, et al. The USNO-B Catalog. *Astronomical Journal*, 125:984–993, February 2003. doi: 10.1086/345888. [119](#)
- Jorge J. Moré. *The Levenberg-Marquardt algorithm: Implementation and theory*, pages 105–116. Springer Berlin Heidelberg, Berlin, Heidelberg, 1978. ISBN 978-3-540-35972-2. doi: 10.1007/BFb0067700. [149](#)
- Jorge J. Moré and Stephen J. Wright. *Optimization Software Guide*. Society for Industrial & Applied Mathematics (SIAM), jan 1993. doi: 10.1137/1.9781611970951. [149](#)
- W. W. Morgan, P. C. Keenan, and E. Kellman. *An atlas of stellar spectra, with an outline of spectral classification*. 1943. [76](#)
- H. Müller and B. D. Serot. Relativistic mean-field theory and the high-density nuclear equation of state. *Nuclear Physics A*, 606:508–537, February 1996. doi: 10.1016/0375-9474(96)00187-X. [154](#)
- S. Müller, C. Ferrigno, M. Kühnel, et al. No anticorrelation between cyclotron line energy and X-ray flux in 4U 0115+634. *Astronomy & Astrophysics*, 551:A6, March 2013. doi: 10.1051/0004-6361/201220359. [182](#)
- A. A. Mushtukov, J. Poutanen, V. F. Suleimanov, et al. On the origin of cyclotron lines in the spectra of X-ray pulsars. In *European Physical Journal Web of Conferences*, volume 64 of *European Physical Journal Web of Conferences*, page 02005, January 2014. doi: 10.1051/epjconf/20136402005. [183](#)
- A. A. Mushtukov, V. F. Suleimanov, S. S. Tsygankov, and J. Poutanen. The critical accretion luminosity for magnetized neutron stars. *Monthly Notices of the Royal Astronomical Society*, 447:1847–1856, February 2015a. doi: 10.1093/mnras/stu2484. [140](#), [149](#), [180](#)
- A. A. Mushtukov, V. F. Suleimanov, S. S. Tsygankov, and J. Poutanen. On the maximum accretion luminosity of magnetized neutron stars: connecting X-ray pulsars and ultraluminous X-ray sources. *Monthly Notices of the Royal Astronomical Society*, 454:2539–2548, December 2015b. doi: 10.1093/mnras/stv2087. [11](#), [17](#), [97](#), [140](#), [149](#), [155](#), [170](#)
- A. A. Mushtukov, V. F. Suleimanov, S. S. Tsygankov, and A. Ingram. Optically thick envelopes around ULXs powered by accreting neutron stars. *Monthly Notices of the Royal Astronomical Society*, 467:1202–1208, May 2017a. doi: 10.1093/mnras/stx141. [177](#), [178](#)
- A. A. Mushtukov, V. F. Suleimanov, S. S. Tsygankov, and A. Ingram. Optically thick envelopes around ULXs powered by

- accreting neutron stars. *Monthly Notices of the Royal Astronomical Society*, January 2017b. doi: 10.1093/mnras/stx141. [171](#), [181](#), [184](#)
- H. Müther, M. Prakash, and T. L. Ainsworth. The nuclear symmetry energy in relativistic Brueckner-Hartree-Fock calculations. *Physics Letters B*, 199:469–474, December 1987. doi: 10.1016/0370-2693(87)91611-X. [154](#)
- W. Nagel. Radiative Transfer in a Strongly Magnetized Plasma - Part Two - Effects of Comptonization. *Astrophysical Journal*, 251:288, December 1981. doi: 10.1086/159464. [6](#), [16](#), [108](#), [168](#)
- H. Negoro, M. Nakajima, N. Kawai, et al. MAXI/GSC detection of a hard X-ray transient MAXI J0058-721 in the SMC. *The Astronomer's Telegram*, 9348, August 2016. [167](#)
- I. Negueruela, D. M. Smith, P. Reig, S. Chaty, and J. M. Torrejón. Super-giant Fast X-ray Transients: A New Class of High Mass X-ray Binaries Unveiled by INTEGRAL. In A. Wilson, editor, *The X-ray Universe 2005*, volume 604 of *ESA Special Publication*, page 165, January 2006. [7](#), [57](#), [60](#)
- R. W. Nelson, J. C. L. Wang, E. E. Salpeter, and I. Wasserman. A potential cyclotron line signature in low-luminosity X-ray sources. *Astrophysical Journal Letters*, 438:L99–L102, January 1995. doi: 10.1086/187725. [139](#)
- R. W. Nelson, L. Bildsten, D. Chakrabarty, et al. On the Dramatic Spin-up/Spin-down Torque Reversals in Accreting Pulsars. *Astrophysical Journal Letters*, 488: L117–L120, October 1997. doi: 10.1086/310936. [187](#)
- A. T. Okazaki. Long-term V/R variations of Be stars due to global one-armed oscillations of equatorial disks. *Publications of the Astronomical Society of Japan*, 43: 75–94, February 1991. [93](#)
- A. T. Okazaki and I. Negueruela. A natural explanation for periodic X-ray outbursts in Be/X-ray binaries. *Astronomy & Astrophysics*, 377:161–174, October 2001. doi: 10.1051/0004-6361:20011083. [93](#)
- A. T. Okazaki, K. Hayasaki, and Y. Moritani. Origin of Two Types of X-Ray Outbursts in Be/X-Ray Binaries. I. Accretion Scenarios. *Publications of the Astronomical Society of Japan*, 65:41, April 2013. [7](#), [67](#)
- L. M. Oskinova, A. Feldmeier, and P. Kretschmar. Clumped stellar winds in supergiant high-mass X-ray binaries: X-ray variability and photoionization. *Monthly Notices of the Royal Astronomical Society*, 421:2820–2831, April 2012. doi: 10.1111/j.1365-2966.2012.20507.x. [8](#)
- F. Özel and P. Freire. Masses, Radii, and the Equation of State of Neutron Stars. *Ann. Rev. Astron. Astrophys.*, 54: 401–440, September 2016. doi: 10.1146/annurev-astro-081915-023322. [154](#), [199](#)
- F. Özel, D. Psaltis, Z. Arzoumanian, S. Morsink, and M. Bauböck. Measuring Neutron Star Radii via Pulse Profile Modeling with NICER. *Astrophysical Journal*, 832:92, November 2016. doi: 10.3847/0004-637X/832/1/92. [154](#)
- A. Paizis and L. Sidoli. Cumulative luminosity distributions of supergiant fast X-ray transients in hard X-rays. *Monthly Notices of the Royal Astronomical Society*, 439:3439–3452, April 2014. doi: 10.1093/mnras/stu191. [63](#), [64](#)
- I. E. Papadakis and A. Lawrence. Improved Methods for Power Spectrum Modelling of Red Noise. *Monthly Notices of the Royal Astronomical Society*, 261:612, April 1993. doi: 10.1093/mnras/261.3.612. [52](#)
- G. Pappas and T. A. Apostolatos. Effectively Universal Behavior of Rotating Neutron Stars in General Relativity Makes Them Even Simpler than Their Newtonian Counterparts. *Physical Review*

## REFERENCES

---

- Letters*, 112(12):121101, March 2014. doi: 10.1103/PhysRevLett.112.121101. [97](#)
- K. Parfrey and A. Tchekhovskoy. General-relativistic Simulations of Four States of Accretion onto Millisecond Pulsars. *Astrophysical Journal Letters*, 851:L34, December 2017. doi: 10.3847/2041-8213/aa9c85. [10](#), [11](#), [106](#), [175](#), [179](#)
- K. Parfrey, D. Giannios, and A. M. Beloborodov. Black hole jets without large-scale net magnetic flux. *Monthly Notices of the Royal Astronomical Society*, 446:L61–L65, January 2015. doi: 10.1093/mnras/slul62. [189](#)
- K. Parfrey, A. Spitkovsky, and A. M. Beloborodov. Torque Enhancement, Spin Equilibrium, and Jet Power from Disk-Induced Opening of Pulsar Magnetic Fields. *Astrophysical Journal*, 822:33, May 2016a. doi: 10.3847/0004-637X/822/1/33. [9](#), [186](#)
- K. Parfrey, A. Spitkovsky, and A. M. Beloborodov. Simulations of the magnetospheres of accreting millisecond pulsars. *ArXiv e-prints*, August 2016b. [175](#)
- K. Parfrey, A. Spitkovsky, and A. M. Beloborodov. Simulations of the magnetospheres of accreting millisecond pulsars. *Monthly Notices of the Royal Astronomical Society*, 469:3656–3669, August 2017. doi: 10.1093/mnras/stx950. [6](#), [12](#)
- B. Paul, P. C. Agrawal, A. R. Rao, and R. K. Manchanda. A double peaked pulse profile observed in GX 1 + 4. *Bulletin of the Astronomical Society of India*, 24:729, December 1996. [108](#)
- B. Paul, P. C. Agrawal, A. R. Rao, and R. K. Manchanda. A double peaked pulse profile observed in GX 1+4. *Astronomy & Astrophysics*, 319:507–510, March 1997. [16](#), [108](#), [140](#)
- B. Paxton, L. Bildsten, A. Dotter, et al. Modules for Experiments in Stellar Astrophysics (MESA). *Astrophysical Journal Suppl. Ser.*, 192:3, January 2011. doi: 10.1088/0067-0049/192/1/3. [58](#)
- J. A. Petterson. Hercules X-1 - A neutron star with a twisted accretion disk. *Astrophysical Journal Letters*, 201:L61–L64, October 1975. doi: 10.1086/181942. [189](#)
- G. Pietrzyński, D. Graczyk, W. Gieren, et al. An eclipsing-binary distance to the Large Magellanic Cloud accurate to two per cent. *Nature*, 495:76–79, March 2013. doi: 10.1038/nature11878. [21](#), [54](#), [57](#), [118](#)
- W. Pietsch, Z. Misanovic, F. Haberl, et al. XMM-Newton survey of the Local Group galaxy <ASTROBJ>M 33</ASTROBJ>. *Astronomy & Astrophysics*, 426:11–24, October 2004. doi: 10.1051/0004-6361:20047068. [26](#)
- W. Pietsch, M. Freyberg, and F. Haberl. An XMM-Newton survey of M 31. *Astronomy & Astrophysics*, 434:483–496, May 2005. doi: 10.1051/0004-6361:20041990. [26](#)
- F. Pintore, L. Zampieri, L. Stella, et al. Pulsator-like Spectra from Ultraluminous X-Ray Sources and the Search for More Ultraluminous Pulsars. *Astrophysical Journal*, 836:113, February 2017. doi: 10.3847/1538-4357/836/1/113. [177](#)
- B. Popescu, M. M. Hanson, and B. G. Elmegreen. Age and Mass for 920 Large Magellanic Cloud Clusters Derived from 100 Million Monte Carlo Simulations. *Astrophysical Journal*, 751:122, June 2012. doi: 10.1088/0004-637X/751/2/122. [94](#)
- D. Porquet and J. Dubau. X-ray photoionized plasma diagnostics with helium-like ions. Application to warm absorber-emitter in active galactic nuclei. *Astronomy & Astrophysics Supplement*, 143:495–514, May 2000. doi: 10.1051/aas:2000192. [139](#)
- J. M. Porter and T. Rivinius. Classical Be Stars. *PASP*, 115:1153–1170, October 2003. doi: 10.1086/378307. [7](#)

- K. A. Postnov, M. I. Gornostaev, D. Klochkov, et al. On the dependence of the X-ray continuum variations with luminosity in accreting X-ray pulsars. *Monthly Notices of the Royal Astronomical Society*, 452:1601–1611, September 2015a. doi: 10.1093/mnras/stv1393. [16](#), [18](#), [171](#)
- K. A. Postnov, A. I. Mironov, A. A. Lutovinov, et al. Spin-up/spin-down of neutron star in Be-X-ray binary system GX 304-1. *Monthly Notices of the Royal Astronomical Society*, 446:1013–1019, January 2015b. doi: 10.1093/mnras/stu2155. [6](#)
- K. Pottschmidt, R. Ballhausen, J. Wilms, et al. NuSTAR Observations of SMC X-3. *The Astronomer's Telegram*, 9404, August 2016. [167](#)
- J. Poutanen and M. Gierliński. On the nature of the X-ray emission from the accreting millisecond pulsar SAX J1808.4-3658. *Monthly Notices of the Royal Astronomical Society*, 343:1301–1311, August 2003. doi: 10.1046/j.1365-8711.2003.06773.x. [154](#)
- J. Poutanen, G. Lipunova, S. Fabrika, A. G. Butkevich, and P. Abolmasov. Supercritically accreting stellar mass black holes as ultraluminous X-ray sources. *Monthly Notices of the Royal Astronomical Society*, 377:1187–1194, May 2007. doi: 10.1111/j.1365-2966.2007.11668.x. [8](#), [176](#)
- J. Poutanen, A. A. Mushtukov, V. F. Suleimanov, et al. A Reflection Model for the Cyclotron Lines in the Spectra of X-Ray Pulsars. *Astrophysical Journal*, 777:115, November 2013. doi: 10.1088/0004-637X/777/2/115. [17](#), [18](#), [152](#), [170](#)
- P. Pradhan, B. Paul, and E. Bozzo. SFXTs vs sgHMXBs: does the difference lie in the companion wind? In M. Serino, M. Shidatsu, W. Iwakiri, and T. Mihara, editors, *7 years of MAXI: monitoring X-ray Transients, held 5-7 December 2016 at RIKEN.*, page 163, 2017. [8](#)
- M. Prakash, J. R. Cooke, and J. M. Lattimer. Quark-hadron phase transition in protoneutron stars. *Physical Review D*, 52:661–665, July 1995. doi: 10.1103/PhysRevD.52.661. [154](#)
- A. F. Rajoelimanana, P. A. Charles, and A. Udalski. Very long-term optical variability of high-mass X-ray binaries in the Small Magellanic Cloud. *Monthly Notices of the Royal Astronomical Society*, 413:1600–1622, May 2011. doi: 10.1111/j.1365-2966.2011.18243.x. [30](#), [59](#), [90](#), [93](#), [104](#), [121](#), [123](#), [124](#), [125](#), [199](#)
- N. Rea, G. L. Israel, T. Di Salvo, L. Burderi, and G. Cocozza. Timing and spectral changes of the Be X-ray transient EXO 0531-6609.2 through high and low state. *Astronomy & Astrophysics*, 421:235–239, July 2004. doi: 10.1051/0004-6361:20035685. [16](#), [108](#), [140](#), [149](#)
- P. Reig. Be/X-ray binaries. *Astrophysics and Space Science*, 332:1–29, March 2011. doi: 10.1007/s10509-010-0575-8. [5](#)
- P. Reig and J. Fabregat. Long-term variability of high-mass X-ray binaries. I. Photometry. *Astronomy & Astrophysics*, 574:A33, February 2015. doi: 10.1051/0004-6361/201425008. [138](#)
- P. Reig, A. Słowikowska, A. Zezas, and P. Blay. Correlated optical/X-ray variability in the high-mass X-ray binary SAX J2103.5+4545. *Monthly Notices of the Royal Astronomical Society*, 401:55–66, January 2010. doi: 10.1111/j.1365-2966.2009.15656.x. [59](#), [138](#)
- P. Reig, J. M. Torrejón, and P. Blay. Accreting magnetars: a new type of high-mass X-ray binaries? *Monthly Notices of the Royal Astronomical Society*, 425:595–604, September 2012. doi: 10.1111/j.1365-2966.2012.21509.x. [80](#)
- O.-G. Richter, G. A. Tammann, and W. K. Huchtmeier. H I observations of galaxies in a catalog of nearby galaxies. II - The motion of the sun and the galaxy and the

## REFERENCES

---

- velocity dispersion of 'field' galaxies. *Astronomy & Astrophysics*, 171:33–40, January 1987. [70](#), [104](#), [106](#)
- M. S. Riquelme, J. M. Torrejón, and I. Negueruela. Circumstellar emission in Be/X-ray binaries of the Magellanic Clouds and the Milky Way. *Astronomy & Astrophysics*, 539:A114, March 2012. doi: 10.1051/0004-6361/201117738. [59](#)
- T. P. Roberts, M. J. Middleton, A. D. Sutton, et al. ULX behaviour: The ultraluminous state, winds and interesting anomalies. *Astronomische Nachrichten*, 337:534, May 2016. doi: 10.1002/asna.201612343. [176](#)
- W. R. J. Rolleston, C. Trundle, and P. L. Dufton. The present-day chemical composition of the LMC. *Astronomy & Astrophysics*, 396:53–64, December 2002. doi: 10.1051/0004-6361:20021088. [62](#), [71](#), [86](#), [98](#), [115](#)
- S. R. Rosen, N. A. Webb, M. G. Watson, et al. The XMM-Newton serendipitous survey. VII. The third XMM-Newton serendipitous source catalogue. *Astronomy & Astrophysics*, 590:A1, May 2016. doi: 10.1051/0004-6361/201526416. [26](#)
- S. C. Russell and M. A. Dopita. Abundances of the heavy elements in the Magellanic Clouds. III - Interpretation of results. *Astrophysical Journal*, 384:508–522, January 1992. doi: 10.1086/170893. [148](#)
- G. B. Rybicki and A. P. Lightman. *Radiative processes in astrophysics*. 1979. [12](#), [180](#)
- N. Sanduleak. A deep objective-prism survey for Large Magellanic Cloud members. *Contributions from the Cerro Tololo Inter-American Observatory*, 89, 1970. [51](#)
- M. Sasaki, D. Müller, U. Kraus, C. Ferrigno, and A. Santangelo. Analysing X-ray pulsar profiles. Geometry and beam pattern of 4U 0115+63 and V 0332+53. *Astronomy & Astrophysics*, 540:A35, April 2012. doi: 10.1051/0004-6361/201016304. [140](#), [149](#)
- G. J. Savonije and E. P. J. van den Heuvel. On the rotational history of the pulsars in massive X-ray binaries. *Astrophysical Journal Letters*, 214:L19–L22, May 1977. doi: 10.1086/182433. [79](#), [94](#)
- R. D. Saxton, A. M. Read, P. Esquej, et al. The first XMM-Newton slew survey catalogue: XMMSL1. *Astronomy & Astrophysics*, 480:611–622, March 2008. doi: 10.1051/0004-6361:20079193. [111](#)
- S. Sazonov, E. Churazov, M. Revnivtsev, A. Vikhlinin, and R. Sunyaev. Identification of 8 INTEGRAL hard X-ray sources with Chandra. *Astronomy & Astrophysics*, 444:L37–L40, December 2005. doi: 10.1051/0004-6361:200500205. [111](#)
- J. D. Scargle. Studies in astronomical time series analysis. II - Statistical aspects of spectral analysis of unevenly spaced data. *Astrophysical Journal*, 263:835–853, December 1982. doi: 10.1086/160554. [29](#), [60](#), [79](#), [89](#), [114](#), [135](#)
- E. F. Schlafly and D. P. Finkbeiner. Measuring Reddening with Sloan Digital Sky Survey Stellar Spectra and Recalibrating SFD. *Astrophysical Journal*, 737:103, August 2011. doi: 10.1088/0004-637X/737/2/103. [119](#)
- P. C. Schmidtke, A. P. Cowley, L. M. Frattare, et al. LMC stellar X-ray sources observed with ROSAT. 1: X-ray data and search for optical counterparts. *PASP*, 106:843–857, August 1994. doi: 10.1086/133452. [83](#), [89](#)
- P. C. Schmidtke, A. P. Cowley, and A. Udalski. An analysis of optical periods in individual Small Magellanic Cloud Be/X-ray pulsars. *Monthly Notices of the Royal Astronomical Society*, 431:252–278, May 2013. doi: 10.1093/mnras/stt159. [7](#), [30](#), [59](#)
- G. Schönherr, J. Wilms, P. Kretschmar, et al. A model for cyclotron resonance scattering features. *Astronomy & Astrophysics*, 472:353–365, September 2007a.

- doi: 10.1051/0004-6361:20077218. [139](#), [140](#)
- G. Schönherr, J. Wilms, P. Kretschmar, et al. A model for cyclotron resonance scattering features. *Astronomy & Astrophysics*, 472:353–365, September 2007b. doi: 10.1051/0004-6361:20077218. [16](#)
- M. Schulz and M. Mudelsee. REDFIT: estimating red-noise spectra directly from unevenly spaced paleoclimatic time series. *Computers and Geosciences*, 28:421–426, April 2002. doi: 10.1016/S0098-3004(01)00044-9. [121](#)
- M. Schurch, A. Udalski, and M. Coe. OGLE-III counterpart to SMC X-2 reveals 18.62 day binary period. *The Astronomer's Telegram*, 1670, August 2008. [157](#)
- V. Scowcroft, W. L. Freedman, B. F. Madore, et al. The Carnegie Hubble Program: The Distance and Structure of the SMC as Revealed by Mid-infrared Observations of Cepheids. *Astrophysical Journal*, 816:49, January 2016. doi: 10.3847/0004-637X/816/2/49. [130](#)
- N. J. Secrest, R. P. Dudik, B. N. Dorland, et al. Identification of 1.4 Million Active Galactic Nuclei in the Mid-Infrared using WISE Data. *Astrophysical Journal Suppl. Ser.*, 221:12, November 2015. doi: 10.1088/0067-0049/221/1/12. [51](#)
- V. Sguera, L. Ducci, L. Sidoli, A. Bazzano, and L. Bassani. XMM-Newton and INTEGRAL study of the SFXT IGR J18483-0311 in quiescence: hint of a cyclotron emission feature? *Monthly Notices of the Royal Astronomical Society*, 402:L49–L53, February 2010. doi: 10.1111/j.1745-3933.2009.00798.x. [139](#)
- N. Shakura and K. Postnov. Wind Accretion - Observations Vs Theory. *ArXiv e-prints*, February 2017. [61](#), [62](#)
- N. Shakura, K. Postnov, A. Kochetkova, and L. Hjalmarsdotter. Theory of quasi-spherical accretion in X-ray pulsars. *Monthly Notices of the Royal Astronomical Society*, 420:216–236, February 2012. doi: 10.1111/j.1365-2966.2011.20026.x. [8](#), [45](#), [61](#), [62](#), [63](#), [188](#)
- N. Shakura, K. Postnov, L. Sidoli, and A. Paizis. Bright flares in supergiant fast X-ray transients. *Monthly Notices of the Royal Astronomical Society*, 442:2325–2330, August 2014. doi: 10.1093/mnras/stu1027. [62](#), [63](#), [64](#)
- N. I. Shakura and R. A. Sunyaev. Black holes in binary systems. Observational appearance. *Astronomy & Astrophysics*, 24:337–355, 1973. [12](#), [107](#), [176](#)
- J. M. Shull and M. van Steenberg. The ionization equilibrium of astrophysically abundant elements. *Astrophysical Journal Suppl. Ser.*, 48:95–107, January 1982. doi: 10.1086/190769. [107](#)
- N. R. Sibgatullin and R. A. Sunyaev. Energy Release During Disk Accretion onto a Rapidly Rotating Neutron Star. *Astronomy Letters*, 26:699–724, November 2000. doi: 10.1134/1.1323277. [12](#), [122](#), [168](#)
- L. Sidoli. Supergiant Fast X-ray Transients - a short review. *ArXiv e-prints*, October 2017. [7](#)
- L. Sidoli, S. Mereghetti, V. Sguera, and F. Pizzolato. The XMM-Newton view of supergiant fast X-ray transients: the case of IGR J16418-4532. *Monthly Notices of the Royal Astronomical Society*, 420:554–561, February 2012. doi: 10.1111/j.1365-2966.2011.20063.x. [60](#)
- L. Sidoli, G. L. Israel, P. Esposito, G. A. Rodríguez Castillo, and K. Postnov. AX J1910.7+0917: the slowest X-ray pulsar. *Monthly Notices of the Royal Astronomical Society*, 469:3056–3061, August 2017a. doi: 10.1093/mnras/stx1105. [44](#), [45](#), [62](#)
- L. Sidoli, A. Tiengo, A. Paizis, et al. XMM-Newton and NuSTAR Simultaneous X-Ray Observations of IGR J11215-5952. *Astrophysical Journal*, 838:133,

## REFERENCES

---

- April 2017b. doi: 10.3847/1538-4357/aa671a. [55](#), [60](#)
- M. F. Skrutskie, R. M. Cutri, R. Stiening, et al. The Two Micron All Sky Survey (2MASS). *Astronomical Journal*, 131: 1163–1183, February 2006. doi: 10.1086/498708. [27](#), [41](#), [42](#), [74](#), [119](#)
- A. P. Smale, J. Homan, and E. Kuulkers. The Complete Z Diagram of LMC X-2. *Astrophysical Journal*, 590:1035–1040, June 2003. doi: 10.1086/375047. [47](#)
- N. Smirnov. Table for estimating the goodness of fit of empirical distributions. *Ann. Math. Statist.*, 19(2):279–281, 06 1948. doi: 10.1214/aoms/1177730256. [133](#)
- N. Smith. Mass Loss: Its Effect on the Evolution and Fate of High-Mass Stars. *Ann. Rev. Astron. Astrophys.*, 52: 487–528, August 2014. doi: 10.1146/annurev-astro-081913-040025. [189](#)
- H. C. Spruit and R. E. Taam. An instability associated with a magnetosphere-disk interaction. *Astrophysical Journal*, 402:593–604, January 1993. doi: 10.1086/172162. [11](#), [153](#)
- L. Stella, N. E. White, and R. Rosner. Intermittent stellar wind accretion and the long-term activity of Population I binary systems containing an X-ray pulsar. *Astrophysical Journal*, 308:669–679, September 1986. doi: 10.1086/164538. [12](#), [153](#)
- J. B. Stevens, P. Reig, M. J. Coe, et al. Multiwavelength observations of the Be/X-ray binary 4U1145-619. *Monthly Notices of the Royal Astronomical Society*, 288:988–994, July 1997. [76](#)
- H. Stiele, W. Pietsch, F. Haberl, et al. The deep XMM-Newton Survey of M 31. *Astronomy & Astrophysics*, 534:A55, October 2011. doi: 10.1051/0004-6361/201015270. [26](#)
- H. Stiele, W. Yu, and A. K. H. Kong. Millihertz Quasi-periodic Oscillations in 4U 1636-536: Putting Possible Constraints on the Neutron Star Size. *Astrophysical Journal*, 831:34, November 2016. doi: 10.3847/0004-637X/831/1/34. [154](#)
- L. Strüder, U. Briel, K. Dennerl, et al. The European Photon Imaging Camera on XMM-Newton: The pn-CCD camera. *Astronomy & Astrophysics*, 365:L18–L26, January 2001. doi: 10.1051/0004-6361:20000066. [26](#), [48](#), [69](#), [84](#), [127](#), [157](#)
- M. Stuhlinger, B. Altieri, M. P. Esquej, et al. Status of the XMM-Newton Cross-Calibration with SASv6.5.0. In A. Wilson, editor, *The X-ray Universe 2005*, volume 604 of *ESA Special Publication*, page 937, January 2006. [71](#), [86](#), [98](#), [114](#)
- R. Sturm, F. Haberl, M. J. Coe, et al. The XMM-Newton survey of the Small Magellanic Cloud: discovery of the 11.866 s Be/X-ray binary pulsar XMMU J004814.0-732204(SXP11.87). *Astronomy & Astrophysics*, 527:A131, March 2011a. doi: 10.1051/0004-6361/201015798. [91](#)
- R. Sturm, F. Haberl, and W. Pietsch. Swift J053041.9-665426: a new LMC X-ray transient. *The Astronomer’s Telegram*, 3747:1, November 2011b. [69](#), [80](#)
- R. Sturm, F. Haberl, and W. Pietsch. Swift J053041.9-665426 is most likely a Be/X-ray binary. *The Astronomer’s Telegram*, 3753:1, November 2011c. [69](#), [80](#)
- R. Sturm, F. Haberl, W. Pietsch, S. Immler, and A. Udalski. Swift J053321.3-684121 - A candidate HMXB in the LMC. *The Astronomer’s Telegram*, 3993, March 2012. [48](#), [51](#)
- R. Sturm, F. Haberl, W. Pietsch, et al. The XMM-Newton survey of the Small Magellanic Cloud: The X-ray point-source catalogue. *Astronomy & Astrophysics*, 558:A3, October 2013a. doi: 10.1051/0004-6361/201219935. [26](#), [35](#), [51](#), [85](#), [97](#), [113](#), [128](#), [145](#)

- R. Sturm, F. Haberl, W. Pietsch, et al. The XMM-Newton survey of the Small Magellanic Cloud: The X-ray point-source catalogue. *ArXiv e-prints*, July 2013b. [71](#)
- R. Sturm, S. Carpano, F. Haberl, P. Maggi, and G. Vasilopoulos. Swift J0513.4-6547 in outburst. *The Astronomer's Telegram*, 6483, September 2014a. [36](#)
- R. Sturm, F. Haberl, G. Vasilopoulos, et al. Discovery of SXP 265, a Be/X-ray binary pulsar in the Wing of the Small Magellanic Cloud. *Monthly Notices of the Royal Astronomical Society*, 444:3571–3580, November 2014b. doi: 10.1093/mnras/stu1680. [59](#), [60](#), [152](#)
- M. Sugizaki, T. Mihara, M. Nakajima, and K. Makishima. Correlation between the luminosity and spin-period changes during outbursts of 12 Be binary pulsars observed by the MAXI/GSC and the Fermi/GBM. *Publications of the Astronomical Society of Japan*, 69:100, December 2017. doi: 10.1093/pasj/psx119. [6](#)
- R. A. Sunyaev and L. G. Titarchuk. Comptonization of X-rays in plasma clouds - Typical radiation spectra. *Astronomy & Astrophysics*, 86:121–138, June 1980. [131](#), [133](#)
- A. D. Sutton, T. P. Roberts, and M. J. Middleton. The ultraluminous state revisited: fractional variability and spectral shape as diagnostics of super-Eddington accretion. *Monthly Notices of the Royal Astronomical Society*, 435:1758–1775, October 2013. doi: 10.1093/mnras/stt1419. [184](#)
- H. Tananbaum, H. Gursky, E. M. Kellogg, et al. Discovery of a Periodic Pulsating Binary X-Ray Source in Hercules from UHURU. *Astrophysical Journal Letters*, 174:L143, June 1972. doi: 10.1086/180968. [15](#)
- T. M. Tauris, M. Kramer, P. C. C. Freire, et al. Formation of Double Neutron Star Systems. *Astrophysical Journal*, 846:170, September 2017. doi: 10.3847/1538-4357/aa7e89. [5](#)
- J. H. Telting, M. H. M. Heemskerk, H. F. Henrichs, and G. J. Savonije. Observational evidence for a prograde one-armed density structure in the equatorial disc of a Be star. *Astronomy & Astrophysics*, 288: 558–560, August 1994. [105](#), [137](#)
- S. P. Tendulkar, F. Fürst, K. Pottschmidt, et al. NuSTAR Discovery of a Cyclotron Line in the Be/X-Ray Binary RX J0520.5-6932 during Outburst. *Astrophysical Journal*, 795:154, November 2014. doi: 10.1088/0004-637X/795/2/154. [100](#), [106](#), [182](#)
- A. J. Tetarenko, G. R. Sivakoff, J. C. A. Miller-Jones, et al. Extreme jet ejections from the black hole X-ray binary V404 Cygni. *Monthly Notices of the Royal Astronomical Society*, 469:3141–3162, August 2017. doi: 10.1093/mnras/stx1048. [5](#)
- A. Tiengo, P. Esposito, S. Mereghetti, et al. A variable absorption feature in the X-ray spectrum of a magnetar. *Nature*, 500: 312–314, August 2013. doi: 10.1038/nature12386. [183](#)
- J. Timmer and M. Koenig. On generating power law noise. *Astronomy & Astrophysics*, 300:707, August 1995. [52](#)
- J. A. Tomsick, S. Chaty, J. Rodriguez, et al. An XMM-Newton Spectral and Timing Study of IGR J16207 - 5129: An Obscured and Non-Pulsating HMXB. *Astrophysical Journal*, 694:344–353, March 2009. doi: 10.1088/0004-637X/694/1/344. [55](#)
- L. J. Townsend, M. J. Coe, R. H. D. Corbet, and A. B. Hill. On the orbital parameters of Be/X-ray binaries in the Small Magellanic Cloud. *Monthly Notices of the Royal Astronomical Society*, 416:1556–1565, September 2011. doi: 10.1111/j.1365-2966.2011.19153.x. [93](#), [152](#), [157](#), [159](#)

## REFERENCES

---

- L. J. Townsend, J. A. Kennea, M. J. Coe, et al. The 2016 super-Eddington outburst of SMC X-3: X-ray and optical properties and system parameters. *arXiv:1701.02336*, January 2017. [167](#)
- J. E. Trümper, K. Dennerl, N. D. Kylafis, Ü. Ertan, and A. Zezas. An Accretion Model for the Anomalous X-Ray Pulsar 4U 0142+61. *Astrophysical Journal*, 764:49, February 2013. doi: 10.1088/0004-637X/764/1/49. [6](#), [16](#), [17](#), [108](#), [168](#), [171](#)
- S. S. Tsygankov, A. A. Lutovinov, V. Doroshenko, et al. Propeller effect in two brightest transient X-ray pulsars: 4U 0115+63 and V 0332+53. *Astronomy & Astrophysics*, 593:A16, August 2016. doi: 10.1051/0004-6361/201628236. [12](#), [153](#)
- S. S. Tsygankov, V. Doroshenko, A. A. Lutovinov, A. A. Mushtukov, and J. Poutanen. SMC X-3: the closest ultraluminous X-ray source powered by a neutron star with non-dipole magnetic field. *ArXiv e-prints*, February 2017. [139](#), [167](#)
- W. H. Tucker and R. J. Gould. Radiation from a Low-Density Plasma at  $10^6 - 10^8$  K. *Astrophysical Journal*, 144:244, April 1966. doi: 10.1086/148601. [13](#)
- M. J. L. Turner, A. Abbey, M. Arnaud, et al. The European Photon Imaging Camera on XMM-Newton: The MOS cameras : The MOS cameras. *Astronomy & Astrophysics*, 365:L27–L35, January 2001. doi: 10.1051/0004-6361:20000087. [26](#), [48](#), [69](#), [84](#), [127](#), [157](#)
- A. Udalski. The Optical Gravitational Lensing Experiment. Real Time Data Analysis Systems in the OGLE-III Survey. *Acta Astronomica*, 53:291–305, December 2003. [27](#)
- A. Udalski. XROM and RCOM: Two New OGLE-III Real Time Data Analysis Systems. *Acta Astronomica*, 58:187–192, September 2008. [27](#), [60](#), [103](#), [121](#), [135](#), [150](#)
- A. Udalski, M. Szymanski, J. Kaluzny, M. Kubiak, and M. Mateo. The Optical Gravitational Lensing Experiment. *Acta Astronomica*, 42:253–284, 1992. [27](#), [120](#)
- A. Udalski, M. K. Szymanski, I. Soszynski, and R. Poleski. The Optical Gravitational Lensing Experiment. Final Reductions of the OGLE-III Data. *Acta Astronomica*, 58:69–87, June 2008. [27](#)
- A. Udalski, M. K. Szymański, and G. Szymański. OGLE-IV: Fourth Phase of the Optical Gravitational Lensing Experiment. *Acta Astronomica*, 65:1–38, March 2015. [27](#), [59](#), [103](#), [120](#), [127](#), [150](#), [167](#)
- M. A. Urbaneja, R.-P. Kudritzki, W. Gieren, et al. LMC Blue Supergiant Stars and the Calibration of the Flux-weighted Gravity-Luminosity Relationship. *Astronomical Journal*, 154:102, September 2017. doi: 10.3847/1538-3881/aa79a8. [58](#)
- S. Štefl, A. T. Okazaki, T. Rivinius, and D. Baade. V/R Variations of Binary Be Stars. In A. T. Okazaki, S. P. Owocki, and S. Stefl, editors, *Active OB-Stars: Laboratories for Stellare and Circumstellar Physics*, volume 361 of *Astronomical Society of the Pacific Conference Series*, page 274, March 2007. [138](#)
- W. D. Vacca, C. D. Garmany, and J. M. Shull. The Lyman-Continuum Fluxes and Stellar Parameters of O and Early B-Type Stars. *Astrophysical Journal*, 460:914, April 1996. doi: 10.1086/177020. [93](#)
- E. P. J. van den Heuvel, S. F. Portegies Zwart, D. Bhattacharya, and L. Kaper. On the origin of the difference between the runaway velocities of the OB-supergiant X-ray binaries and the Be/X-ray binaries. *Astronomy & Astrophysics*, 364:563–572, December 2000. [80](#), [94](#)
- M. van der Klis. Fourier Techniques in X-ray Timing. In *Timing Neutron Stars*, eds. H. Ogelman and E.P.J. van den Heuvel. *NATO ASI Series C*, Vol. 262, p. 27-70.

- Dordrecht: Kluwer, 1988.*, volume 262, pages 27–70, 1988. [52](#)
- N. van Jaarsveld, D. A. Buckley, V. A. McBride, et al. New High Mass X-ray Binaries in the LMC. In *BeXRB 2017 conference, September 2017, Heraklion, Greece. Abstracts available online at <https://sites.google.com/site/bexrb2017/>*, 2017a. [60](#)
- N. van Jaarsveld, D. A. H. Buckley, V. A. McBride, et al. Identification of High Mass X-ray Binaries selected from XMM-Newton observations of the LMC. *ArXiv e-prints*, December 2017b. [1](#)
- N. van Jaarsveld, D. A. H. Buckley, V. A. McBride, et al. Identification of high-mass X-ray binaries selected from XMM-Newton observations of the LMC. *Monthly Notices of the Royal Astronomical Society*, 475:3253–3261, April 2018. doi: 10.1093/mnras/stx3270. [36](#), [38](#), [39](#), [40](#), [41](#), [42](#)
- J. T. VanderPlas. Understanding the Lomb-Scargle Periodogram. *ArXiv e-prints*, March 2017. [29](#)
- G. Vasilopoulos, P. Maggi, F. Haberl, et al. Swift J053041.9-665426, a new Be/X-ray binary pulsar in the Large Magellanic Cloud. *Astronomy & Astrophysics*, 558:A74, October 2013a. doi: 10.1051/0004-6361/201322335. [36](#), [55](#), [125](#), [146](#), [152](#)
- G. Vasilopoulos, P. Maggi, F. Haberl, et al. Swift J053041.9-665426, a new Be/X-ray binary pulsar in the Large Magellanic Cloud. *Astronomy & Astrophysics*, 558:A74, October 2013b. doi: 10.1051/0004-6361/201322335. [1](#)
- G. Vasilopoulos, P. Maggi, R. Sturm, et al. X-ray outburst of RX J0520.5-6932, confirmed as a Be/X-ray binary. *The Astronomer's Telegram*, 4748:1, January 2013c. [36](#), [83](#)
- G. Vasilopoulos, R. Sturm, F. Haberl, P. Maggi, and A. Udalski. Swift J045558.9-702001, a new HMXB in the LMC. *The Astronomer's Telegram*, 5540, November 2013d. [36](#)
- G. Vasilopoulos, F. Haberl, R. Sturm, P. Maggi, and A. Udalski. Spectral and temporal properties of RX J0520.5-6932 (LXP 8.04) during a type-I outburst. *Astronomy & Astrophysics*, 567:A129, July 2014a. doi: 10.1051/0004-6361/201423934. [36](#), [55](#), [59](#), [95](#), [104](#), [123](#), [146](#), [152](#)
- G. Vasilopoulos, F. Haberl, R. Sturm, P. Maggi, and A. Udalski. Spectral and temporal properties of RX J0520.5-6932 (LXP 8.04) during a type-I outburst. *Astronomy & Astrophysics*, 567:A129, July 2014b. doi: 10.1051/0004-6361/201423934. [1](#)
- G. Vasilopoulos, R. Sturm, P. Maggi, and F. Haberl. The X-ray outburst of RX J0520.5-6932 is reaching the Eddington luminosity. *The Astronomer's Telegram*, 5760:1, January 2014c. [36](#)
- G. Vasilopoulos, F. Haberl, V. Antoniou, and A. Zezas. X-ray outburst of XMMU J004855.5-734946: confirmation as a Be/X-ray binary pulsar. *The Astronomer's Telegram*, 9229, July 2016a. [143](#)
- G. Vasilopoulos, F. Haberl, C. Delvaux, R. Sturm, and A. Udalski. Multi-wavelength properties of IGR J05007-7047 (LXP 38.55) and identification as a Be X-ray binary pulsar in the LMC. *Monthly Notices of the Royal Astronomical Society*, 461:1875–1884, September 2016b. doi: 10.1093/mnras/stw1408. [36](#), [55](#), [60](#), [137](#), [146](#), [152](#)
- G. Vasilopoulos, F. Haberl, C. Delvaux, R. Sturm, and A. Udalski. Multi-wavelength properties of IGR J05007-7047 (LXP 38.55) and identification as a Be X-ray binary pulsar in the LMC.

## REFERENCES

---

- Monthly Notices of the Royal Astronomical Society*, 461:1875–1884, September 2016c. doi: 10.1093/mnras/stw1408. [1](#)
- G. Vasilopoulos, F. Haberl, and P. Maggi. Identification of IGR J01217-7257 with the transient SMC pulsar XTE J0119-731 (SXP 2.16) using XMM-Newton. *Monthly Notices of the Royal Astronomical Society*, 470:1971–1981, September 2017a. doi: 10.1093/mnras/stx1359. [1](#)
- G. Vasilopoulos, F. Haberl, and P. Maggi. Identification of IGR J01217-7257 with the transient SMC pulsar XTE J0117-731 (SXP 2.16) using XMM-Newton. *MNRAS submitted*, 0:0, 0 2017b. doi: 0. [153](#)
- G. Vasilopoulos, A. Zezas, V. Antoniou, and F. Haberl. SXP 15.6: X-ray spectral and temporal properties of a newly discovered pulsar in the Small Magellanic Cloud. *Monthly Notices of the Royal Astronomical Society*, 470:4354–4362, October 2017c. doi: 10.1093/mnras/stx1507. [47](#), [60](#)
- G. Vasilopoulos, A. Zezas, V. Antoniou, and F. Haberl. SXP 15.6: X-ray spectral and temporal properties of a newly discovered pulsar in the Small Magellanic Cloud. *Monthly Notices of the Royal Astronomical Society*, 470:4354–4362, October 2017d. doi: 10.1093/mnras/stx1507. [1](#)
- G. Vasilopoulos, C. Maitra, F. Haberl, D. Hatzidimitriou, and M. Petropoulou. Identification of two new HMXBs in the LMC: an 2013 s pulsar and a probable SFXT. *Monthly Notices of the Royal Astronomical Society*, 475:220–231, March 2018. doi: 10.1093/mnras/stx3139. [1](#), [8](#), [36](#), [188](#)
- D. A. Verner, G. J. Ferland, K. T. Korista, and D. G. Yakovlev. Atomic Data for Astrophysics. II. New Analytic FITS for Photoionization Cross Sections of Atoms and Ions. *Astrophysical Journal*, 465:487, July 1996. doi: 10.1086/177435. [53](#), [115](#), [129](#), [147](#)
- V. A. Villar, E. Berger, R. Chornock, et al. The Intermediate Luminosity Optical Transient SN 2010da: The Progenitor, Eruption, and Aftermath of a Peculiar Supergiant High-mass X-Ray Binary. *Astrophysical Journal*, 830:11, October 2016. doi: 10.3847/0004-637X/830/1/11. [189](#)
- E. A. Vitrichenko, D. K. Nadyozhin, and T. L. Razinkova. Mass-luminosity relation for massive stars. *Astronomy Letters*, 33:251–258, April 2007. doi: 10.1134/S1063773707040044. [62](#)
- N. R. Walborn and E. L. Fitzpatrick. Contemporary optical spectral classification of the OB stars - A digital atlas. *PASP*, 102:379–411, April 1990. doi: 10.1086/132646. [76](#), [77](#)
- R. Walter, A. A. Lutovinov, E. Bozzo, and S. S. Tsygankov. High-mass X-ray binaries in the Milky Way. A closer look with INTEGRAL. *Astronomy & Astrophysics Review*, 23:2, August 2015. doi: 10.1007/s00159-015-0082-6. [8](#)
- D. J. Walton, F. A. Harrison, B. W. Grefenstette, et al. Broadband X-Ray Spectra of the Ultraluminous X-Ray Source Holmberg IX X-1 Observed with NuSTAR, XMM-Newton, and Suzaku. *Astrophysical Journal*, 793:21, September 2014. doi: 10.1088/0004-637X/793/1/21. [183](#)
- D. J. Walton, M. J. Middleton, V. Rana, et al. NuSTAR, XMM-Newton, and Suzaku Observations of the Ultraluminous X-Ray Source Holmberg II X-1. *Astrophysical Journal*, 806:65, June 2015. doi: 10.1088/0004-637X/806/1/65. [183](#)
- D. J. Walton, F. Fürst, F. A. Harrison, et al. Super-Eddington accretion on to the neutron star NGC 7793 P13: Broad-band X-ray spectroscopy and ultraluminous X-ray sources. *Monthly Notices of the Royal Astronomical Society*, 473:4360–4376, February 2018. doi: 10.1093/mnras/stx2650. [8](#)
- Y.-M. Wang. Disc accretion by magnetized neutron stars - A reassessment of the

- torque. *Astronomy & Astrophysics*, 183: 257–264, September 1987. [9](#)
- Y.-M. Wang. On the Torque Exerted by a Magnetically Threaded Accretion Disk. *Astrophysical Journal Letters*, 449:L153, August 1995. doi: 10.1086/309649. [9](#), [187](#), [188](#)
- Y.-M. Wang and J. Frank. Plasma infall and X-ray production in the magnetic funnel of an accreting neutron star. *Astronomy & Astrophysics*, 93:255–268, January 1981. [171](#)
- M. G. Watson, A. C. Schröder, D. Fyfe, et al. The XMM-Newton serendipitous survey. V. The Second XMM-Newton serendipitous source catalogue. *Astronomy & Astrophysics*, 493:339–373, January 2009. doi: 10.1051/0004-6361:200810534. [26](#), [50](#), [70](#), [84](#), [97](#), [113](#), [128](#)
- W. Wegner. Absolute magnitudes of OB and Be stars based on Hipparcos parallaxes - II. *Monthly Notices of the Royal Astronomical Society*, 371:185–192, September 2006. doi: 10.1111/j.1365-2966.2006.10549.x. [58](#)
- B. F. West, K. D. Wolfram, and P. A. Becker. A New Two-fluid Radiation-hydrodynamical Model for X-Ray Pulsar Accretion Columns. *Astrophysical Journal*, 835:129, February 2017a. doi: 10.3847/1538-4357/835/2/129. [178](#), [179](#), [180](#)
- B. F. West, K. D. Wolfram, and P. A. Becker. Dynamical and Radiative Properties of X-Ray Pulsar Accretion Columns: Phase-averaged Spectra. *Astrophysical Journal*, 835:130, February 2017b. doi: 10.3847/1538-4357/835/2/130. [131](#), [141](#), [180](#)
- N. E. White, J. H. Swank, and S. S. Holt. Accretion powered X-ray pulsars. *Astrophysical Journal*, 270:711–734, July 1983. doi: 10.1086/161162. [16](#), [108](#)
- J. Wilms, A. Allen, and R. McCray. On the Absorption of X-Rays in the Interstellar Medium. *Astrophysical Journal*, 542:914–924, October 2000. doi: 10.1086/317016. [14](#), [53](#), [71](#), [86](#), [98](#), [115](#), [129](#), [130](#), [147](#), [148](#), [161](#)
- H. Wolter. Spiegelsysteme streifenden Einfallstrahlen als abbildende Optiken für Röntgenstrahlen. *Annalen der Physik*, 445:94–114, 1952. doi: 10.1002/andp.19524450108. [25](#)
- A. K. Yoldağ, T. Krühler, J. Greiner, et al. First Results of GROND. In M. Galassi, D. Palmer, and E. Fenimore, editors, *American Institute of Physics Conference Series*, volume 1000 of *American Institute of Physics Conference Series*, pages 227–231, May 2008. doi: 10.1063/1.2943450. [119](#)
- D. G. York, J. Adelman, J. E. Anderson, Jr., et al. The Sloan Digital Sky Survey: Technical Summary. *Astronomical Journal*, 120:1579–1587, September 2000. doi: 10.1086/301513. [119](#)
- D. Zaritsky, J. Harris, I. B. Thompson, and E. K. Grebel. The Magellanic Clouds Photometric Survey: The Large Magellanic Cloud Stellar Catalog and Extinction Map. *Astronomical Journal*, 128:1606–1614, October 2004. doi: 10.1086/423910. [27](#), [41](#), [42](#), [74](#), [76](#), [77](#)
- A. A. Zdziarski, W. N. Johnson, and P. Magdziarz. Broad-band  $\gamma$ -ray and X-ray spectra of NGC 4151 and their implications for physical processes and geometry. *Monthly Notices of the Royal Astronomical Society*, 283:193–206, November 1996. doi: 10.1093/mnras/283.1.193. [131](#)
- E. R. Zimmerman, R. Narayan, J. E. McClintock, and J. M. Miller. Multitemperature Blackbody Spectra of Thin Accretion Disks with and without a Zero-Torque Inner Boundary Condition. *Astrophysical Journal*, 618:832–844, January 2005. doi: 10.1086/426071. [12](#), [13](#)
- P. T. Życki, C. Done, and D. A. Smith. The 1989 May outburst of the soft X-ray transient GS 2023+338 (V404 Cyg). *Monthly Notices of the Royal Astronomical Society*, 309:561–575, November 1999. doi: 10.1046/j.1365-8711.1999.02885.x. [131](#)

## REFERENCES

---

## Acronyms

<b>AEF</b>	accelerated epoch folding.
<b>AGN</b>	Active Galactic Nucleus.
<b>AXP</b>	Anomalous X-Ray Pulsars.
<b>BB</b>	Black Body.
<b>BeXRB</b>	Be X-ray Binary.
<b>BH</b>	Black Hole.
<b>BXA</b>	Bayesian X-ray analysis.
<b>DBB</b>	Disc Blackbody.
<b>EF</b>	epoch folding.
<b>EPIC</b>	European Photon Imaging Camera.
<b>GRB</b>	Gamma Ray Burst.
<b>HMXB</b>	High Mass X-ray Binary.
<b>HR</b>	Hardness Ratio.
<b>INTEGRAL</b>	International Gamma-ray Astrophysics Laboratory.
<b>ISM</b>	Inter Stellar Medium.
<b>LMBH</b>	low-mass black holes.
<b>LMC</b>	Large Magellanic Cloud.
<b>LMC-VLP</b>	LMC very large program.
<b>LMXB</b>	Low Mass X-ray Binary.
<b>LPP</b>	Long Period Pulsars.
<b>LS</b>	Lomb-Scargle.
<b>MCPS</b>	Magellanic Clouds Photometric Survey.
<b>MCs</b>	Magellanic Clouds.
<b>MHD</b>	Magneto Hydro Dynamics.
<b>MPE</b>	Max Planck Institute for extraterrestrial Physics.
<b>MTB</b>	Multitemperature Blackbody.
<b>MTC</b>	multi-temperature components.
<b>NS</b>	Neutron Star.

## Acronyms

---

<b>OGLE</b>	Optical Gravitational Lensing Experiment.
<b>PF</b>	Pulsed Fraction.
<b>PL</b>	power-law.
<b>SF</b>	Star Formation.
<b>SFH</b>	Star Formation History.
<b>SFXT</b>	Supergiant Fast X-ray Transient.
<b>Sg</b>	Supergiant.
<b>SgXRB</b>	Supergiant X-ray binary.
<b>SMC</b>	Small Magellanic Cloud.
<b>SNR</b>	Supernova Remnant.
<b>SSS</b>	Super-soft sources.
<b>ToO</b>	target of opportunity.
<b>TUM</b>	Technische Universität München.
<b>UCXB</b>	Ultra-compact X-ray Binary.
<b>ULX</b>	Ultra-luminous X-ray source.
<b>ULXP</b>	Ultra-luminous X-ray Pulsar.
<b>WD</b>	White Dwarf.
<b>XRB</b>	X-ray binary.
<b>XRP</b>	X-ray Pulsar.